

AD-524161

RIA-79-U674

met

~~CONFIDENTIAL~~

UNCLASSIFIED

AFRPL-TR-72-133

5 0712 01014470 6



USADACS Technical Library

**AN INVESTIGATION OF EXTERNAL
BURNING PROPULSION FOR THE
75MM PROJECTILE (U)**

Harvey L. Fein
Dwight E. Shelor

Atlantic Research Corporation

**TECHNICAL REPORT AFRPL-TR-72-133
January 1973**

Classified by AFRPL/MK
Subject to General Declassification
Schedule of Executive Order 11652
Automatically Downgraded at Two Year Intervals
Declassified on 31 December 1979

This material contains information affecting the national defense of the United States within the meaning of the espionage laws, Title 18, U.S.C. Sections 793 and 794, the transmission or revelation of which in any manner to an unauthorized person is prohibited by law.

Air Force Rocket Propulsion Laboratory
Director of Laboratories
Air Force Systems Command
United States Air Force
Edwards, California

UNCLASSIFIED

~~CONFIDENTIAL~~

COPY NO. 56

cm 45608

~~CONFIDENTIAL~~
UNCLASSIFIED (THIS PAGE IS UNCLASSIFIED)

SPECIAL NOTICES

When U.S. Government drawings, specifications, or other data are used for any purpose other than a definitely related Government procurement operation, the Government thereby incurs no responsibility nor any obligation whatsoever, and the fact that the Government may have formulated, furnished, or in any way supplied the said drawings, specifications or other data, is not to be regarded by implication or otherwise, or in any manner licensing the holder or any other person or corporation, or conveying any rights or permission to manufacture use, or sell any patented invention that may in any way be related thereto.

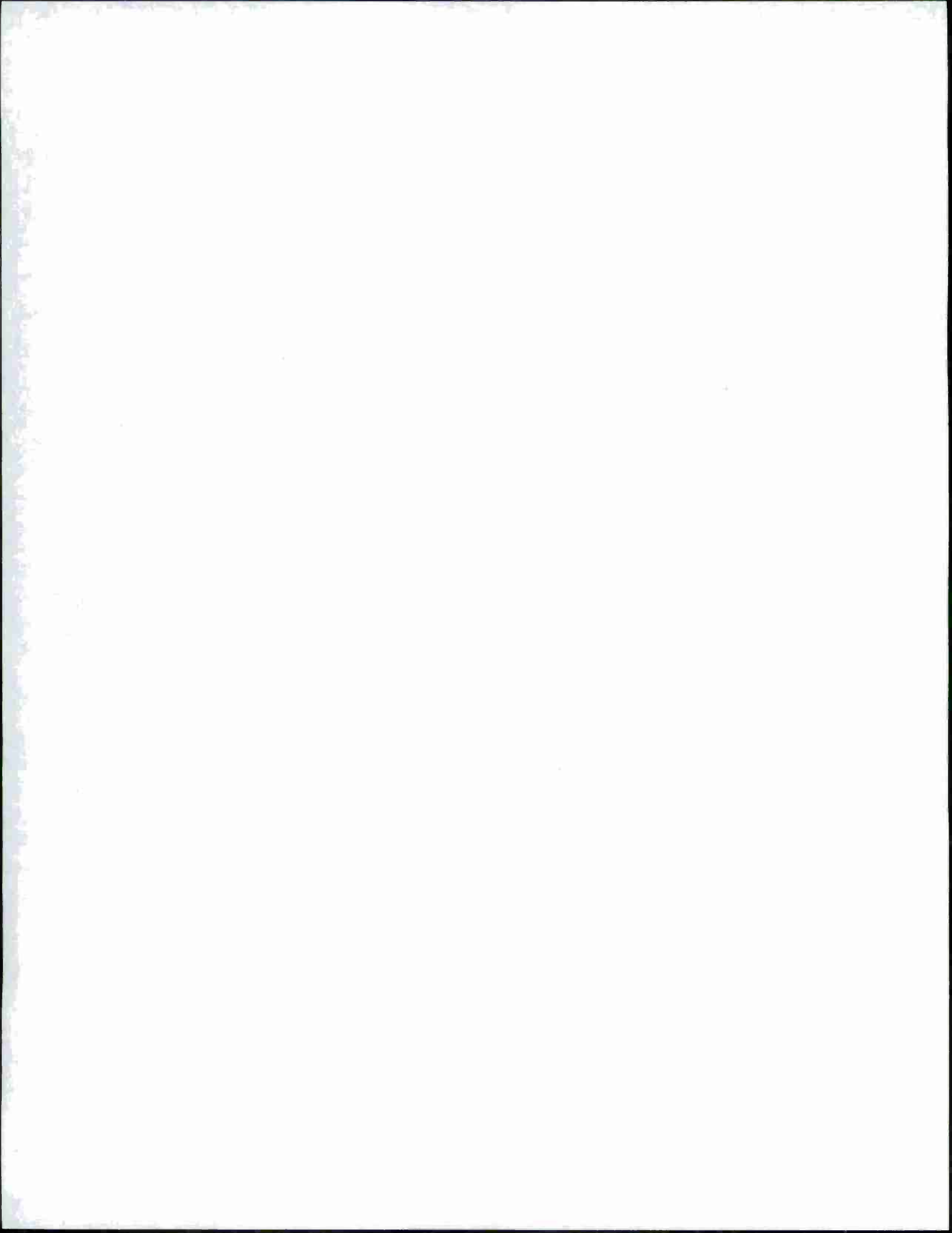
UNCLASSIFIED

~~CONFIDENTIAL~~
(THIS PAGE IS UNCLASSIFIED)

THIS REPORT HAS BEEN DELIMITED
AND CLEARED FOR PUBLIC RELEASE
UNDER E.O. DIRECTIVE 5200.20 AND
NO RESTRICTIONS ARE IMPOSED UPON
ITS USE AND DISCLOSURE.

DISTRIBUTION STATEMENT A

APPROVED FOR PUBLIC RELEASE;
DISTRIBUTION UNLIMITED.



~~CONFIDENTIAL~~

UNCLASSIFIED

AN INVESTIGATION OF EXTERNAL
BURNING PROPULSION FOR THE
75MM PROJECTILE (U)

Harvey L. Fein
Dwight E. Shelor
Atlantic Research Corporation

Classified by AFRPL/MK
Subject to General Declassification
Schedule of Executive Order 11652
Automatically Downgraded at Two Year Intervals
Declassified on 31 December 1979

This material contains information affecting the national defense of the United States within the meaning of the espionage laws, Title 18, U.S.C. Sections 793 and 794, the transmission or revelation of which in any manner to an unauthorized person is prohibited by law.

UNCLASSIFIED

~~CONFIDENTIAL~~

~~CONFIDENTIAL~~

(THIS PAGE IS UNCLASSIFIED)

UNCLASSIFIED

FOREWORD

(U) This is the Final Technical Report issued under Contract F04611-72-C-0044, "External Burning Assisted Projectile Feasibility Demonstration," and covers work performed during the period 1 March 1972 through 30 November 1972. The work described in this report was conducted under Project 3148, Task 10, Program Element 62302F. The contract was assigned to Atlantic Research Corporation, Alexandria, Virginia. Lt. Albert T. Clary (AFRPL/MKCD), Air Force Rocket Propulsion Laboratory, Edwards Air Force Base, Edwards, California, was the Technical Monitor.

(U) The technical effort on this program was performed by the Engineering Research Department, Dr. K. E. Woodcock, Manager, under the Director of Research and Technology, Mr. Charles B. Henderson. Dr. Harvey L. Fein was the Program Manager and Principal Investigator. Mr. Dwight E. Shelor was responsible for hardware design and generation of test data. Dr. G. A. Hosack and Mr. R. A. O'Leary of Rocketdyne Division, North American Rockwell Corporation, performed analytical studies under subcontract to Atlantic Research Corporation.

(U) This report contains no classified information extracted from other classified documents.

(U) This technical report has been reviewed and is approved.

Charles R. Cooke
Chief, Solid Rocket Division

UNCLASSIFIED

~~CONFIDENTIAL~~

(THIS PAGE IS UNCLASSIFIED)

UNCLASSIFIED

ABSTRACT

(U) Twenty external burning combustion tests were conducted with a 75mm half-model using the exhausts from fuel-rich solid propellants as the fuels. Test conditions simulated Mach 2.5 and Mach 2.0 flight at both sea level and an altitude of 15,000 feet. Base pressure ratios up to 0.85 were obtained at sea level, while at altitude these ratios were greater than unity. There was strong evidence that a wind tunnel interference effect severely restricted the measured base pressure rises. Since this interference effect would not be present in a real flight environment, flight performance should be significantly better than indicated by the current results.

UNCLASSIFIED

UNCLASSIFIED

UNCLASSIFIED

UNCLASSIFIED

TABLE OF CONTENTS

Section	Page
I SUMMARY	1
II INTRODUCTION	2
III APPARATUS AND PROCEDURE	4
1. Atlantic Research High Pressure Air Facility	4
2. Test Configuration	4
3. Instrumentation	7
a. Summary of Measurements	7
b. Locations of Pressure Measurements	8
c. Description of Schlieren System	11
d. Description of Spectrograph	11
4. Propellants	11
a. Thermodynamic Properties	11
b. Propellant Burning Rates	13
c. Fuel Flow Rate Determination	13
5. Test Conditions	20
6. Test Procedure	22
IV RESULTS	25
1. Tests with ARCADENE 129A	25
2. Tests with ARCADENE 168A at Mach 2.5, Sea-Level Flight Conditions	32
3. Test 14 with ARCADENE 300	55
4. ARCADENE 168A Tests at Mach 2.5, 15,000-foot Altitude Flight Conditions	58
5. Tests with ARCADENE 168A at Mach 2.0, 15,000-foot Altitude Flight Conditions	63
6. Tests with ARCADENE 168A at Mach 2.0, Sea-Level Flight Conditions	68
V DISCUSSION OF RESULTS	73
1. Base Pressures Without Fuel Injection	73
2. Downstream Pressure Distributions Without Fuel Injection	76
3. Base Pressures with Fuel Injection	80

UNCLASSIFIED

TABLE OF CONTENTS (Continued)

Section	Page
a. ARCADENEs 168A and 300, Sea Level, Mach 2.5	80
b. ARCADENE 168A, 15,000-foot Altitude, Mach 2.5	83
c. ARCADENE 168A, Sea-Level and 15,000-foot Altitude, Mach 2.0	83
d. ARCADENE 129A, Sea Level, Mach 2.5	83
4. Significance of the Measured Base Pressures	83
5. Downstream Pressure Distributions with Fuel Injection	86
6. The Effect of Shock Wave Reflections on Base Pressure	89
7. Lip Pressures	92
8. Base Flow Temperatures	99
9. Specific Impulse	99
VI CONCLUSIONS AND RECOMMENDATIONS	104
1. Conclusions	104
2. Recommendations	105
APPENDIX I – JET PENETRATION AND MIXING CALCULATIONS	
APPENDIX II – ANALYTICAL EFFORT CONDUCTED BY ROCKETDYNE DIVISION NORTH AMERICAN ROCKWELL CORPORATION	
REFERENCES	

UNCLASSIFIED

LIST OF ILLUSTRATIONS

Figure		Page
1	Schematic Diagram of the External Burning Propulsion Concept	2
2	Schematic Diagram of Atlantic Research High Pressure Air Facility	5
3	External Burning Test Configuration	6
4	Pressure Tap Locations for 9-Nozzle Normal Injection Configuration	9
5	Pressure Tap Locations for 5-Nozzle Normal Injection Configuration	11
6	Diagram of Schlieren System	12
7	Strand Burning Rates for Propellants	15
8	Pressure-Time Trace for ARCADENE 168A Test Firing	17
9	Throat Area Variation for ARCADENE 168A Test Firing	18
10	Mass Flow Rate Versus Time for ARCADENE 168A Test Firing	19
11	Results from Test 1	26
12	Results from Test 2	27
13	Results from Test 3	28
14	Downstream Pressure Distributions, Test 1	29
15	Downstream Pressure Distributions, Test 2	30
16	Downstream Pressure Distributions, Test 3	31
17	Results from Test 4	33
18	Results from Test 5	34
19	Results from Test 6	35
20	Results from Test 7	36

UNCLASSIFIED

LIST OF ILLUSTRATIONS (Continued)

Figure		Page
21	Results from Test 8	37
22	Results from Test 9	38
23	Results from Test 10	39
24	Results from Test 11	40
25	Results from Test 12	41
26	Results from Test 13	42
27	Downstream Pressure Distributions, Test 4	43
28	Downstream Pressure Distributions, Test 5	44
29	Downstream Pressure Distributions, Test 6	45
30	Downstream Pressure Distributions, Test 7	46
31	Downstream Pressure Distributions, Test 8	47
32	Downstream Pressure Distributions, Test 9	48
33	Downstream Pressure Distributions, Test 10	49
34	Downstream Pressure Distributions, Test 11	50
35	Downstream Pressure Distributions, Test 12	51
36	Downstream Pressure Distributions, Test 13	52
37	Results from Test 14	56
38	Downstream Pressure Distributions, Test 14	57
39	Results from Test 15	59
40	Results from Test 16	60

UNCLASSIFIED

LIST OF ILLUSTRATIONS (Continued)

Figure		Page
41	Downstream Pressure Distributions, Test 15	61
42	Downstream Pressure Distributions, Test 16	62
43	Results from Test 17	64
44	Results from Test 18	65
45	Downstream Pressure Distributions, Test 17	66
46	Downstream Pressure Distributions, Test 18	67
47	Results from Test 19	69
48	Results from Test 20	70
49	Downstream Pressure Distributions, Test 19	71
50	Downstream Pressure Distributions, Test 20	72
51	Base Pressure Ratios Before Fuel Injection for Mach 2.5, Sea-Level Tests	75
52	Base Pressure Ratios for Sea-Level, Mach 2.5 Tests with ARCADENE 168A and 300	81
53	Base Pressure Ratios for 15,000-foot Altitude, Mach 2.5 Tests	84
54	Base Pressure Ratios for Mach 2.0 Tests	85
55	Diagram Showing Interaction Shock Wave Reflection and Relation to Downstream Pressure Distributions	88
56	Downstream Pressure Distributions for Air Injection Test	91
57	Lip Pressures on Line with Port for Mach 2.5 Tests with ARCADENE 168A and 300	93
58	Lip Pressures Between Ports for Mach 2.5 Tests with ARCADENE 168A and 300	94

UNCLASSIFIED

LIST OF ILLUSTRATIONS (Continued)

Figure		Page
59	Lip Pressures on Line with Port for Mach 2.0 Tests	96
60	Lip Pressures Between Ports for Mach 2.0 Tests	97
61	Lip Pressure Ratios for Tests 1, 2 and 3 with ARCADENE 129A	98
62	Base Flow Temperatures	100
63	Corrected Specific Impulse Values for Mach 2.5 Tests Conducted with ARCADENE 168A and ARCADENE 300	101
64	Specific Impulse Values for Mach 2.0 Tests	103
65	Generalized Model Configuration for Gaseous Secondary Injection into a Supersonic Free Stream	107
66	Overall Computer Program Flow Chart	143
67	Inputs Needed for Method of Characteristics and Base Pressure with Heat Addition Computer Program	144
68	Coordinate System for Shock Shape Analysis	146
69	Ideal Method to Determine \dot{q}' for a Given Wind Tunnel Value of P_B	149
70	Actual Method Used to Obtain \dot{q}' Required to Match Experimental Base Pressure	150
71	Predictions for Test 104	155
72	Predictions for Test 106	156
73	Predictions for Test 108	157
74	Predictions for Test 110	158

UNCLASSIFIED

LIST OF TABLES

Table	Page
I Selected Properties of Propellants	14
II Propellant and Injection Geometry Data for External Burning Tests	21
III Air Stream Conditions for External Burning Tests	23
IV Base Pressures Without Fuel Injection	74
V Comparison of Downstream Pressure Distributions Without Fuel Injection	77
VI Flow Parameters for Angular Injection Tests	110
VII Results of Jet Penetration and Mixing Calculations for Test 1-1	112
VIII Results of Jet Penetration and Mixing Calculations for Test 1-2	113
IX Results of Jet Penetration and Mixing Calculations for Test 1-3	114
X Results of Jet Penetration and Mixing Calculations for Test 1-4	115
XI Results of Jet Penetration and Mixing Calculations for Test 1-5	116
XII Results of Jet Penetration and Mixing Calculations for Test 1-6	117
XIII Results of Jet Penetration and Mixing Calculations for Test 1-7	118
XIV Results of Jet Penetration and Mixing Calculations for Test 1-8	119
XV Results of Jet Penetration and Mixing Calculations for Test 1-9	122
XVI Results of Jet Penetration and Mixing Calculations for Test 1-10	123
XVII Results of Jet Penetration and Mixing Calculations for Test 1-11	124
XVIII Results of Jet Penetration and Mixing Calculations for Test 1-12	125
XIX Results of Jet Penetration and Mixing Calculations for Test 1-13	126
XX Results of Jet Penetration and Mixing Calculations for Test 1-14	127

UNCLASSIFIED

LIST OF TABLES (Continued)

Table	Page
XXI Results of Jet Penetration and Mixing Calculations for Test 1-15	128
XXII Results of Jet Penetration and Mixing Calculations for Test 1-16	129
XXIII Results of Jet Penetration and Mixing Calculations for Test 1-17	130
XXIV Results of Jet Penetration and Mixing Calculations for Test 1-18	131
XXV Results of Jet Penetration and Mixing Calculations for Test 1-19	132
XXVI Results of Jet Penetration and Mixing Calculations for Test 1-20	133
XXVII Results of Jet Penetration and Mixing Calculations for Test 1-21	134
XXVIII Results of Jet Penetration and Mixing Calculations for Test 1-22	135
XXIX Results of Jet Penetration and Mixing Calculations for Test 1-23	136
XXX Results of Jet Penetration and Mixing Calculations for Test 1-24	137
XXXI Results of Jet Penetration and Mixing Calculations for Test 1-25	138
XXXII Results of Jet Penetration and Mixing Calculations for Test 1-26	139
XXXIII Results of Jet Penetration and Mixing Calculations for Test 1-27	140
XXXIV Results of Jet Penetration and Mixing Calculations for Test 1-28	141
XXXV Computer Inputs	153
XXXVI Computer Results	154

~~CONFIDENTIAL~~

SECTION I

SUMMARY

(C) Theoretical analyses^(1,2) and experimental results^(3,4) have indicated that an external burning propulsion concept using the exhaust from a solid propellant as the fuel can offer significant performance gains for a projectile over what can be achieved using a conventional RAP. In this propulsion concept, the exhaust from a fuel-rich solid propellant is injected transversely through the vehicle boundary layer into the supersonic air stream surrounding the separation bubble at the vehicle base. There, mixing and supersonic combustion occur, and the resulting pressure rise is transmitted to the vehicle base through the subsonic separation bubble. The analysis of Reference (1) and the experiments of References (3) and (4) indicate that base pressures above the free-stream static pressure are achievable with this concept.

(U) The experiments referred to above were conducted with a 5-inch-diameter half-model. The objective of the present program was to establish the feasibility of the external burning propulsion concept as applied to a 75mm projectile.

(U) In order to conduct the experiments, a full-scale 75mm half-model was fabricated, and this served as the centerbody for two semicircular annular nozzles. The nozzles were contoured to provide Mach 2.0 and Mach 2.5 exit flows. Twenty external burning tests were then conducted: fourteen at Mach 2.5, sea-level flight conditions; two at Mach 2.5, 15,000-foot altitude flight conditions; two at Mach 2.0, 15,000-foot altitude flight conditions, and two at Mach 2.5, sea-level flight conditions. In addition to pressure measurements on the model and in the wake downstream from the base, color movies and black and white Schlieren movies were obtained for each test. Also, for some tests, emission spectra in the combustion zones and base flow temperatures were recorded.

(C) The tests showed that external burning of ARCADENE[®] 168A propellant provides significant base pressure rises. This propellant is composed of 35 percent aluminum, 53 percent ammonium perchlorate, and 12 percent of a hydrocarbon type binder. At the Mach 2.5, sea-level test conditions, base pressure ratios increased to 0.85; and at Mach 2.0, 15,000-foot altitude test conditions, base pressure ratios greater than unity were measured. The maximum indicated specific impulse was 280 at the Mach 2.5, sea-level, test conditions. Color movies of the tests and the emission spectra indicated that significant combustion occurred.

(C) During the tests, strong disturbances to the pressure distributions in the wake downstream from the base were noted. These disturbances resulted from reflections from the free-jet boundary of the injection interaction shock waves. These shock waves reflect as expansion waves which interact with the recompression process in the near wake. There is strong evidence that the decrease in pressure associated with these expansion waves was transmitted to the model base, significantly restricting the measured base pressure rises. Since the shock reflections would not be present in a real flight environment, flight performance should be significantly better than is indicated by the current test results.

~~CONFIDENTIAL~~

SECTION II

INTRODUCTION

(U) External burning has been studied for a variety of propulsion applications, e.g., generation of control forces,⁽⁵⁾ propulsion,⁽⁶⁾ and base drag reduction.^(7,8) In the present program, the concept of using external burning to provide net positive thrust to a 75mm projectile was experimentally investigated. This concept is referred to as an external burning assisted projectile (EBAP).

(U) The EBAP concept using a solid propellant as the fuel is shown schematically in Figure 1. Here the exhaust from a fuel-rich solid propellant is injected transversely through the vehicle boundary layer into the supersonic stream surrounding the separation bubble at the vehicle base. Combustion in this region causes a local stream tube area increase which in turn causes a pressure increase in the shear layer adjacent to the separation bubble. This pressure increase tends to entrap and compress the separation bubble giving rise to increased base pressures.

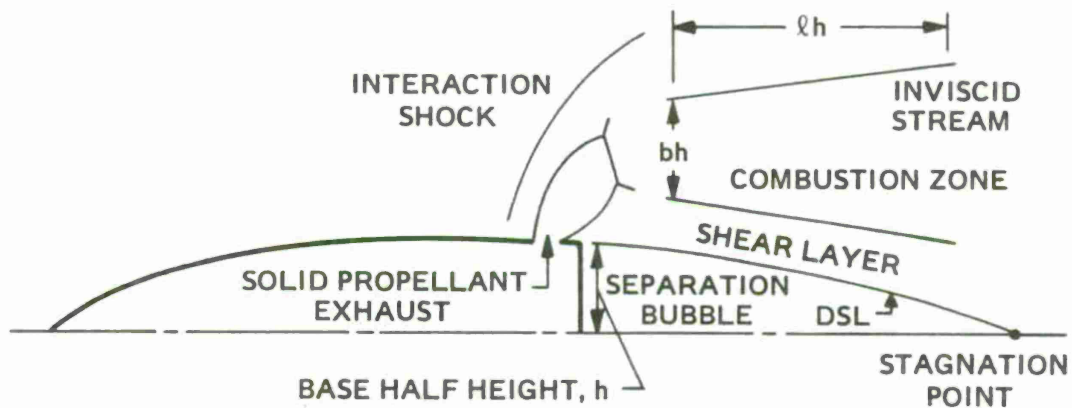


Figure 1. Schematic Diagram of the External Burning Propulsion Concept.

(U) The effect of heat release in the supersonic stream was analyzed by Strahle,⁽¹⁾ who computed the achievable base pressure rise as a function of the length and strength of the heat addition zone. Strahle's base pressure rises were simply computed by coupling a two-dimensional Crocco-Lees mixing theory⁽⁹⁾ treatment of the base flow to a combination of a one-dimensional and a linearized two-dimensional treatment of the supersonic heat release process. The results were very encouraging in that pressures significantly greater than the free-stream static pressure were computed, suggesting that net positive vehicle thrust can be obtained with this concept.

~~CONFIDENTIAL~~

(C) In Reference (2) the base pressure rises computed by Strahle were used to compute effective specific impulse values for fuel-rich solid propellants in an external burning assisted projectile. These specific impulse values were then used to compute the range or explosive weight improvement offered by the EBAP concept over that of a 5-inch, 54-caliber, rocket-assisted projectile. It was concluded that the external burning assisted projectile theoretically provides a significant range and/or explosive weight improvement over what is currently available with a rocket-assisted projectile. Specific impulse values ranging from 361 to 452 lbf-sec/lbm were computed for the EBAP concept using ARCADENE 168A, a moderately fuel-rich, state-of-the-art, solid propellant. The corresponding range improvement amounted to 64 percent above what is available with a rocket-assisted projectile. Alternatively, an explosive weight increase at constant range of at least 88 percent was computed.

(C) In experimental feasibility studies conducted for the Navy,^(3,4) eleven external burning propulsion tests were conducted with a 5-inch-diameter half-model at the simulated flight conditions of Mach 2 and a 15,000-foot altitude. Two state-of-the-art, fuel-rich, solid propellants were tested. For 90-degree sonic injection with a metal-free propellant designated ARCADENE 129A, base pressures 29 percent above the free-stream static pressure were measured. For an aluminum-containing propellant designated ARCADENE 168A, the base pressure rose to 18 percent above the free-stream static pressure. This latter base pressure rise corresponds to a fuel specific impulse of 402 lbf-sec/lbm. For sonic fuel injection 45 degrees aftward, the base pressure rose to 10 percent above the free-stream static pressure. If it is assumed that the same base pressure rise could be obtained with Mach 2 jets, then the total of the specific impulse associated with the base pressure rise and the axial component of the momentum of the fuel jets would be 460 lbf-sec/lbm. This specific impulse value closely approximates what is predicted theoretically.

(U) It was the objective of this program to experimentally determine the feasibility of the external burning propulsion concept as applied to the Air Force 75mm projectile now under development. To this end, a full-scale half-model was fabricated and installed in the Atlantic Research High Pressure Air Facility. Twenty external burning tests were then conducted at simulated flight conditions of Mach 2.0 and Mach 2.5 at both sea level and a 15,000-foot altitude. For these tests, the exhausts from fuel-rich solid propellants were used as fuels. The details of these tests, their results, and conclusions drawn from these results are presented in the following sections of this report. Recommendations for future work are also presented.

~~CONFIDENTIAL~~

SECTION III

APPARATUS AND PROCEDURE

1. ATLANTIC RESEARCH HIGH PRESSURE AIR FACILITY

(U) All of the external burning tests in this program were conducted in the Atlantic Research High Pressure Air Facility, which is shown schematically in Figure 2. This facility consists of a 625-cubic foot air reservoir capable of storing compressed air at 2500 psia, a pebble-bed heater capable of operating at 1500 psia with an exit air temperature of 3500°R, an air transfer system capable of operating at 1000 psia and 2400°R air temperature, and associated flow control systems and instrumentation. A Schlieren flow visualization system is available with high-speed photographic recording capabilities as well as spectrographic recording equipment. A closed-circuit TV system is available for remote visual observation of the test area during testing.

2. TEST CONFIGURATION

(U) A schematic drawing of the test configuration is presented in Figure 3. During a test, air flowed from the plenum, through the nozzle, and past the fuel injector body and cap. For sea-level tests, the air then exhausted to the atmosphere. For altitude tests, the air flowed into an enclosed free-jet test section and then exhausted to the atmosphere through a variable area diffuser.

(C) The fuels, which were the fuel-rich exhausts from the solid propellant rocket motor, flowed through the injector body to the fuel injection ports located in the fuel injector cap. From the injection ports, the fuel was injected into the air stream.

(U) The cross section of the nozzle centerbody was semicircular, and the air flow passage consisted of the semi-annular space between the centerbody and the contoured semicylindrical outer wall of the nozzle.

(U) Two outer nozzle contours were used: one to provide a Mach 2.5 flow at the exit, and the other to provide a Mach 2.0 exit flow. These contours were calculated with an axisymmetric method of characteristics computation and were corrected for turbulent boundary layer growth along the outer wall. No correction was made for boundary layer growth along the centerbody.

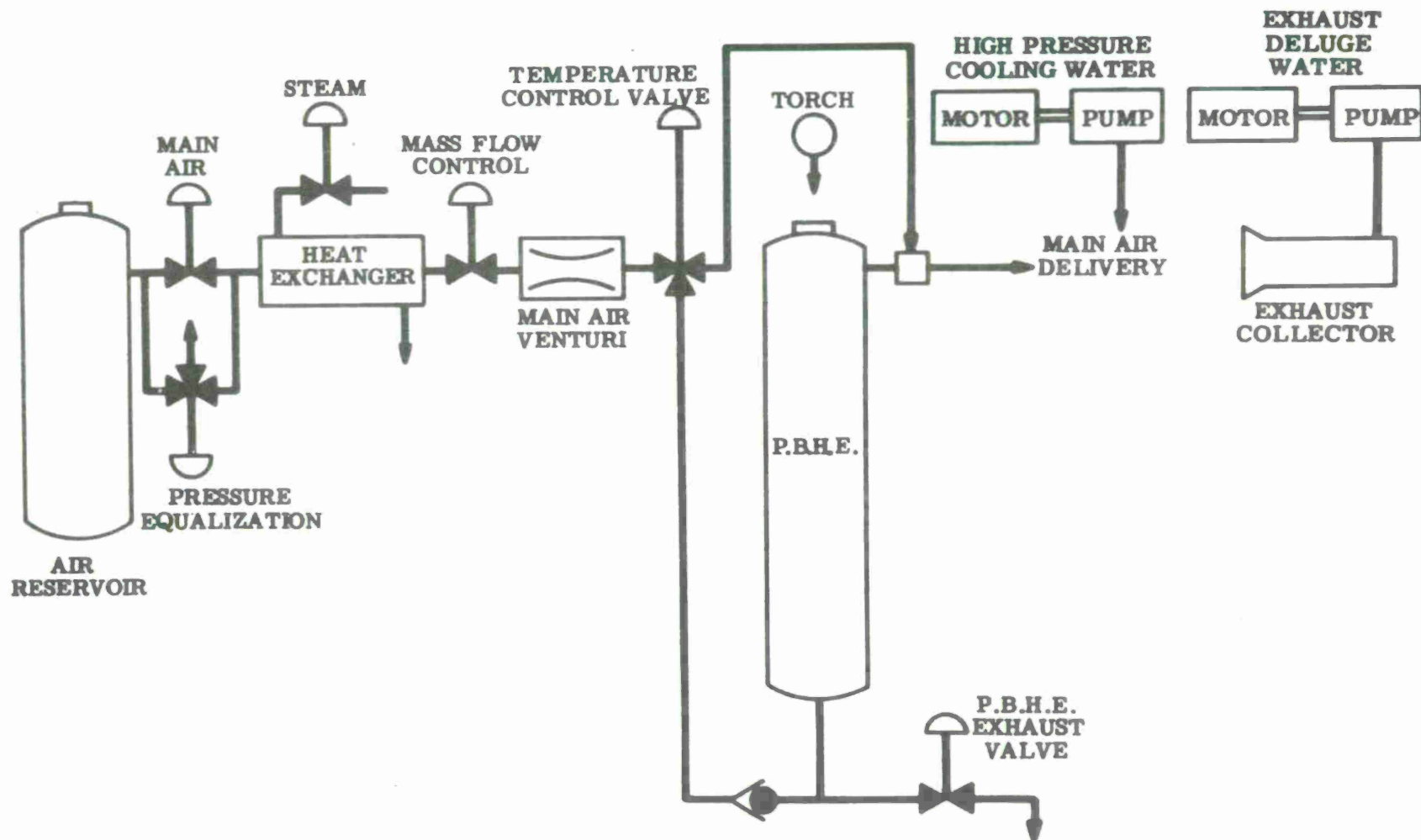
(U) The subsonic portion of the centerbody was a 20-degree semi-cone followed by a 5-inch-radius spherical section which was tangent to the cone and to a 37.5-mm (1.476-inch) semicylinder. The subsonic portions of the outer nozzle contours were semi-ogives with radii of 4.00 inches for both the Mach 2.5 and Mach 2.0 contours. These ogives were tangent to the outer nozzle walls at the throats.

(C) Three different injection configurations were used in the test program:

- a. Nine ports injecting normal to the flow 0.6 inch upstream from the model base
- b. Five ports injecting normal to the flow 0.6 inch upstream from the model base

UNCLASSIFIED

5



UNCLASSIFIED

Figure 2. Schematic Diagram of Atlantic Research High Pressure Air Facility.

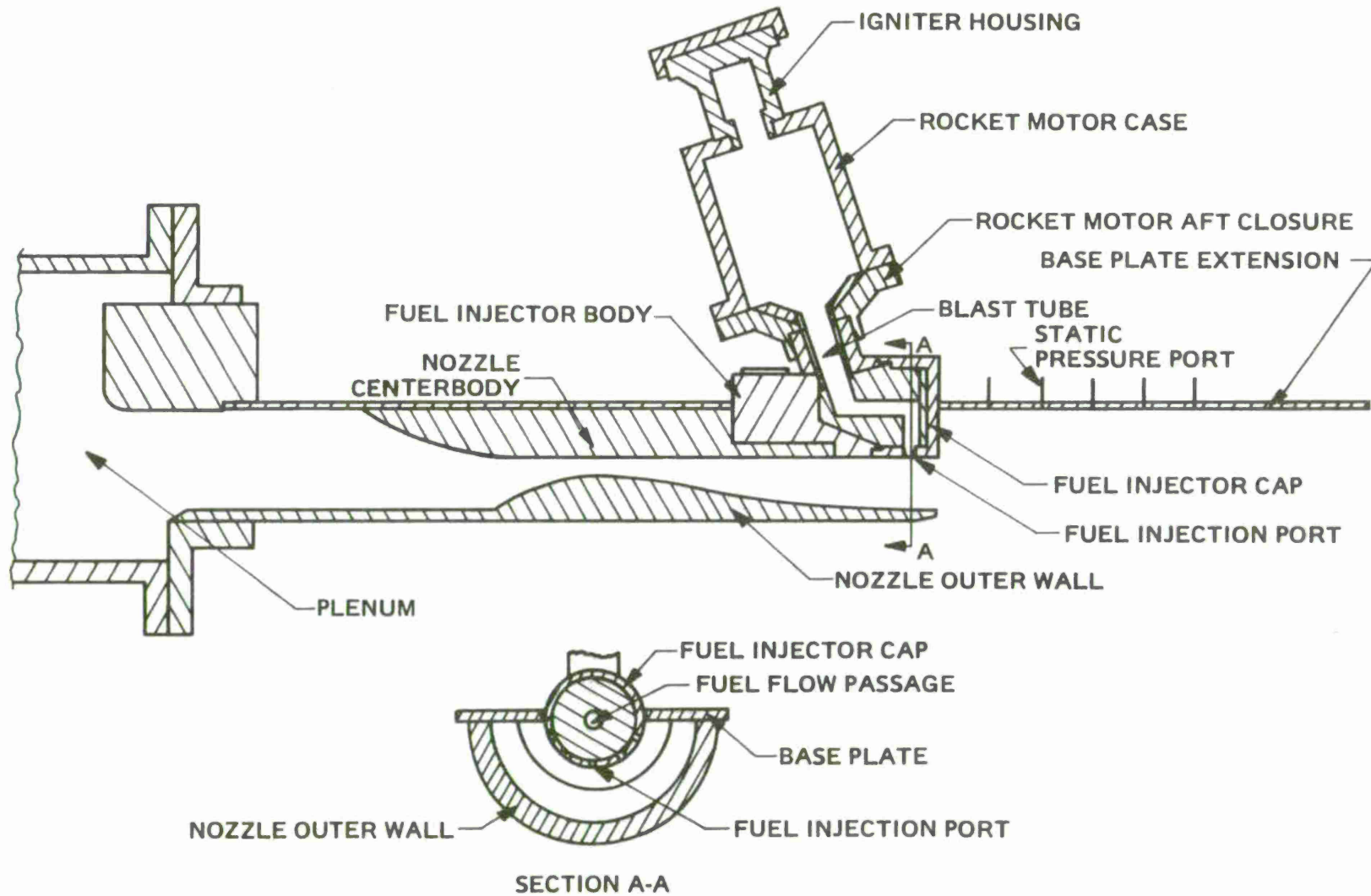


Figure 3. External Burning Test Configuration.

- c. Nine ports injecting 45 degrees downstream through the base corner

The entire injector body was filled with molded asbestos-phenolic insulation except for the 0.5-inch-diameter flow passage and 0.5-inch-wide semicircular gap between the insulation in the injector body and the insulated injector cap. The injection nozzle inserts were fabricated from ATJ graphite and insulated with an asbestos-phenolic sleeve.

(U) The rocket motor case had an inside diameter of 4.5 inches and the length was adequate to accommodate a 6-inch-long grain. An asbestos-phenolic sleeve and disc were used both to insulate the motor case and to fill the excess volume not occupied by the propellant grain. The motor aft closure was insulated with molded silica-phenolic insulation.

(U) The lower half of the fuel injector cap served as the half-model of the projectile base. Extending 12.75 inches downstream from the cap was a base plate extension. This base plate extension was tapped for static pressure measurements along its centerline.

(U) For the tests conducted at 15,000-foot altitude flight conditions, the model was mated to a free-jet enclosure and diffuser. The nozzle exit plane and the area two radii downstream from the base were observable through two 8-inch-diameter windows mounted in the sides of the enclosure. The windows permitted obtaining both Schlieren and conventional color movies of the tests as well as emission spectra.

(U) The dimensions of the free-jet enclosure were 10.0 inches in the vertical direction and 13.0 inches in the span-wise direction. The length of the test section from the model base to the entrance of the diffuser was 23.0 inches.

(U) The throat area of the diffuser was variable and controlled during a test to maintain the static pressure in the test section equal to the static pressure of the supersonic free stream.

3. INSTRUMENTATION

- a. Summary of Measurements

(U) During a test the following data were obtained:

- (1) Total pressures (2) upstream of the metering venturi in the air supply system
- (2) Total temperatures (2) upstream of the metering venturi in the air supply system
- (3) Static pressure downstream of the metering venturi in the air supply system
- (4) Static pressure at the exit from the pebble-bed heater
- (5) Static pressure in the cold air bypass line of the air supply system

- (6) Static pressure in the combustion chamber of the solid propellant rocket motor
- (7) Static pressure in the flow passage of the fuel injector body
- (8) Static pressures (2) in the subsonic section of the air nozzles at an area ratio of 1.62 for the Mach 2.5 nozzle and 1.39 for the Mach 2.0 nozzle
- (9) Total temperatures (2) in the plenum upstream from the air nozzle
- (10) Static pressure on the nozzle centerbody upstream from the fuel injector body (see below for location)
- (11) Static pressures (2) on the cylindrical surface of the fuel injector cap (see below for location)
- (12) Static pressures (4) on the base of the fuel injector cap (see below for location)
- (13) Static pressures (5) on the base plate extension (see below for location)
- (14) Static pressure on the outside of the nozzle outer wall for Tests 15 through 18
- (15) Temperature in the base recirculation bubble approximately 0.5 inch downstream of the model base for Tests 6 through 12 and 14
- (16) Schlieren and color movies of the flow field downstream of the model base
- (17) Emission spectra for Tests 14 through 20

b. Locations of Pressure Measurements

(U) The locations of the model pressure measurements are given in Figure 4 for nine-nozzle, normal injection configurations and in Figure 5 for five-nozzle, normal injection configurations. The four pressures PB-1, PB-2, PB-3, and PB-4 were measured on the base at the locations indicated in the figures. These ports were spaced to provide an indication of the pressure variation across the base. PL-1 and PL-2 refer to lip pressures measured on the cylindrical surface 0.125 inch upstream from the model base. The angular locations of the lip pressures were as shown in the figures. Since one injection port was always coaxial with the base centerline and the other ports positioned symmetrically on either side, PL-1 was always directly downstream of an injection port and PL-2 was downstream of and between two injection ports (except for Test 9 — see below.) The two free-stream static pressures, PS-1 and PS-2, were measured on the model cylindrical surface 3.00 inches upstream from the base. Their angular locations were as shown in the figures.

(U) For the nine-nozzle configurations with 45-degree injection through the base corner, it was impossible to measure a lip pressure downstream of an injection port. For this configuration both PL-1 and PL-2 were measured just upstream of and between two injection ports.

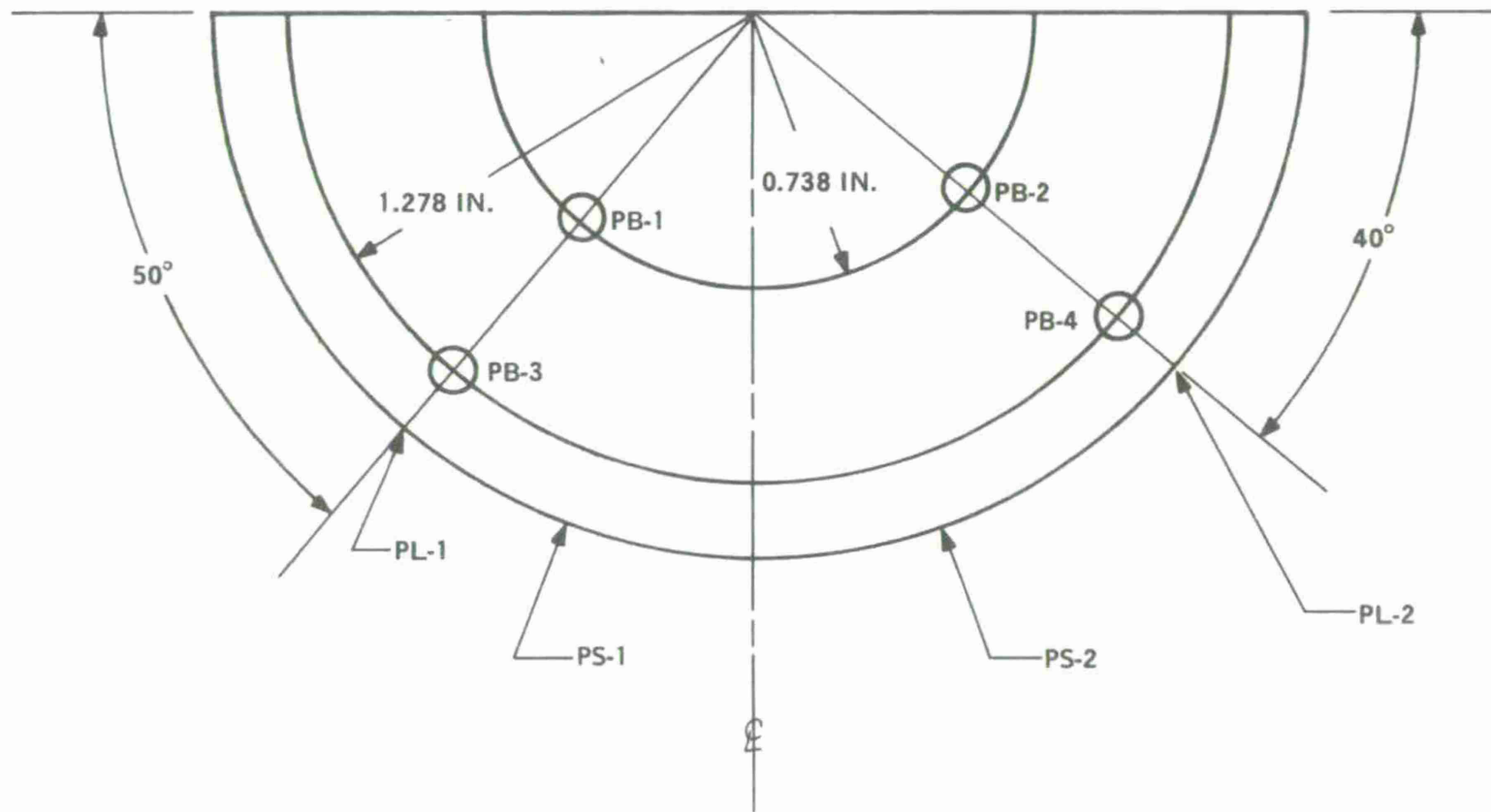


Figure 4. Pressure Tap Locations for 9-Nozzle Normal Injection Configurations.

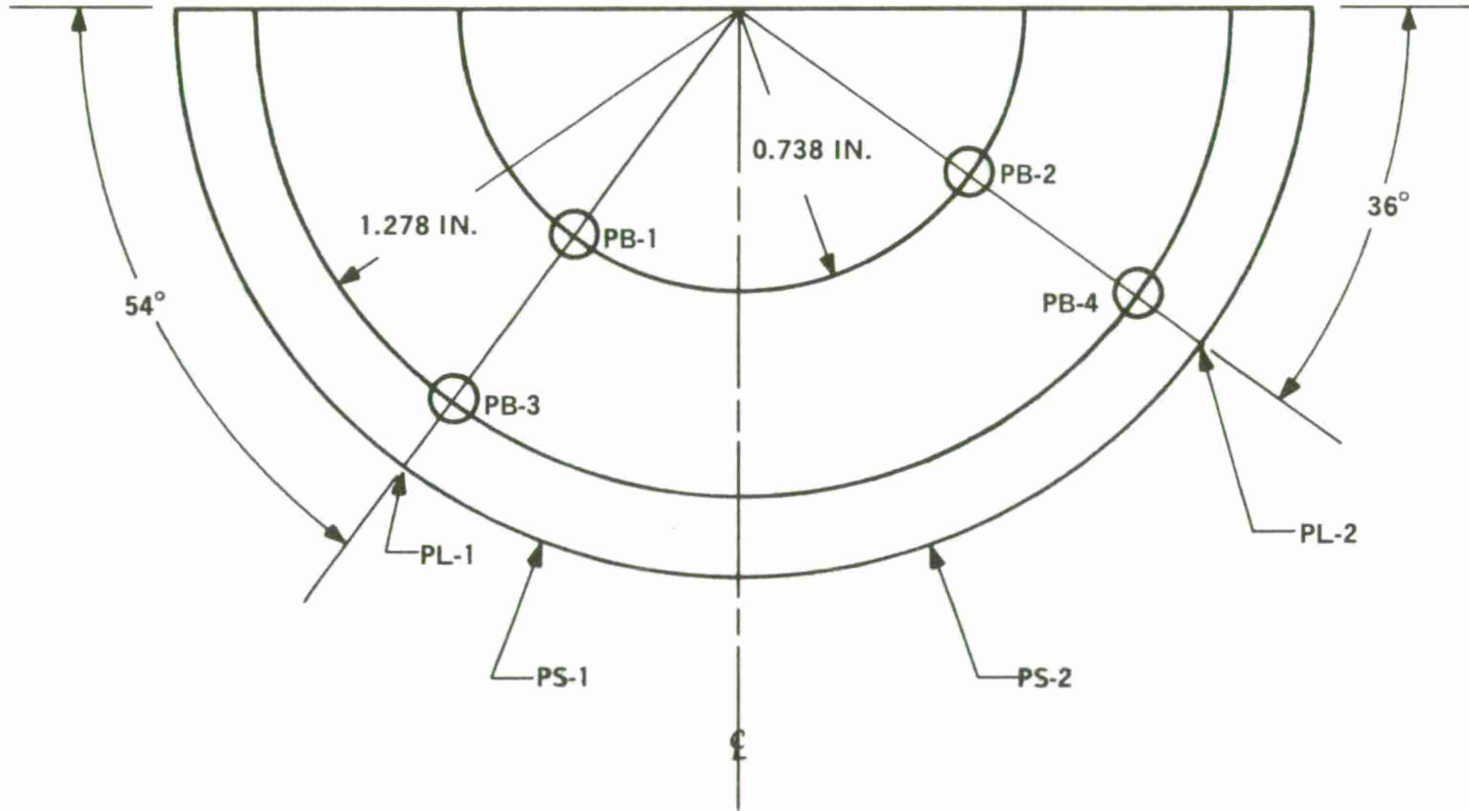


Figure 5. Pressure Tap Locations for 5-Nozzle Normal Injection Configuration.

(U) Five static pressure measurements were made on the base plate extension. These were positioned on the plate centerline 1, 2, 3, 4, and 5 base radii downstream from the model base.

(U) All of the pressure measurements on the model were made with Statham PM280TC ΔP transducers. Depending upon the requirements for the individual measurements, the pressure range of the transducer was 5, 10, or 15 psia.

c. Description of Schlieren System

(U) The Schlieren system was of the single pass type and consisted of the following components:

- (1) 100-watt short arc mercury lamp and power supply
- (2) Source focusing lens and adjustable source slit
- (3) Two 8-inch-diameter parabolic front surface mirrors with 65-inch focal lengths
- (4) 2-by 2-inch front surface flat folding mirror
- (5) One adjustable knife edge
- (6) One convex viewing lens and 16 mm movie camera

(U) The source slit was located at the focal point of one of the parabolic mirrors with a minimum angular offset from the mirror center. The flat mirror was used to turn the light rays so that the viewing lens and camera could be mounted in line with the knife edge. The knife edge was mounted vertically at the focal point of the second parabolic mirror. A diagram of the Schlieren system is given in Figure 6.

d. Description of Spectrograph

(U) The spectrograph used was designed primarily for the study of the combustion of single metal particles. As used here it was composed of a 4 by 5 view camera fitted with the collimator and objective optics from a medium Hilger-Watts quartz spectrograph together with a Bausch and Lomb slit and transmission grating. The speed was $f/5$. Light was collected and focused on the slit with a 70 mm lens. Exposures were 0.10 second using Royal Pan film. The spectral range in focus extended from about 3300Å to 6000Å.

4. PROPELLANTS

a. Thermodynamic Properties

(C) Three state-of-the-art solid propellants were used as fuel generators in this program. The first of these was ARCADENE 129A, a metal-free, fuel-rich propellant. The second was ARCADENE 168A, a fuel-rich propellant containing 35 percent by weight aluminum. The third propellant was ARCADENE 300, a fuel-rich propellant containing 15 percent aluminum and formulated to have the same adiabatic flame temperature as ARCADENE 168A.

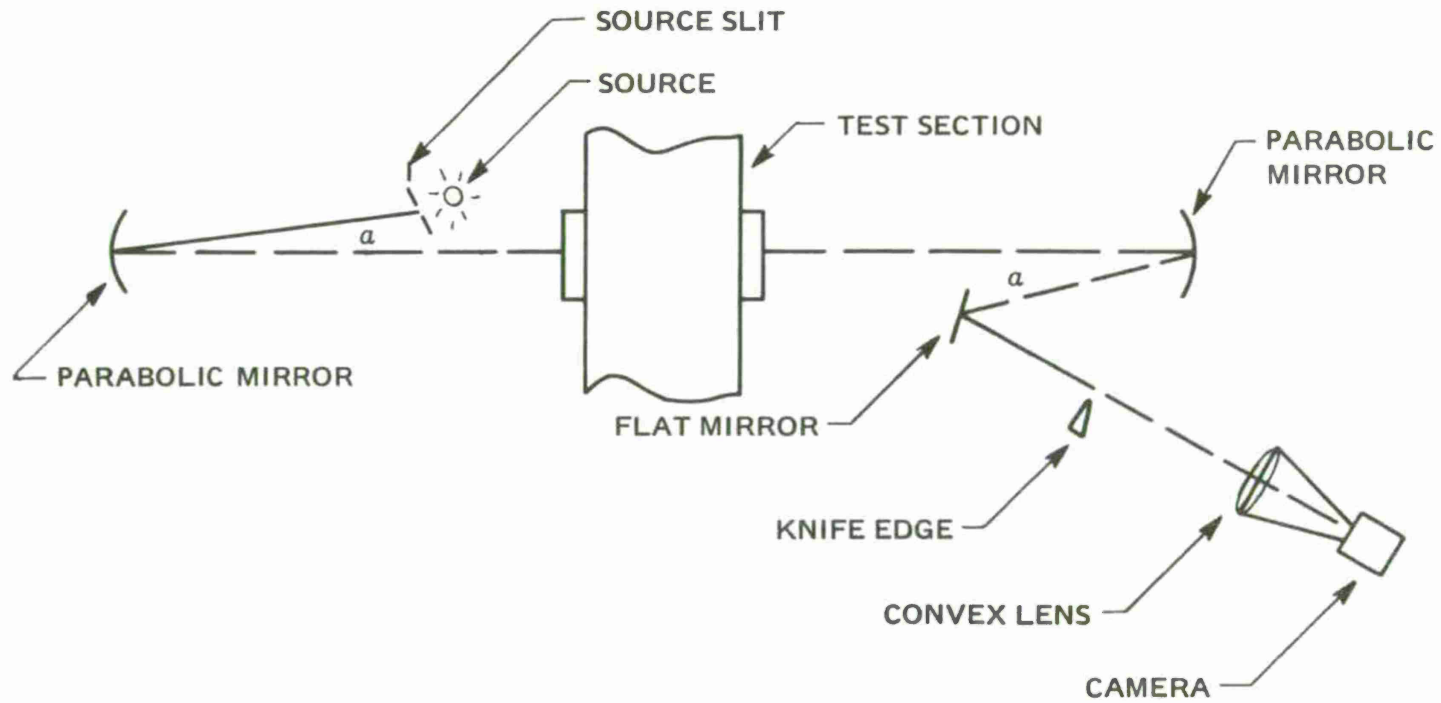


Figure 6. Diagram of Schlieren System.

(C) Selected properties of the three propellants are given in Table I. ARCADENE 129A is the least fuel-rich of the three propellants, having a heat of combustion of only 2.18 kcal/gm. The flame temperature of this propellant is also the lowest, 2361°K. However, this propellant is metal-free, and, as a result, its exhaust products are all gaseous. The absence of condensed phases in the exhaust almost eliminates, for test purposes, hardware erosion and deposition problems.

(C) ARCADENES 168A and 300 were formulated to give the same equilibrium flame temperature, 3180°K. However, ARCADENE 168A is considerably more fuel-rich than is ARCADENE 300. ARCADENE 168A contains 35 percent aluminum and has a heat of combustion of 3.87 kcal/gm while ARCADENE 300 contains only 15 percent aluminum and has a heat of combustion of 2.85 kcal/gm.

(C) The combustible exhaust species for ARCADENES 129A and 300 are principally H₂(g) and CO(g) while the exhaust from ARCADENE 168A also contains significant quantities of AlCl(g). Because of the very fuel-rich stoichiometry of the ARCADENE 168A formulation, its exhaust may also contain significant quantities of unburned liquid aluminum even though this product is not predicted thermodynamically. ARCADENE 168A poses serious hardware erosion and deposition problems, and particular care must be exercised in the design of components to be used with this formulation.

b. Propellant Burning Rates

(C) Strand burning rates for ARCADENES 129A, 168A, and 300 are given in Figure 7. The burning rates for the three propellants are adequately represented by the following equations:

$$\text{ARCADENE 129A} \quad r = 0.40 \left(\frac{P}{1000} \right)^{0.52}$$

$$\text{ARCADENE 168A} \quad r = 0.23 \left(\frac{P}{1000} \right)^{0.33}$$

$$\text{ARCADENE 300} \quad r = 0.23 \left(\frac{P}{1000} \right)^{0.33}$$

Here r is the burning rate (in/sec) and P is pressure (psia)

c. Fuel Flow Rate Determination

(U) Because the exhaust products from ARCADENE 129A are fuel-rich and contain no condensed phases, essentially no nozzle erosion occurs with this propellant. Also, the C* efficiencies for this propellant are essentially 100 percent.⁽¹⁰⁾ Accordingly, the propellant mass flow rate during a firing can be simply computed as

Table I. (C) Selected Properties of Propellants (U).

Designation ARCADENE	Composition (weight percent)	Density (gm/cc)	Heats of combustion ^a		Flame temperature at 1000 psia (°K)	Principal combustible exhaust species (1000 → 14.7 psia)	Weight percent condensed phases in exhaust (1000 → 14.7 psia)
			(kcal/gm)	(kcal/cc)			
129A	80 AP ^b + 20 CTPB ^c	1.59	2.18	3.47	2361	H ₂ (g), CO(g)	0.00
168A	35 Al + 53 AP+ 12 CTPB	1.87	3.87	7.24	3180	AlCl(g), H ₂ (g), CO(g)	32.9 (Al ₂ O ₃ (s))
300	15 Al + 68.4 AP+ 16.6 CTPB	1.70	2.85	4.85	3180	H ₂ (g), CO(g)	27.0 (Al ₂ O ₃ (s))

^aCombustion products are H₂O(g), CO₂(g) and Al₂O₃(s) at 298°K.

^bAmmonium perchlorate.

^cCarboxyl terminated polybutadiene.

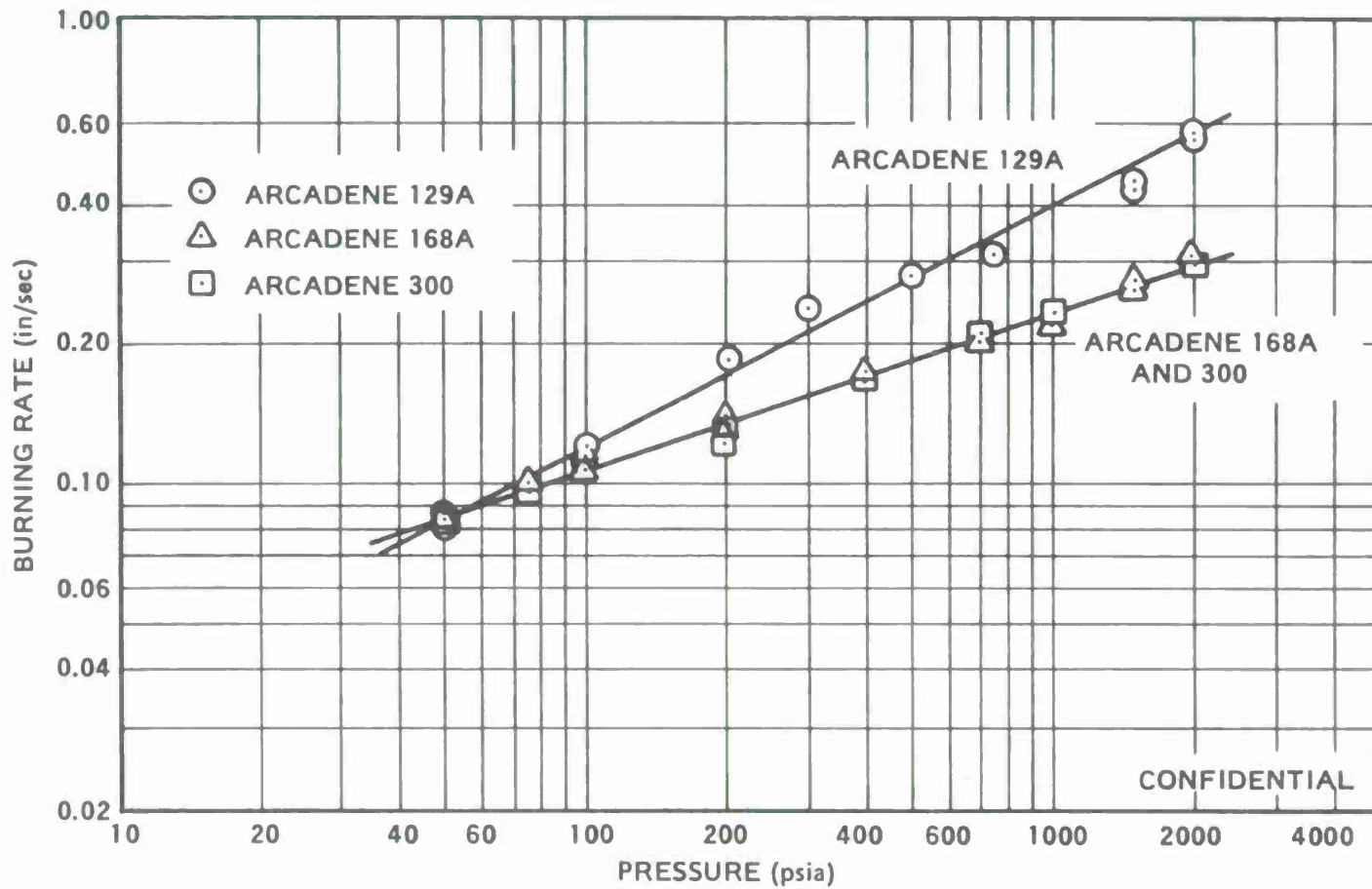


Figure 7. (C) Strand Burning Rates for Propellants (U).

$$\dot{m} = C_D A_t P_{CAV}$$

where:

\dot{m} = propellant mass flow rate (lbm/sec)

C_D = propellant discharge coefficient (lbm/sec-lbf)

A_t = total throat area (in²)

P_{CAV} = pressure in the injector cavity (psia)

For ARCADENE 129A, the theoretical discharge coefficient was assumed constant with pressure and equal to 0.00684 lbm/sec-lbf. This value is exact at 200 psia, and the maximum error over a pressure range from 100 to 1,600 psia is 0.1 percent. The C* efficiency was assumed constant at 98 percent,⁽¹⁰⁾ so the actual discharge coefficient used in the calculations was 0.00698 lbm/sec-lbf.

(U) With the aluminum containing propellants, and particularly with ARCADENE 168A, considerable nozzle deposition occurs in the early part of a firing. Because of this deposition, the instantaneous propellant mass flow rate cannot be computed as $C_D A_t P_{CAV}$, for the throat area is not known as a function of time. However, if we assume that the motor burning rates are essentially equal to the strand burning rates and that the propellant burning surface regresses linearly, then it is possible to numerically integrate $r dt$ during the firing using the measured pressure-time trace. During each interval of the integration, the burning surface (A_s) can be computed, and the mass flow rate is then given by $\rho_p A_s r$. Also, the throat area at any interval can be computed from $A_t = \dot{m} / C_D P$. The validity of assuming strand burning rates and linear burning surface regression can be determined by comparing the integral of $r dt$ from ignition to tail-off to the initial web thickness of the grain. Close agreement between these numbers would indicate that the assumptions are valid. Alternatively, the integral of $\dot{m} dt$ can be compared to the total fuel weight.

(U) Figures 8, 9, and 10 illustrate the application of this method for computing fuel flow rate to an ARCADENE 168A test firing. Figure 8 shows the rocket motor chamber pressure as a function of time. For this and all ARCADENE 168A and ARCADENE 300 firings, ignition was accomplished with a small pyrogen igniter sized to burn over a period of 0.5 second. Slow ignition was necessary to preheat the nozzle surfaces before excessive deposition of aluminum oxide occurred. If ignition were effected with the fast burning B-KNO₃ pellets, as with ARCADENE 129A firings, then aluminum oxide would deposit and freeze on the cold nozzle surfaces, and the throats would completely close before the nozzles were heated to the melting point of aluminum oxide. The preheat afforded by the pyrogen igniter allowed this melting point to be reached in the nozzle throats before the nozzles became completely blocked.

(U) In the pressure-time trace of Figure 8, the igniter burnout at 0.5 second is clearly shown followed by a rapid pressure rise to about 340 psia as deposition occurred on the nozzles. The minimum throat area occurred at 1.2 seconds, after which time movies of the firing showed aluminum oxide being sloughed off the nozzles.

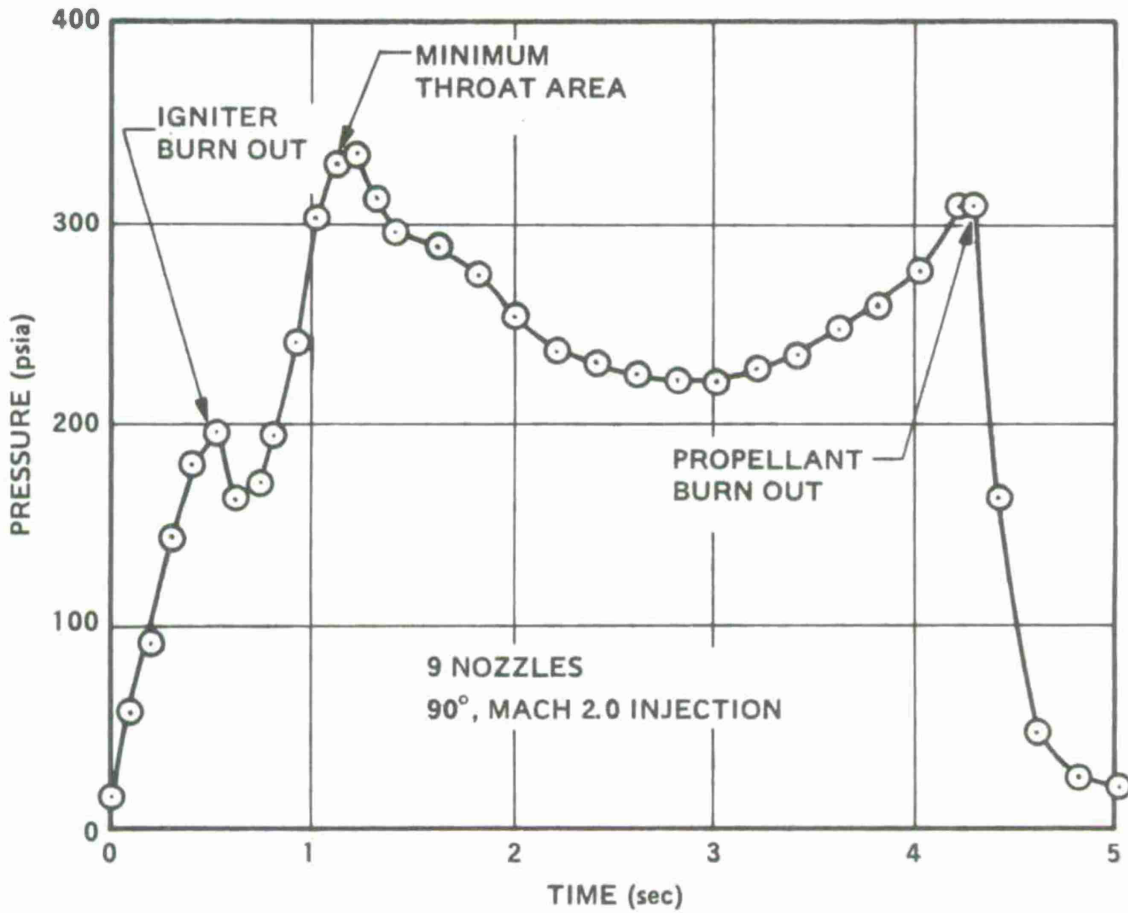


Figure 8. Pressure-Time Trace for ARCADENE 168A Test Firing.

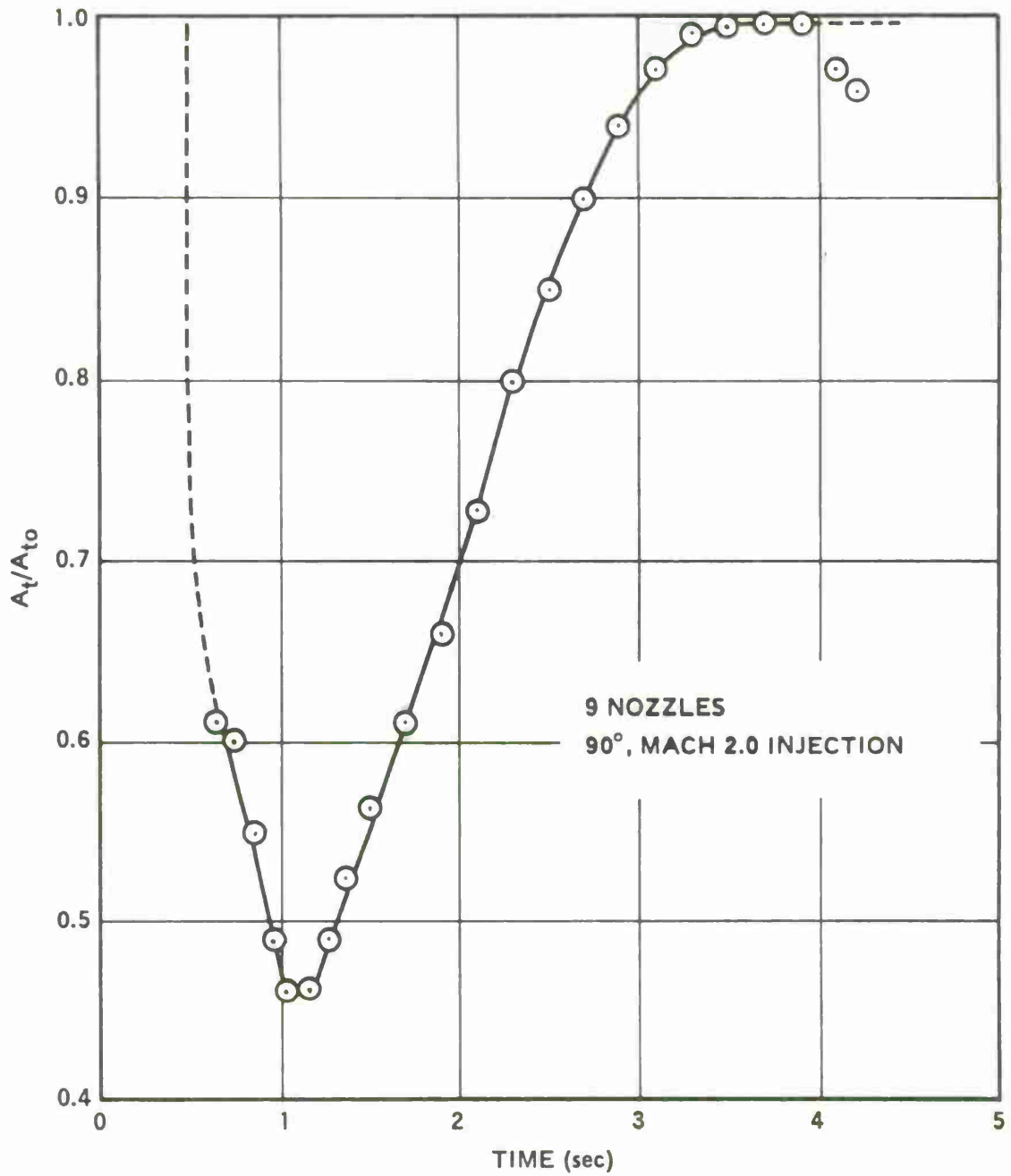


Figure 9. Throat Area Variation for ARCADENE 168A Test Firing.

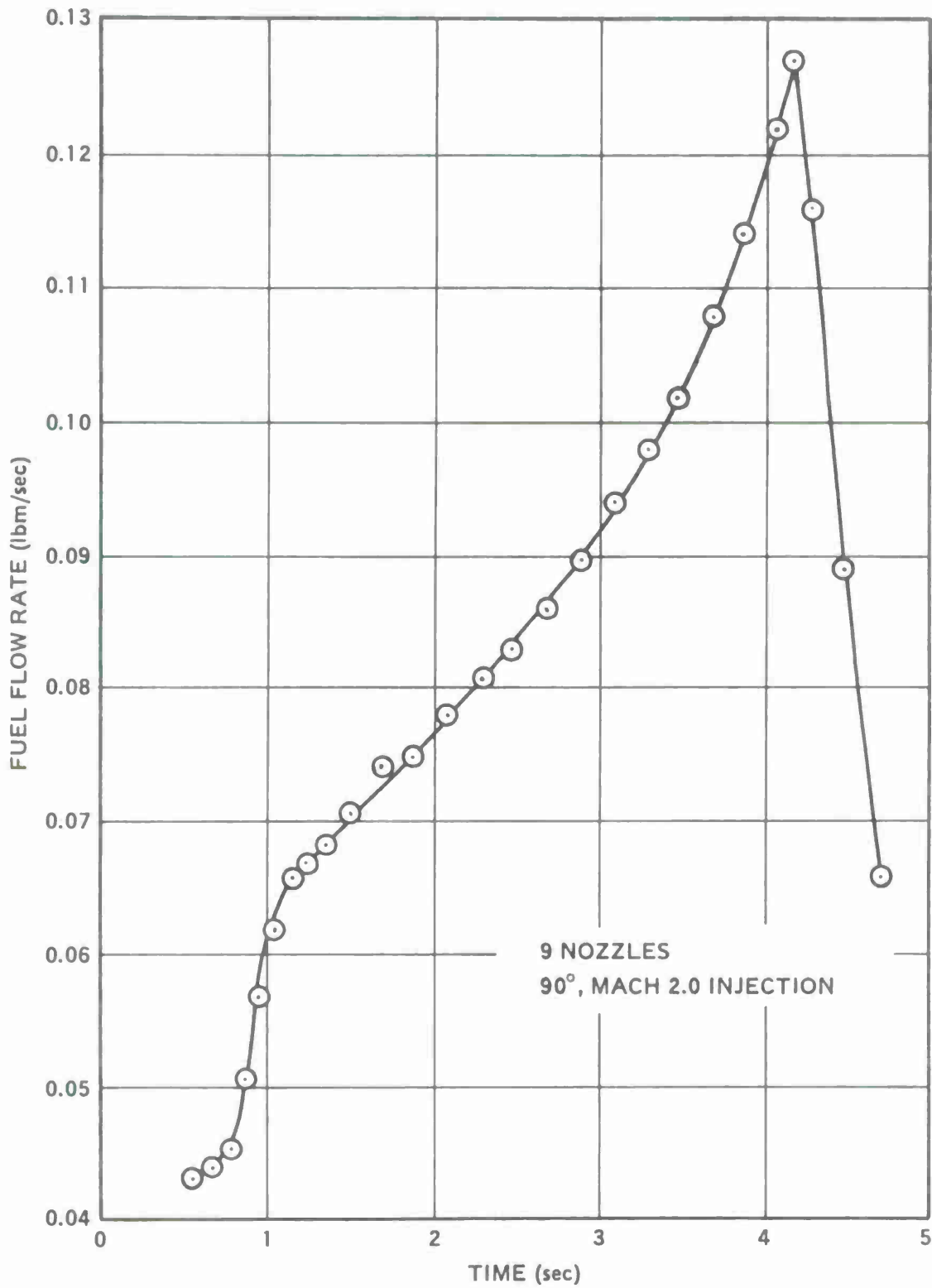


Figure 10. Mass Flow Rate Versus Time for ARCADENE 168A Test Firing.

UNCLASSIFIED

(U) The computed throat area variation with time for this test firing is shown in Figure 9. The value of the discharge coefficient used for this calculation was 0.00790 lbm/sec-lbf. The minimum throat area, about 46 percent of the initial throat area, occurs at 1.1 seconds. After this time, the throat area increases monotonically to its initial value.

(U) The propellant mass flow rate computed from the numerical integration is presented in Figure 10. The flow rate just after igniter burnout was about 0.04 lbm/sec, and it increased to about 0.13 lbm/sec at 4.2 seconds. The grain tested here was a center-perforated cylinder burning on the port surface only. The grain outside diameter was 1.99 inches and the initial port diameter was 0.75 inch. The grain length was 2.00 inches.

5. TEST CONDITIONS

(U) Many of the test parameters were selected to complement the previous Navy data, obtained with a 5-inch model. Test results at Mach 2.0 and a 15,000-foot altitude were to be compared to the Navy data to indicate the effect of model size at this flight condition. Also, the Mach number and altitude variations in this program were selected to indicate the effects of these parameters with a 75mm model.

(U) The fuel mass flow rate ranges and the 90-degree injection configuration were scaled from the Navy test conditions. The fuel flow rates required for a given specific impulse were assumed to be proportional to the model base area and the free-stream static pressure. This assumption is thermodynamically realistic except that the effect of Mach number is ignored. The distance upstream from the base of the 90-degree fuel injection ports was 0.4 model radii in both the current and the Navy programs.

(U) A summary of the propellant and injection geometry data for the external burning tests is given in Table II. The first three tests were conducted with ARCADENE 129A using center-perforated grains burning on the inside surface only. This geometry gave progressive mass flow rate curves with a range from about 0.12 to 0.27 lbm/sec. All of these tests were made with 90-degree injection, 0.6 inch upstream from the model base. Nine-nozzle and five-nozzle configurations were tested, and the injection Mach numbers examined were 2 and 1. The simulated flight conditions for these tests were Mach 2.5 at sea level.

(U) Tests 4 to 13 were conducted with ARCADENE 168A, again at the Mach 2.5, sea-level flight condition. The propellant grains were center-perforated burning on the port surface only, and the grain length was varied to give two nominal fuel flow rate ranges: 0.05 to 0.15 lbm/sec and 0.15 to 0.31 lbm/sec. Except for Tests 9 and 13, injection was from five 90-degree injection ports located 0.6 inch upstream from the model base. In Test 9, injection was from nine 45-degree injection ports through the base corner of the model. In Test 13, a one-model-radius base extension was positioned adjacent to the injector cap, effectively moving the model base one radius downstream. The injection ports were then 2.08 inches upstream from the new base.

(U) Test 14 was the only test conducted with ARCADENE 300. The flight conditions were again Mach 2.5 at sea level, and the injection geometry consisted of five 90-degree, Mach 2 nozzles, 0.6 inch upstream from the model base.

UNCLASSIFIED

Table II. Propellant and Injection Geometry Data for External Burning Tests.

Test no.	Date	Formulation ARCADENE	Grain weight (lbm)	Grain length (in)	Grain O.D. (in)	Grain I.D. (in)	Fuel flow rate range (lbm/sec)	Injection ports				
								Mach no.	No.	Angle (deg)	Total throat area (in ²)	Distance from base (in)
1	5/24/72	129A	0.576	1.60	3.48	2.00	0.12 - 0.27	2	9	90	0.0779	0.60
2	5/26/72	129A	0.576	1.60	3.48	2.00	0.12 - 0.27	1	9	90	0.0779	0.60
3	5/31/72	129A	0.583	1.60	3.48	2.00	0.12 - 0.27	1	5	90	0.0779	0.60
4	6/1/72	168A	0.360	2.03	1.99	0.75	0.05 - 0.13	1	5	90	0.0542	0.60
5	6/5/72	168A	0.376	2.05	1.99	0.75	0.06 - 0.13	2	5	90	0.0542	0.60
6	6/9/72	168A	0.877	4.78	1.99	0.75	0.15 - 0.27	2	5	90	0.0542	0.60
7	6/16/72	168A	0.367	2.00	1.99	0.75	0.05 - 0.14	1	5	90	0.0542	0.60
8	6/21/72	168A	0.367	2.00	1.99	0.75	0.06 - 0.14	1	5	90	0.0542	0.60
9	6/26/72	168A	0.367	2.00	1.99	0.75	0.06 - 0.14	1	9	45	0.0542	0.00
10	6/28/72	168A	0.367	2.00	1.99	0.75	0.06 - 0.15	2	5	90	0.0362	0.60
11	6/29/72	168A	0.367	2.00	1.99	0.75	0.06 - 0.15	2	5	90	0.0362	0.60
12	7/5/72	168A	0.861	4.78	2.00	0.75	0.15 - 0.31	2	5	90	0.0770	0.60
13	7/7/72	168A	0.360	2.00	1.99	0.75	0.05 - 0.13	2	5	90	0.0515	2.08
14	7/12/72	300	0.717	5.00	1.85	0.75	0.15 - 0.33	2	5	90	0.0726	0.60
15	9/13/72	168A	0.266	1.83	1.89	0.75	0.05 - 0.11	1	5	90	0.0311	0.60
16	10/11/72	168A	0.266	1.83	1.89	0.75	0.05 - 0.11	1	5	90	0.0311	0.60
17	10/19/72	168A	0.266	1.83	1.89	0.75	0.05 - 0.11	1	5	90	0.0311	0.60
18	10/20/72	168A	0.572	3.94	1.89	0.75	0.11 - 0.24	1	5	90	0.0603	0.60
19	10/25/72	168A	0.346	2.38	1.89	0.75	0.06 - 0.15	1	5	90	0.0385	0.60
20	10/26/72	168A	0.583	4.01	1.89	0.75	0.12 - 0.27	1	5	90	0.0603	0.60

UNCLASSIFIED

21

UNCLASSIFIED

UNCLASSIFIED

(U) Tests 15 to 18 were conducted with ARCADENE 168A at a simulated altitude of 15,000 feet using the enclosed free-jet test section described above. Tests 15 and 16 were made at Mach 2.5 while Tests 17 and 18 were at Mach 2.0. Tests 19 and 20 also employed ARCADENE 168A and were conducted at Mach 2.0, sea level. The injection geometry for these six tests (15 to 20) consisted of 90-degree injection from five sonic nozzles, 0.6 inch upstream from the model base.

(U) The measured air stream conditions just before ignition are presented in Table III. The measured flow rate was computed from duplicate total pressure and total temperature measurements upstream of the metering venturi in the air supply system. The total temperature, total pressure, and static pressure presented are also the average of two measurements as indicated in Section 3a above. The principal exceptions to this statement are the free-stream static pressures for Tests 15 through 18. Here, the static pressure was out of the range of one of the transducers, so the values presented are those measured with the one transducer that was in range.

(U) From the ratio of the free-stream static pressure to the total pressure we can compute the free-stream Mach number. These values are presented in Table III. For Tests 1 to 16, using the Mach 2.5 nozzle, the computed Mach numbers range from 2.47 to 2.51. This relatively small variation attests to the precision of the static and total pressure measurements. Similarly, for Tests 17 to 20 using the Mach 2.0 nozzle, the indicated Mach numbers range from 2.00 to 2.03.

(U) From the nozzle throat area, the air total temperature, and the air total pressure, it is possible to compute the isentropic air mass flow rate through the annular nozzle. The results of this calculation are presented in Table III as the computed isentropic air flow rate and as K_c , the ratio of the air flow rate measured at the metering venturi to the isentropic air flow rate. The exact reason for the observed variations in K_c is not known at present. However, the precision of the computed Mach numbers suggests that the air total pressure at the plenum is correct. Also, only an inordinately large error in the air temperature could account for the wide variations in K_c . Thus it appears that the computed isentropic air flow rates are correct, consistent with the limits of the isentropic assumption, and the variations in K_c are attributable to discrepancies between the mass flow rate in the nozzle and that indicated at the metering venturi.

6. TEST PROCEDURE

(U) After all of the hardware components were assembled in the proper configuration, electrical calibrations were performed for all instrumentation. The Schlieren light source was turned on, and the alignment of the Schlieren system was verified. Prior to the test series, all of the pressure transducers were calibrated with a deadweight tester.

(U) Once the readiness of the instrumentation was verified, the air mass flow control valve was opened over a period of approximately 30 seconds until the required mass flow rate was established. During this start-up period for the tests at altitude, the diffuser throat area was controlled manually to maintain approximately 8.3 psia in the free-jet test section. When the required flow rate was established, the diffuser was switched to feedback control. The temperature control valve to the pebble-bed heater was slowly opened over a period of about 15 seconds until the required air temperature was attained. At this point, the movie cameras and data acquisition recorders were started. The primary rocket firing circuit was then armed and the motor ignited. The spectrograph camera shutter was tripped about 1 second after rocket ignition.

Table III. Air Stream Conditions for External Burning Tests.

Test no.	Measured air flow rate (lbm/sec)	Total temperature (°K)	Total pressure (psia)	Free stream static pressure (psia)	Mach no.	Isentropic air flow rate (lbm/sec)	K_c
1	19.0	503	249	14.4	2.51	22.2	0.856
2	20.7	508	252	14.6	2.51	22.4	0.925
3	20.5	514	257	14.8	2.51	22.7	0.903
4	20.6	513	254	15.3	2.48	22.4	0.918
5	20.4	499	243	14.7	2.48	21.8	0.937
6	20.5	548	248	15.0	2.48	21.3	0.964
7	22.0	513	240	14.4	2.48	21.2	1.037
8	21.2	504	232	13.9	2.48	20.7	1.025
9	20.9	516	222	13.4	2.48	19.7	1.064
10	22.2	517	235	14.0	2.49	20.8	1.069
11	22.8	502	234	14.3	2.47	20.9	1.093
12	21.7	514	226	13.7	2.48	20.0	1.087
13	21.8	516	250	14.9	2.49	22.1	0.987
14	21.6	492	255	15.4	2.48	22.9	0.942
15	11.1	555	139	8.33	2.48	11.8	0.939
16	10.8	588	149	8.67	2.50	12.3	0.878
17	12.6	482	67.1	8.20	2.03	13.3	0.947
18	12.8	486	66.4	8.48	2.00	13.2	0.973
19	21.8	462	112	13.8	2.02	22.7	0.960
20	23.4	432	118	14.5	2.02	24.8	0.942

CONFIDENTIAL

(C) At the end of the firing, the air flow through the pebble-bed heater was reduced to zero, and the air mass flow control valve closed. The cameras, recorders, and Schlieren light source were then turned off.

CONFIDENTIAL

~~CONFIDENTIAL~~

SECTION IV

RESULTS

1. TESTS WITH ARCADENE 129A

(C) The principal results for Tests 1, 2, and 3 are presented in Figures 11 to 16. These tests were conducted with ARCADENE 129A at Mach 2.5, sea-level flight conditions. Figures 11, 12, and 13 present the pressures measured on the model and the fuel flow rate as functions of time. Figures 14, 15, and 16 present the downstream pressure distributions measured on the centerline of the base plate extension at four discrete times during each test.

(C) For these tests using ARCADENE 129A, the fuel flow rates presented were computed from $\dot{m} = C_D A_t P_{CAV}$ as described in Section III. The base pressures plotted are the area weighted averages of the four base pressures measured. P_∞ is the reading obtained at pressure port PS-2, which was essentially identical to that measured at PS-1. PL-1 and PL-2 are, respectively, the lip pressure measured just downstream of and on line with an injection port and the lip pressure measured just downstream of and between two injection ports.

(C) For each of these tests a progressive fuel flow rate schedule was obtained. At the start of the test the fuel flow rate was about 0.15 lbm/sec, and it increased to about 0.30 lbm/sec at the end of the test. The test duration was about 3 seconds. During this time, the free-stream static pressure (P_∞) was essentially constant, decreasing about 0.1 to 0.2 psia during the test.

(C) Very little base pressure change was observed in any of these tests. In the first 0.4 second, the base pressure decreased less than 1.0 psia and then slowly increased during the remainder of the test. Only in Test 3, with five sonic nozzles, did the base pressure rise back to its initial value before the firing. The initial decrease in base pressure was largest for Tests 1 and 3 and smallest for Test 2.

(C) The lip pressure variations observed in Test 3 would be identical in form to those in Test 1 if the labels on the curves were reversed. Although it is tempting to propose that the data channels for PL-1 and PL-2 somehow were interchanged for this test, there is no evidence to support this proposition. Study of the test procedures indicates that, although such an interchange was possible, it was not probable.

(C) The downstream pressure distributions for Tests 1, 2, and 3 are essentially the same with respect to their main features. Prior to the tests (time $t = 0$), the base pressure ratio is about 0.45. After perhaps a slight decrease in pressure ratio one radius downstream from the base, the pressure ratio rises rapidly to about 1.3 at x/r equals 5.

(C) With fuel injection, the downstream pressure distributions show two main features. First, the recompression process begins significantly closer to the base with fuel injection than it does with "air only." Second, there is a pronounced minimum in the pressure distribution at $x/r = 4$. The value of P/P_∞ at the minimum decreases as the propellant flow rate increases. Also, at given fuel flow rates, the value of P/P_∞ at the minimum is smaller in Test 3 than in Tests 1 and 2.

~~CONFIDENTIAL~~

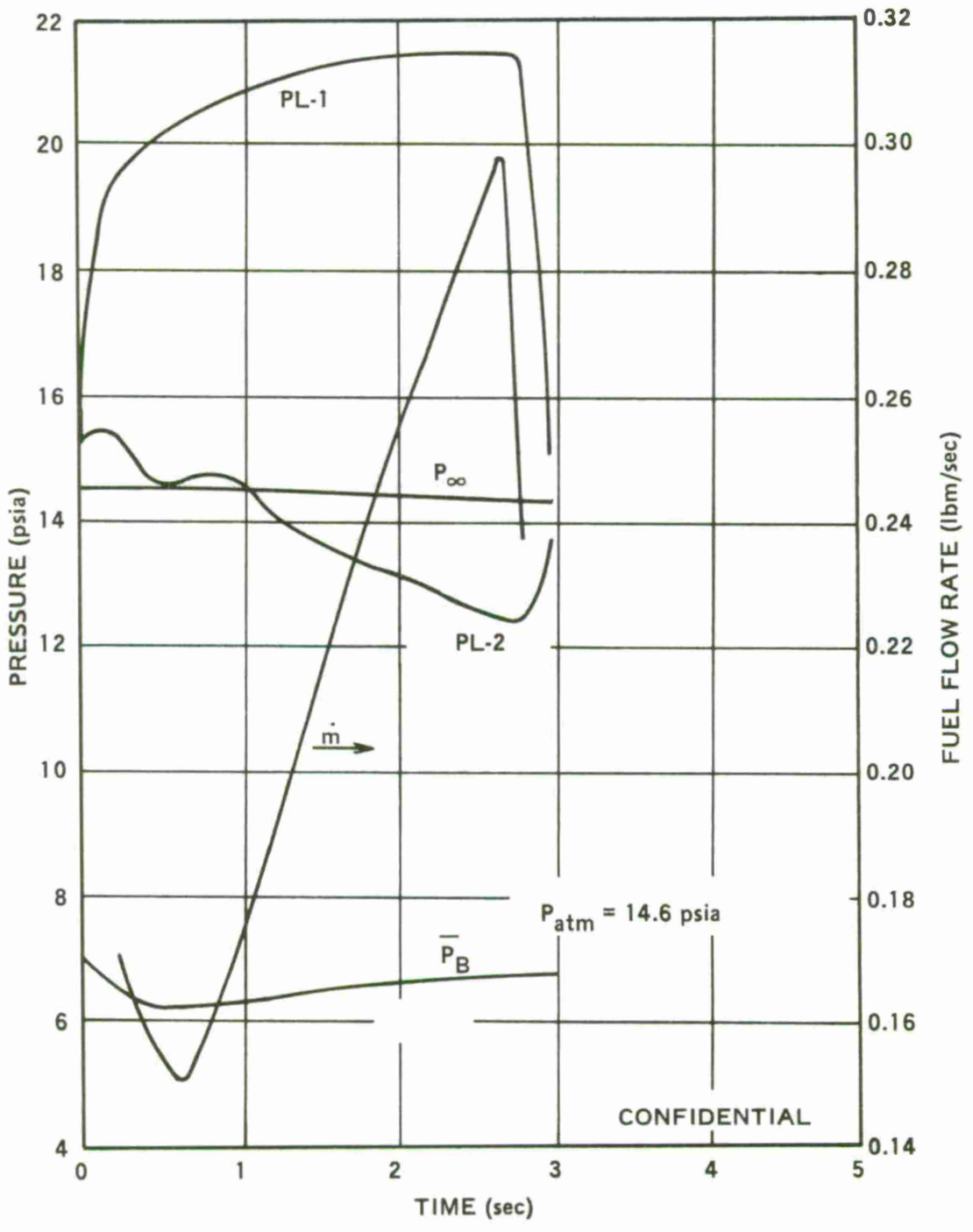


Figure 11. (C) Results from Test 1 (U).

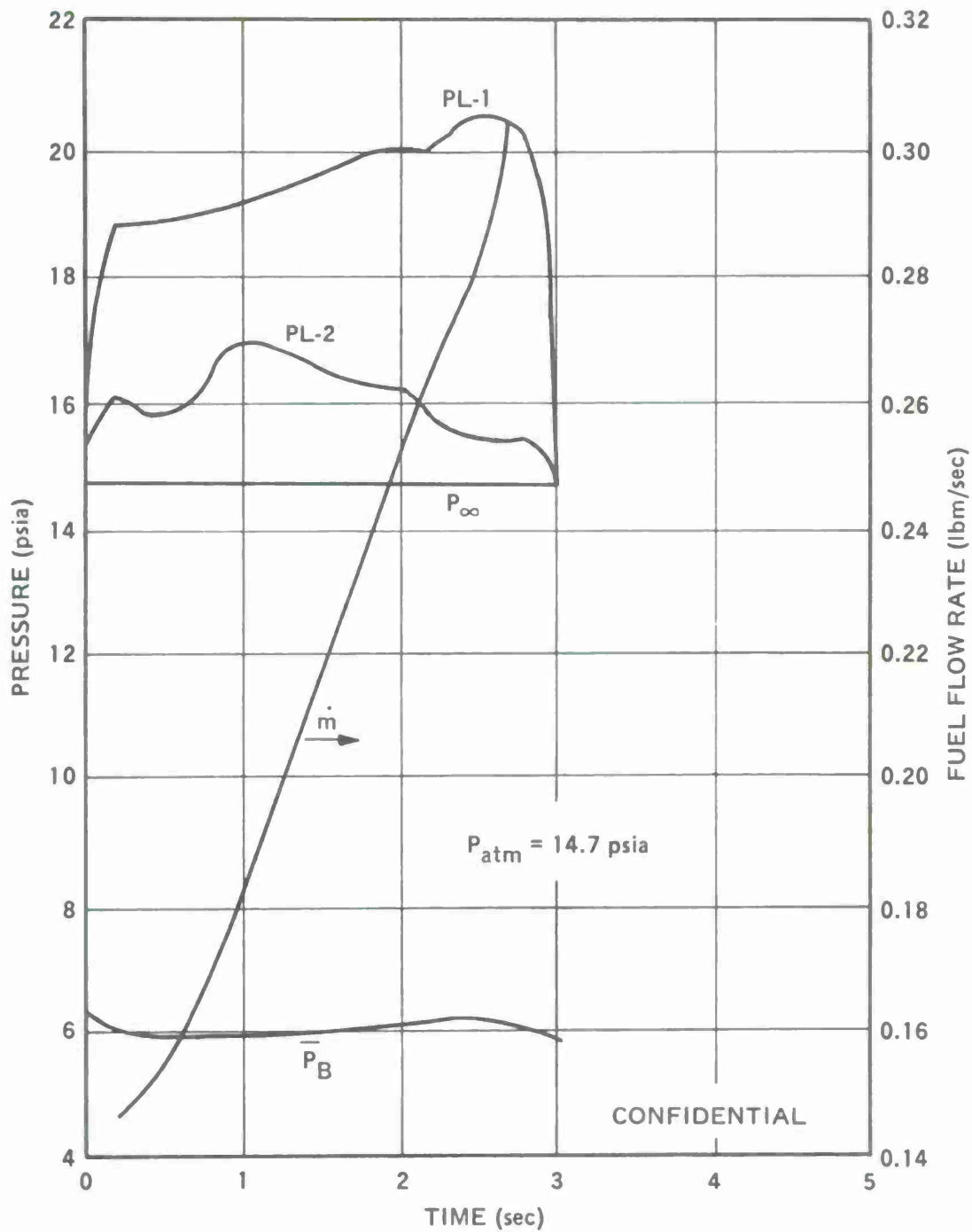


Figure 12. (C) Results from Test 2 (U).

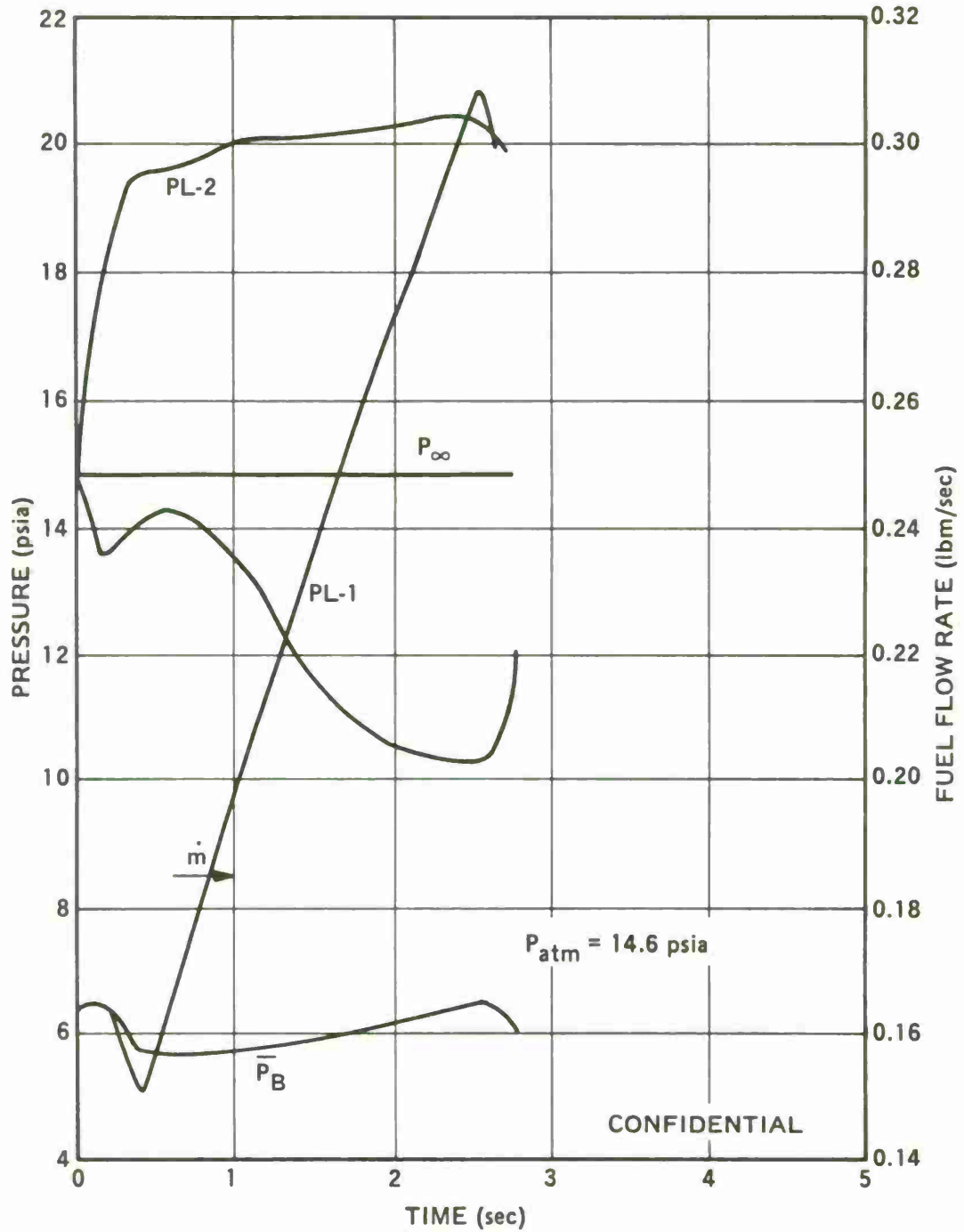


Figure 13. (C) Results from Test 3 (U).

~~CONFIDENTIAL~~

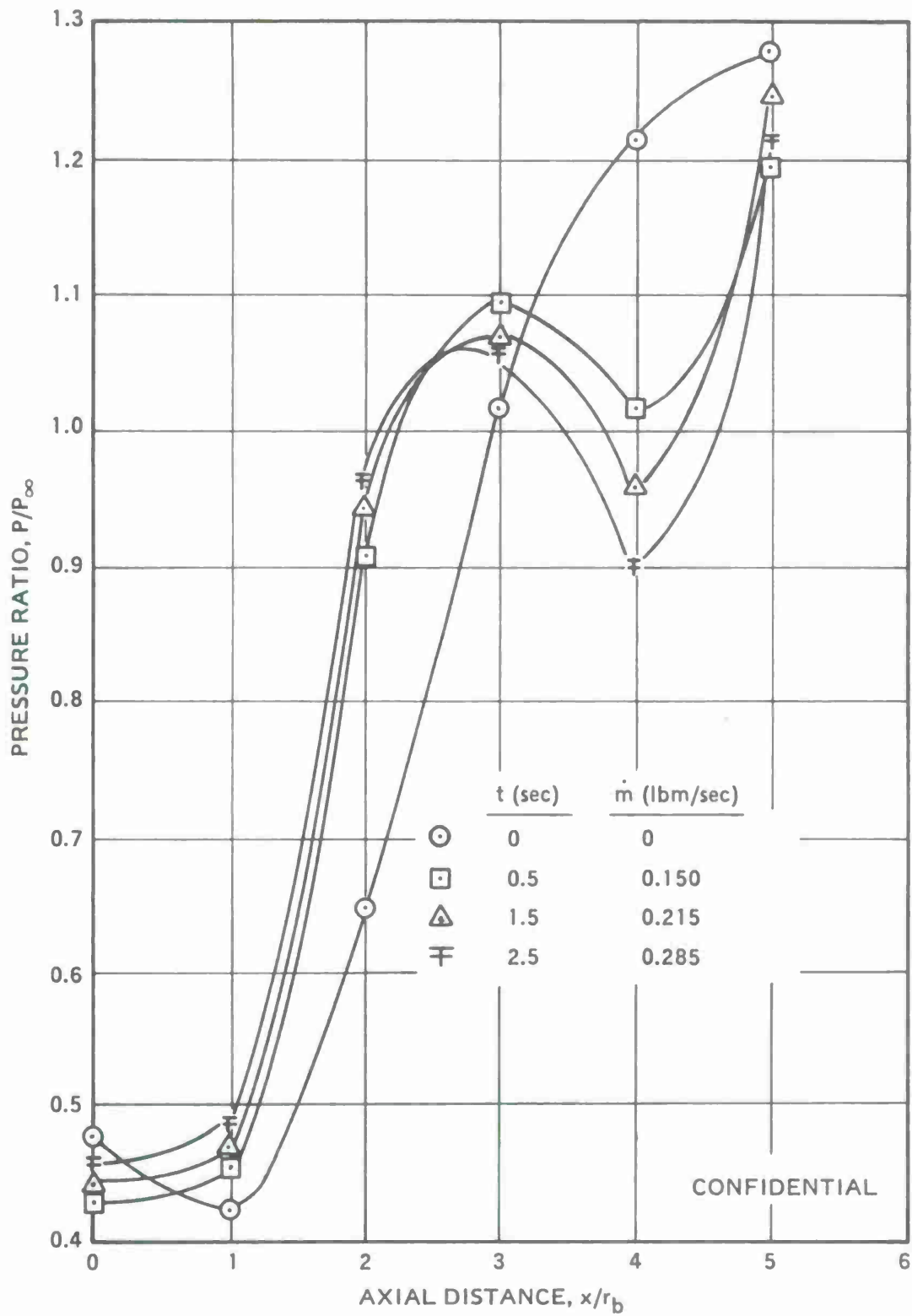


Figure 14. (C) Downstream Pressure Distributions, Test 1 (U).

~~CONFIDENTIAL~~

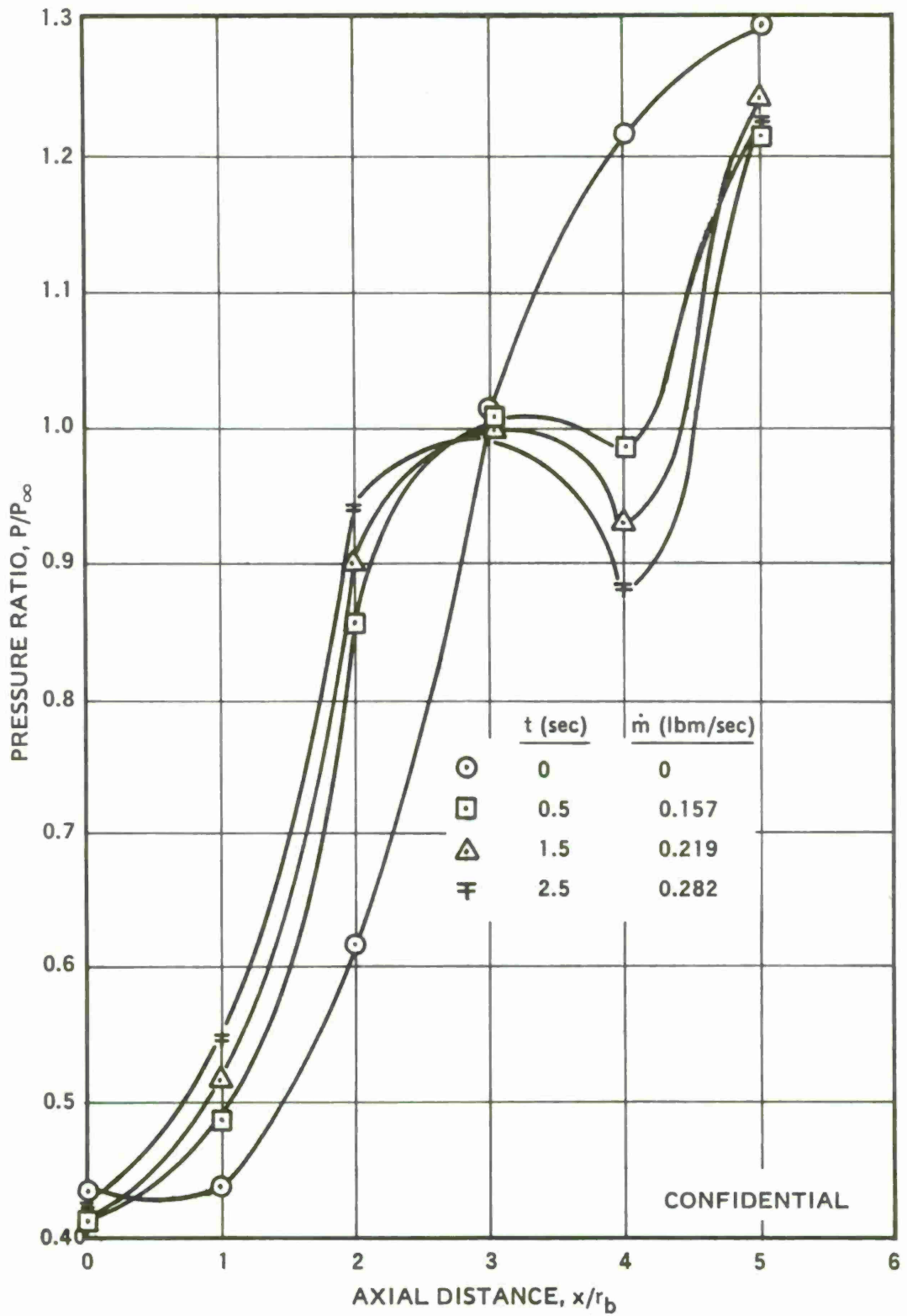


Figure 15. (C) Downstream Pressure Distributions, Test 2 (U).

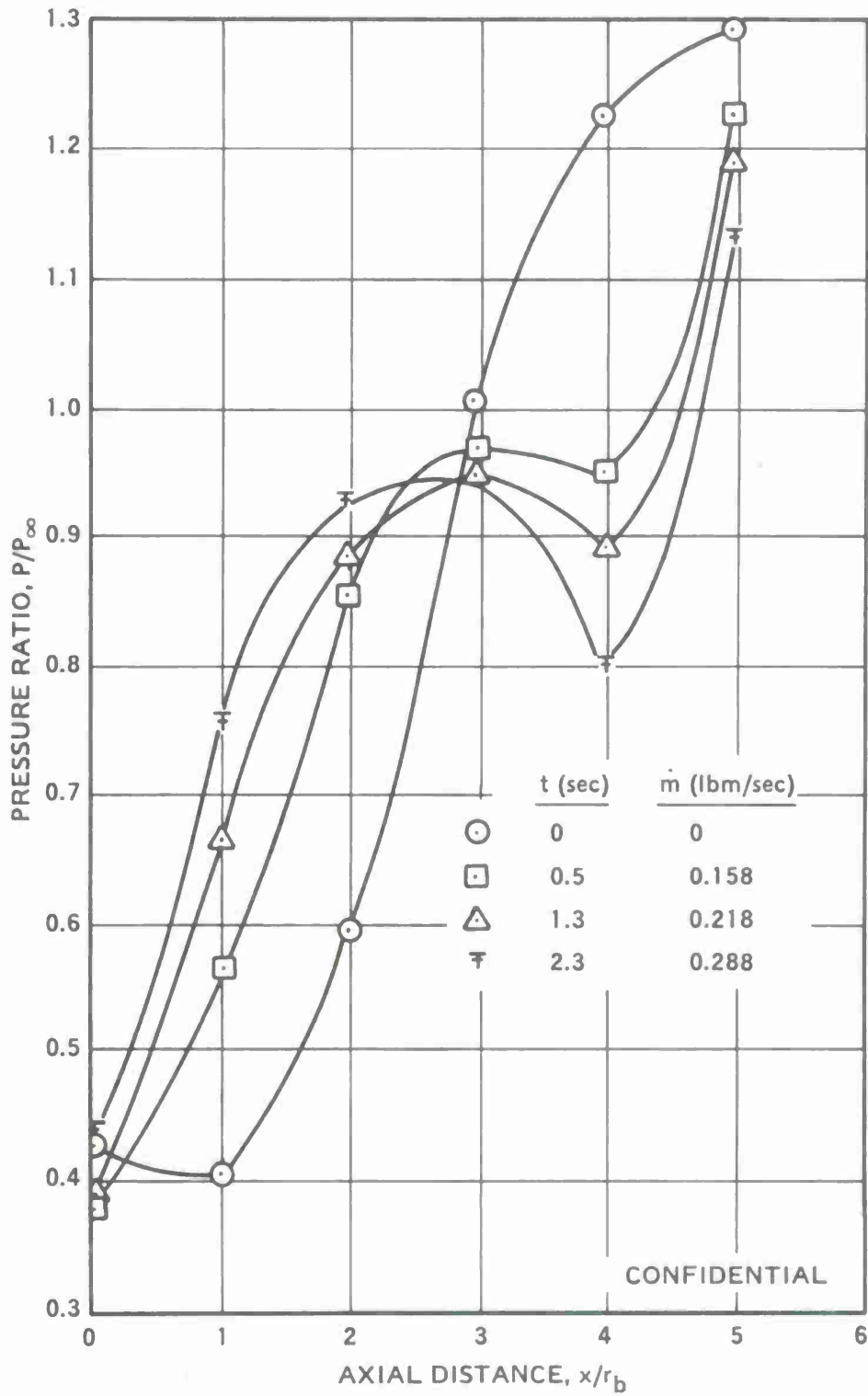


Figure 16. (C) Downstream Pressure Distributions, Test 3 (U).

(U) The color movies for Tests 1, 2, and 3 did not show evidence of vigorous combustion. Some pale blue flame could be seen at the very end of Tests 2 and 3 just downstream from the injection ports. But, except for this flame and a bright flash upon ignition, the movies were dark. However, radiation from the igniter (B-KNO₃) exhaust suggested that penetration into the supersonic stream was accomplished.

(U) The Schlieren movies of these tests indicated a high quality flow field with essentially no strong disturbances prior to fuel injection. Clearly visible were the detailed features of the base flow, including the expansion fan at the model lip and the inner boundary of the shear layer from the model base through the neck region. Some weak disturbances from the injector nozzles and model joints were also visible.

(U) Upon fuel injection, the strong jet interaction shock wave was clearly visible from the point where it emerged from the nozzle to where it was reflected from the free-jet boundary as an expansion fan. The leading and trailing waves in this expansion fan could also be seen.

2. TESTS WITH ARCADENE 168A AT MACH 2.5, SEA-LEVEL FLIGHT CONDITIONS

(C) Tests 4 to 13 were conducted with ARCADENE 168A propellant at Mach 2.5, sea-level flight conditions. The principal results from these ten tests are presented in Figures 17 to 26 and 27 to 36. Figures 17 to 26 contain the model pressures and fuel mass flow rates as functions of time. For Tests 6 to 12 the temperatures measured in the base recirculation bubble are also presented as functions of time. In Figures 27 to 36, the downstream pressure distributions are presented for four discrete times during the firing.

(U) Tests 4, 5, 7, 10, and 11 were all conducted with 90-degree fuel injection and a nominal fuel flow rate range of about 0.05 to 0.15 lbm/sec. The conditions for Tests 4 and 7 were nominally the same, and fuel injection was through five sonic nozzles. The conditions for Test 5 were the same as for 4 and 7 except that the fuel injection Mach number was 2. In Test 10, five Mach 2 nozzles were again used, but the total throat area was reduced from 0.0542 to 0.0362 in², so the rocket motor pressure range was from about 300 to 600 psia rather than from 100 to 300 psia as in the above tests. Test 11 used three Mach 2 nozzles with the same total throat area as in Test 10, so the rocket motor pressure range was again approximately 300 to 600 psia.

(U) As in the tests with ARCADENE 129A, the free-stream static pressure remained essentially unchanged throughout these tests. This situation was required if meaningful data were to be obtained, and it prevailed throughout all of the tests except Number 15 (see below).

(C) The base pressure variation was essentially the same for Tests 4, 5, 7, 10, and 11. During the first 0.2 to 0.4 second of the tests, the base pressure decreased 0.5 to 1.5 psia from its initial value. Within about the next 1 second of the test, the base pressure rose to near 10 psia and then increased only slightly during the last 2 seconds of the test. The final base pressure level was slightly lower in Tests 10 and 11 employing the high rocket pressure range.

(C) The variation of PL-1 in these tests was erratic, but somewhat similar. In all cases this pressure decreased slightly during the first 0.2 to 0.4 second of the tests and then increased.

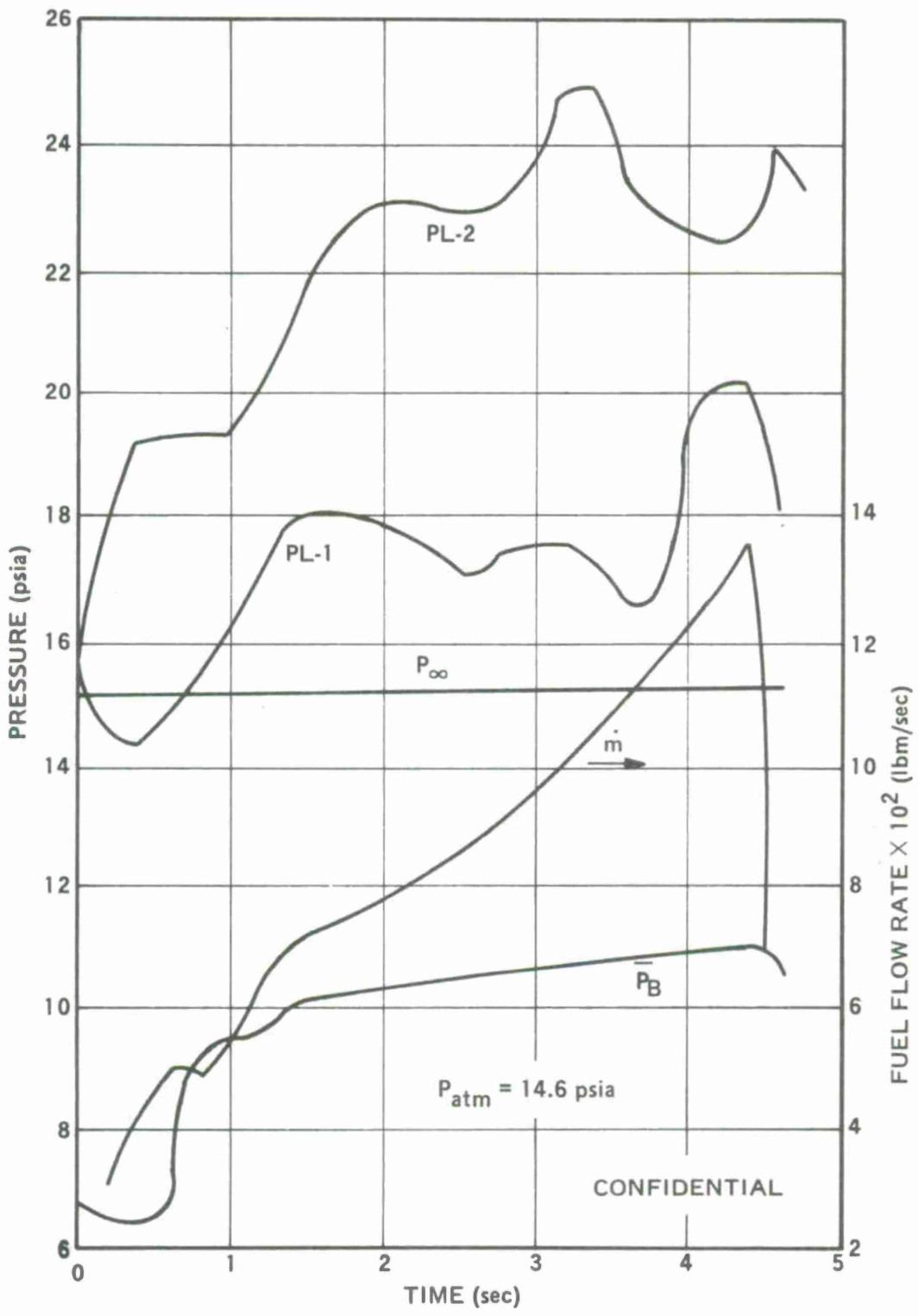


Figure 17. (C) Results from Test 4 (U).

~~CONFIDENTIAL~~

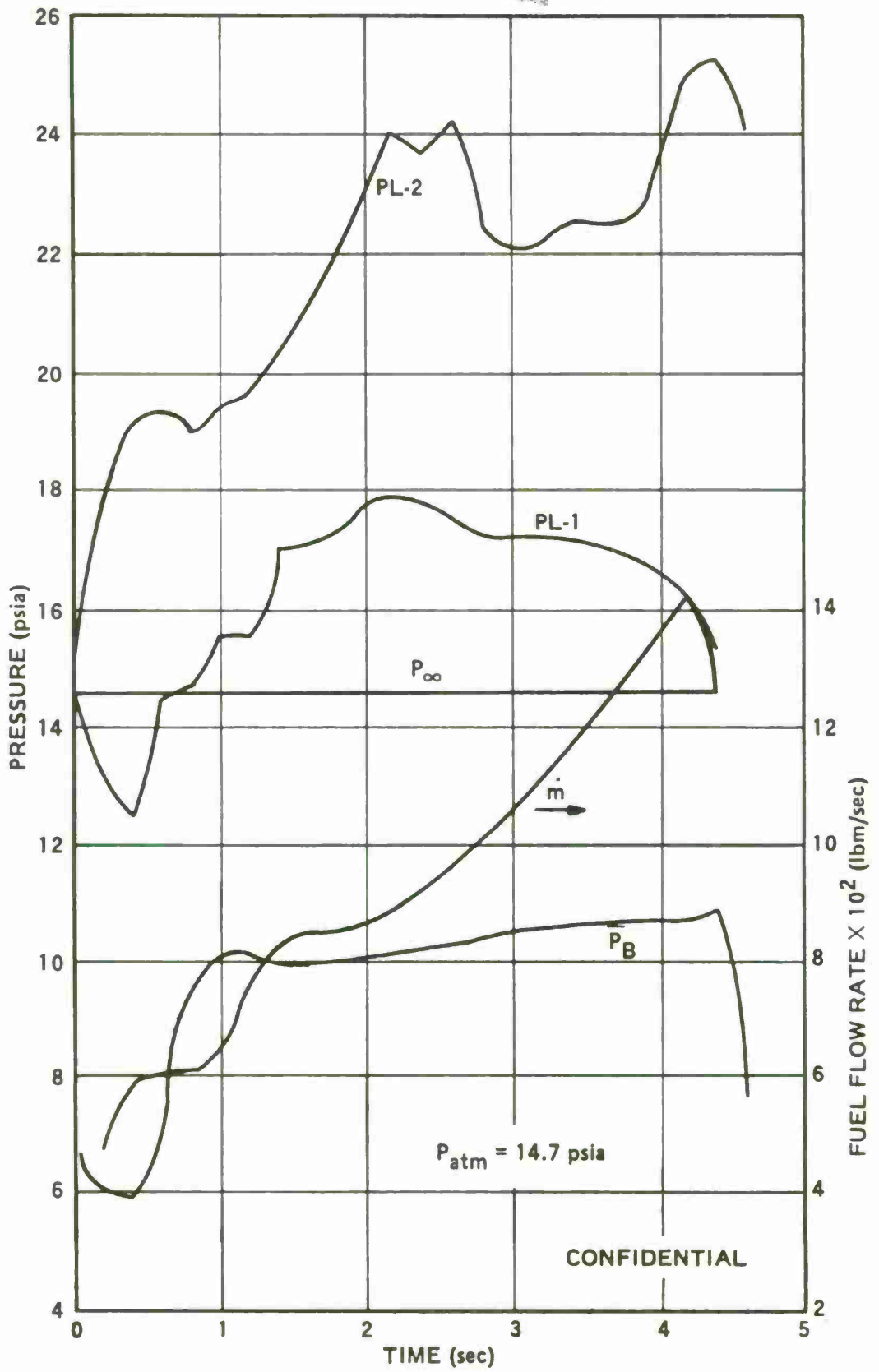


Figure 18. (C) Results from Test 5 (U).

~~CONFIDENTIAL~~

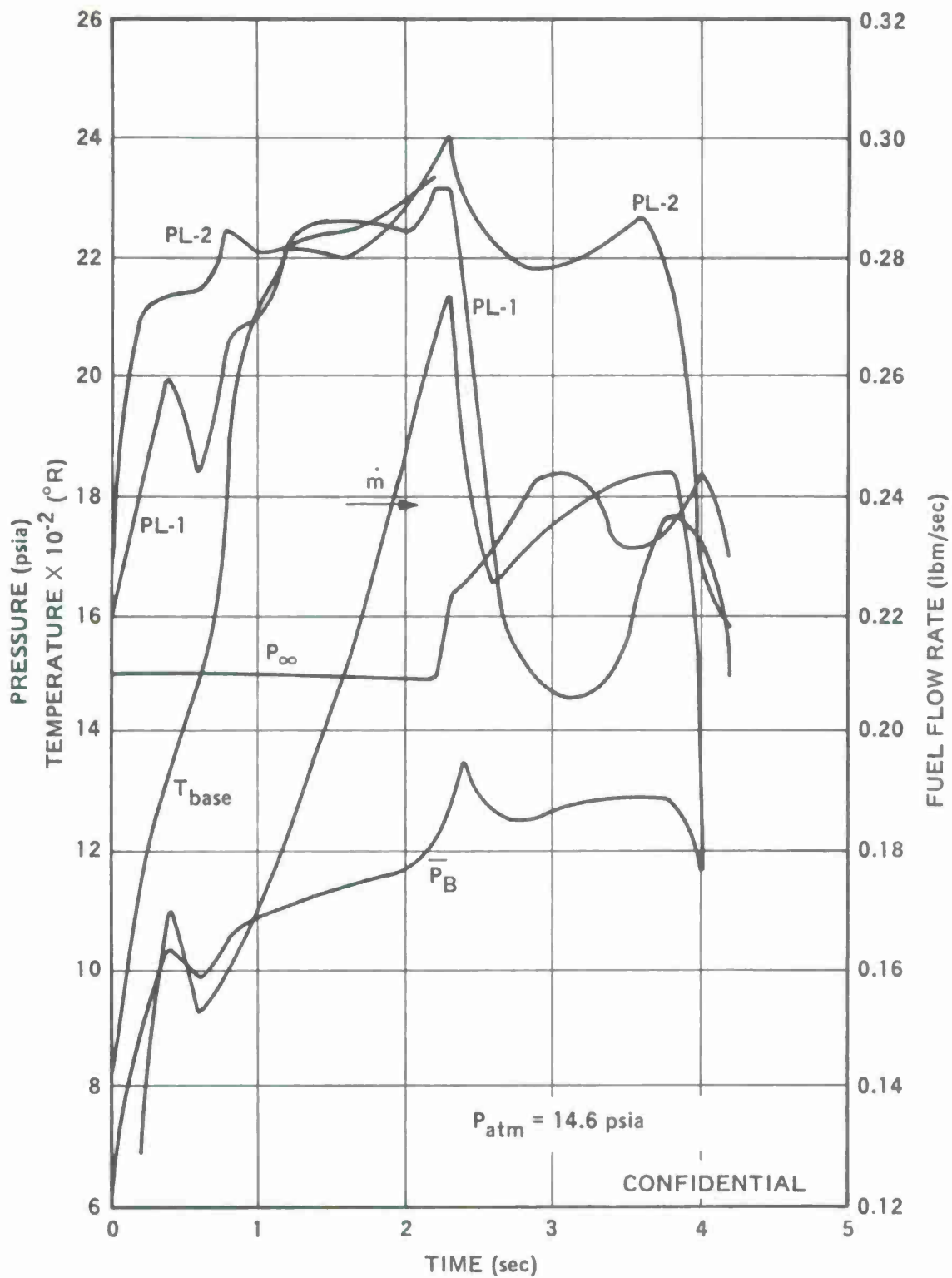


Figure 19. (C) Results from Test 6 (U).

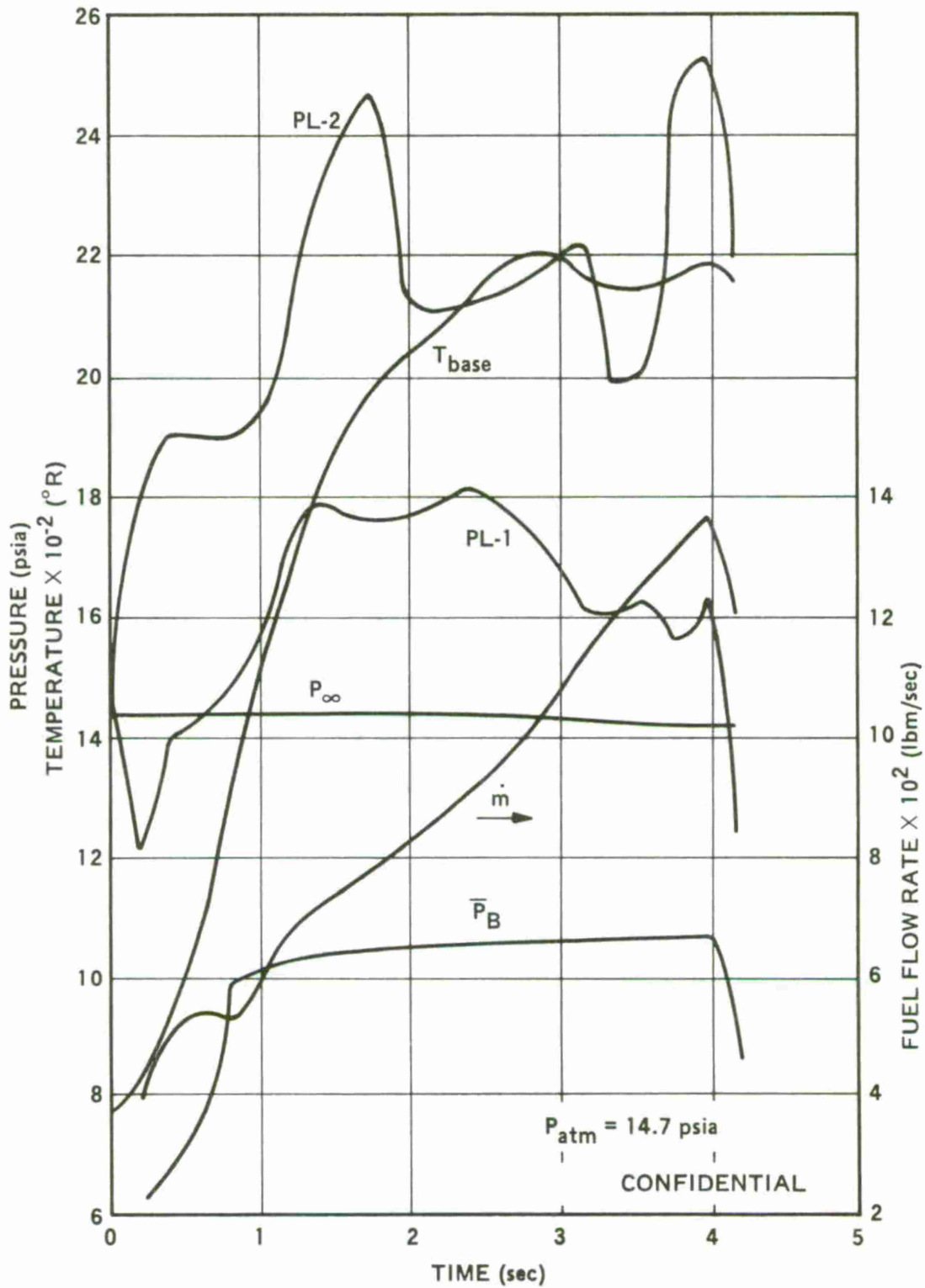


Figure 20. (C) Results from Test 7 (U).

~~CONFIDENTIAL~~

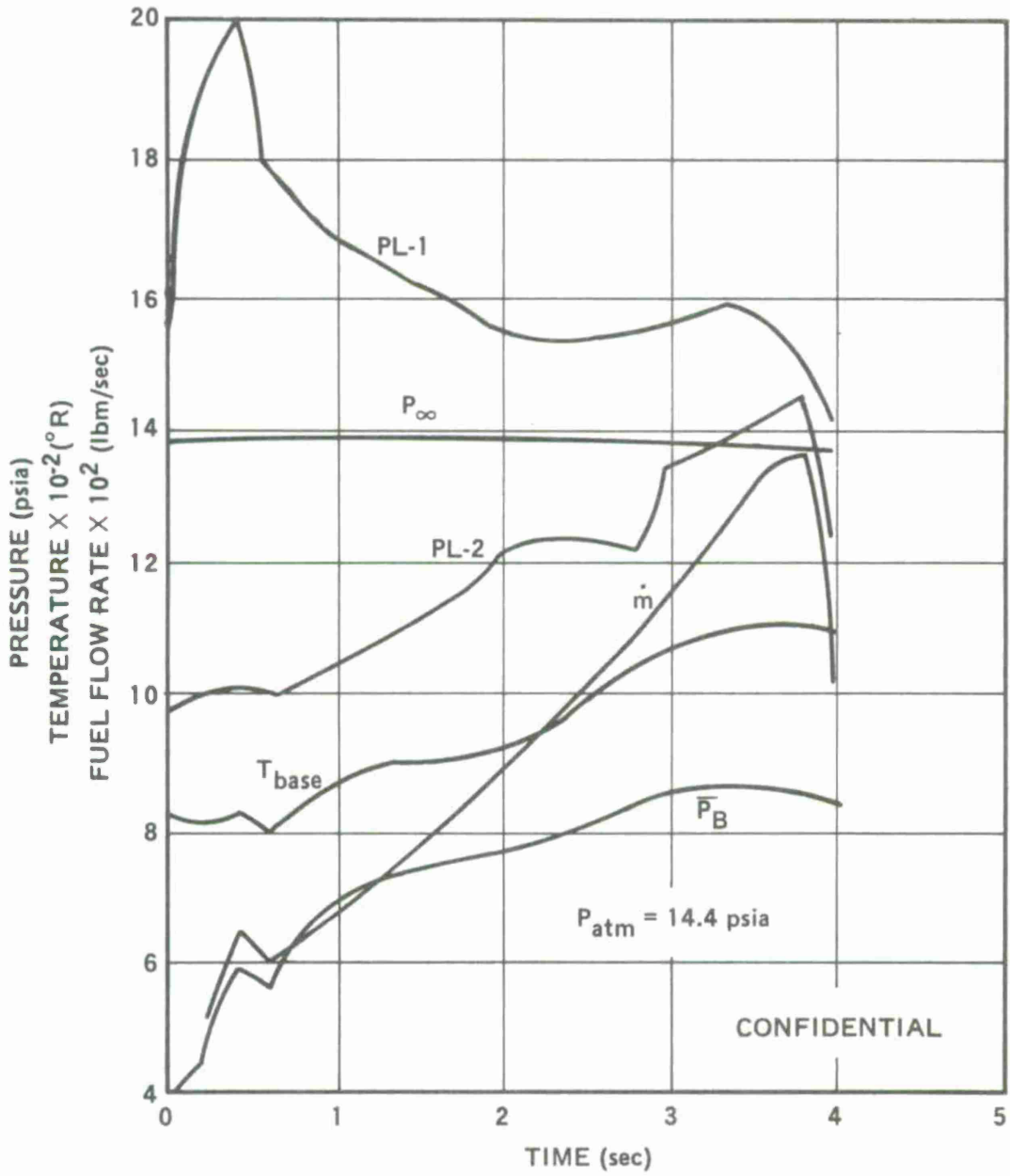


Figure 21. (C) Results from Test 8 (U).

~~CONFIDENTIAL~~

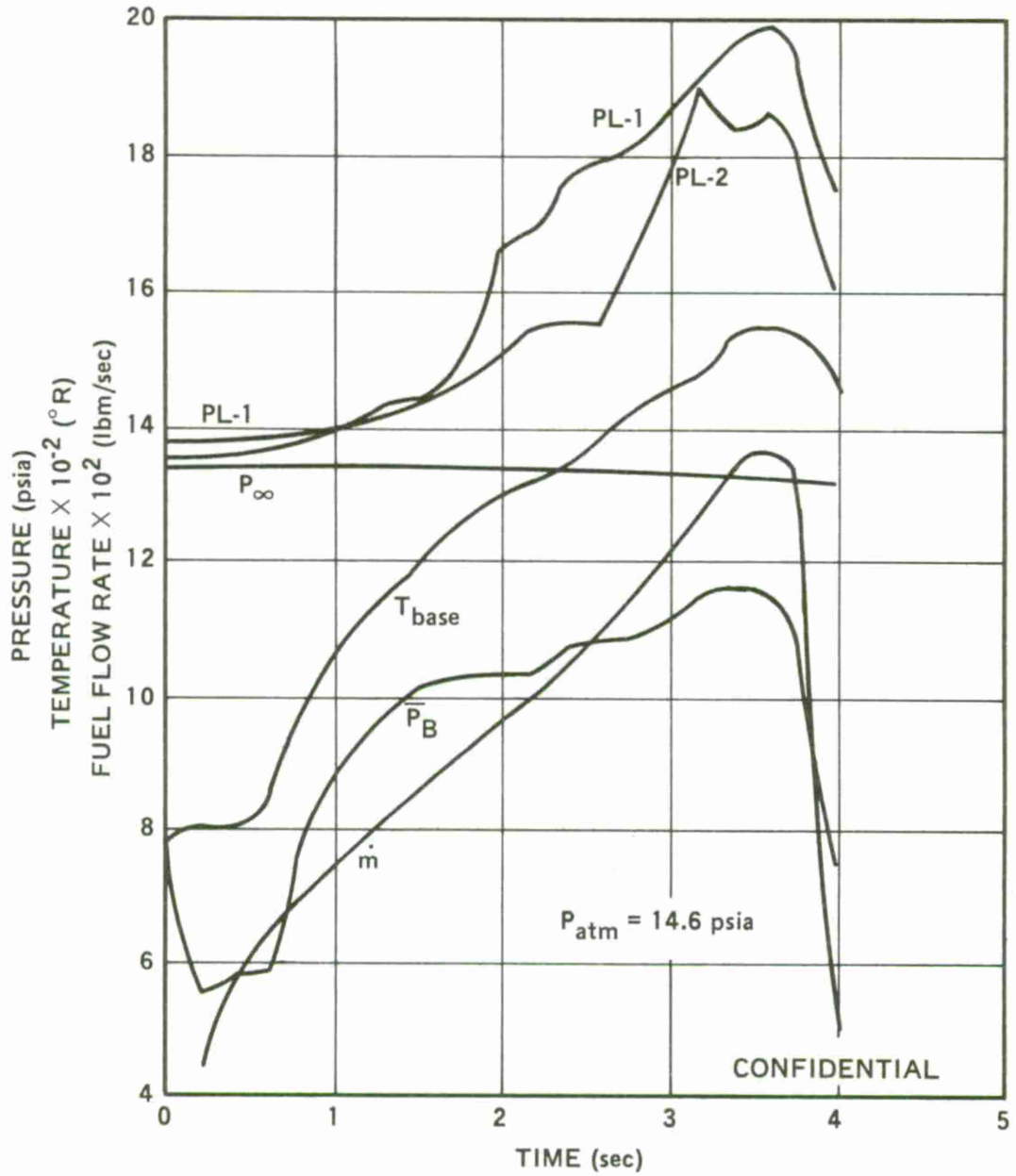


Figure 22. (C) Results from Test 7 (U).

CONFIDENTIAL

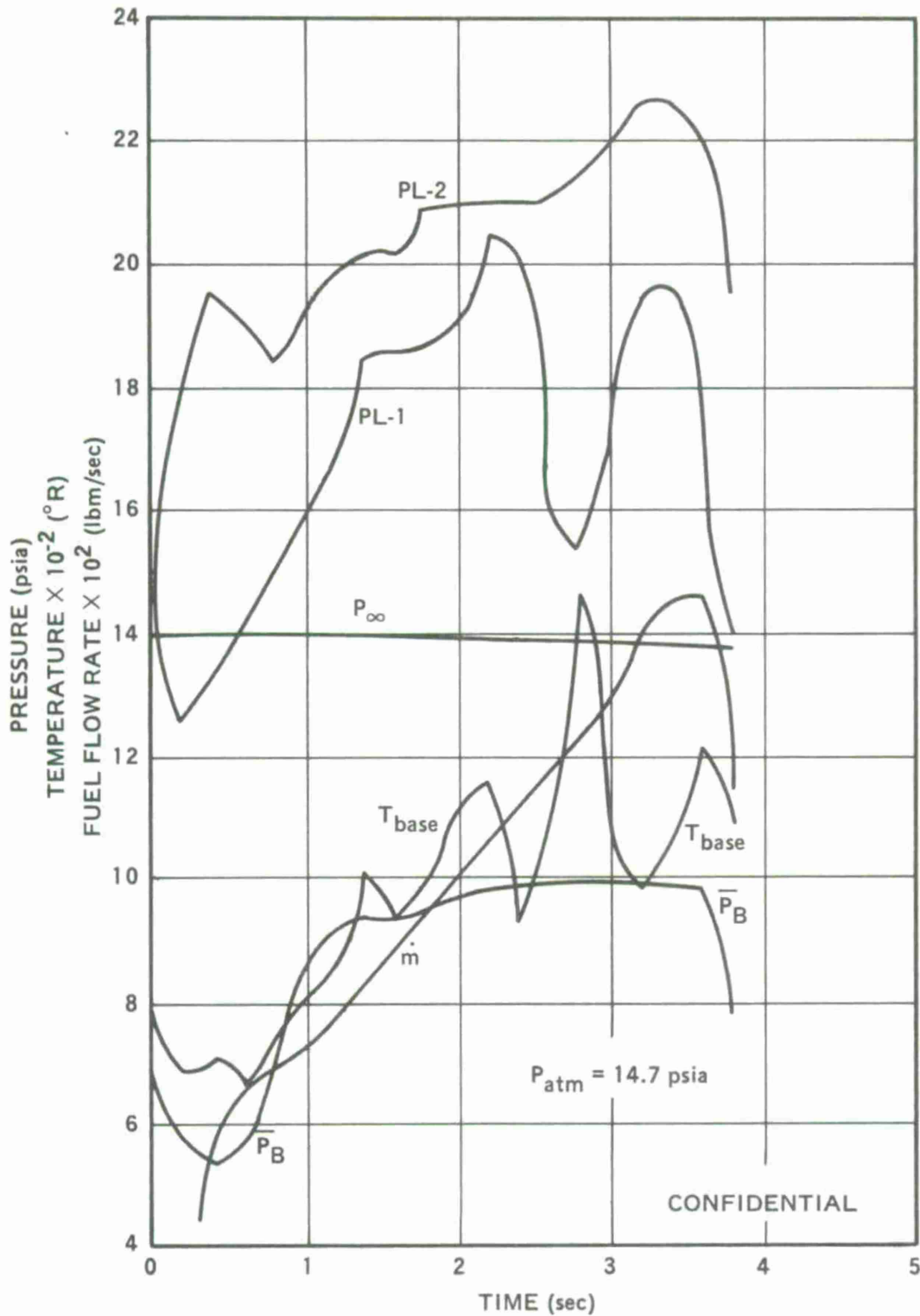


Figure 23. (C) Results from Test 10 (U).

CONFIDENTIAL

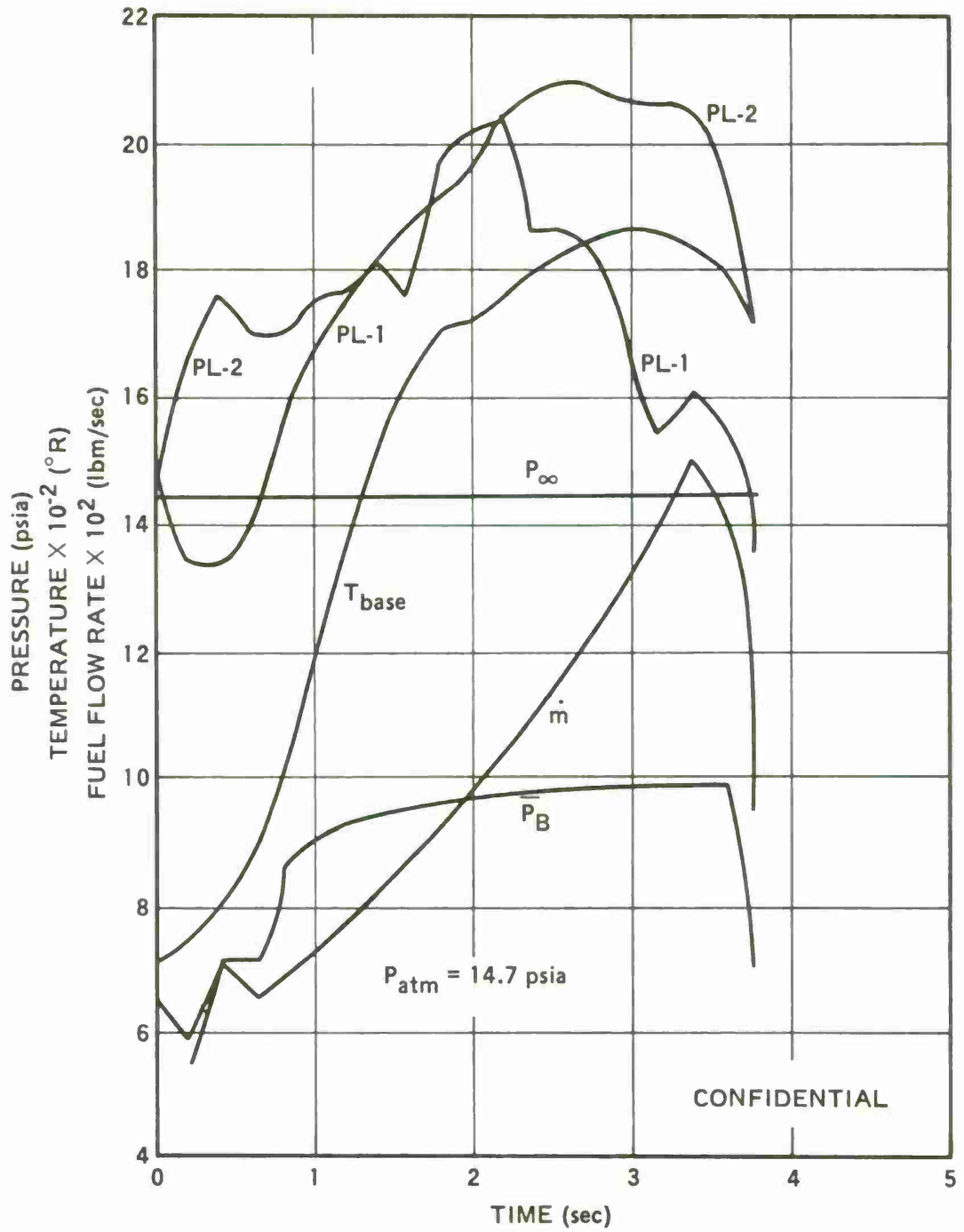


Figure 24. (C) Results from Test 11 (U).

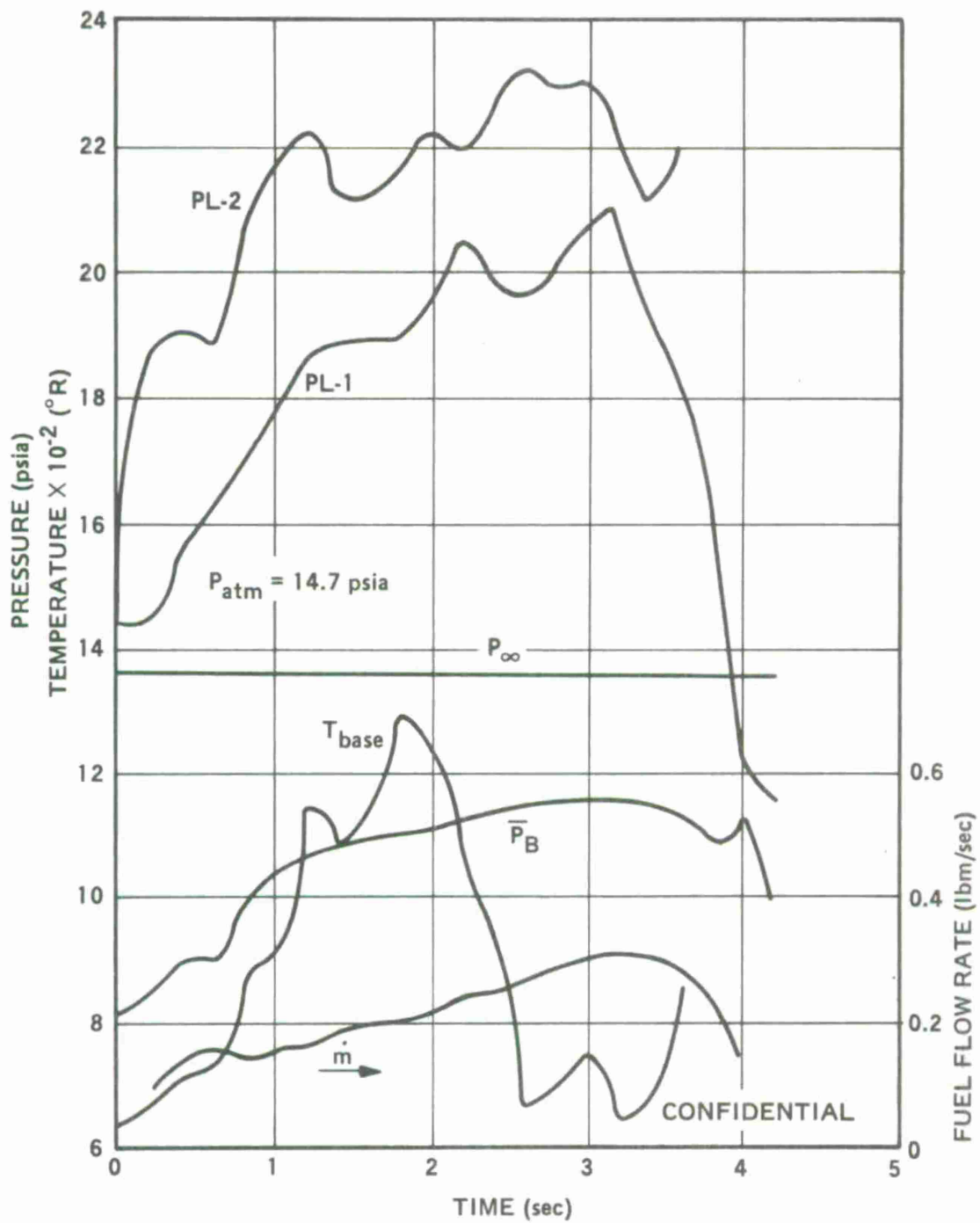


Figure 25. (C) Results from Test 12 (U).

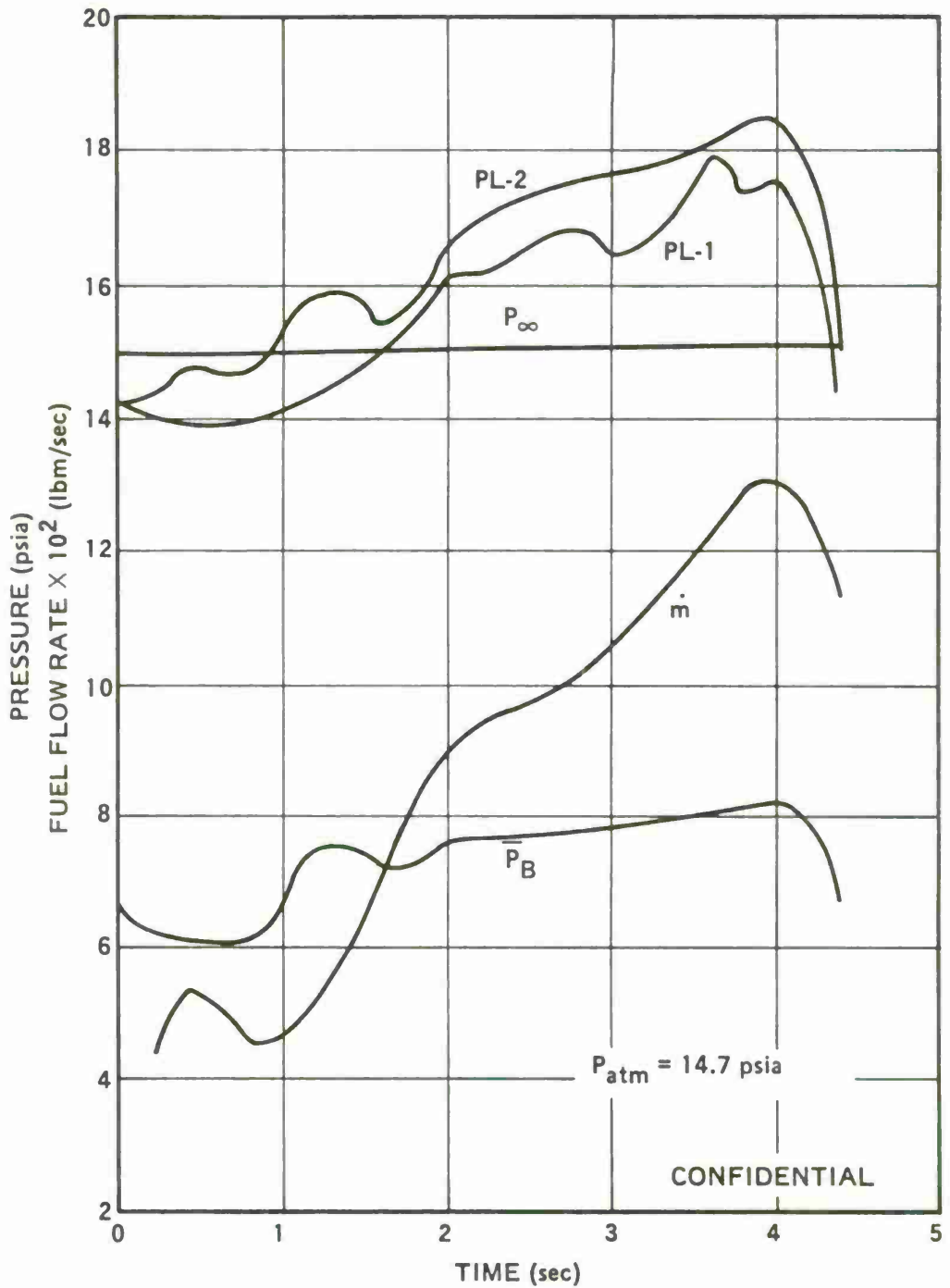
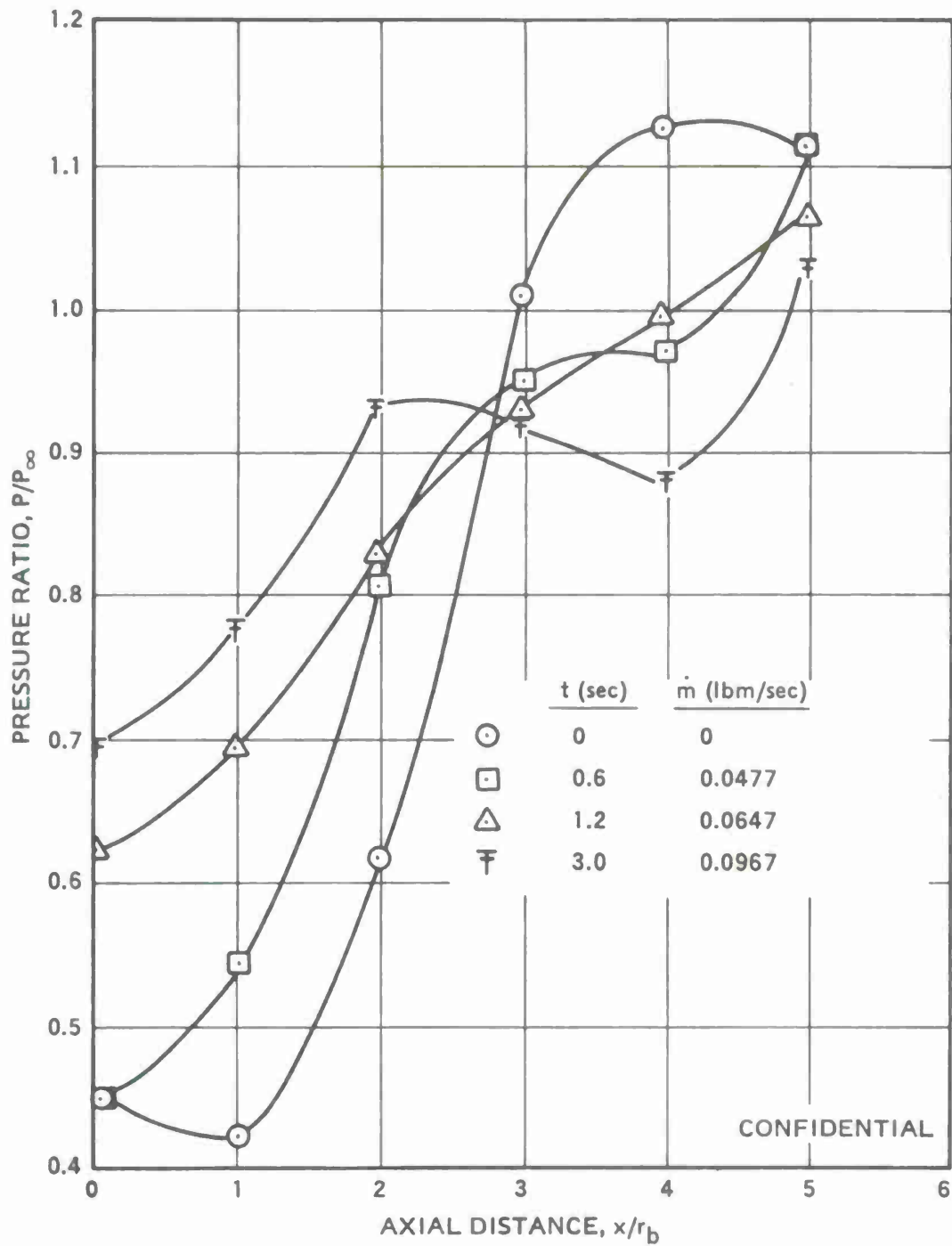


Figure 26. (C) Results from Test 13 (U).



CONFIDENTIAL

Figure 27. (C) Downstream Pressure Distributions, Test 4 (U).

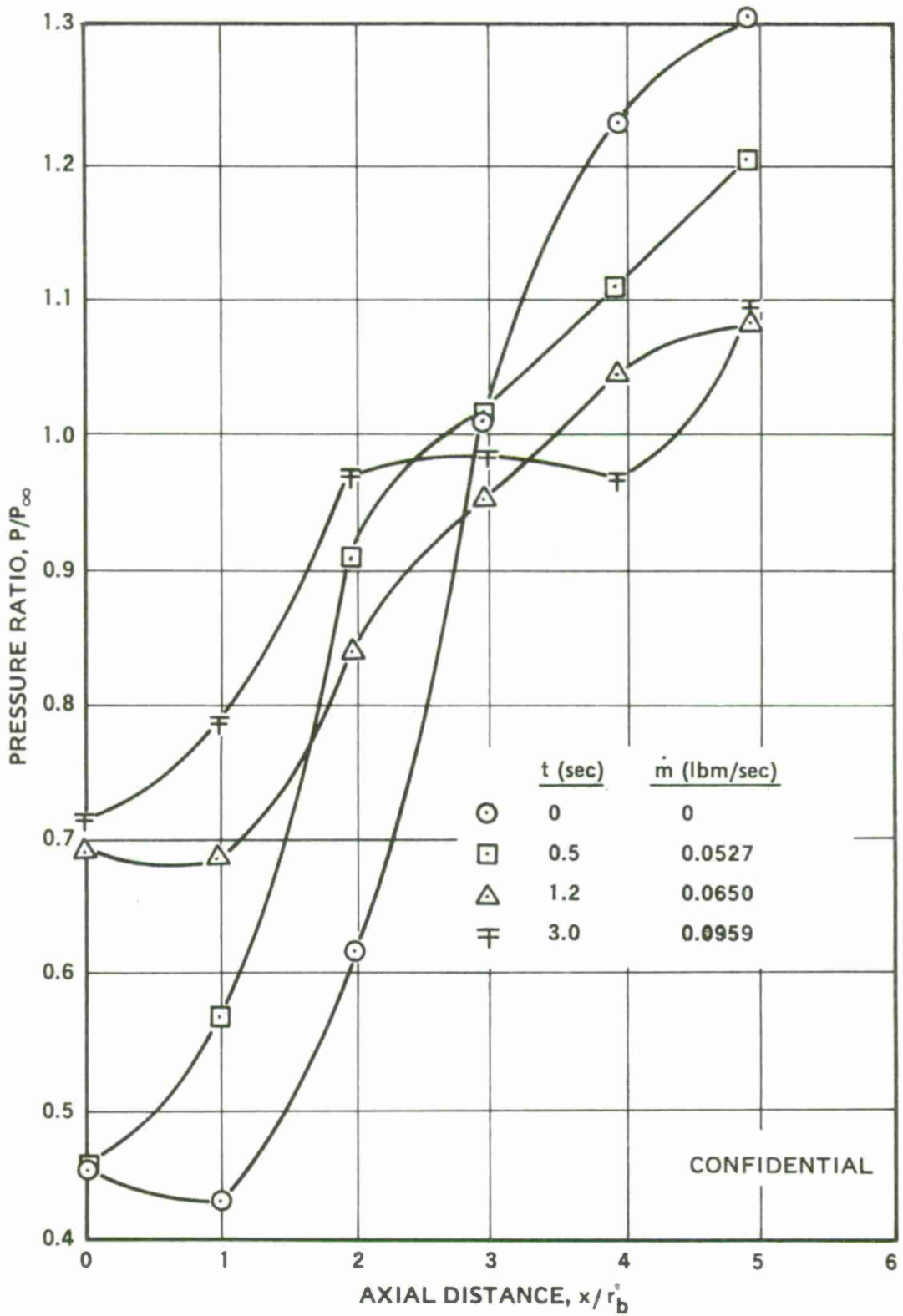


Figure 28. (C) Downstream Pressure Distributions, Test 5 (U).

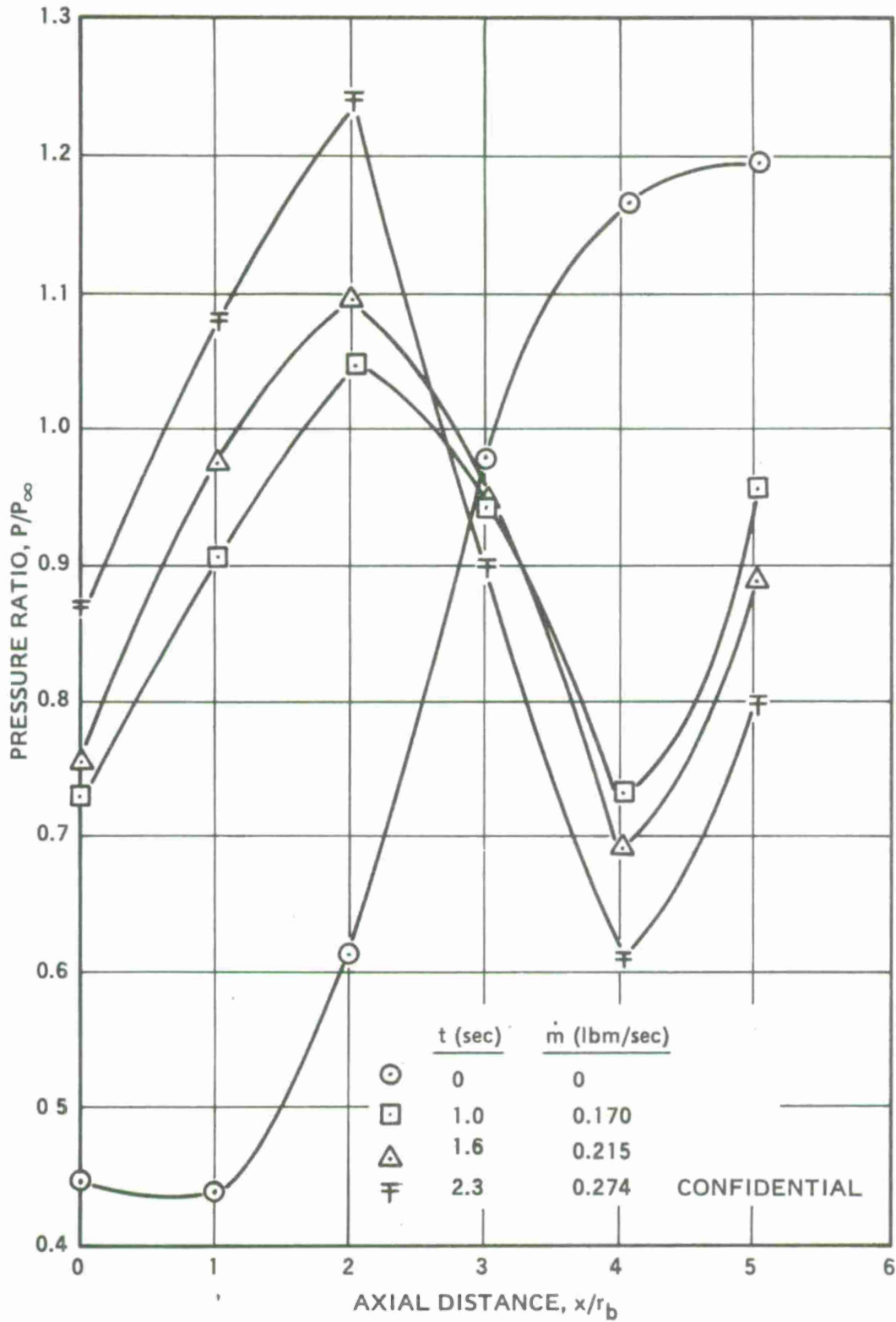


Figure 29. (C) Downstream Pressure Distributions, Test 6 (U).

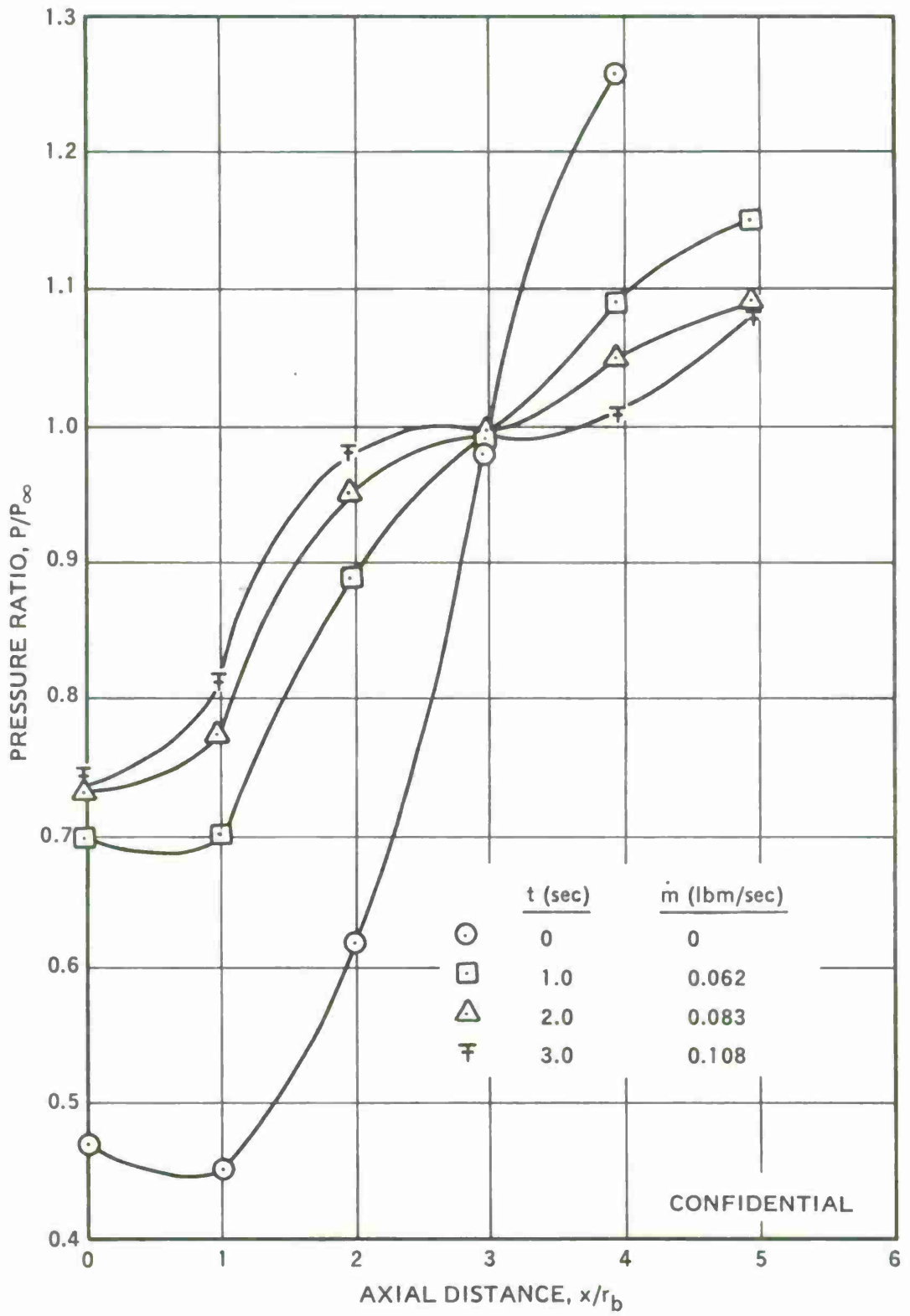


Figure 30. (C) Downstream Pressure Distributions, Test 7 (U).

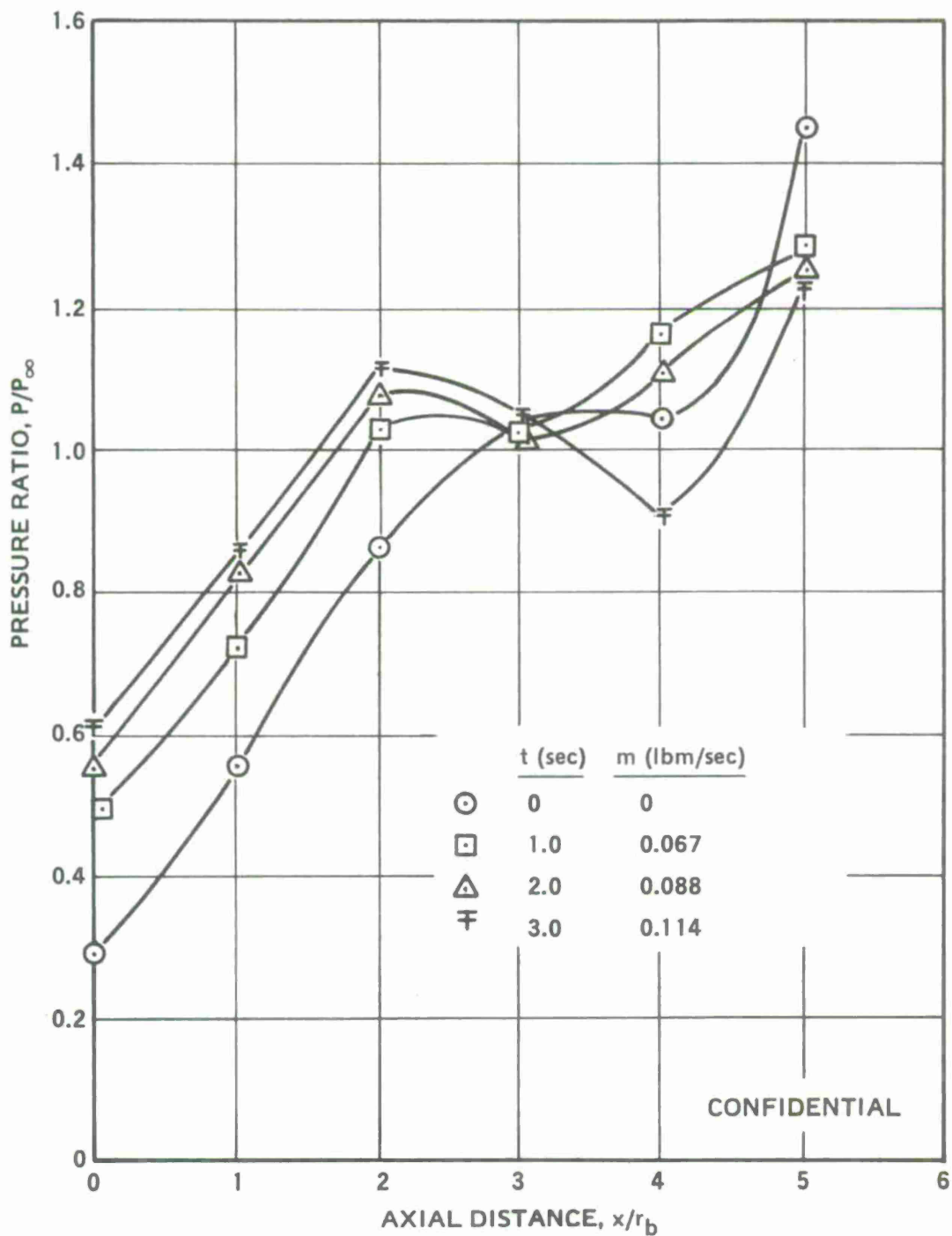


Figure 31. (C) Downstream Pressure Distributions, Test 8 (U).

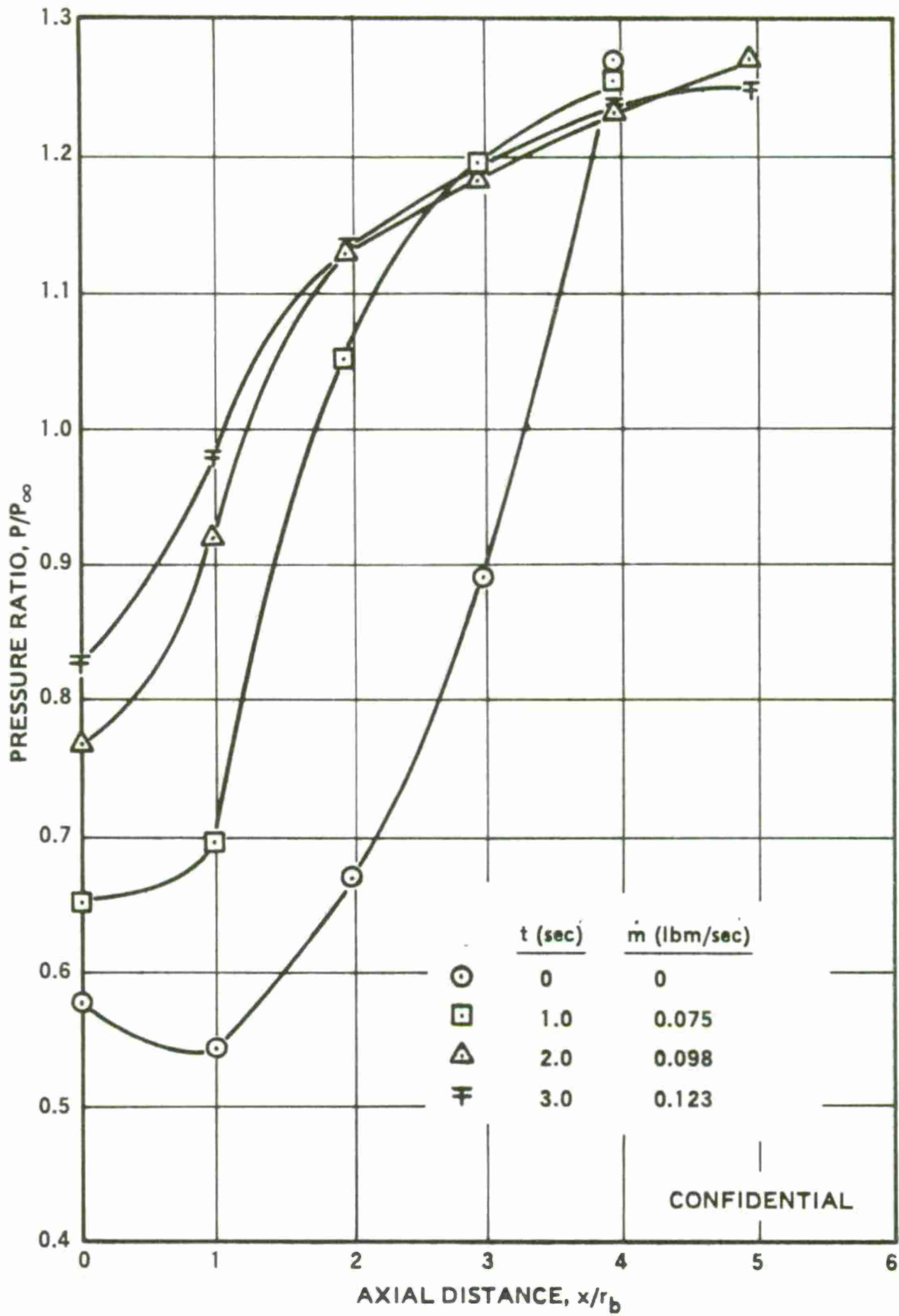
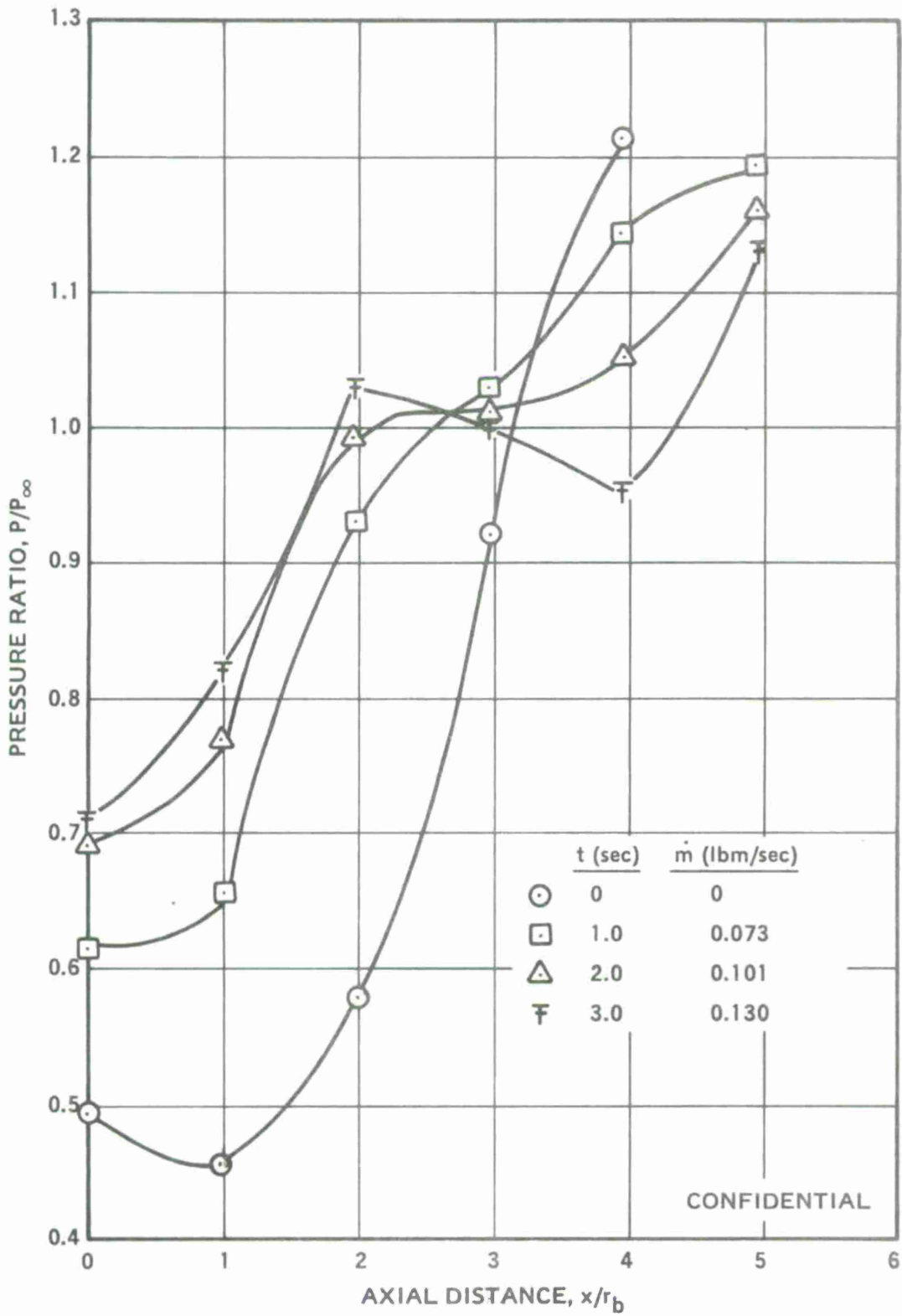


Figure 32. (C) Downstream Pressure Distribution, Test 9 (U).



CONFIDENTIAL

Figure 33. (C) Downstream Pressure Distributions, Test 10 (U).

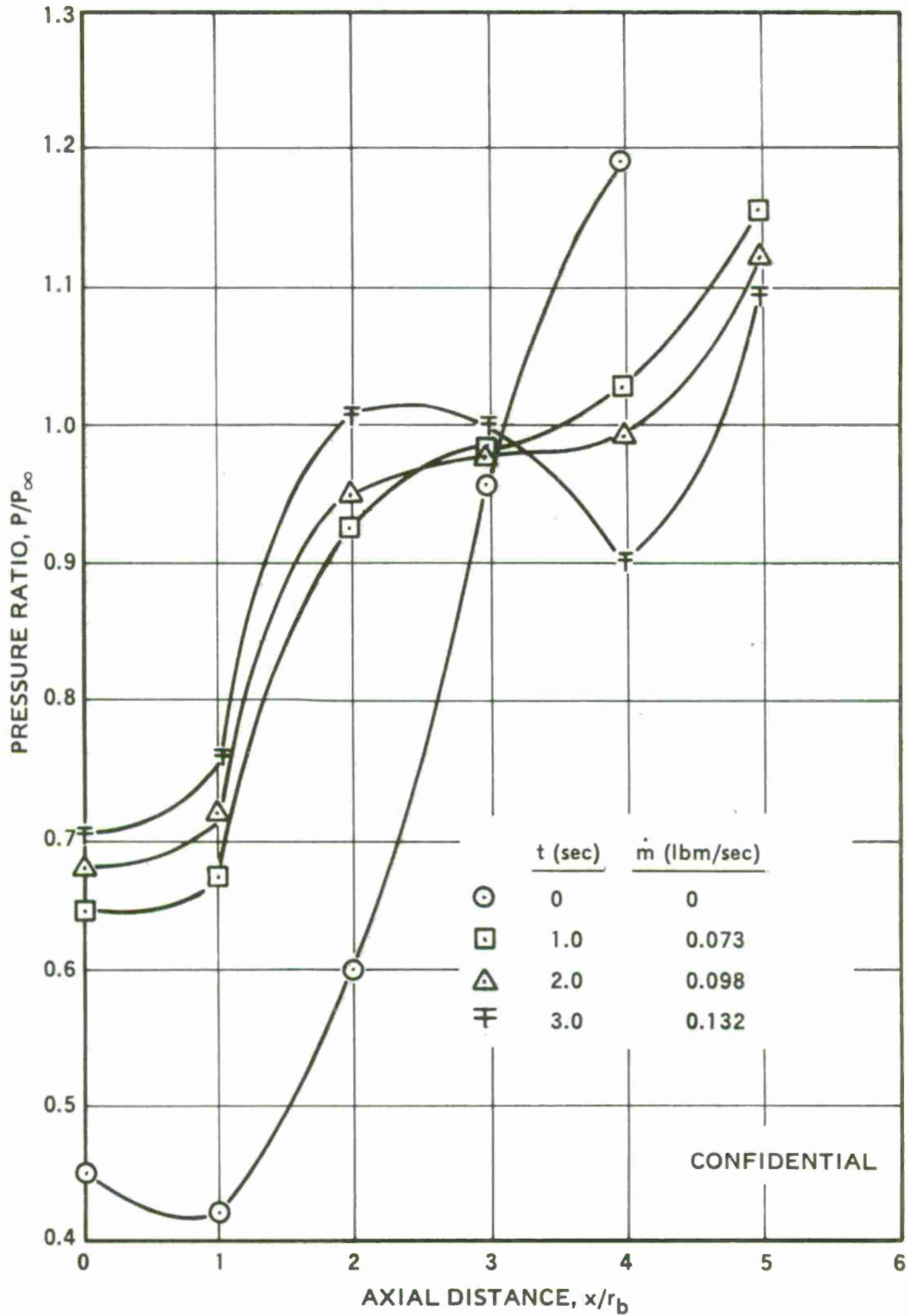


Figure 34. (C) Downstream Pressure Distributions, Test 11(U).

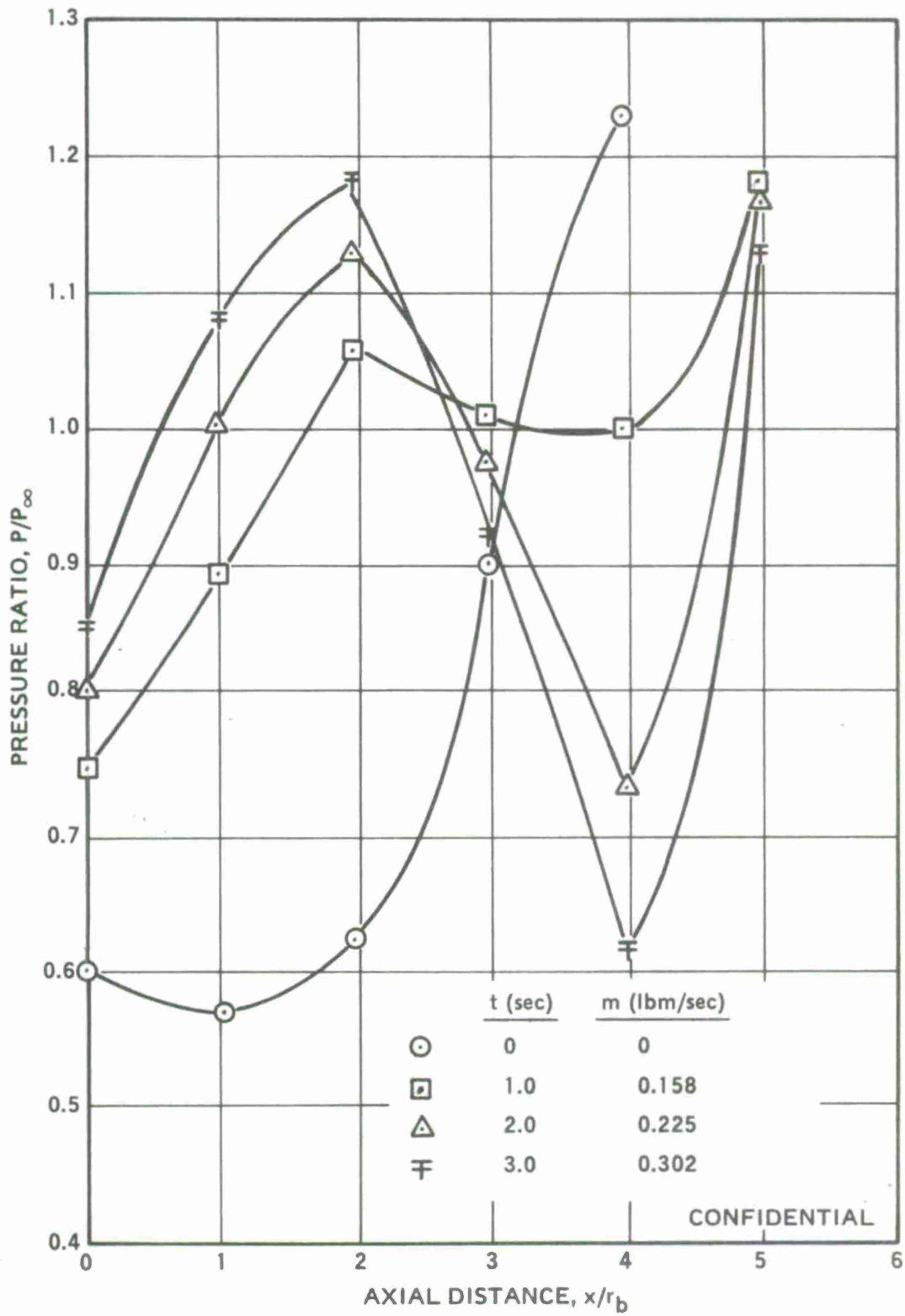


Figure 35. (C) Downstream Pressure Distributions, Test 12 (U).

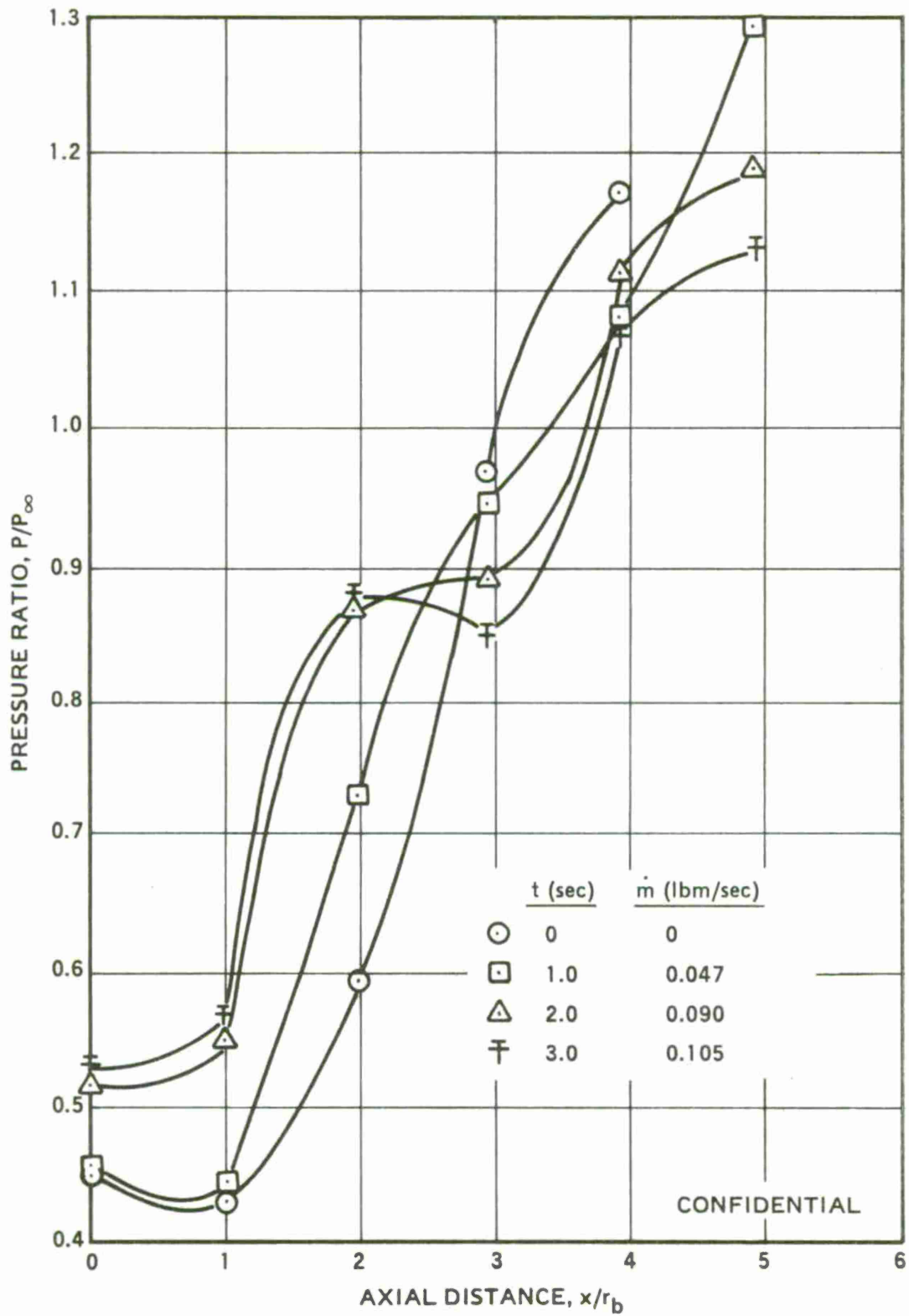


Figure 36. (C) Downstream Pressure Distributions, Test 13 (U).

(C) The variations of PL-2 were somewhat less erratic than for PL-1. In all of these tests PL-2 increased rather than decreased at the start of the test, and the maximum values obtained for PL-2 were always higher than those for PL-1.

(U) The base flow temperature was measured with a shielded thermocouple in Tests 7, 10, and 11. The base flow temperature was not measured in Tests 4 and 5.

(U) In Test 7, the recorded base flow temperature increased almost uniformly throughout the test. The maximum value of about 2500°R was measured at the end of the test. During this test, however, the joint between the thermocouple and its cylindrical shield softened and the shield orientation relative to the thermocouple bead changed.

(U) For Test 10, the temperature variation during the test was very erratic, but the general trend was that of a temperature increasing with time. The maximum recorded temperature was about 1450°R. For Test 11, the recorded temperature variation was not erratic at all, and the temperature increased uniformly throughout the test to a maximum value of about 1850°R.

(C) The downstream pressure distributions for Tests 4, 5, 7, 10, and 11 are given in Figures 27, 28, 30, 33, and 34. In general they are quite similar to those obtained in the tests with ARCADENE 129A. At x/r values less than 3, the pressures are generally higher than the "air only" levels, while at x/r values greater than 3, they are less than the "air only" values. At the later times in the tests, when the fuel flow rates were highest, there is a local maximum in the curves at $x/r = 2$, and this is generally followed by a local minimum at $x/r = 4$.

(C) In Tests 6 and 12, the magnitude of the fuel flow rates was approximately double the values used in the tests described above. Principal results from these tests are presented in Figures 19 and 25.

(C) In Test 6 (Figure 19), the injector body failed at $t = 2.2$ seconds. The large fuel flow rate impinging on the insulation in the injector body eroded through to the steel, which promptly melted, allowing the fuel to be injected into the air stream through a single port about 3 inches upstream from the model base. The condensed phases in the fuel stream penetrated to the nozzle outer wall. The time of failure is indicated by the rise in the static pressure measurement caused by the boundary layer separation occurring upstream of the failure point.

(C) Prior to the time of the failure, the base pressure increased to about 12 psia and both lip pressures increased to about 23 psia. The rise of PL-2 was somewhat more rapid than for PL-1.

(C) During the 0.2 second following the time of failure, a 1.5 psia base pressure increase was observed. This was followed by a decrease back to an extrapolation of the initial base pressure curve, and then the base pressure continued its rise to the end of the firing at essentially the same rate as observed before the failure.

(C) The temperature recorded in Test 6 increased to 2330°R at $t = 2.2$ seconds. At this point the shield became separated from the thermocouple body, and the thermocouple failed.

(U) The conditions for Test 12 were intended to be identical to those for Test 6, except that the hardware failure was avoided by the use of graphite insulation in the injector body at the point where the fuel flow from the motor blast tube impinged on the injector body wall. However, the free-stream static pressure in Test 12 was significantly less than for Test 6, 13.7 psia versus 15.0.

(C) The base pressure in Test 12 increased uniformly throughout the test reaching a maximum value of 11.7 psia. Both lip pressures increased somewhat erratically throughout the test, PL-1 reaching 21 psia and PL-2 rising to 23 psia. The base flow temperature increased to 1300°R during the first 1.8 seconds of the test, and then decreased to its initial value of about 650°R.

(C) The downstream pressure distributions for Tests 6 and 12 are presented in Figures 29 and 35. With the larger fuel flow rates of these tests, the maximum in the distribution at $x/r = 2$ and the minimum at $x/r = 4$ are much more pronounced than in the tests with the lower fuel flow rates. For Test 12, the "air only" pressure distribution is distorted, the pressure ratios at $x/r < 3$ being larger than nominal.

(C) Test 8 was conducted with five 90-degree sonic nozzles, but the nozzles were extended 0.25 inch into the air stream in order to obtain greater fuel penetration. Principal results for this test are contained in Figure 21, and the downstream pressure distributions are contained in Figure 31.

(C) The results in Figure 21 are quite different from others presented above. First of all, the initial base pressure before fuel injection is only 4.0 psia as compared to the nominal value of about 6.6 psia. The base pressure increases throughout the test to a maximum value of about 8.7 psia.

(C) The lip pressure PL-1 increases from 14.2 to 20.0 psia during the first 0.4 second of the test and then decreases thereafter. On the other hand, PL-2 is abnormally low before ignition, 9.8 psia, and increases throughout the test, finally reaching 14.4 psia.

(C) The recorded base flow temperature increases throughout the test, but reached a maximum value of only 870°R.

(C) The downstream pressure distributions in Figure 31 are also somewhat unusual. First, the "air only" distribution has a saddle extending from $x/r = 3$ to $x/r = 4$. Such a disturbance in the distribution has heretofore been observed only during fuel injection. Second, as in the "air only" case, the base pressure ratios with fuel injection are smaller than observed in other tests with ARCADENE 168A.

(C) For Test 9, injection was from nine sonic nozzles directed through the base corner at an angle of 45 degrees. Principal results from this test are in Figure 22, and the downstream pressure distributions are in Figure 32.

(C) The free-stream static pressure for Test 9 was initially only 13.4 psia as compared to a target value of 14.7 psia. On the other hand, the initial base pressure before ignition was higher than the nominal value, 7.6 psia versus 6.6 psia. In the first 0.2 second of the test, the base pressure decreased to 5.5 psia and then increased throughout the remainder of the test reaching a maximum of 11.6 psia.

(C) For this test only, both PL-1 and PL-2 were measured just upstream of and between injection ports. Because injection was through the base corner, a lip pressure could not be measured on line with an injection port. Both PL-1 and PL-2 increased gradually throughout the test, reaching maximum values of 19 and 20 psia.

(C) The measured base flow temperature increased continuously from its initial value of 780°R to the maximum value of 1990°R .

(U) For Test 13, a semicylindrical extension was added to the model base. This extension was one model radius long (1.48 inches), so the five Mach 2, 90-degree nozzles were 2.08 inches upstream from the new base.

(C) The plots in Figure 26 show that the base pressure increased to only 8.2 psia during fuel injection. PL-1 decreased slightly on ignition and then increased gradually to about 18 psia. PL-2 increased upon ignition and reached a final value of 18.5 psia. The base flow temperature was not measured in this test.

(C) The downstream pressure distributions for Test 13 are presented in Figure 36. Perhaps the most interesting feature in this test is that the minimum in the curve for $t = 3.0$ seconds occurs at $x/r = 3$ rather than at $x/r = 4$ as in previous tests.

(C) The color movies for the tests with ARCADENE 168A were all essentially the same. Intermittent bright flames were clearly visible, and these appeared to be associated with condensed phases that penetrated further into the supersonic stream than did the injected gases. The gas flow could be traced by the presence of a pale blue flame that extended approximately 3 inches downstream from the injection ports. For Test 9, using 45-degree injection, the bright flames appeared less displaced from the base separation bubble in the radial direction.

(U) The Schlieren movies for the tests with ARCADENE 168A revealed all of the features described above for tests with ARCADENE 129A. In addition, the pictures showed dark streaks which appeared to be the locus of the condensed phase trajectories. These were, in general, slightly inclined toward the model axis downstream from the base. For Test 9, these streaks appeared less inclined toward the model axis and more nearly parallel to it. Prior to fuel injection in Test 8, shock waves originating from the nozzle extensions were clearly visible.

3. TEST 14 WITH ARCADENE 300

(C) The results for Test 14 with ARCADENE 300 propellant are contained in Figures 37 and 38. For this test, five 90-degree, Mach 2 nozzles were positioned 0.6 inch upstream from the model base. The higher fuel flow rate range was used, 0.15 to 0.33 lbm/sec, and the test conditions simulated Mach 2.5 flight at sea level.

(C) The base pressure curve in Figure 37 shows the base pressure decreasing during the first 0.2 second of the test, increasing rapidly to 9 psia at $t = 0.8$ second, and then increasing gradually throughout the remainder of the test, reaching a final value of 10.8 psia before tailoff.

(C) The temperature variation during Test 14 was most striking in that it was negligible, the temperature remaining about 600°R throughout the test.

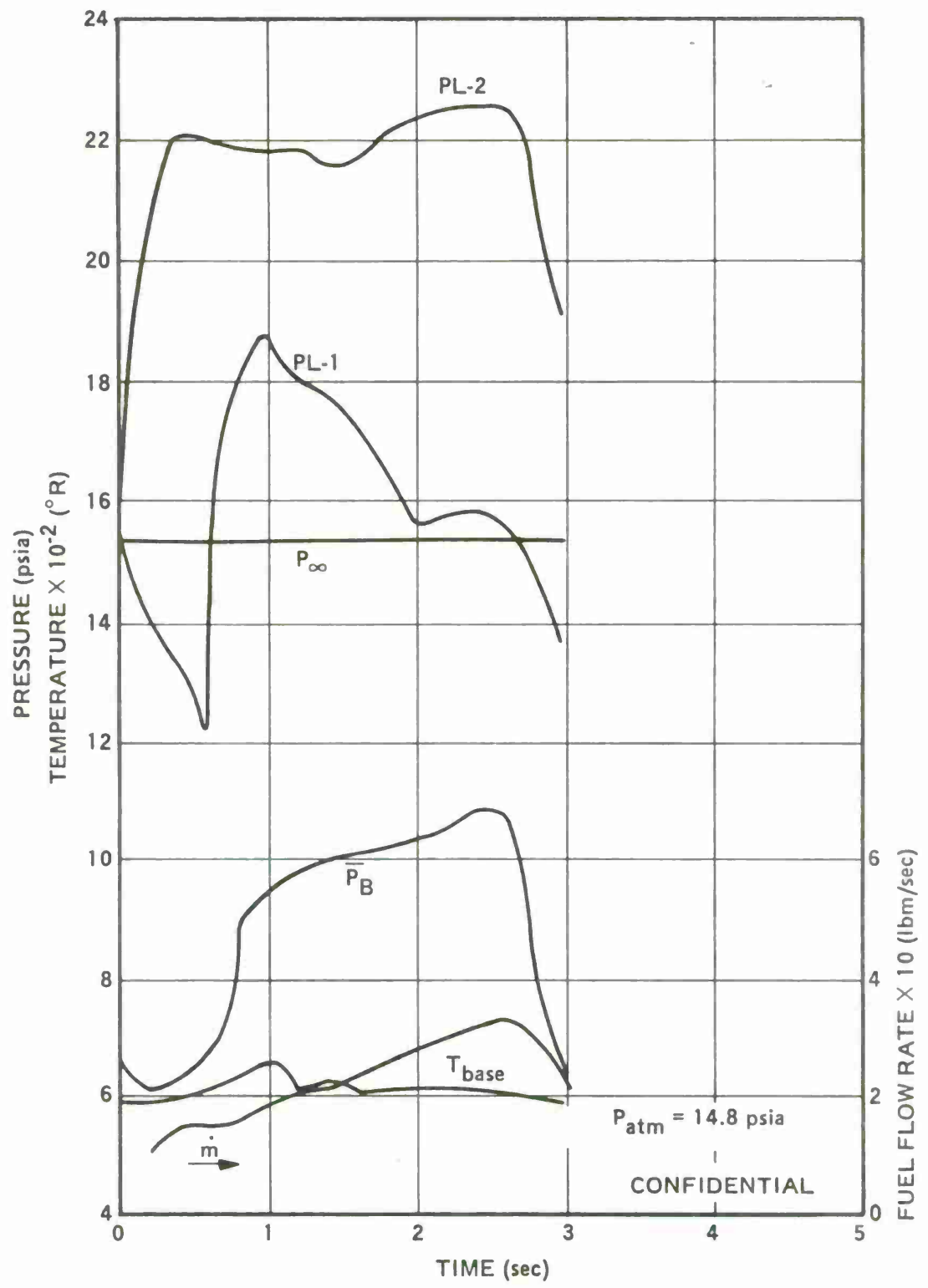
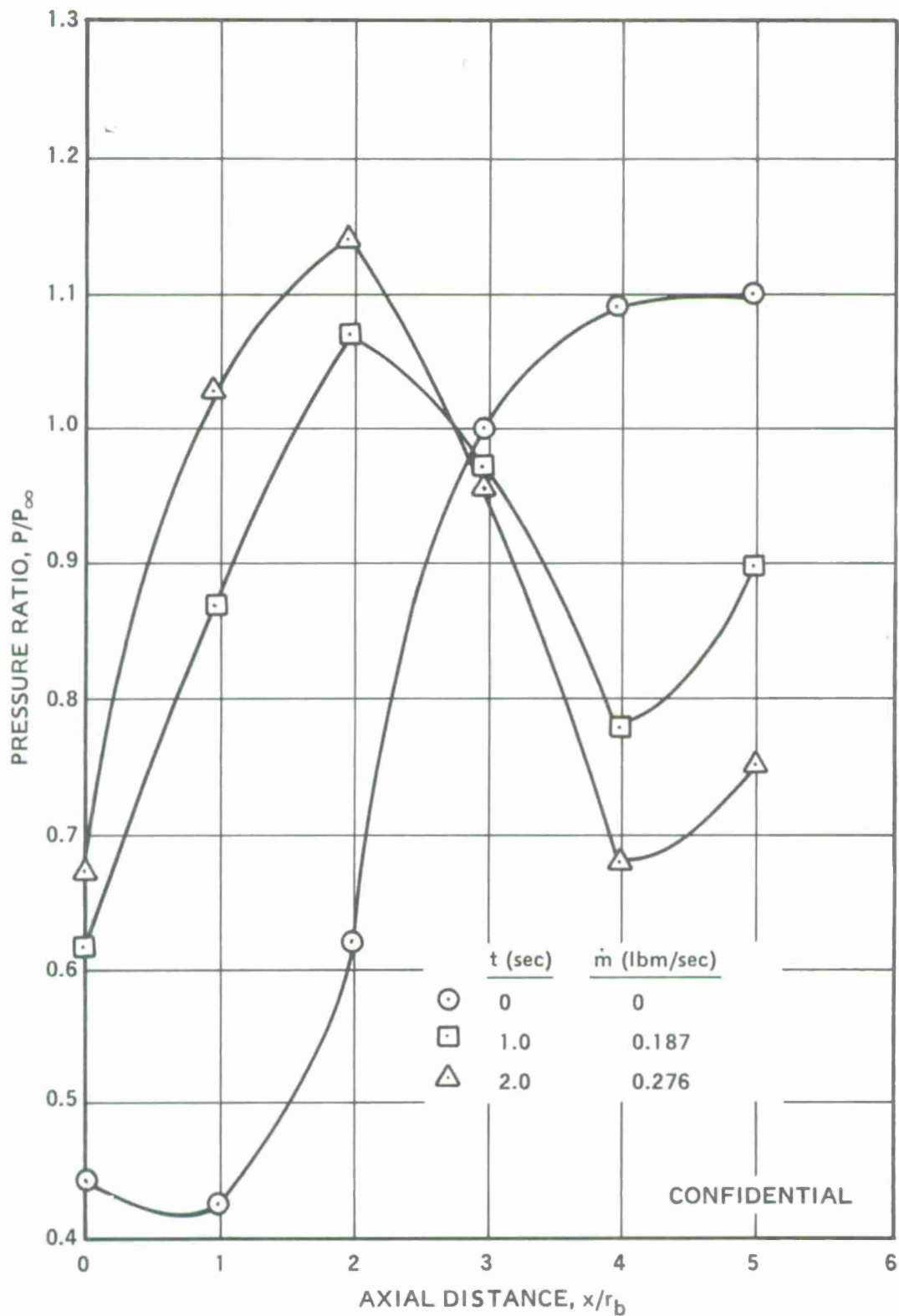


Figure 37. (C) Results from Test 14 (U).



CONFIDENTIAL

Figure 38. (C) Downstream Pressure Distributions, Test 14 (U).

(C) The downstream pressure distributions for Test 14 are contained in Figure 38. They are essentially the same as those for the two previous tests using the larger mass flow rate range, Tests 6 and 12. The local maximum at $x/r = 2$ and the local minimum at $x/r = 4$ are quite pronounced.

(C) The color movies for Test 14 were significantly different from those for tests with ARCADENE 168A. No bright flames were visible. The Schlieren movies showed the same features as evidenced in the ARCADENE 168A tests.

(U) Test 14 was the first test during which an emission spectra was recorded. However, only five bands could be observed. Three of these were bright and appeared at 3840, 3770, and 3720 Å. The other two bands, 3890 and 3960 Å were very weak. None of these bands has been firmly identified, but the three bright bands are believed to originate from NH, which would be present in the decomposition products of ammonium perchlorate.

4. ARCADENE 168A TESTS AT MACH 2.5, 15,000-FOOT ALTITUDE FLIGHT CONDITIONS

(C) Two tests were conducted with ARCADENE 168A at Mach 2.5, 15,000-foot altitude flight conditions. There was no difference in nominal test conditions for these tests, both of them using 90-degree sonic injection from five nozzles and a relatively low fuel flow rate range of 0.05 to 0.11 lbm/sec. The results from these tests, designated 15 and 16, are contained in Figures 39 to 42.

(C) Principal results for Test 15 are presented in Figure 39. In addition to the usual information, this figure also contains a graph of the test section static pressure (P-FB), measured on the outside of the outer nozzle wall. The variation of this pressure is indicative of the degree to which the test section pressure was controlled by varying the diffuser throat area.

(U) During Test 15, the variable area diffuser did not operate properly, and the test section pressure increased from 8.2 to 10.8 psia. However, the test section pressure was reasonably constant for the first 1.4 seconds of the test.

(C) The base pressure for Test 15 decreased during the first 0.4 second and then increased to 5.7 psia at $t = 1.4$ seconds. It then increased rapidly to about 7.5 psia and remained at this level until tailoff at $t = 3$ seconds.

(C) Both lip pressures increased at the beginning of Test 15 with the rise in PL-2 being faster than that for PL-1. PL-2 then climbed relatively uniformly to about 14.5 psia at tailoff. PL-1 behaved more erratically, increasing rapidly, then decreasing, and then climbing back to 12.5 psia at tailoff.

(C) The downstream pressure profiles for Test 15 are given in Figure 41. After the rapid rise in test section pressure, the profiles appear somewhat unusual with a local minimum at $x/r = 3$. The pressure ratios at x/r values of 4 and 5 are larger than generally observed.

(C) Results for Test 16 are plotted in Figure 40. Here the test section pressure was controlled, but it still varied between 8.4 and a single peak at 9.8 psia. The base pressure decreased slightly on ignition and then rose to about 7 psia at $t = 1.6$ seconds. It remained at this level for the rest of the test.

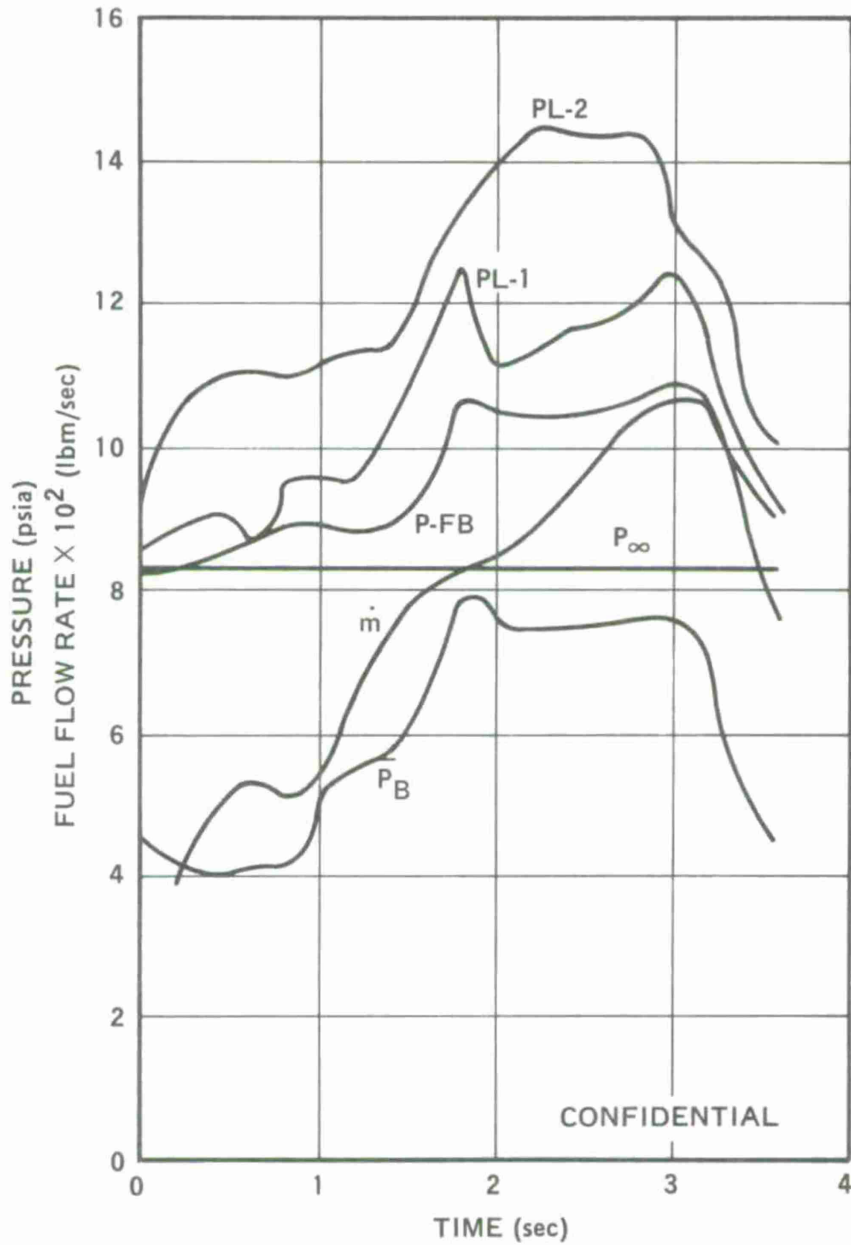


Figure 39. (C) Results from Test 15 (U).

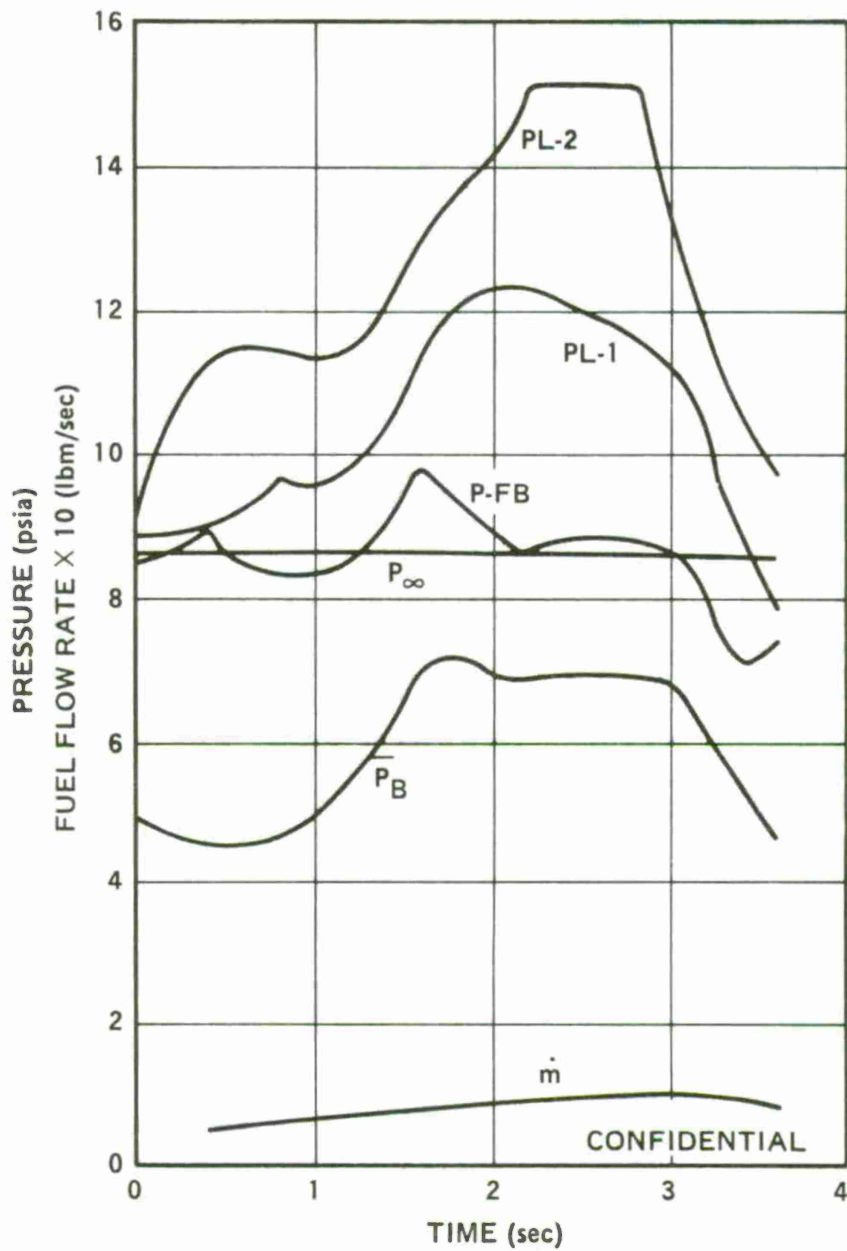


Figure 40. (C) Results from Test 16 (U).

CONFIDENTIAL

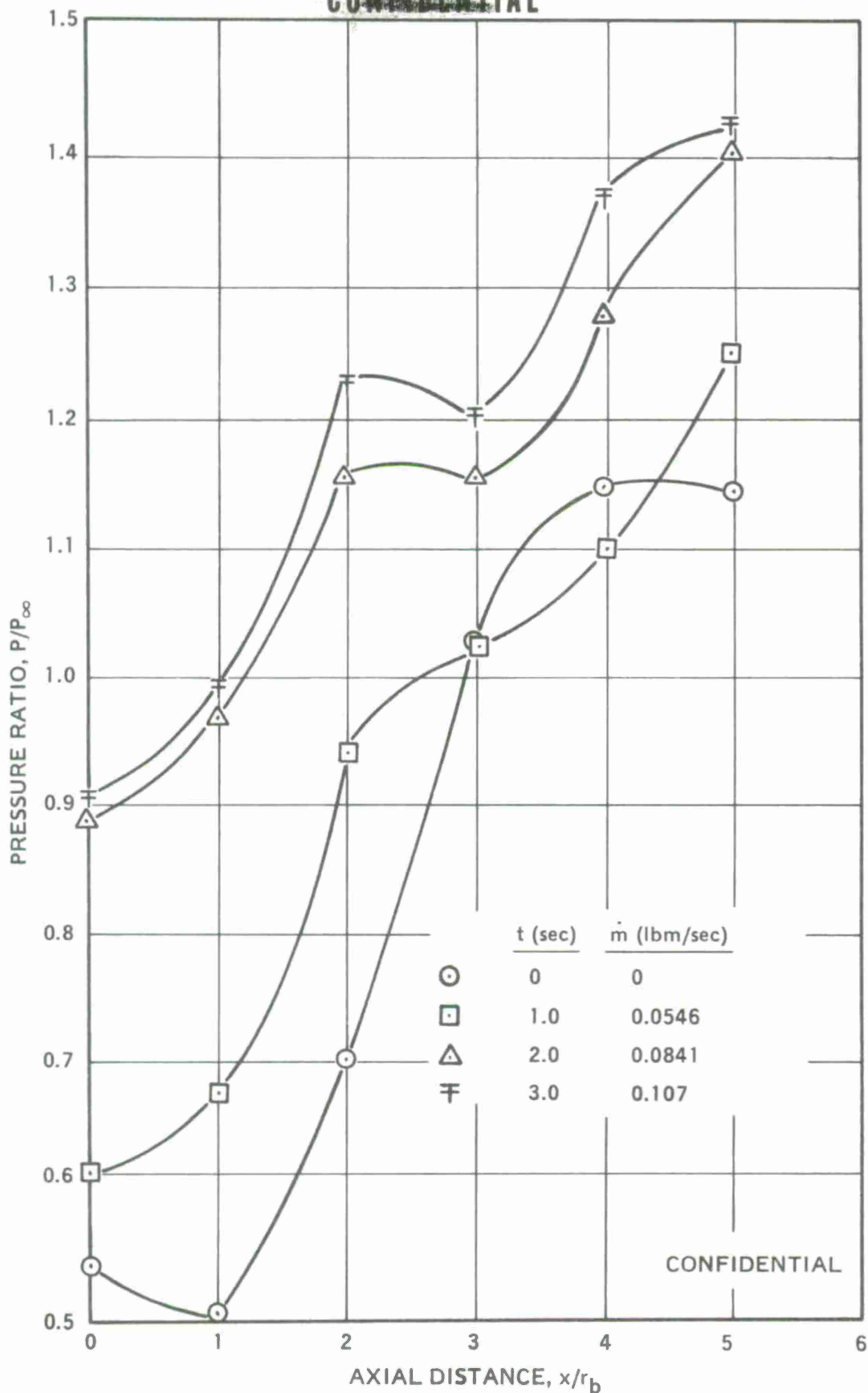


Figure 41. (C) Downstream Pressure Distributions, Test 15 (U).

CONFIDENTIAL

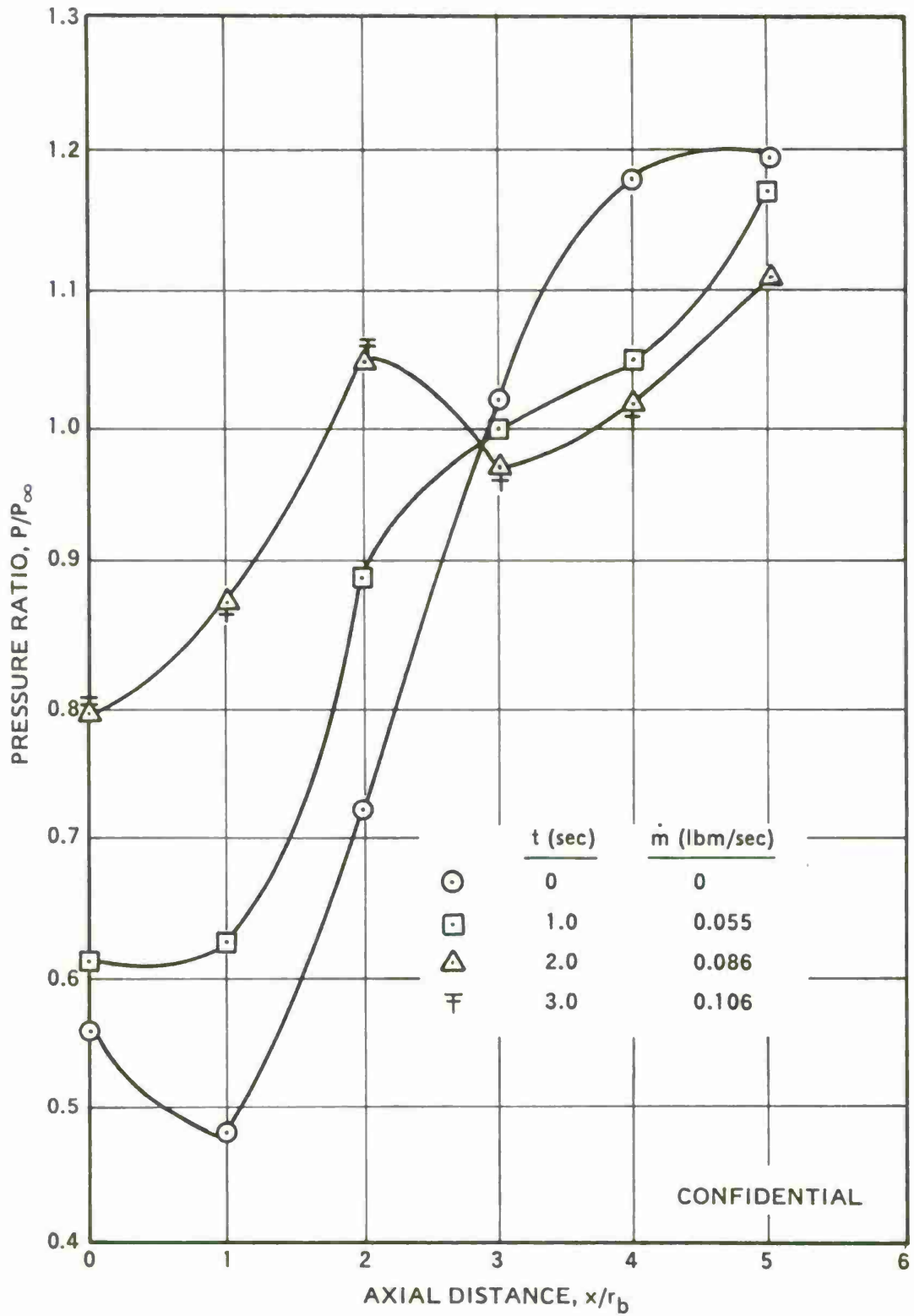


Figure 42. (C) Downstream Pressure Distributions, Test 16 (U).

(C) The color movies for Tests 15 and 16 were not much different from those for the sea-level tests with ARCADENE 168A. Bright intermittent flames could be seen along with the pale blue gaseous flame. The Schlieren movies showed the same features described above.

(U) A spectra was again recorded for Test 16. It showed the same bands attributed to NH in Test 14, but they were less intense here. Also faintly visible were lines attributed to Al at 3969, 3999, and 4046 Å. Very weak bands were discernible at 4971, 4835, and 4646 Å; these can be attributed to AlO.

5. TESTS WITH ARCADENE 168A AT MACH 2.0,
15,000-FOOT ALTITUDE FLIGHT CONDITIONS

(C) Two test were made with ARCADENE 168A at Mach 2.0, 15,000-foot flight conditions. Injection was from five 90-degree sonic nozzles. For Test 17, the fuel flow rate range was 0.05 to 0.11 lbm/sec, and for Test 18, the fuel flow rate range was 0.12 to 0.24 lbm/sec. The results of these tests are presented in Figures 43 to 46.

(C) For Test 17, Figure 43, the test section pressure was maintained within 6.5 and 8.0 psia. The base pressure decreased during the first 0.6 second and then increased to about 6.4 psia at $t = 2.0$ seconds. From that time on, the base pressure remained essentially constant until tailoff. PL-1 also decreased during the first 0.6 second and then increased. On the other hand, PL-2 increased gradually throughout the first second of the test. From $t = 1.0$ second onward, both lip pressures increased together to about 14 psia just before tailoff.

(C) The downstream pressure distributions for Test 17 are contained in Figure 45. These distributions look similar to those obtained at Mach 2.5, sea-level flight conditions, except that the minimum in the curve occurs at $x/r = 3$ rather than at $x/r = 4$.

(C) Results for Test 18 are given in Figure 44. Although feedback control of the diffuser throat area was achieved, the test section pressure varied erratically between 7.2 and 9 psia. The base pressure decreased slightly in the first 0.2 second and then increased to 7.5 psia at $t = 0.6$ second. After this time, the base pressure increased continuously to 9.0 psia just before tailoff.

(C) The downstream pressure distributions for Test 18 are given in Figure 46. At $t = 2.0$ seconds, the distributions are similar to previous ones obtained at high mass flow rates, except that the maximum occurs at $x/r = 1$ rather than at $x/r = 2$, and the minimum occurs at $x/r = 3$ rather than at $x/r = 4$. At $t = 2.8$, when the mass flow rate is largest, the pressure at the minimum is well above the minimum pressure at lower fuel flow rates. In past tests, the minimum pressure always became smaller as the fuel flow rate was increased. Note also that at $t = 2.0$ and 2.8, the base pressure ratio is greater than unity.

(C) Nothing particularly unusual was observed in the color or Schlieren movies. However, the bright flame in Test 18 appeared more constant and brighter than it had in previous tests.

(U) Emission spectra were obtained in both Tests 17 and 18. The three bands attributed to NH were visible in both pictures, but were markedly brighter in Test 18 than in Test 17. Both tests also clearly displayed Al lines at 4027, 3961, and 3944 Å. Additional unassigned lines could also be seen at 4194, 4157, and 4039 Å. AlO band heads could be seen at 5072, 4835, 4646, and 4463 Å, and these were more prominent in Test 17 than in Test 18. Both tests showed continuum radiation, and this was much brighter in Test 17 than in Test 18.

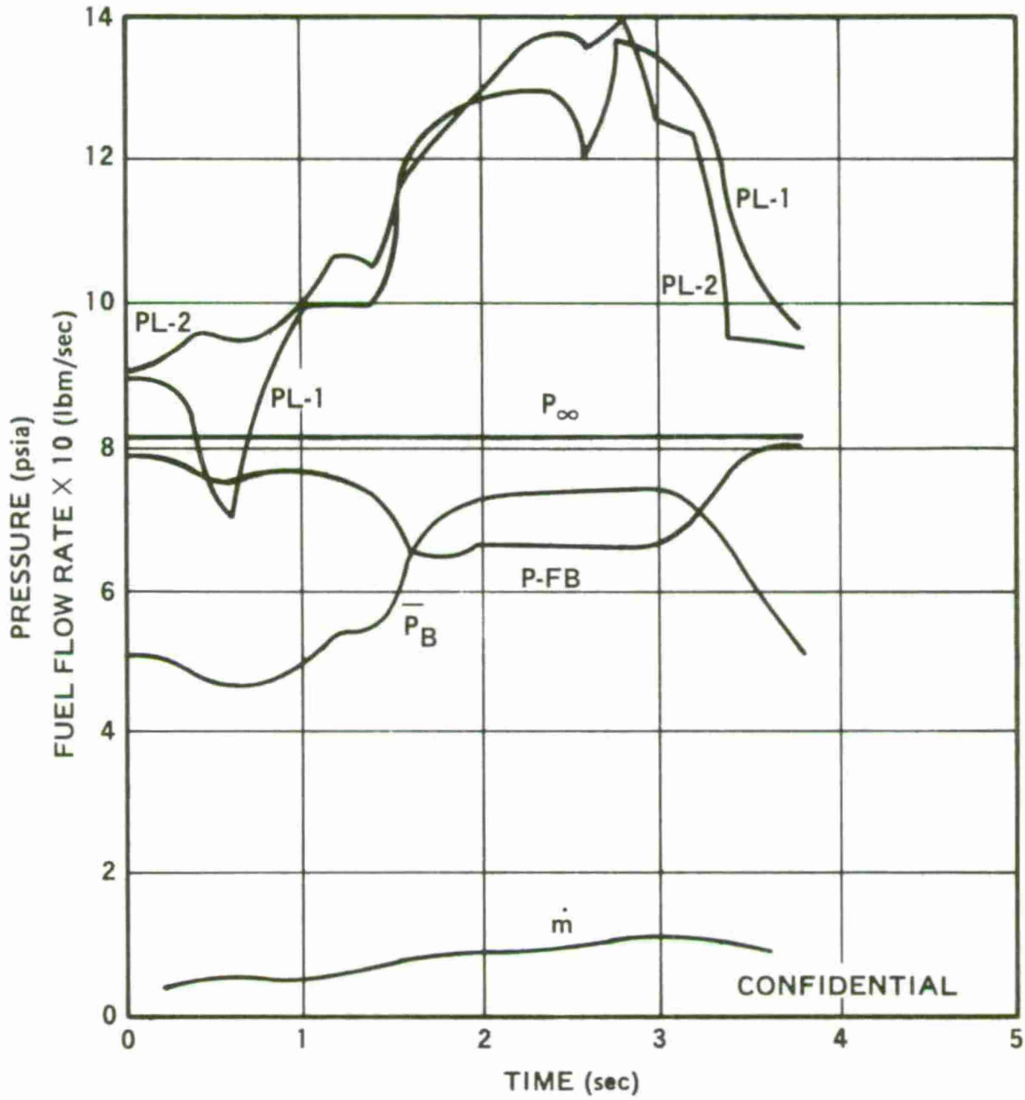


Figure 43. (C) Results from Test 17 (U).

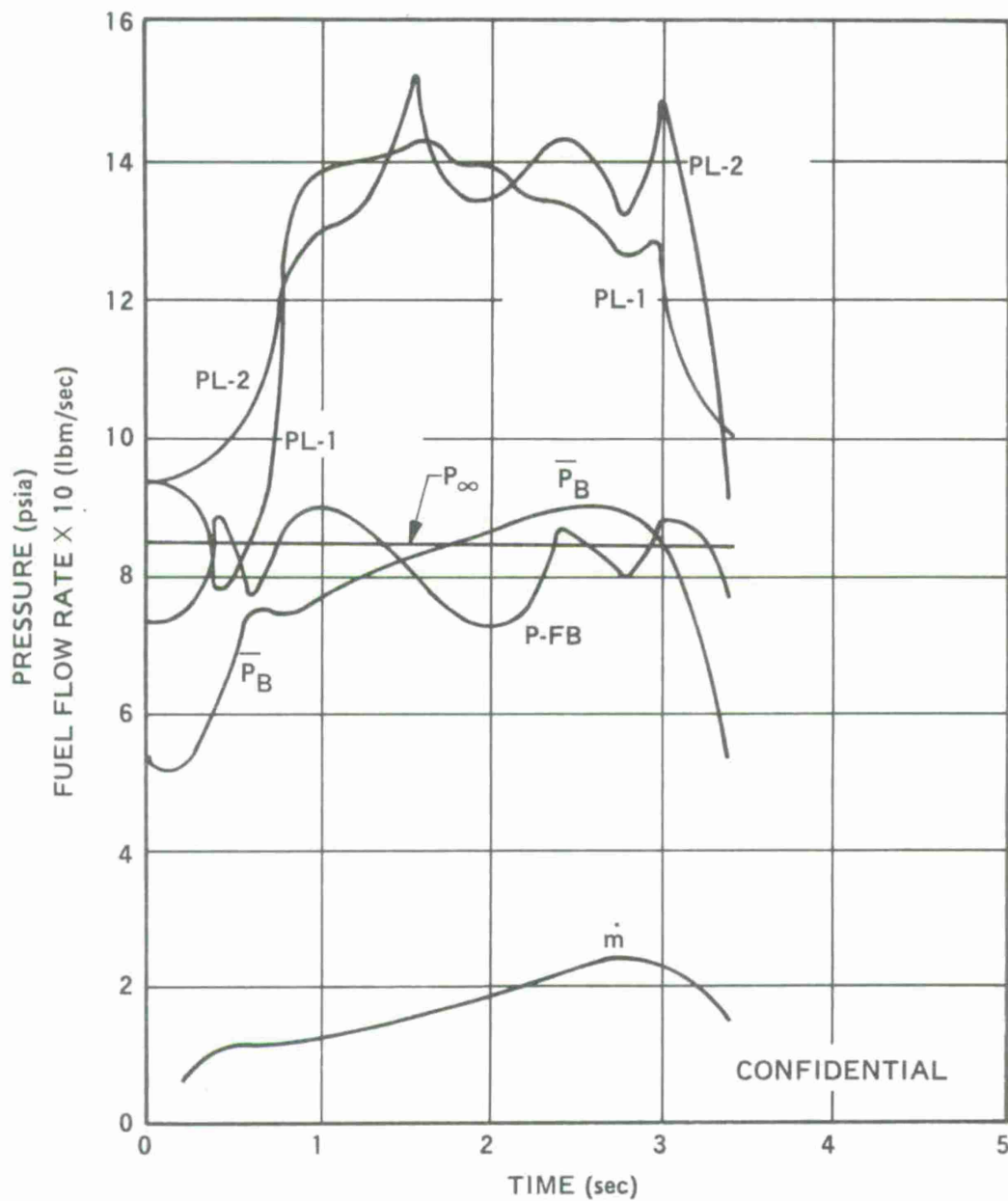
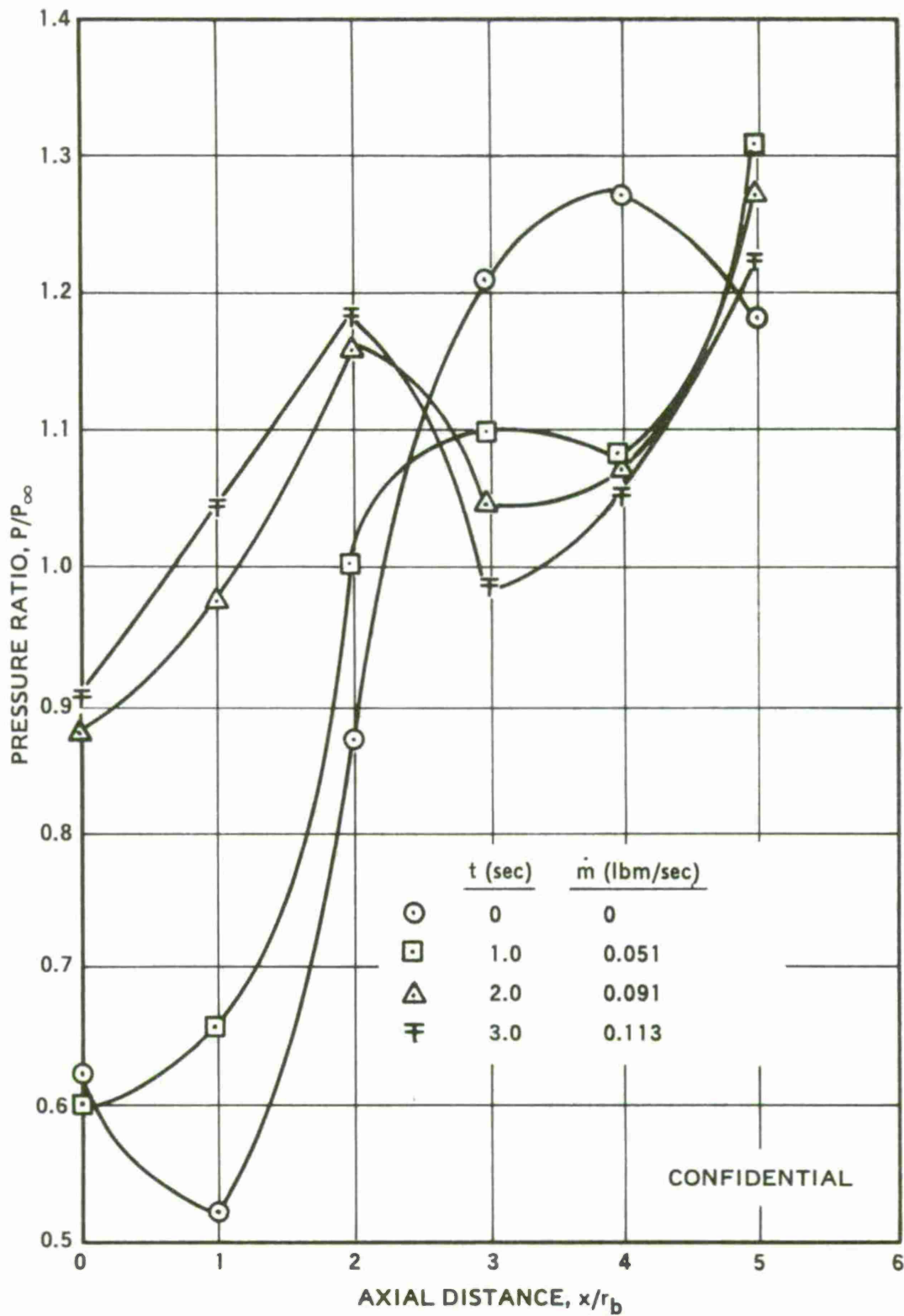
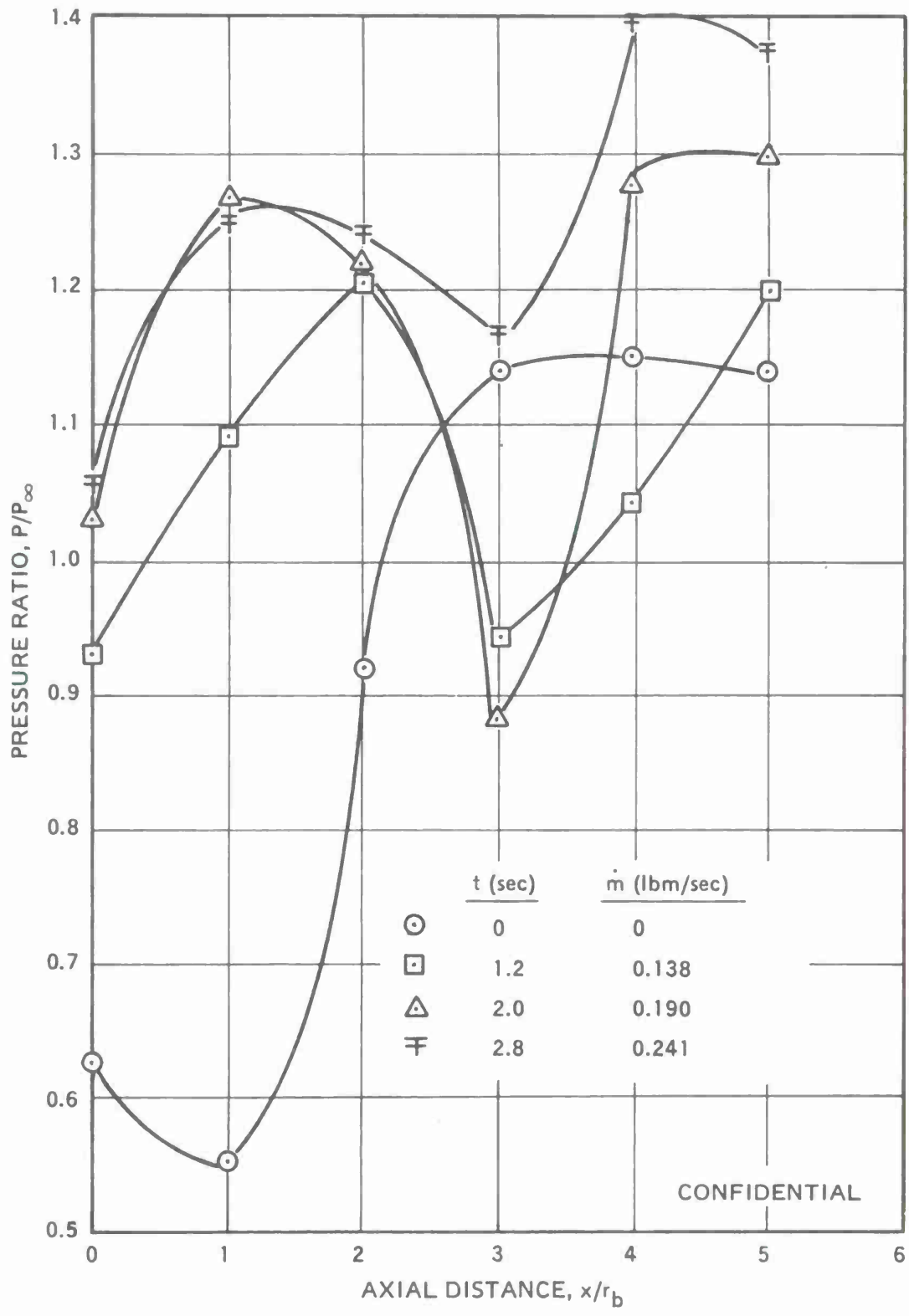


Figure 44. (C) Results from Test 18 (U).



CONFIDENTIAL

Figure 45. (C) Downstream Pressure Distributions, Test 17 (U).



CONFIDENTIAL

Figure 46. (C) Downstream Pressure Distributions, Test 18 (U).

6. TESTS WITH ARCADENE 168A AT MACH 2.0,
SEA-LEVEL FLIGHT CONDITIONS

(C) The last two tests were made with ARCADENE 168A propellant at Mach 2.0, sea-level flight conditions. The injection geometry consisted of five sonic nozzles injecting normal to the flow. For Test 19, the fuel flow rate range was 0.06 to 0.15 lbm/sec, and for Test 20, the fuel flow rate range was 0.12 to 0.27 lbm/sec. The results from these tests are contained in Figures 47 to 50.

(C) For Test 19, Figure 47, the base pressure decreased slightly in the first 0.2 second and then increased throughout the test, reaching about 11 psia before tailoff.

(C) The downstream pressure distributions for Test 19 are presented in Figure 49. They are quite similar to those obtained with ARCADENE 168A at Mach 2.5, sea-level conditions, but the decrease in pressure from the maximum to the minimum is much larger than previously obtained with this fuel flow rate range. Unlike the results obtained at Mach 2.0, 15,000-foot conditions, the local maximum occurs no closer than 2 radii from the base and the local minimum is always at $x/r = 4$.

(C) For Test 20, Figure 48, the shape of the base pressure curve is the same as in Test 19, but the maximum level achieved is higher, 13.2 psia. The lip pressure curves are also similar to those for Test 19, but again with larger maximum values.

(U) The color and the Schlieren movies for these tests were not markedly different from other ARCADENE 168A, sea-level tests.

(U) Emission spectra were obtained for both Tests 19 and 20. These contained all of the features described for Tests 17 and 18 with all of the bands and lines. The continuum radiation was brighter for Test 20 than for Test 19.

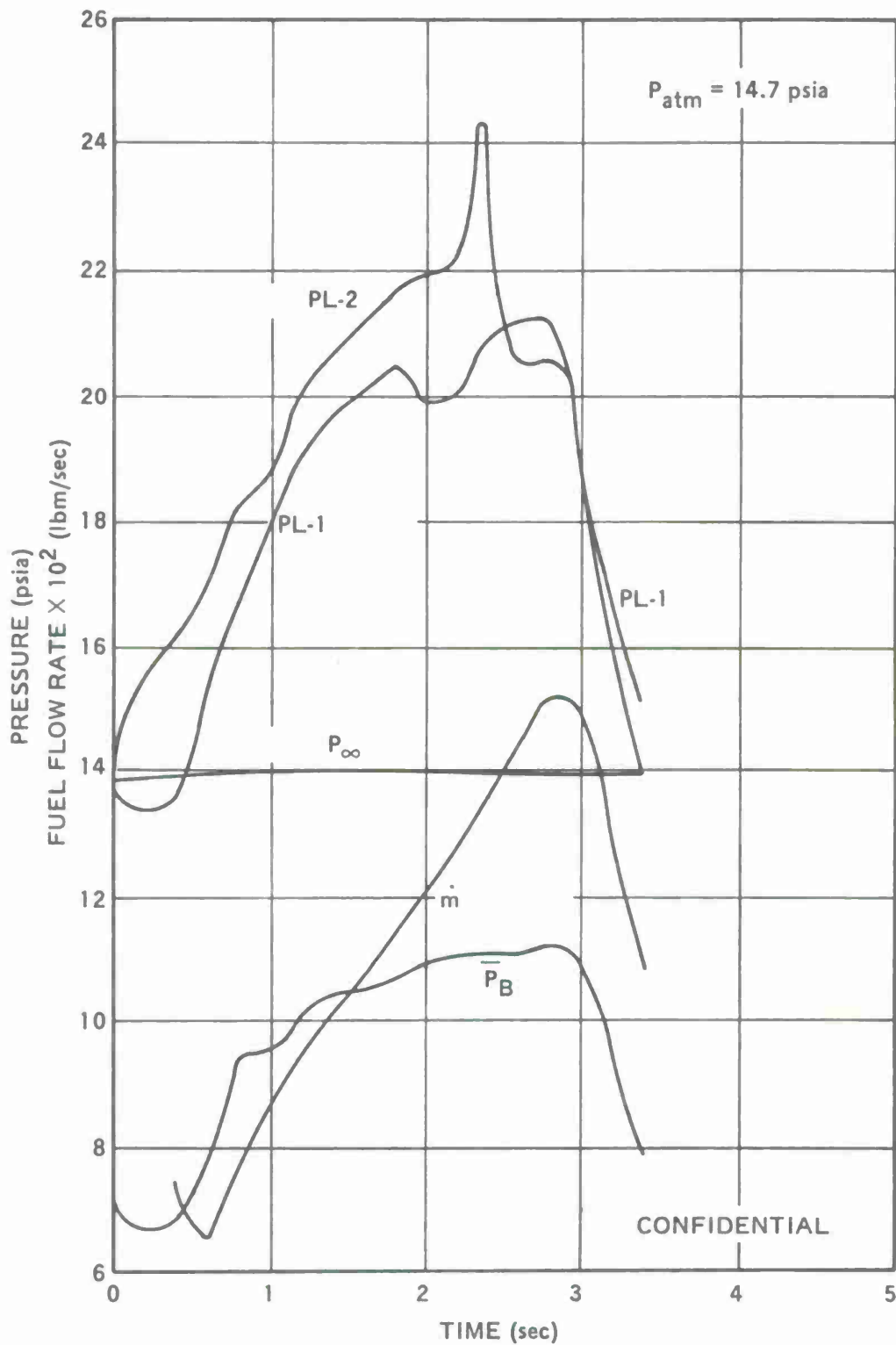


Figure 47. (C) Results from Test 19 (U).

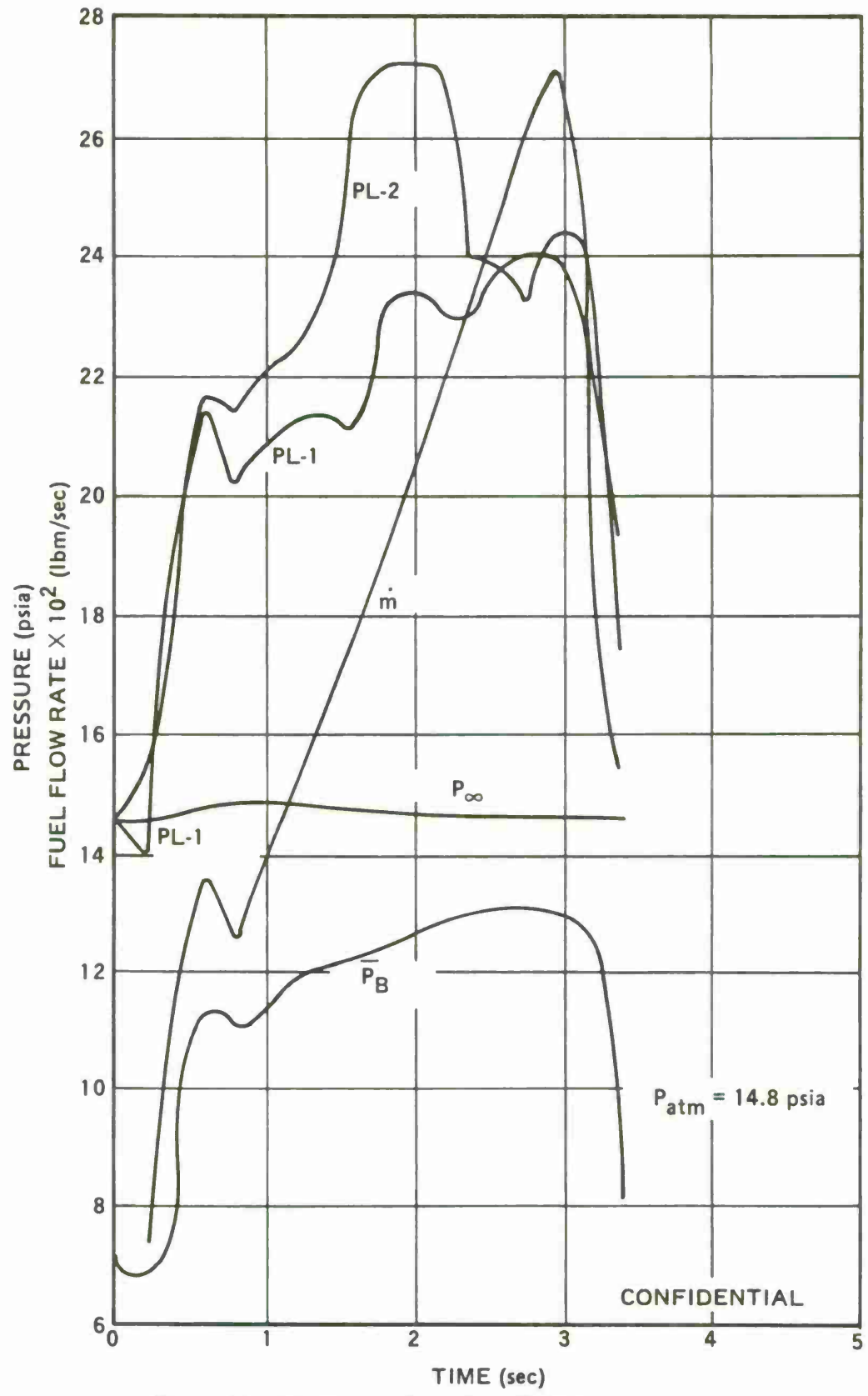


Figure 48. (C) Results from Test 20 (U).

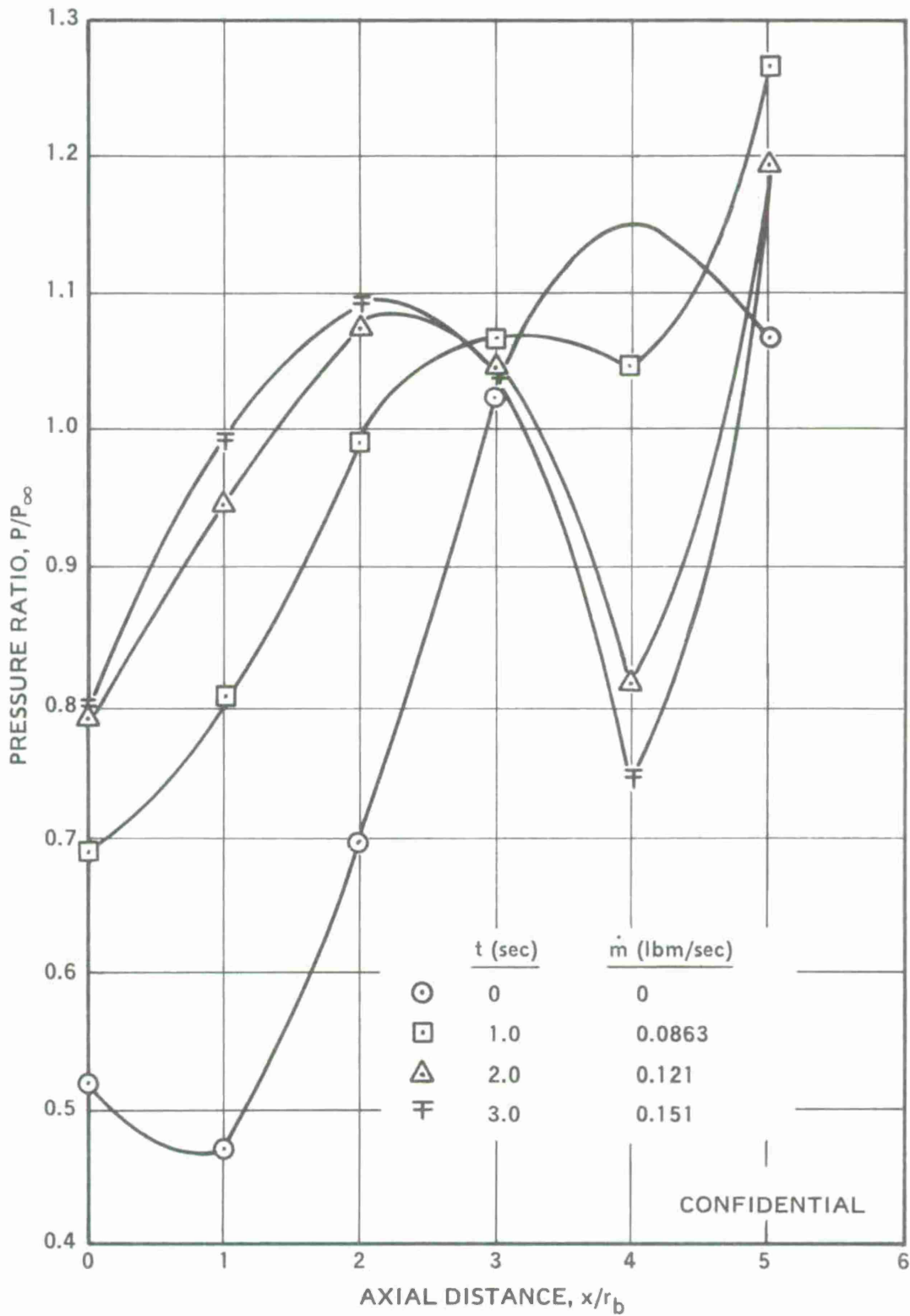


Figure 49. (C) Downstream Pressure Distributions, Test 19 (U).

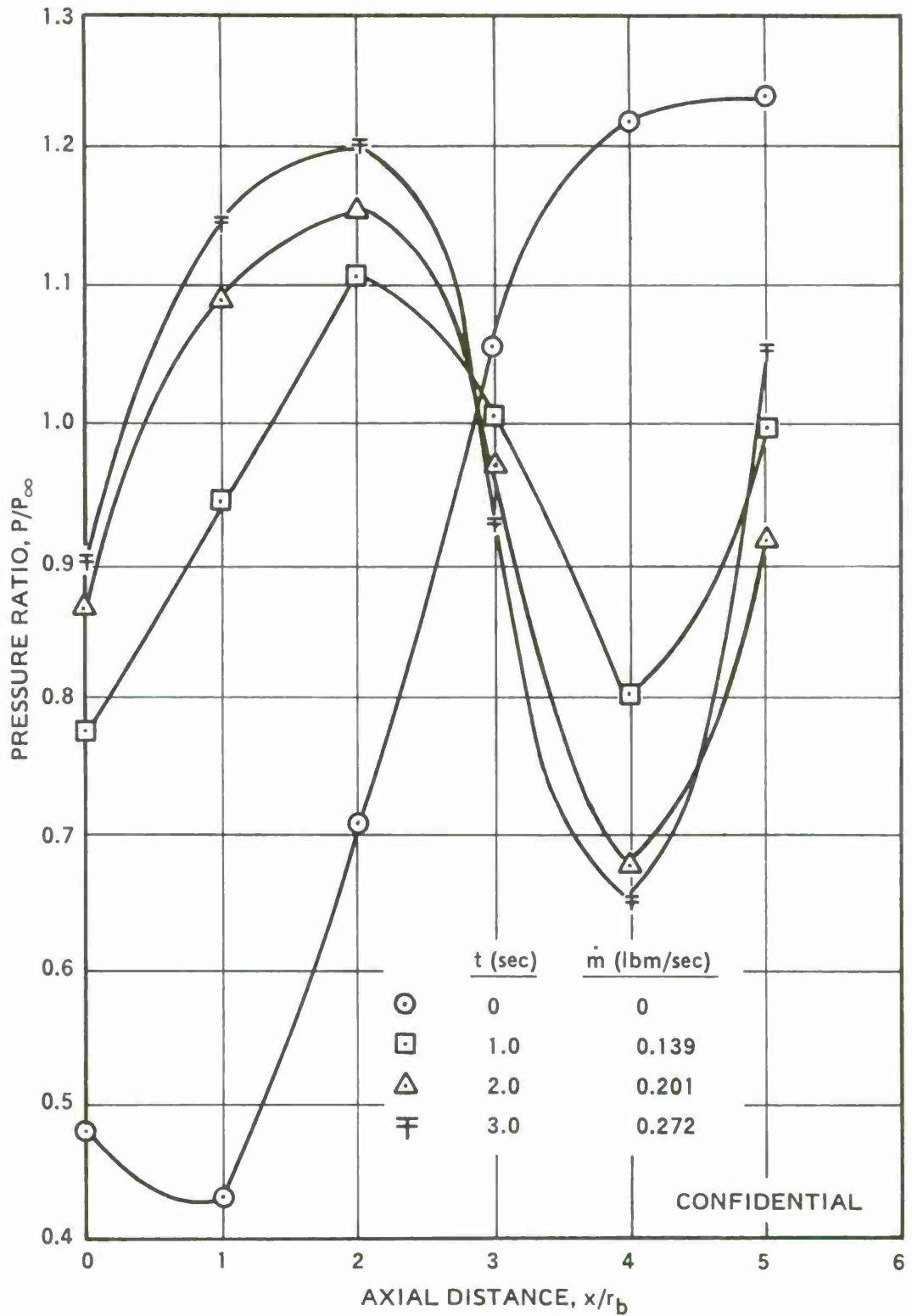


Figure 50. (C) Downstream Pressure Distributions, Test 20 (U).

SECTION V

DISCUSSION OF RESULTS

1. BASE PRESSURES WITHOUT FUEL INJECTION

(U) The average base pressures (\bar{P}_B) prior to fuel injection are listed in Table IV for Tests 1 to 20. The average base pressure is computed as the area weighted average of the four measured base pressures, PB-1, PB-2, PB-3, and PB-4. These values, along with the indicated free-stream Mach number, the free-stream static pressure (P_∞), the standard deviation of the base pressures, and the ratio \bar{P}_B/P_∞ are also listed in Table IV.

(U) Tests 1 to 14 were conducted at Mach 2.5, sea-level test conditions. Neglecting the base pressure ratios for Tests 8, 9, and 12, the average value of \bar{P}_B/P_∞ for the 11 remaining tests conducted at these test conditions is 0.453. The standard deviation for these 11 measurements is 0.0202, and, at the 95 percent confidence level, the range of this average base pressure ratio is 0.413 to 0.493. Thus, the base pressure ratios for Tests 8, 9, and 12 appear statistically different from the others, and this difference justifies their exclusion from the computation of the average.

(U) The average base pressure ratio of 0.453 agrees fairly well with other values reported in the literature. Data summarized by Chang ⁽¹¹⁾ show a range of base pressure ratios from 0.45 to 0.52 for spinning projectiles with turbulent boundary layers.

(U) Tentative explanations can be offered for the discrepancies in base pressure ratios observed for Tests 8, 9, and 12. Tests 9 and 12 both had relatively low free-stream static pressures, 13.4 and 13.7 psia, respectively. Since the atmospheric pressure for these tests was always about 14.7 psia, there was a significant mismatch between the free-stream static pressure and the surrounding atmosphere for these two tests. This mismatch resulted in a compression wave originating in the supersonic stream at the end of the outer nozzle wall, and this wave intersected the base plate extension about 5 model radii downstream from the base. Although the wake flow was undoubtedly supersonic at this point, the pressure rise across the compression wave could still have been transmitted to the base through the boundary layer on the base plate extension. This pressure rise could then cause an unusually large base pressure and base pressure ratio.

(U) If the above explanation is correct, then we should expect to see a correlation of base pressure ratio with free-stream static pressure, and such a correlation is suggested by the data plotted in Figure 51. The base pressure ratio is constant for free-stream static pressures from 14.5 to about 15.4 psia, but the base pressure ratio increases as anticipated at lower free-stream static pressures. For P_∞ greater than 14.7, an expansion fan will originate at the nozzle outer wall, and the leading wave will intersect the base plate extension at about $x/r = 5$. However, the pressure decrease caused by the expansion waves will be quite diffuse at this distance from their origin and should be expected to have negligible influence on the base pressure.

(U) The datum point for Test 8 is significantly displaced from the correlation of Figure 51, and clearly, a different explanation is required to explain the anomalously low base pressure ratio for this test. It will be recalled that for Test 8 the injection ports were extended 0.25 inch into the supersonic stream. These extensions caused

Table IV. Base Pressures Without Fuel Injection.

Test no.	Indicated Mach no.	Free stream static pressure P_{∞} (psia)	Base pressures (psia)				Average base pressure \bar{P}_B (psia)	Standard deviations		\bar{P}_B/P_{∞}
			PB-1	PB-2	PB-3	PB-4		(psia)	(percent)	
1	2.51	14.4	6.90	6.93	6.78	7.09	6.87	0.16	2.3	0.477
2	2.51	14.6	6.67	6.20	6.53	6.70	6.35	0.31	4.8	0.435
3	2.51	14.8	6.59	5.93	6.39	6.20	6.30	0.28	4.5	0.426
4	2.48	15.3	6.97	6.65	6.97	6.96	6.89	0.16	2.3	0.450
5	2.48	14.7	6.74	6.32	6.66	6.93	6.66	0.26	3.8	0.453
6	2.48	15.0	6.69	6.38	6.77	6.51	6.60	0.18	2.7	0.440
7	2.48	14.4	6.77	6.54	6.78	6.99	6.77	0.18	2.7	0.470
8	2.48	13.9	4.00	3.54	4.20	4.37	4.04	0.36	8.9	0.291
9	2.46	13.4	8.17	7.17	7.79	7.73	7.73	0.41	5.3	0.577
10	2.49	14.0	6.79	6.75	6.92	7.20	6.91	0.20	3.0	0.494
11	2.47	14.3	6.35	6.34	6.05	6.77	6.37	0.30	4.5	0.445
12	2.48	13.7	8.39	7.97	8.26	8.25	8.23	0.18	2.2	0.601
13	2.49	14.9	6.87	6.61	6.82	6.66	6.75	0.13	1.9	0.453
14	2.48	15.4	6.95	6.02	7.05	6.87	6.75	0.48	7.1	0.438
15	2.44	8.33	4.38	4.54	4.20	4.87	4.47	0.29	6.4	0.537
16	2.45	8.67	5.13	5.13	4.34	5.09	4.90	0.39	8.0	0.565
17	1.96	8.20	5.08	5.09	4.97	5.25	5.09	0.12	2.3	0.621
18	1.95	8.48	5.28	5.29	5.17	5.57	5.32	0.17	3.2	0.627
19	2.02	13.8	7.06	7.41	6.96	7.19	7.14	0.20	2.7	0.517
20	2.02	14.5	7.03	7.05	6.93	7.08	7.02	0.06	0.9	0.484

UNCLASSIFIED

74

UNCLASSIFIED

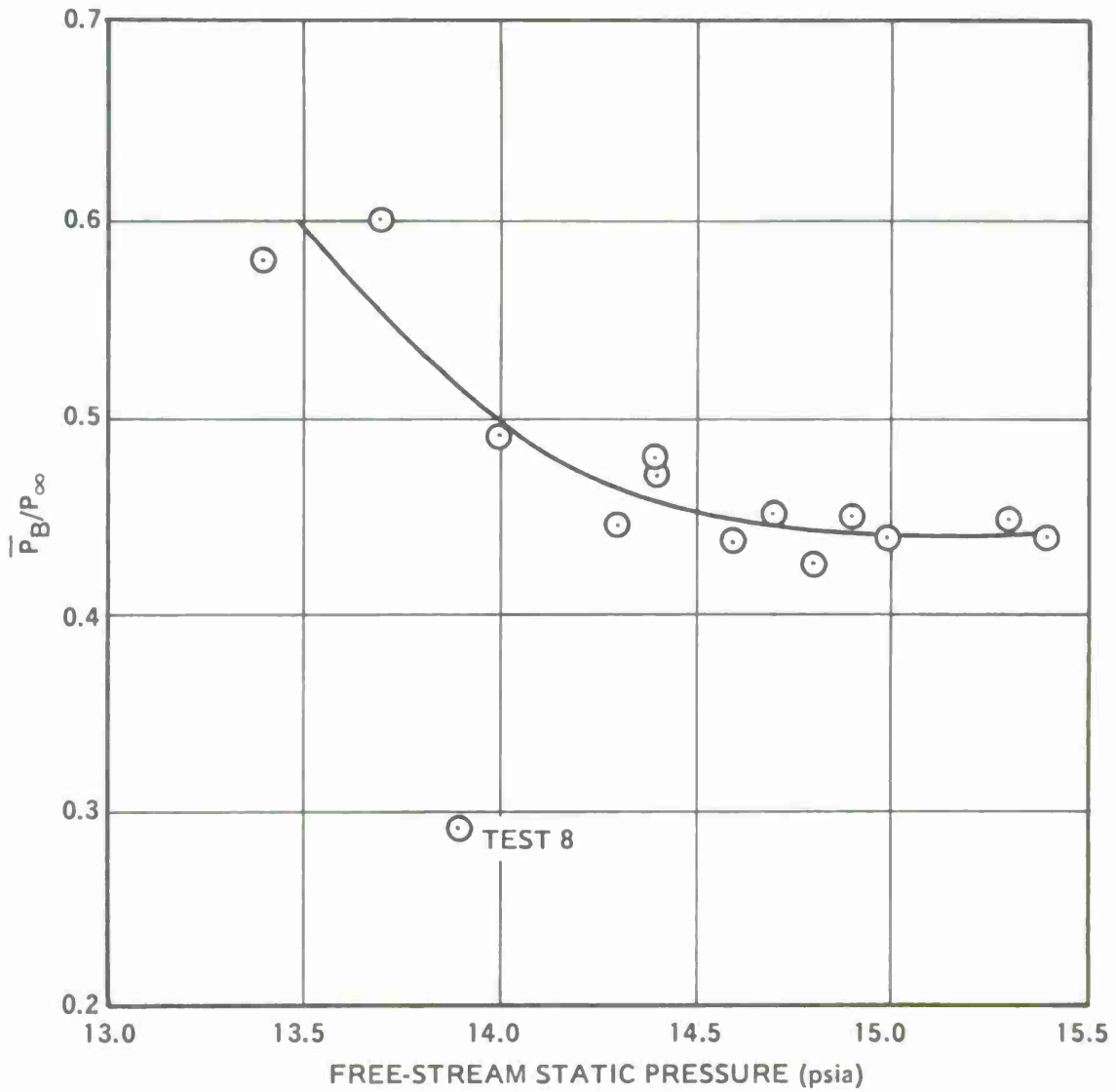


Figure 51. Base Pressure Ratios Before Fuel Injection for Mach 2.5, Sea-Level Tests.

shock waves to form, and these were subsequently reflected from the free-jet boundary as expansion fans. Discussions presented later show that these fans should have intersected the wake between 2 and 4 model radii downstream from the base, and a pressure decrease could then have been transmitted to the base through the wake flow itself or through the boundary layer on the base plate extension. This mechanism could then explain the anomalously low base pressure ratio.

(U) No explanation for the anomalously large base pressure ratios for Tests 15 and 16 conducted at Mach 2.5, 15,000-foot test conditions has been arrived at. Although the Reynolds number is less at 15,000 feet than at sea level, it is still on the order of 12×10^6 per foot, well within the range where the effect of Reynolds number variations on base pressure is negligible. Although there could have been a mismatch between the free-stream static pressure and the test section pressure, it was not apparent from either the pressure measurements or the Schlieren movies. Also, if such a mismatch were to cause anomalous base pressures, it would also be expected to cause significant changes in the downstream pressure distributions (see below). Such changes were not observed for these tests.

(U) For Tests 17 and 18, conducted at Mach 2.0, 15,000-foot test conditions, the base pressure ratios without fuel injection were 0.621 and 0.627. For Tests 19 and 20, conducted at Mach 2.0, sea-level conditions, the base pressure ratios without fuel injection were 0.517 and 0.484. Again, we have a significant difference between the values at altitude and those at sea level, and, again the sea level values are in good agreement with the literature, while the altitude values are too high. Chang,⁽¹²⁾ summarizing data from wind tunnel and flight tests, indicates that the base pressure coefficients for projectiles are approximately -0.18 at a Mach number of 2.0. This figure corresponds to a value for \bar{P}_B/P_∞ of 0.496. As in the case of the Mach 2.5 data, no explanation can be offered at present for the anomalously large base pressure ratios at 15,000-foot altitude test conditions.

(U) The average standard deviation of the four base pressure measurements is 0.24 psia or 4.0 percent. There does not appear to be any consistent variation of pressure across the base.

2. DOWNSTREAM PRESSURE DISTRIBUTIONS WITHOUT FUEL INJECTION

(U) The downstream pressure distributions for all of the tests prior to fuel injection are compared in Table V. The comparison is made by listing the ratios of the measured downstream pressures to the free-stream static pressure at x/r values from 0 to 5. The zero value refers to the average base pressure ratio. The table also includes for reference the indicated free-stream Mach numbers and static pressures and, for the sea-level tests, the measured atmospheric pressure. Also included in the table is the downstream distribution measured by Reid and Hastings⁽¹³⁾ with a full cylinder model.

(C) The first 14 tests were conducted at Mach 2.5 sea-level conditions, and average pressure ratios are listed in Table V for these tests. The values for Tests 8, 9, and 12 were excluded from the computation of the average, because the above discussion of base pressures indicated that the results for these tests were statistically different from the other results.

UNCLASSIFIED

Table V. Comparison of Downstream Pressure Distributions Without Fuel Injection.

Test no.	Mach no.	Free-stream static pressure P_{∞} (psia)	Atmospheric pressure (psia)	P/P_{∞} at $x/r =$					
				0	1	2	3	4	5
1	2.51	14.4	14.6	0.42	0.40	0.59	1.01	1.23	1.29
2	2.51	14.6	14.7	0.48	0.43	0.65	1.02	1.22	1.28
3	2.51	14.8	14.6	0.43	0.43	0.62	1.02	1.22	1.30
4	2.48	15.3	14.6	0.45	0.42	0.62	1.01	1.13	1.12
5	2.48	14.7	14.7	0.45	0.43	0.61	1.01	1.23	1.30
6	2.48	15.0	14.6	0.44	0.43	0.61	0.98	1.17	1.20
7	2.48	14.4	14.7	0.47	0.45	0.62	0.98	1.26	1.43
8	2.48	13.9	14.4	0.29	0.56	0.87	1.05	1.05	1.45
9	2.48	13.4	14.6	0.58	0.54	0.67	0.89	1.27	1.63
10	2.49	14.0	14.7	0.49	0.46	0.58	0.92	1.21	1.50
11	2.47	14.3	14.7	0.45	0.42	0.60	0.96	1.19	1.40
12	2.48	13.7	14.7	0.60	0.57	0.63	0.90	1.23	1.57
13	2.49	14.9	14.7	0.45	0.43	0.59	0.97	1.17	1.36
14	2.46	15.4	14.8	0.44	0.43	0.62	1.00	1.09	1.10
Average for above excluding tests 8, 9, and 12				0.45	0.43	0.61	0.99	1.19	1.30
15	2.48	8.33	---	0.54	0.51	0.71	1.03	1.15	1.14
16	2.50	8.67	---	0.56	0.48	0.72	1.02	1.18	1.19
17	2.03	8.20	---	0.62	0.52	0.87	1.21	1.27	1.18
18	2.00	8.48	---	0.63	0.55	0.92	1.14	1.15	1.14
19	2.02	13.8	14.7	0.52	0.47	0.70	1.03	---	1.07
20	2.02	14.5	14.8	0.48	0.43	0.71	1.06	1.22	1.24
Reid & Hastings, Mach 2.03 (13)				0.55	0.51	0.72	1.13	1.24	1.22

(U) Examination of the base pressure ratios for the first 14 tests shows that with the exception of Tests 8, 9, and 12, the individual ratios are quite close to the average for x/r values from 0 to 4. However, at $x/r = 5$, there appears to be a greater variation in the pressure ratio.

(U) At $x/r = 5$, the average pressure ratio is computed to be 1.30. The lowest ratio is 1.10 for Test 14, for which the free-stream static pressure was the largest. Because of the pressure mismatch between P_∞ and the atmosphere, an expansion fan originated at the nozzle outer wall and first impinged the base plate extension at $x/r = 5$. Although the pressure drop associated with this fan did not significantly affect the base pressure, it was sensed at $x/r = 5$ and also at $x/r = 4$. Note, however, that, as at the base, the effect was negligible at x/r values of 1, 2, and 3. Also, all of these observations are just as valid for Test 4, where P_∞ was equal to 15.3 psia, and the pressure ratio at $x/r = 5$ was 1.12. See also Test 6.

(U) From the above observations, we can conclude that even though the mismatch resulting from too large a free-stream static pressure does not affect the base pressure ratio, it is sensed in the downstream pressure distribution at x/r values of 4 and 5.

(U) Both Tests 9 and 12 had pressure ratios considerably larger than the average at $x/r = 5$. As discussed above, the pressure mismatch resulted in a compression wave originating from the outer nozzle wall and impinging on the base plate extension near $x/r = 5$. In addition to the anomalously large base pressure ratios, this wave resulted in large pressure ratios as $x/r = 1, 2, \text{ and } 5$. It is interesting to note that at $x/r = 3$, the pressure ratio for these tests was considerably smaller than the average, and at $x/r = 4$, the pressure ratio was only slightly greater than the average.

(U) In addition to Tests 9 and 12, Test 10 also showed a large pressure ratio at $x/r = 5$, and, consistent with our other observations, the free-stream static pressure was significantly lower than the atmospheric pressure. The base pressure ratio for this test, 0.49, was also higher than the average and was almost outside of the range of values indicated at the 95 percent confidence level, 0.413 to 0.493. Perhaps this test should also be excluded from the computation of the averages.

(U) The above observations tend to confirm the existence of a correlation between the base pressure ratio and the free-stream static pressure. Also, the data show that pressure rises, at least, can be transmitted back to the base through the boundary layer on the base plate extension. Whether pressure decreases can be transmitted forward to the base by this mechanism is not yet clear.

(U) In addition to the anomalously low base pressure for Test 8 described above, further anomalies are revealed in the downstream pressure distributions. At x/r values of 1 and 2, the pressure ratios are considerably greater than the computed averages. Between x/r values of 3 and 4, there is a saddle in the curve, and at $x/r = 5$, the pressure ratio is larger than the average value. These anomalies can be explained with the mechanisms cited above.

(U) The protrusions of the injection nozzles into the air flow in Test 8 caused oblique shock waves to run from the nozzles to the free-jet boundary. There they were reflected as expansion waves back toward the wake. Calculations to be described in more detail below indicate that the leading expansion wave intersects the wake at about $x/r = 2$, and the last wave intersects the wake at about $x/r = 4$.

(U) From the above, we construct the following explanation for the observations. The pressure rise across the oblique shock waves causes the pressure in the shear layer adjacent to the wake to be greater than it would be without the shock waves. The higher pressure in the shear layer causes the higher pressures in the wake at x/r equal to 1 and 2. The saddle observed in the distribution from $x/r = 3$ to $x/r = 4$ is caused by the interaction with the wake recompression of the expansion waves reflected from the free-jet boundary. The pressure decrease resulting from the expansion waves is transmitted forward to the base through the boundary layer on the base plate extension and this causes the anomalously low base pressure ratio. Finally, as in Tests 9, 10, and 12, the large pressure ratio at $x/r = 5$ could result from a compression wave caused by the mismatch between the free-stream static pressure and the atmospheric pressure.

(U) In addition to the differences in base pressure ratio described above, there are also differences in the downstream pressure distributions for a 15,000-foot altitude as compared to sea level. At x/r values of 1 and 2, the pressure ratios in Tests 15 and 16 are greater than the averages for the sea-level tests. At x/r values of 3 and 4, the pressure ratios are about the same as the sea-level averages, and at $x/r = 5$, the ratios are less than the sea-level averages. There is no evidence that the anomalously large base pressure ratios result from a pressure mismatch, for, if that were the case, we would expect the pressure ratio at $x/r = 5$ to be greater than the sea-level average, instead of less than it.

(U) For the tests conducted at Mach 2.0, there is also a difference between the downstream pressure distributions obtained at 15,000 feet and those obtained at sea level. From $x/r = 0$ to $x/r = 3$, the pressure ratios measured at 15,000 feet are greater than those measured at sea level. At $x/r = 4$ and $x/r = 5$, the pressure ratios are about the same for the altitude and the sea-level tests.

(U) Also included in Table V is the pressure distribution measured by Reid and Hastings⁽¹³⁾ with a test configuration similar to the one used here, except that a full cylindrical model was used rather than the semicylindrical model used here. The Mach number was 2.03, as in our last four tests, but the stagnation pressures and temperatures were considerably lower than those examined here, 12.3 psia and 536°R, respectively. The Reynolds number for Reid and Hastings' work was 3.24×10^6 per foot, and the model boundary layer was turbulent.

(U) If we compare the distributions of Reid and Hastings (R&H), to our average Mach 2.5 sea-level distribution we see that the pressure ratios at $x/r = 0$ and $x/r = 1$ are smaller for the average distribution than for the R&H distribution. This difference merely reflects the difference in Mach numbers. Interestingly, though, from $x/r = 2$ to $x/r = 5$, the distributions are quite similar. The agreement is even better if we note that the average pressure ratio at $x/r = 5$ is 1.28 if we eliminate Test 10 as well as Tests 8, 9, and 12.

(U) For the four tests conducted at Mach 2, the pressure distributions are not much different from the R&H distribution. At some values of x/r the agreement between the R&H distribution and one or another of the present tests might be good, but none of the tests is in good agreement with the R&H distribution at all x/r values.

3. BASE PRESSURES WITH FUEL INJECTION

a. ARCADENES 168A and 300, Sea Level, Mach 2.5

(C) In Figure 52, base pressure ratio is plotted versus propellant flow rate for all of the sea-level, Mach 2.5 tests made with aluminum-containing propellants. These include Tests 4 to 13 made with ARCADENE 168A and Test 14 made with ARCADENE 300. With the exception of Tests 8, 9, 13, and 14, all of the significant test results fall within the shaded band on the graph. Some of the initial points in some tests have not been included within the correlation band because they were obtained when the base pressure was changing very rapidly, and the values appear erroneously low. Also, three points obtained in Test 6 after the injector burnthrough have been excluded from the correlation band.

(C) For the data falling within the correlation band, the initial base pressure ratio before fuel injection is nominally 0.45. At a fuel flow rate of 0.06 lbm/sec, the base pressure ratio has increased to about 0.65. The shape of the correlation between these points can only be guessed since there are no accurate data. As the fuel flow rate is increased from 0.06 to 0.26 lbm/sec, the base pressure ratio increases from 0.65 to about 0.8.

(C) At 0.1 lbm/sec, the spread of the data band is 12 percent of the mean value. The difference between the results for Tests 4 and 7 is 6 percent of the mean value. These two tests were made with the same nominal test conditions, i.e., normal sonic injection from five nozzles, and the results provide a measure of data reproducibility. The spread of data within the correlation band does not seem so large compared to the indicated reproducibility for these two tests to suggest that any differences within the correlation band are significant. We conclude, then, that the variations in test conditions for tests falling within the band have had no significant effect on the results. These variations include changing the number of injection ports from 5 to 3, increasing the injection Mach number from 1 to 2, and increasing the rocket motor pressure range from 100-300 psia to 200-600 psia.

(C) Of the four tests for which the results fall outside of the correlation band, only Test 9 gave results significantly better than nominal. This test employed Mach 1, 45-degree injection from nine ports located at the shoulder of the model base. It was the only test with an aluminum-containing propellant utilizing either nine nozzles, 45-degree injection, or injection from points closer than 0.6 inch to the model base. Thus, any or all of these variables could be responsible for the apparent improved performance.

(C) Aside from the different injection configurations noted above for Test 9, we have already discussed the fact that the initial base pressure ratio for Test 9 was anomalously large because of a pressure mismatch between the free-stream static pressure and the atmosphere. Thus, the possibility exists that the pressure mismatch, rather than the differences in the injection geometry, is responsible for the large base pressure ratios with fuel injection. However, there are several arguments against this hypothesis.

(C) First, although the magnitude of the difference between Test 9 and the correlation band is the same at time zero and at $\dot{m} = 0.135$ lbm/sec, the difference does not remain constant throughout the mass flow rate range. If the increase in the final base pressures are attributable to the effects of the pressure mismatch, then we would expect the same magnitude of increase throughout the mass flow rate range.

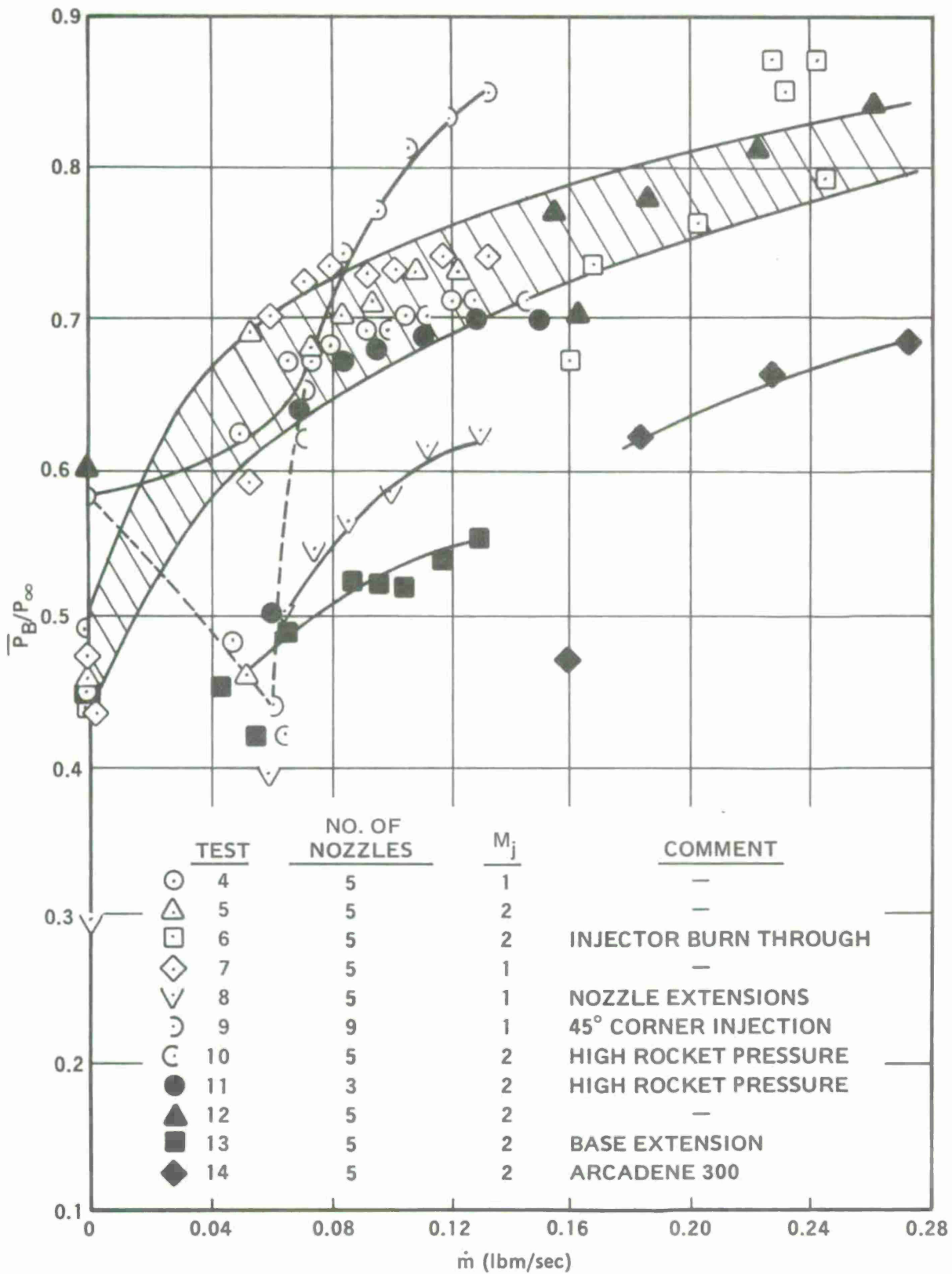


Figure 52. (C) Base Pressure Ratios for Sea-Level Mach 2.5 Tests with ARCADENE 168A and 300. (U).

(C) Second, we note that at the low initial mass flow rates of Test 9, the base pressure ratio has decreased from 0.58 to 0.44. Although the data may be somewhat in error because of insufficient transient response of the instrumentation, it suggests that the initial fuel injection has somehow eliminated the influence of the pressure mismatch on the base pressure. A mechanism might be a shortening of the wake to the point where disturbances impinging the base plate extension five model radii downstream can no longer significantly affect base pressure.

(C) A third argument suggesting that the results for Test 9 reflect the injection geometry and are not caused by the mismatch is provided by the results from Test 12. For this test, the mismatch was even greater than for Test 9, and, yet, the base pressures for Test 12 do not seem significantly greater than other results in the correlation band. However, we note that data to compare to Test 12 are lacking.

(C) Finally, we recall that the Schlieren movies for Test 9 showed the apparent particle trajectories to be less inclined toward the model axis and more nearly parallel to it than in other tests with ARCADENE 168A. For tests in the Atlantic Research-Navy program, where base pressure ratios greater than unity were measured, the particle trajectories appeared parallel to the model axis in the Schlieren movies. Thus, in a qualitative sense, the Schlieren movies for Test 9 confirm the apparent superior results.

(C) Assuming then that the results for Test 9 reflect a superior injection geometry, we note that combustion with 45-degree injection will probably be less displaced from the base separation bubble in the radial direction than it will be with 90-degree injection. In fact, the color movies tended to substantiate this notion. The superior performance obtained in Test 9, then, may be the result of the closer proximity of the combustion zone to the separation bubble. Strahle's analysis⁽¹⁾ indicates that moving the combustion zone closer to the bubble, but still keeping it within the inviscid stream, should increase base pressure.

(C) In Figure 52, the base pressure ratios for Tests 8, 13, and 14 fall significantly below the correlation band. Test 8 employed 0.25-inch nozzle extensions, and we noted above that the anomalously low initial base pressure for this test resulted from the shock waves formed at the protruding nozzles. These shock waves were reflected from the free-jet boundary as expansion fans which impinged the wake between two and four model radii downstream from the base. These expansion fans would still be present during fuel injection and could accordingly be the cause of the lower measured base pressure ratios throughout this test. Note that the displacement from the correlation of the results from Test 8 is nearly constant over the relevant mass flow rate range.

(C) Although we believe the above discussions explain the results for Test 8, we also note that the nozzle extensions probably resulted in increased fuel penetration. Accordingly, combustion probably occurred further from the separation bubble, and Strahle's analysis⁽¹⁾ predicts lower base pressures under this circumstance.

(C) A one-radius-long base extension was used in Test 13, so the injection ports were 2.08 inches upstream from the base as compared to the usual distance of 0.6 inch. The test results suggest that much of the effect of combustion in this test was to merely increase the pressure on the cylindrical surface of the model, rather than on the base. However, below we will present an alternate explanation in conjunction with our discussion of the downstream pressure distributions.

(C) In Test 14, the fuel was ARCADENE 300 as opposed to ARCADENE 168A. Since ARCADENE 300 has a significantly lower heat of combustion than does ARCADENE 168A, we might expect a smaller rise in base pressure at comparable fuel flow rates.

b. ARCADENE 168A, 15,000-Foot Altitude, Mach 2.5

(C) The base pressure ratios for Tests 15 and 16 are plotted versus fuel flow rate in Figure 53. Also included on the figure for reference is the correlation band from Figure 52 for tests with ARCADENE 168A at sea-level, Mach 2.5 test conditions. Tests 15 and 16 were conducted with ARCADENE 168A at 15,000-foot altitude, Mach 2.5 test conditions.

(C) As can be seen from Figure 53, the base pressure ratios in Tests 15 and 16 are greater than the nominal results obtained at sea level. However, the four points for Test 15 showing base pressure ratios of about 0.9 should be disregarded since, at the time in the test that they were obtained, the test section pressure was rising out of control.

c. ARCADENE 168A, Sea Level and 15,000-Foot Altitude, Mach 2.0

(C) The base pressure ratios for Tests 17 to 20 are plotted versus fuel flow rate in Figure 54. Again, the correlation band for the Mach 2.5 sea-level tests has been included for comparison. Tests 17 and 18 were conducted at Mach 2.0, 15,000-foot flight conditions, and Tests 19 and 20 were conducted at Mach 2.0, sea-level flight conditions.

(C) Both test conditions gave base pressure ratios significantly greater than the nominal results for Mach 2.5, sea level. At the larger mass flow rates of Test 18, base pressure ratios as high as 1.06 were measured. These numbers are about 33 percent greater than the ratios in the correlation band.

(C) The results from the sea-level tests are not as encouraging as the altitude tests. At the larger fuel flow rates, the base pressure ratios are 10 to 13 percent greater than the values in the correlation band.

d. ARCADENE 129A, Sea Level, Mach 2.5

(C) Not too much can be said concerning the base pressure ratios for Tests 1, 2, and 3 with ARCADENE 129A beyond saying that they did not change much with fuel injection. The major change observed was a decrease upon propellant ignition, followed by a slow rise toward the initial value as the fuel flow rate increased throughout the test. Only in Test 3 did the final base pressure ratio equal the value prevailing before fuel injection. The significance of these results, along with those for the aluminum-containing propellants, is discussed further in the following paragraphs.

4. SIGNIFICANCE OF THE MEASURED BASE PRESSURES

(C) For all of the tests conducted at sea-level flight conditions, the maximum base pressure ratios achieved were considerably less than unity. The question then arises as to whether or not combustion was achieved in these tests.

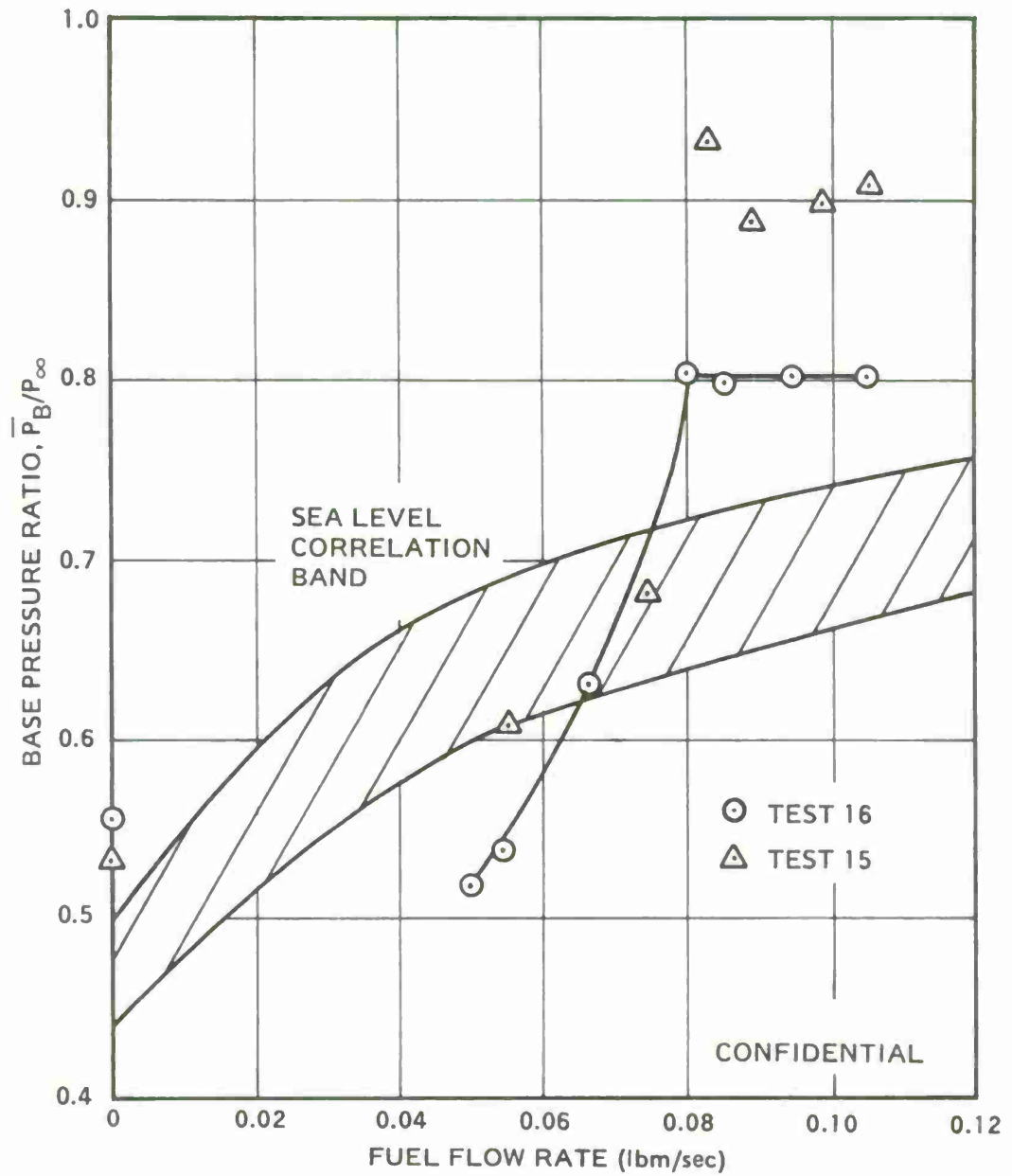


Figure 53. (C) Base Pressure Ratios for 15,000 ft Altitude, Mach 2.5 Tests (U).

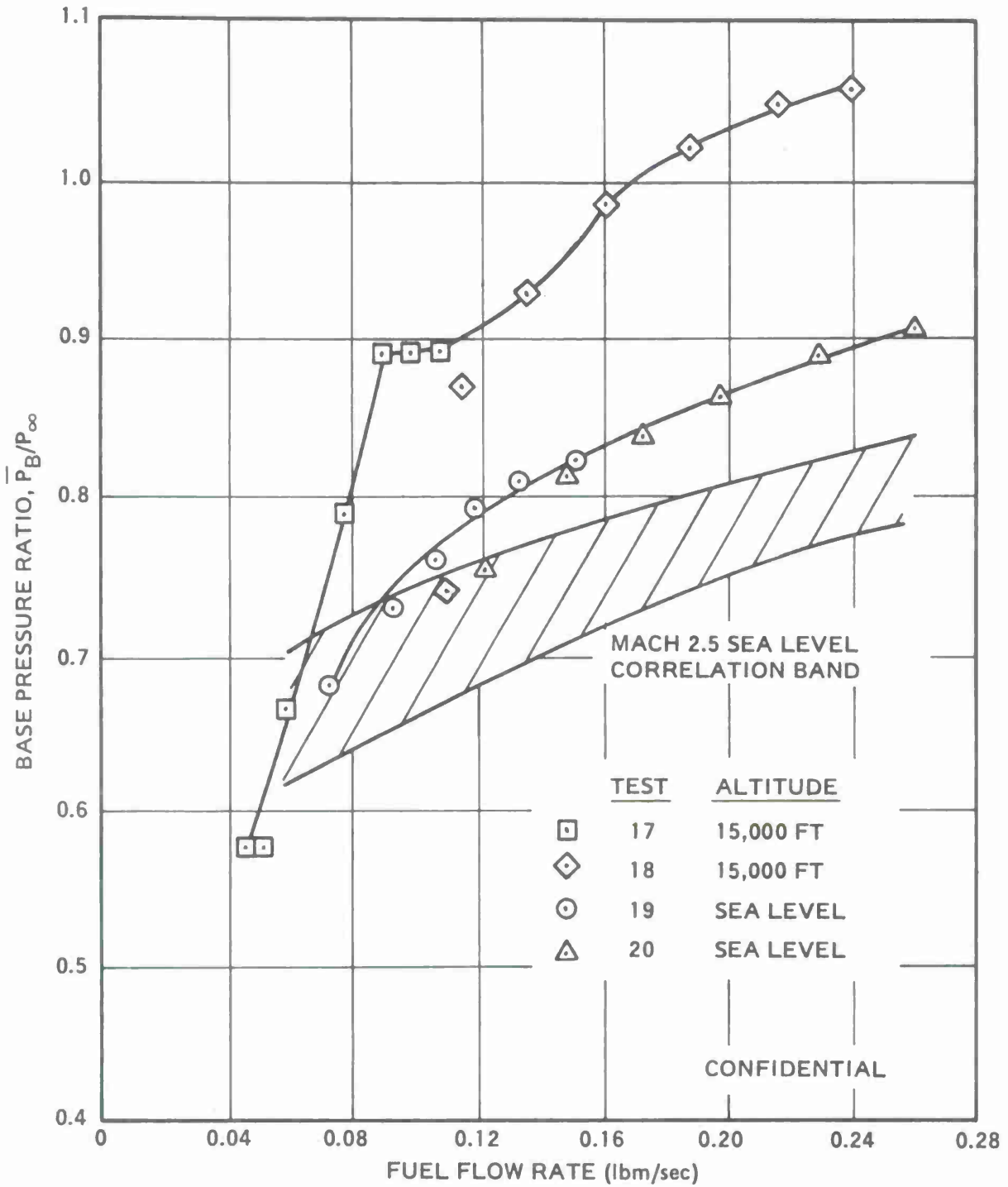


Figure 54. (C) Base Pressure Ratios for Mach 2.0 Tests (U).

(C) For the tests with ARCADENE 168A, we believe that significant combustion did occur. First, flames were clearly visible in the color movies of these tests. Second, there was ample evidence in the emission spectra that combustion was occurring. The static temperature of the propellant exhaust was too low to excite atomic aluminum lines and AIO bands. The emission was probably from local hot spots where aluminum combustion was occurring. Also, the blue continuum radiation can be attributed to a CO flame.

(C) Finally, good confirmation of combustion's occurring is offered by the fact that there was a significant base pressure rise. There is evidence that inert gas injection results in a base pressure decrease with the present test configuration. A single test was conducted where cold ($T^{\circ} = 311^{\circ}\text{K}$) air was injected from the model into the Mach 2.5 air stream at sea level. Injection was from five 90-degree, Mach 2 nozzles located 0.6 inch upstream from the model base. When the injectant flow rate was 0.923 lbm/sec, the base pressure ratio was only 0.334. The initial base pressure ratio was 0.44, so the injection of cold air resulted in a significant decrease in the base pressure from the undisturbed value. The significance of this result will be discussed further below.

(C) With respect to the three tests conducted with ARCADENE 129A, it is difficult to assert that combustion occurred to any great extent. After the initial base pressure decrease in these tests, the base pressure did increase slightly as the fuel flow rate increased. However, this rise is perhaps attributable to merely the increase in sensible enthalpy of the wake provided by the hot propellant exhaust. The air injection test was made with cold air. Some combustion probably did occur with ARCADENE 129A because there were significant increases in the lip pressures. For the air injection tests, both lip pressures decreased. Also, a faint pale blue flame could be observed in the color movies at the end of Tests 1, 2, and 3 when the fuel flow rate was largest.

(C) It is difficult to draw conclusions from the magnitude of the base pressure rises at the various test conditions. Except for Mach 2.0 at 15,000 feet, all of the base pressure ratios were considerably below the levels obtained in the Atlantic Research-Navy programs.^(3,4) There, with tests at Mach 2.0, 15,000 feet with a 5-inch model, base pressure ratios as large as 1.29 were measured. It is tempting to draw an equivalence between those results and the present ones at Mach 2.0, 15,000 feet and then to attribute the poorer results in the other 18 tests to the changed test conditions. However, analysis of the downstream pressure distributions below suggests that other factors may also be important.

5. DOWNSTREAM PRESSURE DISTRIBUTIONS WITH FUEL INJECTION

(C) Most of the tests conducted at Mach 2.5, sea-level conditions show similar changes in the pressure profiles as the fuel flow rate is increased. At the lower fuel flow rates the effect of fuel injection is to raise the pressure, relative to the initial profile, at x/r values less than 3 and to lower the pressures at x/r values greater than 3. At higher fuel flow rates, a maximum is formed in the pressure distributions at $x/r = 2$, and this maximum is generally followed by a local minimum in the distribution at $x/r = 4$.

(C) Two noteworthy exceptions to this behavior are contained in Tests 9 and 13. In Test 9, the only test with 45-degree injection, fuel injection raises the pressure, relative to the initial profile, at x/r values less than 4, and there are no local maximums or minimums. In Test 13, a local maximum and minimum do appear at the largest fuel flow rate, but the maximum is at $x/r = 2$, and the minimum is at $x/r = 3$. The minimum is one base radius closer to the base than normal.

(C) We have already attributed the plateau in the "air only" distribution of Test 8 to the reflection from the free-jet boundary of the shock waves caused by the protruding nozzle extensions. These shock waves reflect as an expansion fan which interacts with the recompression process in the near wake. During fuel injection, the obstruction caused by the fuel jets themselves cause interaction shock waves to form, and the reflections from these waves could affect the downstream pressure distributions so as to produce the maximums and minimums observed.

(C) A scale diagram illustrating the shock wave reflection and its intersection with the wake is shown in Figure 55. The diagram is for a Mach number of 2.5. We have assumed here that the shock angle is 45 degrees, and the virtual origin of the wave on the model surface is 1.0 inch upstream from the base. The interaction shock waves observed in the Schlieren movies are generally inclined at 45 degrees, but these waves are less steeply inclined at the low mass flow rates of a test and become more steeply inclined as the fuel flow rate increases.

(C) For the assumptions given above, the interaction shock wave strikes the free-jet boundary at x/r of about 0.67. At this point it is reflected as an expansion fan back toward the wake. The angle of the leading wave is computed as the Mach angle for the flow behind the interaction shock wave. This angle is $\tan^{-1} 0.844$, corresponding to a Mach number of 1.55. The angle of the trailing wave is computed at the Mach angle for the free-stream flow, and this is $\tan^{-1} 0.437$, corresponding to a Mach number of 2.5.

(C) Also drawn in the diagram of Figure 55 is an estimate of the outer wake boundary and the positions of the dividing streamline and stagnation point without fuel injection. The stagnation point was assumed to be at the same accomplished pressure rise in the "air only" distribution as indicated for the turbulent, two-dimensional base flow as modeled by Alber and Lees.⁽¹⁴⁾ The wake boundary was sketched from the Schlieren movies for the flow prior to fuel injection.

(C) From Figure 55, the leading Mach wave intersects the wake boundary at $x/r = 2$, and the trailing wave intersects at $x/r = 3.67$. These intersections are very near the axial locations of the observed maximums and minimums in the downstream pressure distributions. To emphasize this correlation, pressure distributions from Test 12 are included in Figure 55.

(C) The downstream pressure distributions for Tests 9 and 13 further support attributing the disturbances in the pressure profiles to the reflections of the interaction shock waves. Injection was at an angle of 45 degrees from the base corner in Test 9, and the interaction shock waves should accordingly be weaker and inclined at a shallower angle relative to the model axis. The reflections should also be weaker and should intersect the wake further downstream from the model base. We should then expect a less pronounced minimum in the pressure distribution or no minimum at all. In fact, no minimum was observed in the distribution for Test 9.

(C) In Test 13, injection was from points located one model radius further upstream from the model base than in most of the other tests. Accordingly, the disturbance in the downstream pressure profile should appear one base radius closer to the base. In fact, the minimum in the pressure distribution for Test 13 was one radius closer to the base.

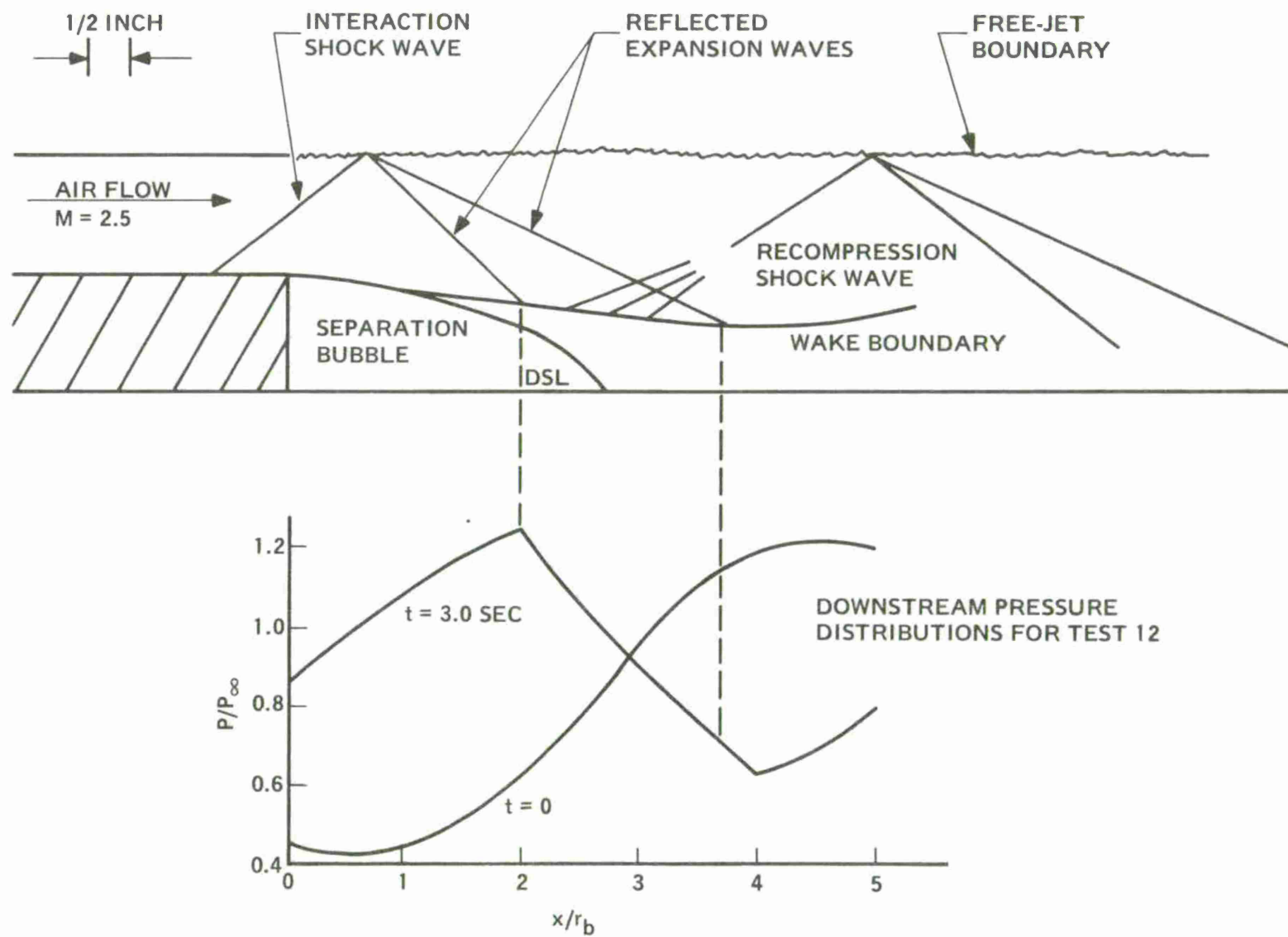


Figure 55. (C) Diagram Showing Interaction Shock Wave Reflection and Relation to Downstream Pressure Distributions (U).

(C) Tests 19 and 20, sea-level, Mach 2.0 test conditions, show essentially the same features in the downstream pressure distributions as appeared at the Mach 2.5, sea-level test conditions. However, at the higher mass flow rates in Test 20, it appears that the effects of the expansion fan are appearing in the distributions at an x/r value between 1 and 2 even though the maximum in the curve is still at $x/r = 2$. Computations show that for the Mach 2.0 test configurations, the expansion fan should impinge the wake slightly closer to the base than it did at Mach 2.5.

(C) For the four tests conducted at 15,000-foot test conditions, the minimum in the pressure distributions occurred at $x/r = 3.0$ rather than at $x/r = 4$ as in most of the sea-level tests. At the altitude conditions, the effective back pressure of the free stream, with respect to jet penetration, will be about 45 percent less than it is at sea level, and Reference (12) indicates that for constant rocket pressure, jet penetration varies inversely with the square root of the effective back pressure. With greater jet penetration at 15,000 feet, the virtual origin of the interaction shock wave will be further upstream from the base, thus moving the reflections closer to the base.

(C) At the large mass flow rates of Test 18, Mach 2.0 at 15,000 feet, both the maximum and the minimum in the downstream pressure distributions are one radius closer to the base than at Mach 2.5, sea-level flight conditions. We have already mentioned that the reflections should intersect the wake nearer to the base in the Mach 2.0 configuration. This change in configuration, coupled with the reduced effective back pressure at 15,000 feet, apparently moves both the maximum and minimum closer to the base.

6. THE EFFECT OF SHOCK WAVE REFLECTIONS ON BASE PRESSURE

(C) The total of the data discussed above suggests that the relatively small base pressure rises obtained to date have been limited by a wind tunnel interference effect and are not fundamental in origin. A strong correlation exists between the measurement of poor performance and the presence of a minimum in the downstream pressure distribution. The existence of this correlation suggests that there is a cause and effect relationship between the disturbance in the downstream pressure distribution and the small base pressure rises. Since the shock reflection would not be present in a real flight environment, flight performance would be significantly better than the measured wind tunnel performance if our hypothesis of a cause and effect relationship is valid. Below, we summarize the observations which constitute the correlation between low base pressure rise and the disturbance in the downstream pressure distributions.

(C) In almost all of the current tests, the base pressure ratios were significantly below the levels achieved in the Atlantic Research-Navy programs,^(3,4) and there were pronounced minimums in the pressure distributions downstream from the model base. In the Navy programs, no local minimums were observed in the downstream pressure distributions at x/r values ranging from 0 to 4.

(C) In the current program, the measured base pressure rises at Mach 2.5, sea-level flight conditions correlate with the nature of the disturbance in the downstream pressure profile. The lowest base pressure rises for ARCADENE 168A were measured in Test 13. For this test a one-radius-long base extension was added to the model, effectively moving the injection ports one model radius further upstream from the model base. The leading wave of the interaction shock reflection accordingly intersected the wake one radius closer to the base, and the minimum in the downstream pressure profile moved from its usual location of four radii downstream from the base to a position three radii downstream from the base. Thus, a lower base pressure rise was measured when the minimum in the pressure profile was one radius closer to the base.

(C) The largest base pressure rises were measured in Test 9, in which the fuel was injected from the base corner through nine 45-degree nozzles. This injection configuration caused the interaction shock waves to be weaker and to intersect the free-jet boundary further downstream from the model base. Although there appeared to be some flattening of the downstream pressure profile three radii from the base, there was no minimum in the curve. Accordingly, the largest base pressure rise at Mach 2.5, sea-level test conditions was obtained when there was no minimum in the downstream pressure distribution.

(C) In Test 8, the base pressure ratio without fuel injection was 0.29, significantly below the nominal range of 0.45 to 0.50 for Mach 2.5, sea-level test conditions. This test employed nozzle extensions which in themselves generated oblique shock waves which were reflected as expansion waves back into the wake from the free-jet boundary. As a result of these reflections, there was a minimum in the pressure profile four radii downstream from the model base. Thus, here we have a low base pressure without fuel injection accompanied by a minimum in the downstream pressure distributions. This minimum became more pronounced during fuel injection, and the base pressure rises observed were to lower levels than generally observed at corresponding fuel flow rates in tests without nozzle extensions. However, the magnitude of the base pressure rise was the same as generally observed, so if the magnitude of the base pressure rise is influenced by a disturbance in the downstream pressure distributions, the reduction resulting from the disturbance generated by the nozzle extensions appears unchanged during the firing.

(C) The downstream pressure distributions from the "air injection test" are given in Figure 56. The distribution without air injection is not unusual. However, with 0.930 lbm/sec of air injection through five 90-degree nozzles, there is a pronounced minimum in the downstream pressure profile, and the base pressure is significantly reduced from its initial value.

(C) Finally, we note that only in Test 18 were base pressure ratios greater than unity obtained, and these were obtained when the downstream pressure distribution was flattening, so as to tend toward a straight line.

(C) The above observations constitute a correlation between the minimum in the downstream pressure profile and the base pressure level. However, we cannot yet demonstrate that there is a cause and effect relationship between the disturbed pressure profiles and the base pressure level. Nevertheless, such a relationship is certainly possible with the current test configuration. The leading Mach wave of the interaction shock reflection is computed to intersect the wake flow about two model radii downstream from the model base. The rear stagnation point without fuel flow is estimated to be about 2.7 radii downstream, and the critical point will be further downstream. Thus, if the critical point does not move too far upstream with combustion, the reduced pressure from the expansion wave can be transmitted to the base through the subsonic portion of the wake. Even if the critical point moves to within two radii, the effects of the expansion wave can still be transmitted to the base through the subsonic portion of the boundary layer on the base plate extension. If this latter mechanism is the prevailing one, then the pressure feedback will not be present in full model tests not using a base plate extension. If the former mechanism is the prevailing one, then some means must be found to eliminate the reflection or move it further downstream. Possibilities are cancellation with a contoured nozzle skirt or porous wall, trapping with a jet stretcher, or shifting downstream with a larger annular gap or a diverging free-jet boundary.

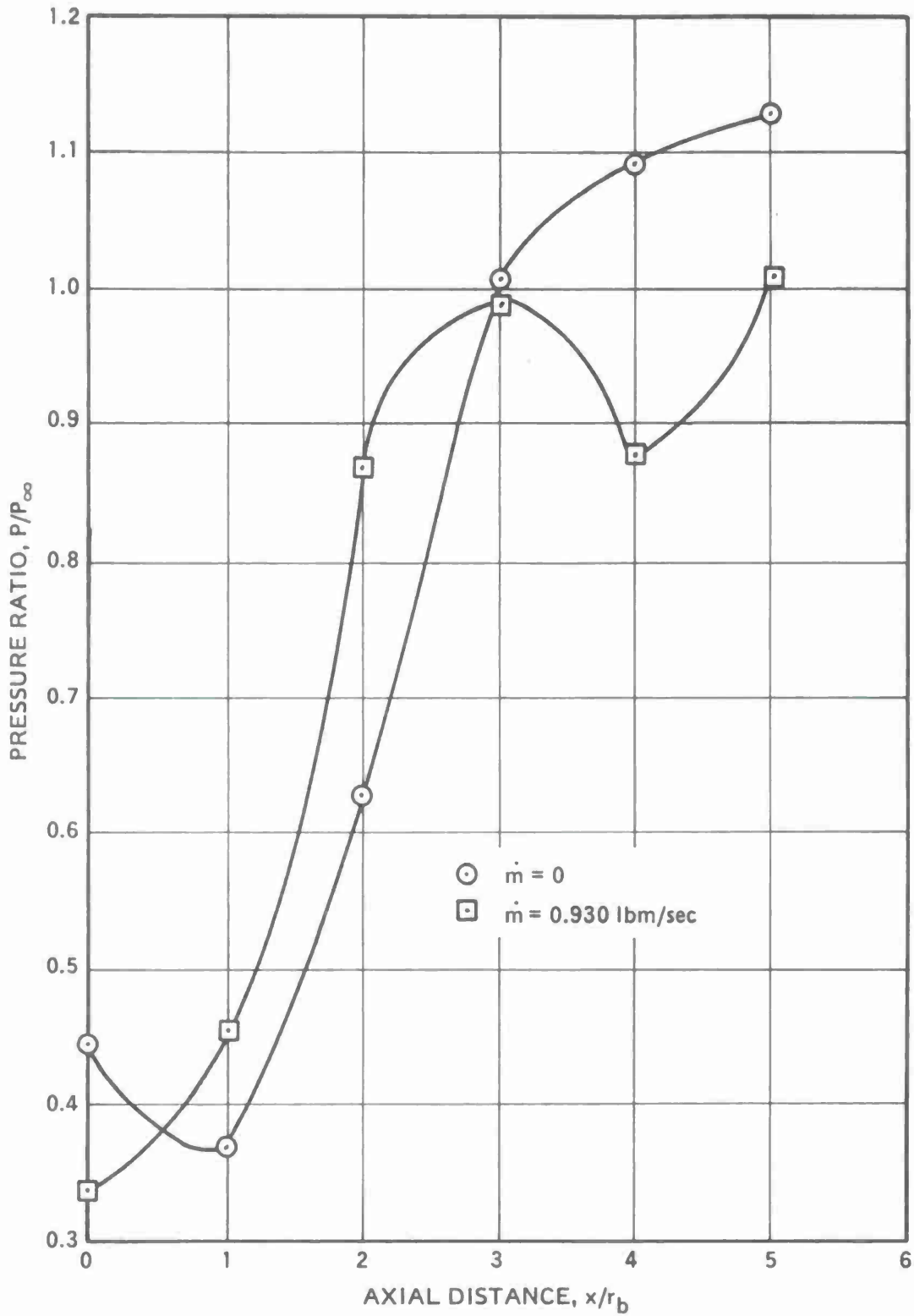


Figure 56. Downstream Pressure Distributions for Air Injection Test.

7. LIP PRESSURES

(C) The lip pressure measurements downstream from an injection port are plotted in Figure 57 for Tests 4 to 15. The data are presented as a graph of the ratio of the lip pressure to the free-stream static pressure versus the fuel mass flow rate. Tests 4 to 13 were conducted with ARCADENE 168A at Mach 2.5, sea-level test conditions. Test 14 was conducted at the same test conditions using ARCADENE 300. Test 15 was conducted with ARCADENE 168A at Mach 2.5, 15,000-foot flight conditions.

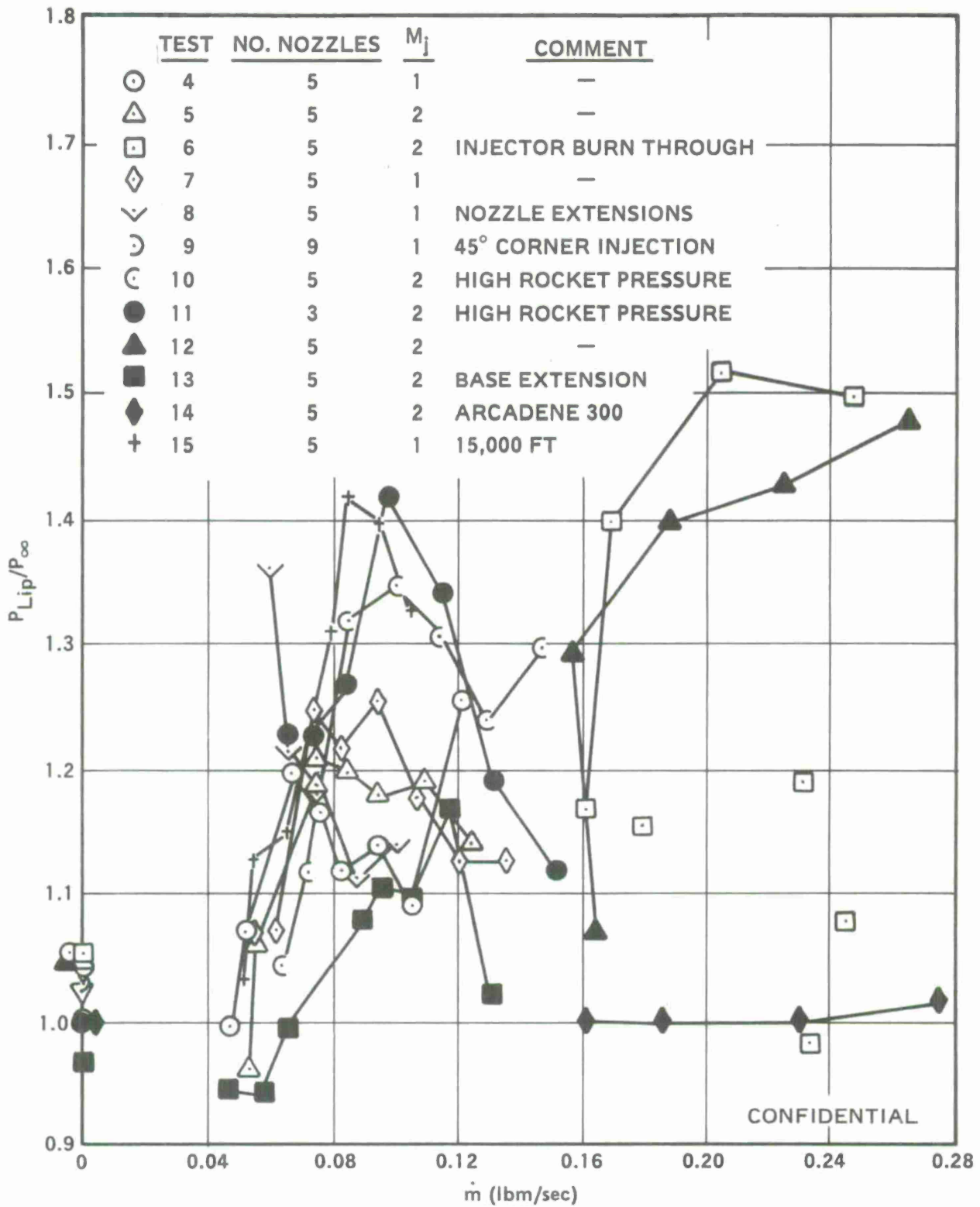
(C) For most of the tests, the lip pressure ratio is about 1.0 at the initial mass flow rate of the tests, increases to about 1.2 to 1.4 as the fuel flow rate increases, and then decreases as the maximum fuel flow rates are approached. The largest lip pressures in the low mass flow rate range were obtained in Test 11 using three Mach 2.0 nozzles with the larger than nominal rocket pressure, in Test 15 using five sonic nozzles at a 15,000-foot altitude, and in Test 10 using five Mach 2.0 nozzles with the larger rocket pressure. There is little difference between the lip pressure ratios for Tests 4, 5, and 7, which were made with five nozzles, the nominal rocket pressure, and either Mach 1.0 or Mach 2.0 injection.

(C) For Test 13, made with the one-radius-long base extension, the lip pressures appear significantly lower than those for the other tests, and in Test 14 with ARCADENE 300, the lip pressure remained unity throughout the duration of the test. In Tests 6 and 12, using greater than nominal mass flow rates of ARCADENE 168A, the lip pressure ratio increases rapidly as the fuel flow rate increases from its initial value. The ratios then remain nearly constant at about 1.5 as the fuel flow rate increases to the maximum. In Test 8 with the nozzle extensions, the lip pressure ratio is higher than for the other tests at very low mass flow rates, but then decreases as the mass flow rate increases. For Test 9, the test using 45-degree corner injection, the lip pressure could not be measured downstream from an injection port.

(C) The lip pressures measured downstream of and between injection ports are presented in Figure 58 for Tests 4 to 15. For the tests made with the nominal (low) mass flow rate range, the lip pressure ratios generally increase as mass flow rate increases initially, reach a maximum, and then decrease as the fuel mass flow rate increases further. Tests 4, 5, and 6 all give about the same maximum, approximately 1.6. For Test 15, the lip pressure ratio reaches 1.76. For Test 11, the maximum ratio appears significantly lower (about 1.5), and the maximum for Test 13 (~1.2) is lower still.

(C) In contrast to the other tests using the nominal mass flow rate range, the lip pressure for Test 9 does not show a maximum. Rather, the ratio is about unity at the initial mass flow rate and increases steadily as mass flow rate increases, reaching a value of 1.4 at the largest mass flow rate of the test.

(C) Of the three tests made with the large mass flow rate range, the one made with ARCADENE 300, Test 14, shows little variation of this lip pressure with increasing mass flow rate. The lip pressure ratio is constant at about 1.4. On the other hand, the two tests using ARCADENE 168A, Tests 6 and 12, show an increase of lip pressure ratio with increasing mass flow rate.



CONFIDENTIAL

Figure 57. (C) Lip Pressures on Line with Port for Mach 2.5 Tests with ARCADENE 168A and 300 (U).

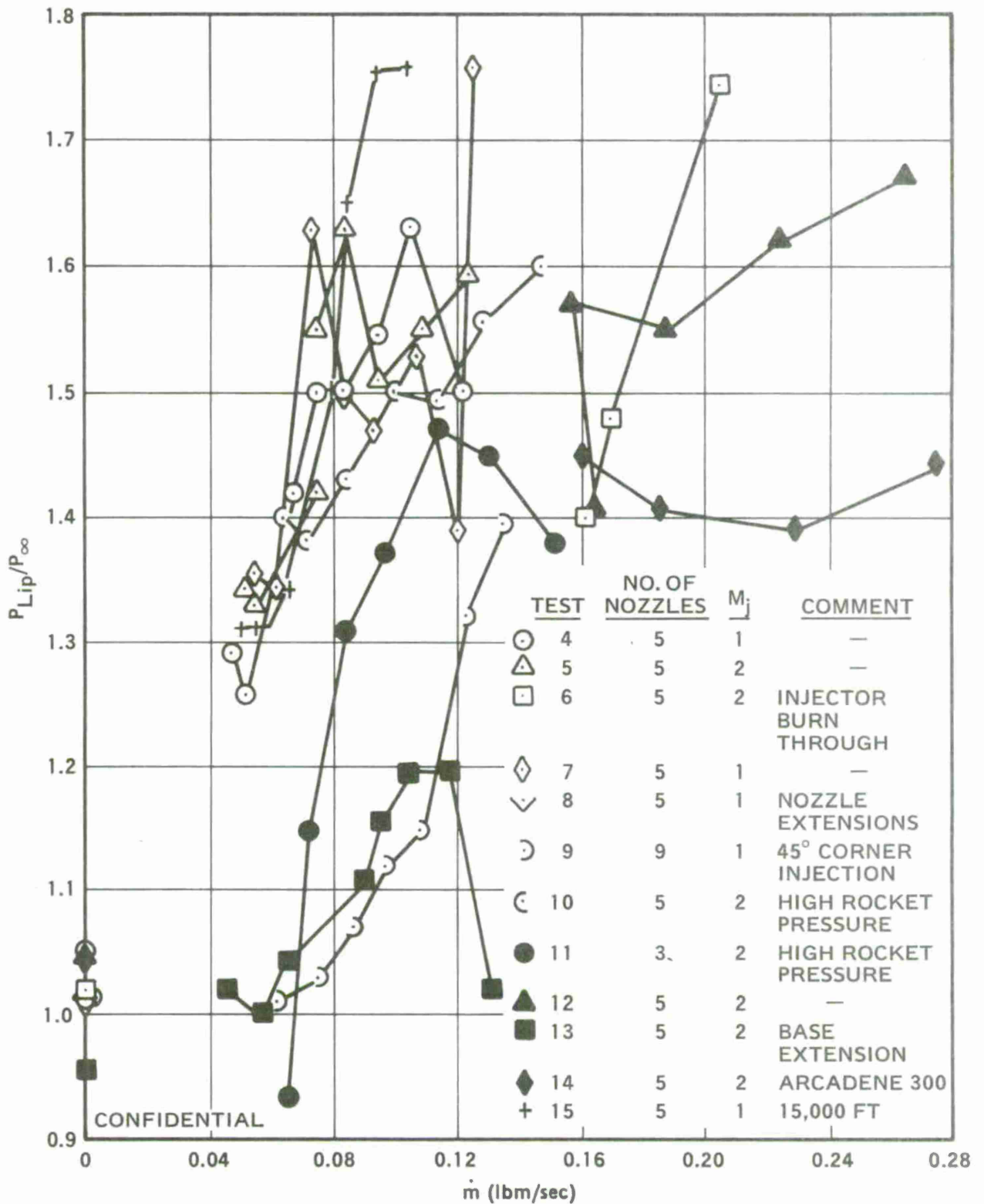


Figure 58. (C) Lip Pressures Between Ports for Mach 2.5 Tests with ARCADENES 168A and 300 (U).

(C) From the above results, it appears that the lip pressures in line with an injection port are largest when the jet penetration is highest. Thus, the largest lip pressures were obtained in Tests 10, 11, and 15. Test 11 used three Mach 2 nozzles, which, with the same mass flow rate, will provide greater jet penetration than five sonic nozzles. Greater penetration will be obtained in Test 15 because of the lower effective back pressure at the 15,000-foot test conditions. Also, one might intuitively expect greater penetration in Test 10 conducted with the higher rocket pressure range, although such an increase is not predicted by the theory of Reference (15).

(C) It appears that most of the rise in lip pressures can be attributed to the effects of combustion. In the air injection test, the lip pressure ratios decreased to a minimum of 0.6 as the air injection rate was increased to 0.93 lbm/sec. Thus, we observe higher lip pressures where combustion might be most intense, e.g., downstream of and between injection ports (PL-2) rather than on line with ports (PL-1).

(C) The eventual decrease in lip pressures as the fuel flow rate increases during a test is still puzzling. We merely note that as fuel flow rate increases, fuel jet penetration increases also, and the vicinity downstream from injection becomes more fuel rich and oxygen starved. One might argue that these conditions reduce the amount of combustion occurring in the vicinity of the lip pressure ports, and the reduced pressure ratios are the result of this reduced combustion. However, the results of Tests 6 and 12, conducted with the high mass flow rate range, seem to contradict this hypothesis. These tests show large lip pressure ratios at large mass flow rates and resulting large jet penetration.

(C) The lip pressure ratios for Mach 2.0 tests with ARCADENE 168A are shown in Figures 59 and 60. The lip pressure ratios on line with an injection port are given in Figure 59, and those between injection ports are given in Figure 60.

(C) The lip pressure ratios on line with injection ports are greater for the Mach 2.0 tests than for Mach 2.5. The peak values at Mach 2.0 reach near 1.7 versus 1.5 for Mach 2.5. The ratios for the two tests conducted at 15,000-foot test conditions are greater than the sea-level results, consistent with the results at Mach 2.5. Note that although in the two altitude tests there is a maximum in the curves, the pressure ratios merely increase with fuel flow rate for the two sea-level tests.

(C) The lip pressure ratios between injection ports for the Mach 2.0 tests are not much larger than the lip pressures on line with ports. At the same fuel flow rate, the ratios at altitude are greater than the ratios at sea level, but the peak values for the sea-level tests are greater. Also, all of the curves show a maximum in pressure ratio as the fuel flow rate increases.

(C) The lip pressure ratios for the three tests conducted with ARCADENE 129A are given in Figure 61. For the two tests conducted with nine injection ports, the lip pressures on line with injection ports (PL-1) are much greater than the ratios between ports (PL-2). These results are opposite to what was observed with ARCADENE 168A using five injection ports. On the other hand, consistent with the ARCADENE 168A results, PL-2 is greater than PL-1 for Test 3, conducted with five injection ports. With nine injection ports, mixing may be so rapid that more vigorous combustion is occurring on line with injection ports than between them. The fact that there is any rise in the lip pressures is indicative that combustion is occurring, consistent with the noting of pale blue flames in the color movies of the ARCADENE 129A tests.

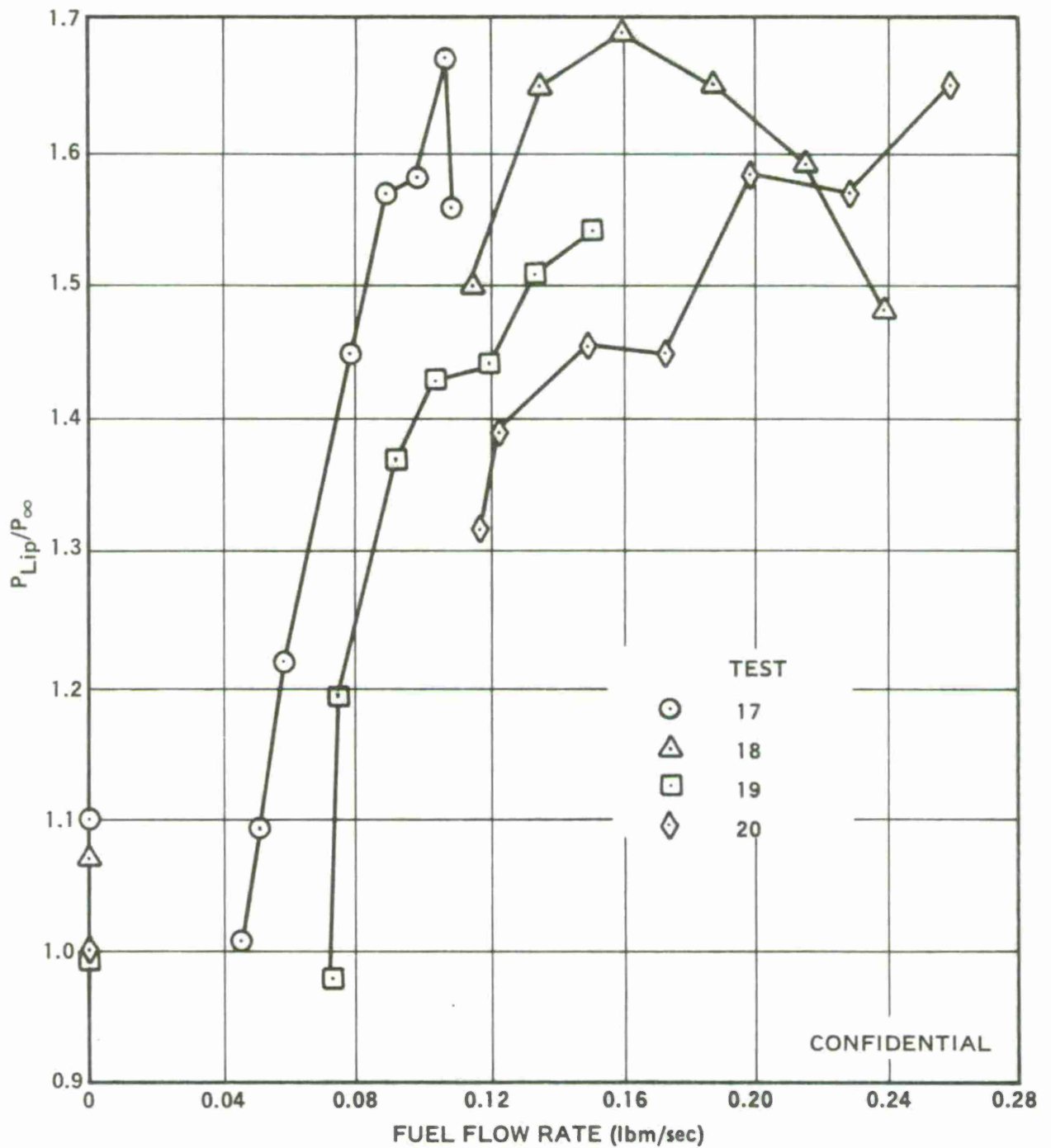
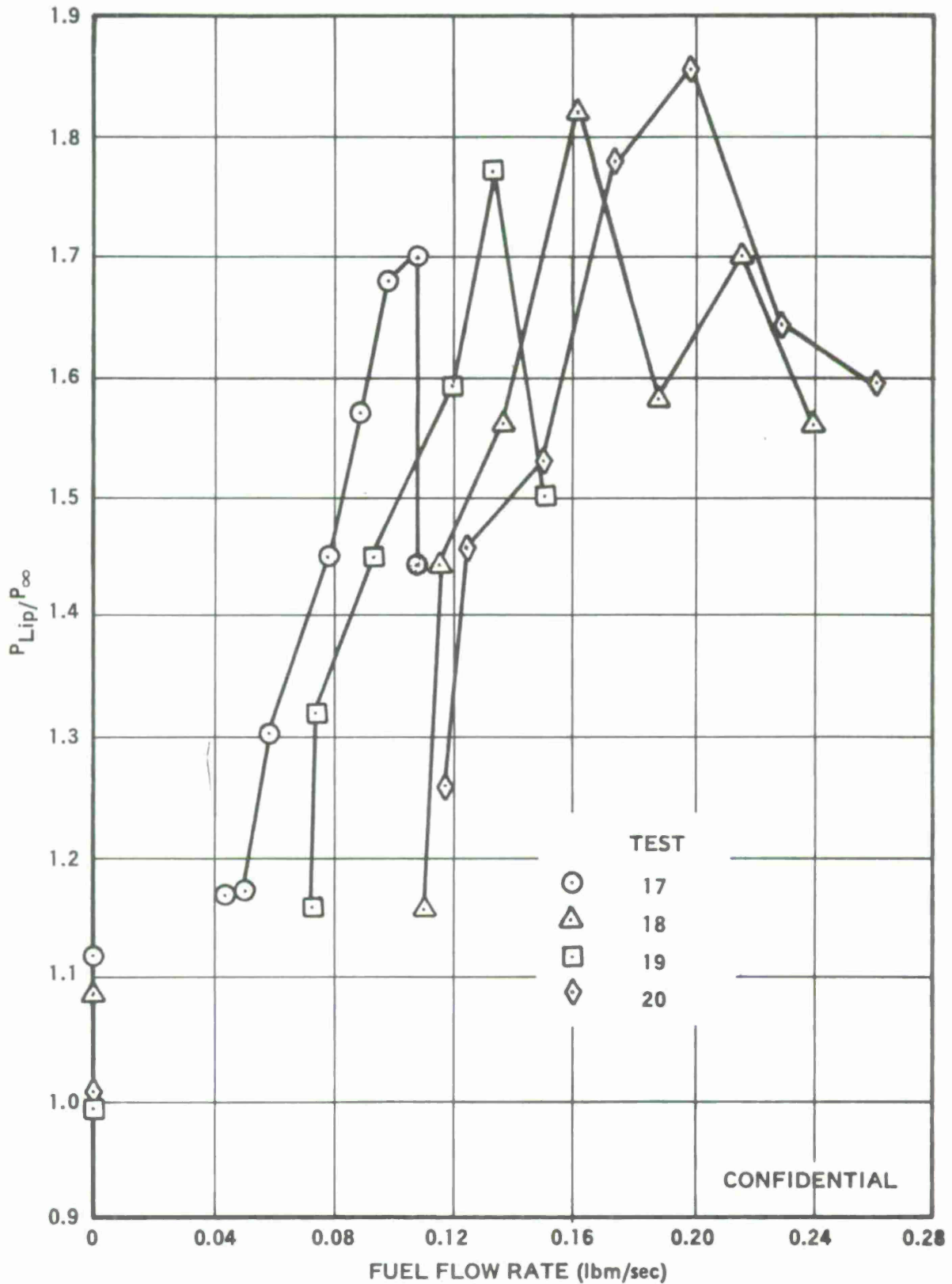


Figure 59. (C) Lip Pressures on Line with Port for Mach 2.0 Tests (U).

~~CONFIDENTIAL~~



CONFIDENTIAL

Figure 60. (C) Lip Pressures Between Ports for Mach 2.0 Tests (U).

~~CONFIDENTIAL~~

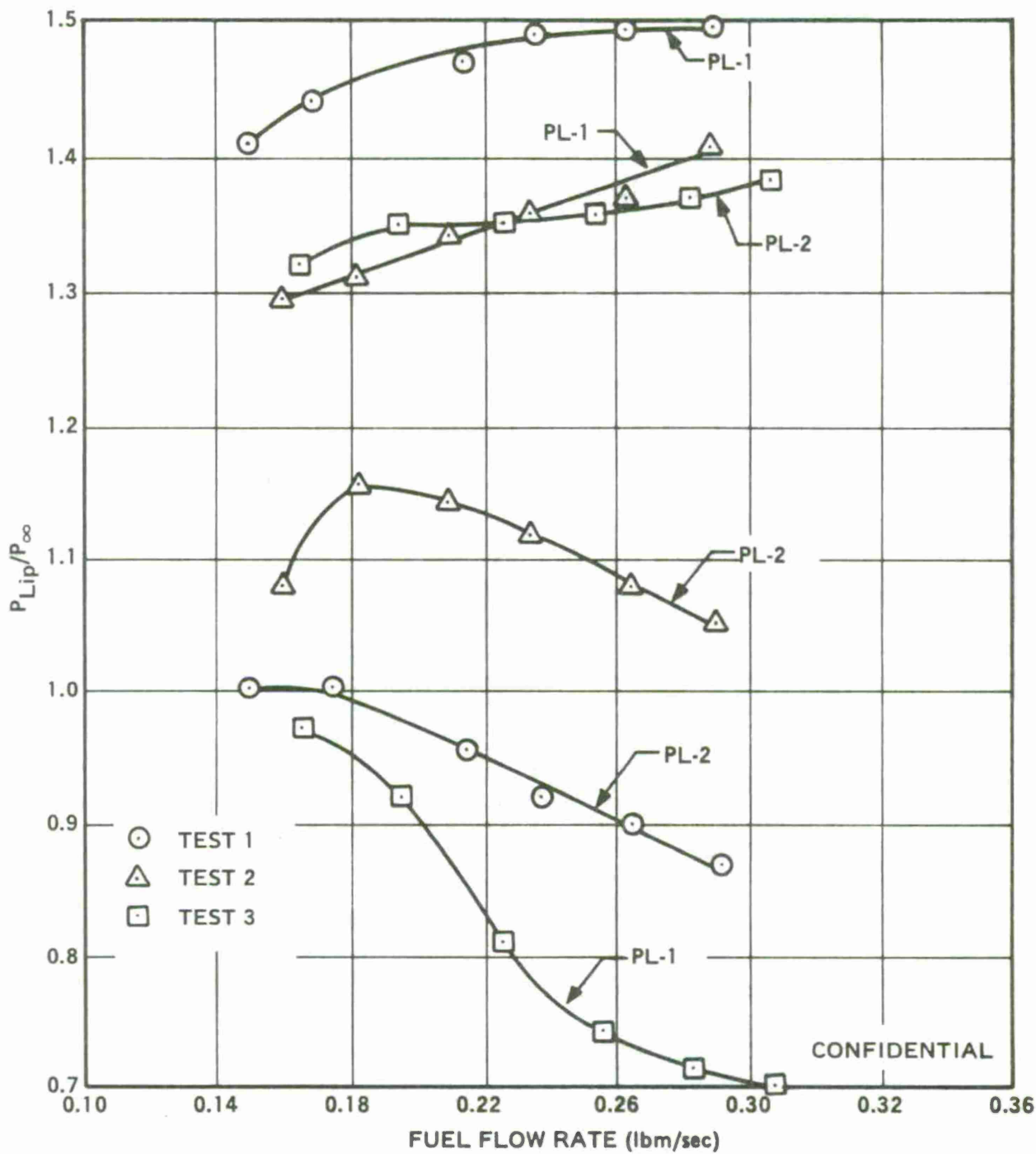


Figure 61. (C) Lip Pressure Ratios for Tests 1, 2 and 3 with ARCADENE 129A (U).

8. BASE FLOW TEMPERATURES

(C) All of the measured base flow temperatures are compared in Figure 62. The largest temperatures were recorded for Tests 6 and 7. During these tests the thermocouple radiation shield did not remain intact, and the high temperatures can be attributed to radiation from the Al_2O_3 particles in the supersonic stream. Of the remaining tests, it is most interesting to note that there was no temperature rise in Test 14 conducted with ARCADENE 300. Since some fuel was undoubtedly entrained in the boundary layer and swept into the recirculation bubble, one must conclude that ignition of this fuel did not occur, even though its theoretical total temperature was $3000^\circ K$. Lack of significant combustion with this propellant is corroborated by the dark color movies of the test and the absence of combustion evidence in the emission spectra.

9. SPECIFIC IMPULSE

(C) Corrected specific impulse values associated with the base pressure rise for Tests 4 to 15 are plotted versus fuel flow rate in Figure 63. These tests were all conducted with a Mach 2.5 flow using either ARCADENE 168A or ARCADENE 300.

(C) Normally we define the specific impulse as

$$I_{sp} = \frac{(\bar{P}_B - \bar{P}_{BO}) A_B}{\dot{m}_f}$$

where:

\bar{P}_B = Average base pressure with fuel flow, psia

\bar{P}_{BO} = Average base pressure before fuel flow, psia

A_B = Base area, in^2

\dot{m}_f = Fuel flow rate, lbm/sec

However, as described above, there was considerable scatter in the values of \bar{P}_{BO} resulting from pressure mismatches which transmitted their effect to the base through the boundary layer on the base plate extension. The fact that a good correlation of \bar{P}_B/P_∞ as a function of \dot{m}_f could be obtained without correction for \bar{P}_{BO} suggests that in most cases \bar{P}_B was independent of \bar{P}_{BO} . Under these circumstances we should not expect a good correlation of I_{sp} as defined above with \dot{m}_f , for scatter in the \bar{P}_{BO} values will impart scatter to the I_{sp} values. Graphs of such I_{sp} values versus fuel flow rate do indeed show such scatter.

(C) To reduce this scatter, and, also, to be consistent with the premise that \bar{P}_B is independent of \bar{P}_{BO} as implied in our \bar{P}_B/P_∞ versus \dot{m}_f correlation, we have taken \bar{P}_{BO} to be equal to $0.45 P_\infty$ in the calculation of I_{sp} . Thus, we have made the reasonable assumption that, without the pressure mismatches, \bar{P}_{BO} would be some constant fraction of P_∞ and we have assumed this fraction to be 0.45, the value indicated by the correlation of Figure 51. We refer to specific impulse values computed with this assumption as corrected specific impulse values.

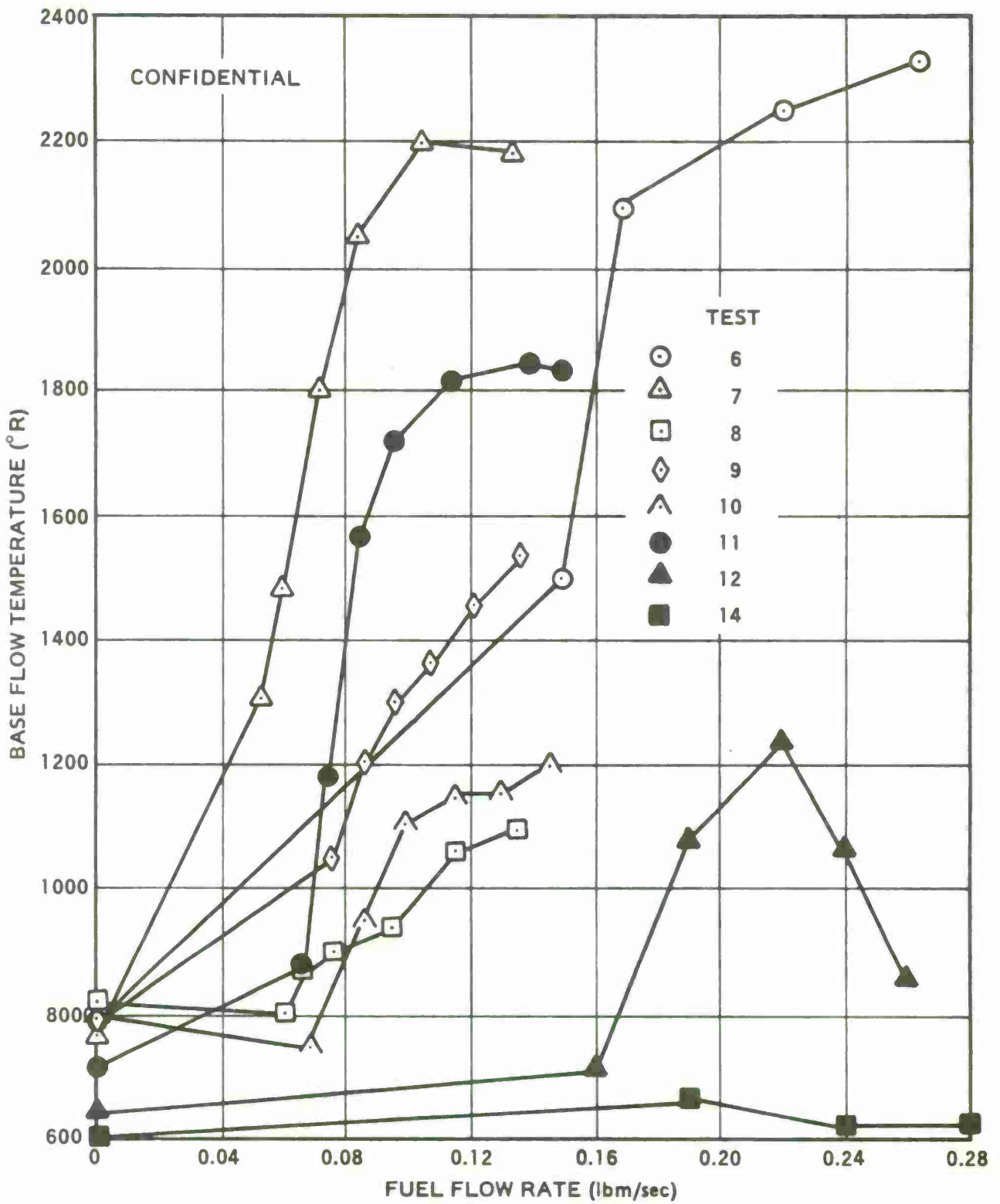


Figure 62. (C) Base Flow Temperatures (U).

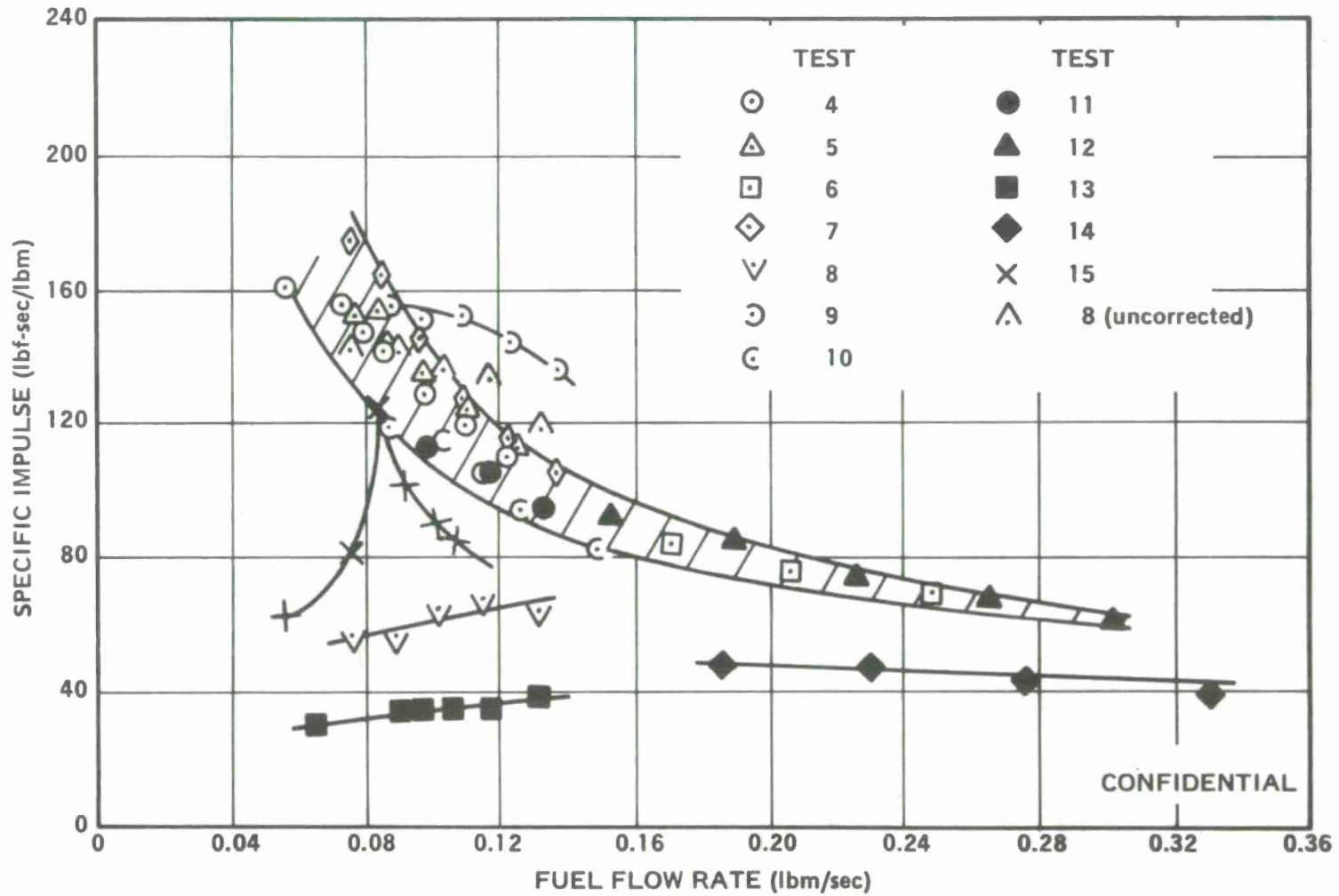


Figure 63. (C) Corrected Specific Impulse Values for Mach 2.5 Tests Conducted with ARCADENE 168A and ARCADENE 300 (U).

CONFIDENTIAL

(C) As required by the good correlation of base pressure ratios with fuel flow rate, the corrected specific impulse values also correlate well with fuel flow rate. Except for Test 15, conducted at the altitude test condition, and Tests 8, 9, 13, and 14, all of the data fall within the shaded correlation band, showing a decrease in specific impulse as fuel flow rate increases. This decrease is the consequence of the only slight rise in base pressure with fuel flow rate once some undefined minimum fuel flow rate is surpassed. However, we should emphasize that if the injection shock wave reflections are limiting base pressure rises, then little significance should be attached to the shape of the correlation band in Figure 63. External burning alone might cause the base pressure to increase rapidly with fuel flow rate, but, because the shock waves would be stronger and the reflections closer to the base at large fuel flow rates, the reflections could be causing a greater decrease in base pressure and thus masking the true effect of external burning.

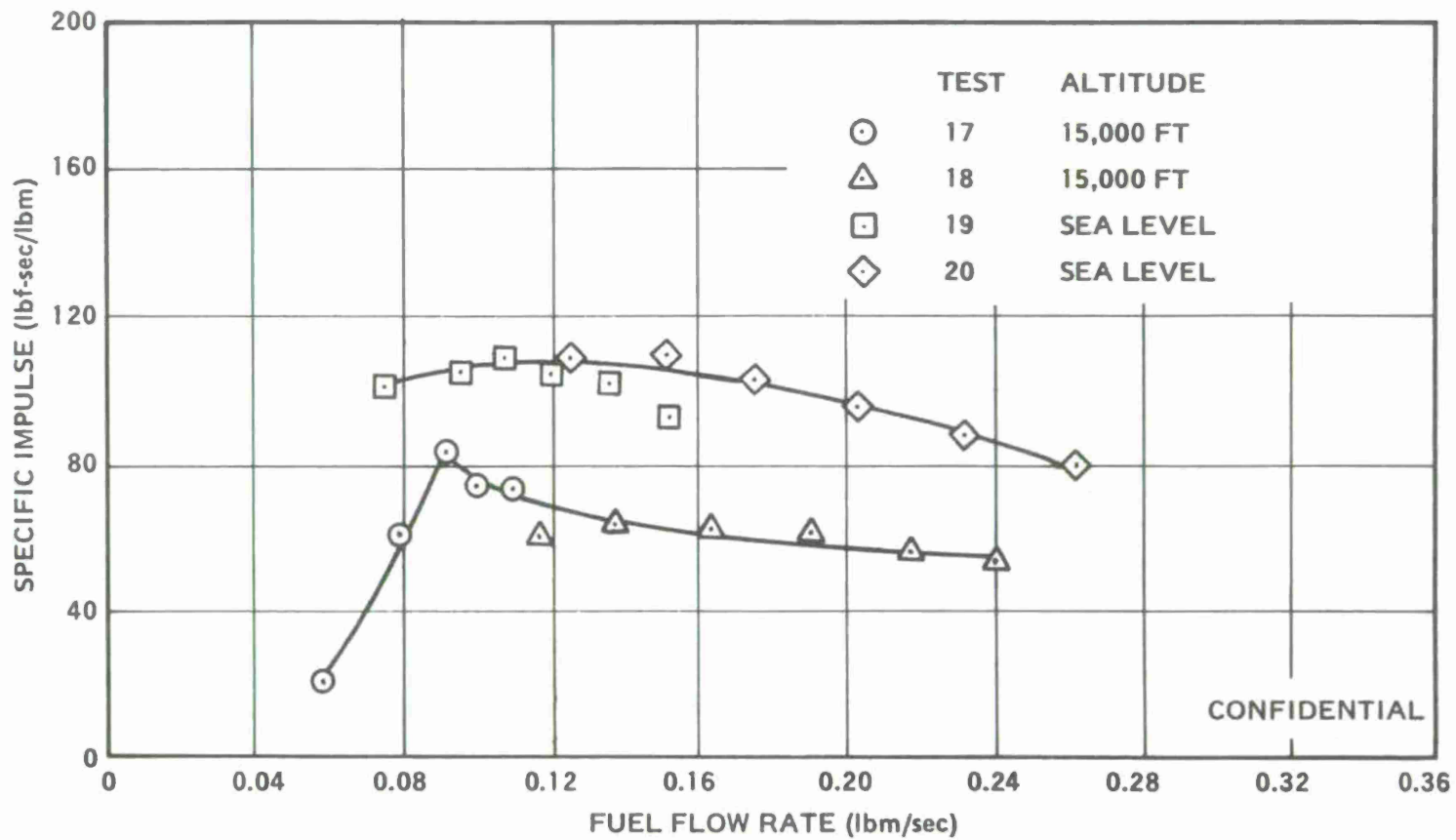
(C) The results of Tests 8, 9, 13, and 14 were also significantly displaced from the base pressure ratio correlation discussed above, and the same possible explanations discussed there are applicable here. However, recall that the low values of both \bar{P}_B and \bar{P}_{BO} for Test 8 could be attributed to the reflections from the shock waves originating from the nozzle extensions. If the effect of these reflections on \bar{P}_B is not altered by fuel injection, then we should expect uncorrected specific impulse values for this test to correlate better than the corrected ones. Uncorrected values have been included in Figure 63, and they fall either within or just above the correlation band.

(C) For the most part, the corrected specific impulse values for Test 15, conducted at the altitude test conditions, fall below the sea-level correlation band. It is interesting to note that the data for this test include the mass flow rate range where $\bar{P}_B - \bar{P}_{BO}$ increases more than linearly with fuel flow rate. Accordingly, the specific impulse first increases and then decreases with increasing fuel flow rate. There are many possible reasons why the altitude results fall below the sea-level ones, but the data are so scarce that it would be unproductive to speculate at this time.

(C) Specific impulse values for Tests 17 to 20 conducted with Mach 2.0 test conditions are plotted versus fuel flow rate in Figure 64. The values plotted are uncorrected because there were insufficient data to establish a standard value for \bar{P}_{BO}/P_∞ . Also, the \bar{P}_{BO} values were not much different for the two tests conducted at altitude nor for the two tests conducted at sea level. However, there was a significant difference between the average \bar{P}_{BO} value at altitude and the average value at sea level.

(C) The data for the four tests fall on two correlation lines, one for the two altitude tests and one for the two sea-level tests. As for the Mach 2.5 results, the sea-level specific impulse values are greater than the altitude ones. However, if a common \bar{P}_{BO} were used to correct both sets of data, the results would fall closer together.

(C) The Mach 2.0, sea-level results are not too much different from the Mach 2.5 results. Because of the different shapes of the curves, the Mach 2.0 results are lower than the Mach 2.5 results at low fuel flow rates and higher than the Mach 2.5 results at higher fuel flow rates. On the other hand, the Mach 2.0, altitude results are generally lower than the Mach 2.5, altitude results, and the indicated curve shapes are quite similar.



CONFIDENTIAL

Figure 64. (C) Specific Impulse Values for Mach 2.0 Tests (U).

~~CONFIDENTIAL~~

SECTION VI

CONCLUSIONS AND RECOMMENDATIONS

1. CONCLUSIONS

- a. (U) Base pressures before fuel injection are affected by pressure mismatches between the free-stream static pressure and the surrounding atmosphere even though such disturbances do not reach the wake centerline closer than 5 model radii from the base. The disturbances are transmitted to the base through the boundary layer on the base plate extension. The effect was observed only when the free-stream static pressure was less than the pressure of the surrounding atmosphere.
- b. (U) Shock waves formed at disturbances on the model upstream from the base can result in inappropriately low base pressures. The shock waves reflect from the free-jet boundary as expansion waves, and the associated pressure drop is transmitted back to the base through either the subsonic portion of the wake or the boundary layer on the base plate extension.
- c. (C) External burning using ARCADENE 168A as the fuel results in significant base pressure rises. At Mach 2.5, sea-level test conditions, base pressure ratios increased to 0.85, and, at Mach 2.0, 15,000-foot altitude test conditions, base pressure ratios greater than unity were measured.
- d. (C) Color movies of the tests and emission spectra indicate that significant combustion occurred with ARCADENE 168A propellant. On the other hand, these data do not provide evidence that significant combustion occurred with either ARCADENE 300 or ARCADENE 129A.
- e. (C) Strong disturbances during fuel injection were noted in the pressure distributions downstream from the model base. These disturbances were caused by the reflections from the free-jet boundary of the injection interaction shock waves.
- f. (C) There is strong evidence that the disturbances caused by the reflections of the interaction shock waves are restricting the measured base pressure rises. Since the shock reflections would not be present in a real flight environment, flight performance should be significantly better than indicated by the current test results.
- g. (C) The maximum specific impulse associated with the base pressure rises was about 160 lbf-sec/lbm, measured with ARCADENE 168A at the Mach 2.5, sea-level flight conditions. If we add 122 lbf-sec/lbm resulting from 45-degree, Mach 2.0 jets, the indicated total specific impulse is about 280.
- h. (C) The maximum specific impulse values, like the base pressures, are restricted by the interaction shock reflections and should be significantly larger in a real flight environment.

~~CONFIDENTIAL~~

UNCLASSIFIED

2. RECOMMENDATIONS

- a. (U) Since the disturbances resulting from the shock reflections could be transmitted to the base through the boundary layer on the base plate extension, reducing this boundary layer thickness could eliminate the effect of these reflections on base pressure. The boundary layer thickness might be reduced by shortening the plate. At its current length, it may be extending into the region of the large pressures associated with the breakdown of the supersonic flow, and the resulting adverse pressure gradient may be causing a thickening of the boundary layer at $x/r \cong 2 - 4$. The current length of the base plate extension is 8.5 model radii. In the Atlantic Research-Navy program, the length of the base plate extension was only 4.3 radii, and no disturbances were observed in the downstream pressure distributions. Accordingly, we recommend a series of external-burning tests using successively shorter lengths of the base plate extension to determine whether or not such shortening can eliminate the effect of the shock reflections on the base pressure.
- b. (U) If the tests recommended in (a) above indicate that the boundary layer is the path through which the disturbances are transmitted to the base, then consideration should be given to testing with a full model, for which there would be no base plate extension and, accordingly, no feedback of the disturbances to the model base.
- c. (U) If the tests recommended in (a) above indicate that the boundary layer is not the path through which the disturbances are transmitted to the base, then some means should be found to eliminate the shock reflections or move them further downstream from the model base. Possibilities are cancellation with a contoured nozzle skirt or porous wall, trapping with a jet stretcher, or shifting downstream with a larger annular gap or a diverging free-jet boundary.
- d. (U) Analysis of the current data should be continued to provide a better understanding of the results obtained to date.
- e. (U) Additional experiments should be planned to determine the potential of external-burning propulsion as applied to larger missiles. Variables to be considered are vehicle diameter, fuel injection configuration, fuel composition, flight altitude and Mach number.

UNCLASSIFIED

UNCLASSIFIED

UNCLASSIFIED

APPENDIX I

JET PENETRATION AND MIXING CALCULATIONS

(U) In the course of selecting test conditions for the experiments in this program, numerous calculations were made of fuel jet penetration and mixing in a supersonic stream. The method of calculation and the results are presented below.

(U) For normal injection, the unified approach of Billig, Orth and Lasky⁽¹⁵⁾ was used to calculate the initial path of the fuel jets prior to their mixing with air. Referring to Figure 65, the flow on the jet centerline is assumed to

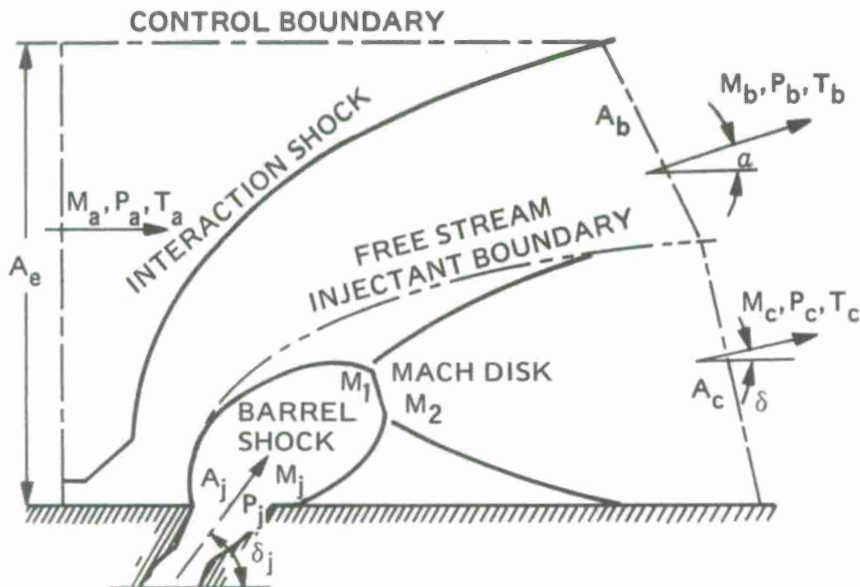


Figure 65. Generalized Model Configuration for Gaseous Secondary Injection into a Supersonic Free Stream.

expand isentropically to a state for which a normal shock will cause the pressure to rise to the effective back pressure, defined as $2/3$ of the free-stream pitot pressure. The flow in the jet which is displaced from the centerline does not expand isentropically but is accelerated by the free-stream pressure field. The height to the center of the Mach disk in Figure 65 is given by the empirical relation

$$y_1/D_j^* = M_j^{1/4} (P_j^*/P_{eb})^{1/2} \quad (1)$$

where:

- y_1 = height to the center of the Mach disk
- D_j^* = diameter of the nozzle throat
- M_j = Mach number of the jet as it leaves the nozzle

UNCLASSIFIED

P_j^* = pressure at the nozzle throat

P_{eb} = effective back pressure

The x coordinate of the Mach disk is also given empirically:

$$x_1/y_1 = 1.25 \left[1 - \exp(-M_a/M_j) \right] \quad (2)$$

A third empirical relation gives the total flow area for the jet at Station (1):¹

$$(A_1/A_j)^{1/2} = 1 + 1.45 \ln(P_j/P_{eb}) \left[1 - \exp(-0.332 y_1/D_j) \right] \quad (3)$$

where:

A_1 = total jet flow area at Station (1)

A_j = nozzle exit area

(U) Assuming adiabatic flow, the average Mach number at Station (2)² can be calculated from the continuity equation:

$$M_2 \left[1 + (\gamma_j - 1) M_2^2/2 \right]^{1/2} = M_j \left[1 + (\gamma_j - 1) M_j^2/2 \right]^{1/2} (P_j/P_{eb})(A_j/A_2) \quad (4)$$

where A_2 is taken to be equal to A_1 , and γ_j is the ratio of the specific heats for the injectant (assumed constant).

(U) From Station (2) to Station (C),³ the jet is assumed to expand isentropically to the undisturbed, free-stream static pressure, P_a . M_c is then given by:

$$M_c^2 = 2 \left\{ \left[1 + (\gamma_j - 1) M_2^2/2 \right] (P_{eb}/P_a)^{(\gamma_j - 1)/\gamma_j} - 1 \right\} / (\gamma_j - 1) \quad (5)$$

and A_c can be computed from

$$(A_c/A_j)^{1/2} = \left[\frac{1 + (\gamma_j - 1) M_c^2/2}{1 + (\gamma_j - 1) M_2^2/2} \right]^{(\gamma_j + 1)/4(\gamma_j - 1)} (M_2/M_c)^{1/2} (A_1/A_j)^{1/2} \quad (6)$$

¹Station (1) refers to the position of the Mach disk shown in Figure 65.

²Station (2) refers to conditions immediately downstream of the Mach disk.

³Station (C) refers to a station downstream of Station(2) where the pressure in the jet is equal to the undisturbed, free-stream static pressure.

UNCLASSIFIED

(U) To compute the axial distance required for the jet to expand from the Mach disk to Station (C), it was assumed that the jet expands through a Prandtl-Meyer turn with the pressure constant at P_a along the jet boundary. In reality, this boundary pressure will not be constant because of the interaction between the jet and the air stream, and, since the boundary pressure will be higher than P_a , the jet expansion angle computed in this way will be larger than the actual angle. Accordingly, the computed distance $x_c - x_1$ will be somewhat smaller than the actual value. With these limitations in mind, the expansion angle (Θ) of the jet was computed from the method of characteristics⁽¹⁶⁾

$$\Theta = \omega_c - \omega_2 \quad (7)$$

$$\omega_i = \sqrt{\frac{\gamma_j + 1}{\gamma_j - 1}} \arctan \frac{\sqrt{(M_i^*)^2 - 1}}{\frac{\gamma_j + 1}{\gamma_j - 1} - (M_i^*)^2} - \arctan \frac{\sqrt{(M_i^*)^2 - 1}}{1 - \frac{\gamma_j - 1}{\gamma_j + 1} (M_i^*)^2} \quad (8)$$

where:

γ_j = specific heat ratio for the jet

M_i^* = local velocity of the stream at Station (i)⁴ divided by the velocity of this stream when it is isentropically accelerated or decelerated to Mach 1.

The distance $x_c - x_1$ is then given by

$$x_c - x_1 = (D_c - D_1)/2 \tan \Theta \quad (9)$$

(U) Downstream from Station (C), the jet mixing was assumed to be described by the semi-empirical analysis of Abramovich:⁽¹⁷⁾

$$db/dx = 0.27 \frac{1 + \bar{\rho}}{2} \cdot \frac{1 - m}{1 + \bar{\rho} m} \quad (10)$$

where:

b = jet width or radius

x = axial distance downstream from Station (C)

⁴The subscript i refers to any station at or between Station (2) and Station (C).

$\bar{\rho}$ = air density (ρ_a) divided by jet density (ρ_c)

m = air velocity (U_a) divided by jet velocity (U_c)

Although db/dx will vary with the axial position in the jet, for this computation it was assumed to be constant and equal to the value computed at Station (C).

(U) The increase in jet flow area was assumed to be equal to the area of the free-stream stream tube entrained by the jet up to any given axial location. The average air/fuel ratio in the jet was then taken to be the mass flow rate of the entrained stream tube divided by the initial mass flow rate of the jet.

(U) The above computation procedure was used for hypothetical Tests 1-1 through 1-4 where normal injection from models without boat tails is employed. Where the injection angle is not 90 degrees and where injection is from boat tail surfaces, the above calculation procedure must be altered. First, the jet penetration height y_1 is reduced from the normal injection case by dividing by $1 + \cos \delta$, where δ is the angle between the jet velocity vector and the air velocity vector. This method of accounting for injection angles other than 90 degrees has been validated experimentally by the work of Cohen, Coulter, and Egan.⁽¹⁸⁾

(U) Second, some assumption must be made concerning the turning of the air at the shoulder of the boat tail. Here it was assumed that the air undergoes a Prandtl-Meyer expansion cornered at the boat tail shoulder. With this assumption, the following flow parameters can be computed.

Table VI. Flow Parameters for Angular Injection Tests.

Test no.	Boattail angle (deg)	Injection angle relative to air flow (deg)	Air properties			
			M	T (°K)	P (psia)	P_{eb} (psia)
1-5	0	45	2.50	222	14.7	83.6
1-6	15	60	3.24	161	4.79	44.7
1-7	30	75	4.27	108	1.16	18.5
1-8	45	90	5.88	63.1	0.180	5.40

(U) Finally, the x coordinate of the Mach disk will be affected by the injection angle. Once y_1 is calculated, x_1 can be computed from the jet trajectory proposed by Shandorov as reported by Abramovich⁽¹⁹⁾

$$x_1 = D_j \left(\frac{q_a}{q_j} \right) \left(\frac{y_1}{D_j} \right)^{2.55} + \frac{y_1}{D_j} \left(1 + \frac{q_a}{q_j} \right) \cot \delta \quad (11)$$

UNCLASSIFIED

where q_a/q_j is the ratio of the dynamic pressure of the local air stream to the dynamic pressure of the jet. x_1 is the displacement of the Mach disk in the direction of the local air flow.

(U) It will be recalled that Equation (3), which permits calculation of A_1 , is empirical. Since no information could be found in the literature showing the effect of injection angle on A_1 , we elected to assume that A_1 is not affected by injection angle. Accordingly y_1 in Equation (3) is given by Equation (1) and is not reduced by the factor $1/(1 + \cos \delta)$. Also, since the flow over the boattail must eventually turn parallel to the projectile axis, for the computation of the jet spreading parameter db/dx , it was assumed that the air flow was isentropically turned parallel to the projectile just downstream of Station (C), i.e., just before the start of mixing.

(U) The results of jet penetration and mixing calculations for eight hypothetical tests are presented in Tables VII to XIV. For each test a progressive grain was assumed with a pressure range of from 186 to 570 psia. The calculations were made for pressures of 186, 286, 386, 486, and 586 psia. For five-nozzle injectors, the flow in each nozzle increases from 0.0200 lbm/sec at a chamber pressure of 186 psia to 0.0630 lbm/sec at a pressure of 586 psia. For nine-nozzle injection, the corresponding nozzle flow rates increase from 0.0111 lbm/sec to 0.0350 lbm/sec. The free-stream Mach number and static pressure were 2.5 and 14.7 psia, respectively, and the propellant was ARCADENE 129A.

(U) In each test, the jet penetration height increases throughout the run, with the penetration height proportional to the square root of the chamber pressure. For five-nozzle injectors, the penetration height is greater than the penetration height for nine nozzle injectors by the factor $\sqrt{9/5}$. This comparison follows from the dependence of y_1 on D_j^* indicated in Equation (1). Also the penetration height for Mach 2 injection is greater than the penetration height for sonic injection by the factor 1.19.

(U) The penetration height for angular injection is different from that for normal injection. For Test 1-5, where injection is 45 degrees aftward from the model corner, the penetration height is reduced by the factor $1/(1 + \cos \delta) = 0.586$ from the corresponding normal injection case (Test 1-4). For Tests 1-6, 1-7, and 1-8, the penetration height is reduced by the factor $1/(1 + \cos \delta)$, but for these tests the effective back pressure, P_{eb} , is reduced because of the expansion at the boattail shoulder (see Table VI). The increase in penetration resulting from the reduced effective back pressure outweighs the reduction resulting from angular injection, and the net effect is increased penetration.

(U) It should be noted that the increase in penetration height with increasing pressure within a test is occurring at constant nozzle throat area, and, accordingly, with increasing nozzle mass flow rate. According to this analysis, the penetration height cannot be increased by merely reducing the nozzle throat area in order to increase the chamber pressure. Although $\sqrt{P_j^*}$ will increase, D_j^* will decrease proportionately, and, according to Equation (1), the penetration height will remain unchanged.

(U) For Tests 1-1 through 1-4, the axial distance to the Mach disk, x_1 , ranges from 0.1 inch to about 0.3 inch. It increases as y_1 is increased, and is only slightly greater for Mach 2 injection than for sonic injection. Qualitatively, x_c varies as does x_1 .

Table VII. Results of Jet Penetration and Mixing Calculations for Test 1-1.

Propellant: ARCADENE 129A
 Number of nozzles: 5
 Initial jet Mach no.: 1.0
 Normal injection - no boattail

Rocket motor pressure (psia)	Jet mass flow rate (lbm/sec)	Penetration height (in)	Distance (in) to station		Jet diameter (in) at station		Jet Mach no. at station		Jet diameter (in) at $\ell =$			Air/fuel ratio at $\ell =$		
			1	C	1	C	2	C	1	2	3	1	2	3
186	0.0200	0.157	0.180	0.232	0.154	0.230	1.03	2.20	0.875	1.39	1.91	47.4	125.0	238.0
286	0.0308	0.194	0.223	0.288	0.188	0.283	1.06	2.22	0.909	1.42	1.94	32.2	84.2	159.0
386	0.0415	0.226	0.259	0.335	0.219	0.329	1.06	2.22	0.938	1.45	1.97	24.7	64.2	121.0
486	0.0523	0.253	0.291	0.376	0.246	0.370	1.05	2.21	0.965	1.48	2.00	20.2	52.3	97.9
586	0.0630	0.278	0.319	0.413	0.272	0.407	1.04	2.21	0.989	1.51	2.02	17.1	44.3	82.7

UNCLASSIFIED

112

UNCLASSIFIED

Table VIII. Results of Jet Penetration and Mixing Calculations for Test 1-2.

Propellant: ARCADENE 129A
 Number of nozzles: 9
 Initial jet Mach no.: 1.0
 Normal injection - no boattail

Rocket motor pressure (psia)	Jet mass flow rate (lbm/sec)	Penetration height (in)	Distance (in) to station		Jet diameter (in) at station		Jet Mach no.: at station		Jet diameter (in) at $\ell =$			Air/fuel ratio at $\ell =$		
			1	C	1	C	2	C	1	2	3	1	2	3
			186	0.0111	0.117	0.134	0.173	0.115	0.171	1.03	2.20	0.838	1.35	1.87
286	0.0171	0.145	0.166	0.215	0.140	0.211	1.06	2.22	0.862	1.38	1.89	54.3	144.0	276.0
386	0.0231	0.168	0.193	0.250	0.163	0.245	1.06	2.22	0.884	1.40	1.92	41.6	110.0	208.0
486	0.0290	0.189	0.217	0.280	0.184	0.276	1.05	2.21	0.904	1.42	1.94	33.9	88.8	168.0
586	0.0350	0.207	0.238	0.307	0.202	0.303	1.04	2.21	0.922	1.44	1.96	28.8	75.0	142.0

UNCLASSIFIED

113

UNCLASSIFIED

Table IX. Results of Jet Penetration and Mixing Calculations for Test 1-3.

Propellant: ARCADENE 129A
 Number of nozzles: 5
 Initial jet Mach no.: 2.0
 Normal injection - no boattail

Rocket motor pressure (psia)	Jet mass flow rate (lbm/sec)	Penetration height (in)	Distance (in) to station		Jet diameter (in) at station		Jet Mach no. at station		Jet diameter (in) at $\ell =$			Air/fuel ratio at $\ell =$		
			1	C	1	C	2	C	1	2	3	1	2	3
186	0.0200	0.186	0.166	0.240	0.0985	0.177	2.13	3.13	0.936	1.55	2.16	56.0	156.0	306.0
286	0.0308	0.231	0.206	0.300	0.119	0.215	2.22	3.22	0.955	1.57	2.18	37.4	104.0	204.0
386	0.0415	0.269	0.239	0.347	0.140	0.253	2.18	3.18	0.970	1.58	2.19	28.0	78.0	152.0
486	0.0523	0.301	0.269	0.388	0.161	0.288	2.11	3.11	0.984	1.59	2.20	22.5	62.3	121.0
586	0.0630	0.331	0.295	0.424	0.181	0.322	2.03	3.04	0.998	1.60	2.20	18.8	51.8	100.0

UNCLASSIFIED

114

UNCLASSIFIED

Table X. Results of Jet Penetration and Mixing Calculations for Test 1-4.

Propellant: ARCADENE 129A
 Number of nozzles: 9
 Initial jet Mach no.: 2.0
 Normal injection - no boattail

Rocket motor pressure (psia)	Jet mass flow rate (lbm/sec)	Penetration height (in)	Distance (in) to station		Jet diameter (in) at station		Jet Mach no. at station		Jet diameter (in) at $l =$			Air/fuel ratio at $l =$		
			1	C	1	C	2	C	1	2	3	1	2	3
			186	0.0111	0.139	0.124	0.179	0.0734	0.132	2.13	3.13	0.916	1.53	2.14
286	0.0171	0.172	0.154	0.223	0.0886	0.160	2.22	3.22	0.932	1.55	2.16	65.5	184.0	361.0
386	0.0231	0.200	0.178	0.259	0.104	0.188	2.18	3.18	0.942	1.55	2.17	49.1	137.0	268.0
486	0.0290	0.225	0.200	0.289	0.120	0.215	2.11	3.11	0.951	1.56	2.17	39.3	109.0	213.0
586	0.0350	0.247	0.220	0.316	0.135	0.247	2.03	3.04	0.960	1.56	2.17	32.8	90.5	176.0

UNCLASSIFIED

115

UNCLASSIFIED

Table XI. Results of Jet Penetration and Mixing Calculations for Test 1-5.

Propellant: ARCADENE 129A
 Number of nozzles: 9
 Initial jet Mach no.: 2.0
 45-degree injection - no boattail

Rocket motor pressure (psia)	Jet mass flow rate (lbm/sec)	Penetration height (in)	Distance (in) to station		Jet diameter (in) at station		Jet Mach no. at station		Jet diameter (in) at $\ell =$			Air/fuel ratio at $\ell =$		
			1	C	1	C	2	C	1	2	3	1	2	3
186	0.0111	0.0814	1.21	1.26	0.0734	0.132	2.13	3.13	0.219	0.829	1.44	3.67	80.1	245.0
286	0.0171	0.101	1.24	1.30	0.0886	0.160	2.22	3.22	0.231	0.846	1.46	2.16	53.6	164.0
386	0.0231	0.117	1.29	1.37	0.104	0.188	2.18	3.18	0.233	0.846	1.46	1.09	39.1	120.0
486	0.0290	0.132	1.35	1.43	0.120	0.215	2.11	3.11	0.232	0.840	1.45	0.351	30.2	93.8
586	0.0350	0.144	1.41	1.50	0.135	0.240	2.03	3.04	0.230	0.833	1.44	0.00	24.1	76.1

Table XII. Results of Jet Penetration and Mixing Calculations for Test 1-6.

Propellant: ARCADENE 129A
 Number of nozzles: 9
 Initial jet Mach no.: 2.0
 45-degree injection - 15-degree boattail

Rocket motor pressure (psia)	Jet mass flow rate (lbm/sec)	Penetration height (in)	Distance (in) to station		Jet diameter (in) at station		Jet Mach no. at station		Jet diameter (in) at $l =$			Air/fuel ratio at $l =$		
			1	C	1	C	2	C	1	2	3	1	2	3
186	0.0111	0.127	0.871	0.956	0.0984	0.213	2.20	3.49	0.485	1.11	1.74	22.8	142.0	355.0
286	0.0171	0.157	0.946	1.05	0.127	0.271	2.07	3.36	0.505	1.13	1.75	14.1	92.9	232.0
386	0.0231	0.182	1.02	1.14	0.154	0.324	1.95	3.24	0.520	1.14	1.75	9.51	68.2	171.0
486	0.0290	0.205	1.10	1.22	0.179	0.373	1.85	3.15	0.533	1.14	1.75	6.64	53.5	134.0
586	0.0350	0.225	1.16	1.30	0.202	0.416	1.77	3.08	0.544	1.15	1.76	4.66	43.6	110.0

Table XIII. Results of Jet Penetration and Mixing Calculations for Test 1-7.

Propellant: ARCADENE 129A
 Number of nozzles: 9
 Initial jet Mach no.: 2.0
 45-degree injection - 30-degree boattail

118

Rocket motor pressure (psia)	Jet mass flow rate (lbm/sec)	Penetration height (in)	Distance (in) to station		Jet diameter (in) at station		Jet Mach no. at station		Jet diameter (in) at $l =$			Air/fuel ratio at $l =$		
			1	C	1	C	2	C	1	2	3	1	2	3
186	0.0111	0.234	0.672	0.807	0.170	0.431	1.88	3.49	0.828	1.45	2.08	59.7	231.0	495.0
286	0.0171	0.291	0.773	0.931	0.224	0.555	1.71	3.33	0.903	1.52	2.14	39.4	156.0	333.0
386	0.0231	0.338	0.862	1.04	0.270	0.659	1.61	3.24	0.965	1.58	2.20	28.7	119.0	253.0
486	0.0290	0.379	0.941	1.14	0.310	0.749	1.55	3.19	1.02	1.63	2.25	21.9	96.2	205.0
586	0.0350	0.416	1.01	1.22	0.346	0.828	1.51	3.16	1.07	1.68	2.29	17.1	80.7	173.0

UNCLASSIFIED

UNCLASSIFIED

Table XIV. Results of Jet Penetration and Mixing Calculations for Test 1-8.

Propellant: ARCADENE 129A
 Number of nozzles: 9
 Initial jet Mach no.: 2.0
 45-degree injection - 45-degree boattail

Rocket motor pressure (psia)	Jet mass flow rate (lbm/sec)	Penetration height (in)	Distance (in) to station		Jet diameter (in) at station		Jet Mach no. at station		Jet diameter (in) at $\ell =$			Air/fuel ratio at $\ell =$		
			1	C	1	C	2	C	1	2	3	1	2	3
186	0.0111	0.547	0.313	0.545	0.363	1.19	1.50	3.52	1.64	2.27	2.90	181.0	475.0	862.0
286	0.0171	0.678	0.352	0.636	0.455	1.36	1.47	3.49	1.89	2.51	3.14	133.0	347.0	622.0
386	0.0231	0.787	0.383	0.715	0.525	1.57	1.49	3.51	2.08	2.70	3.33	106.0	278.0	496.0
486	0.0290	0.884	0.408	0.786	0.582	1.75	1.52	3.53	2.24	2.86	3.49	88.1	235.0	417.0
586	0.0350	0.970	0.429	0.853	0.628	1.91	1.56	3.57	2.37	3.00	3.63	75.3	203.0	362.0

UNCLASSIFIED

(U) For the angular injection Tests 1-5 through 1-8, the x_1 values range up to five times greater than for the corresponding normal injection case. The reason for this trend is the strong dependence of x_1 on δ indicated by Equation (11).

(U) It is interesting to note that even though the penetration height, y_1 , increases continuously from Tests 1-5 to 1-8, x_1 decreases. There are two reasons for this trend. First, even though the injection angle relative to the projectile axis is constant at 45 degrees for these four tests, the injection angle relative to the air flow direction, δ , is continuously increasing so $\cot \delta$ is continuously decreasing. The quantity x_1 is measured from the injection port in the direction of the air flow. Second, since the boattail angle increases from Test 1-5 to Test 1-8, the Mach number also increases. The Mach number increase causes a decrease in the air dynamic pressure, q_a , and, according to Equation (11), a reduction in q_a will cause a reduction in x_1 .

(U) For Tests 1-1 through 1-4, the jet diameters at Station (1) range from about 0.1 to 0.3 inch. They increase with fuel flow rate within a given test and are larger for five-nozzle tests than for nine-nozzle tests. Also, tests with Mach 2.0 injection show smaller jet diameters at Station (1) than do tests with sonic injection.

(U) For the tests with boattails (1-6, 1-7, 1-8), the jet diameter at Station (1) increases as the boattail angle increases. The reason for this trend is that the effective back pressure, P_{eb} , decreases with increasing boattail angle as shown in Table VI. Equation (3) shows that A_1 increases directly because of a reduction in P_{eb} and also indirectly because reducing P_{eb} causes an increase in y_1 as calculated from Equation (1).

(U) The variation with the various test parameters of the jet diameter at Station (C) is qualitatively the same as the variations of the jet diameter at Station (2). The diameter at Station (C) is computed from the diameter at Station (1) by assuming an isentropic expansion from the effective back pressure at Station (2) (where the diameter is D_1) to the free-stream static pressure at Station (C).

(U) For sonic, normal fuel injection, the Mach number at Station (2) is near unity and varies very little with rocket motor pressure. For Mach 2.0 normal injection, the Mach number at Station (2) is approximately 2.0 and, again, essentially invariant with rocket motor pressure.

(U) When injection is from boattail surfaces, the Mach number at Station (2) increases as the boattail angle increases. This trend results from the pressure in the air stream being reduced by the turn parallel to the boattail surface. Although the expansion of the jet to the effective back pressure is not isentropic, it is sufficiently nondissipative to result in an increase in Mach number, and the Mach number increases as the effective back pressure decreases.

(U) As in the case of the jet diameter at Station (C), the jet Mach number at Station (C) displays the same trends as do the Mach numbers at Station (2). The Mach numbers at Station (C) are computed from those at Station (2) by assuming an isentropic expansion from Station (2) to Station (C).

(U) Tables VII to XIV contain the jet diameters and air/fuel ratios in the jet as a function of the axial distance downstream from the model base. Data are presented for three axial locations ($\xi = 1, 2, \text{ and } 3$) corresponding to one, two, and three base radii downstream from the base.

(U) For the first four tests the air/fuel ratio in the jet increases as the number of nozzles increases and is higher for Mach 2.0 injection than for sonic injection. Within a given test, the air/fuel ratio in the jet decreases as the mass flow rate of fuel in the jet increases. The reasons for these trends are given below.

(U) The jet spreading rate, db/dx is essentially the same for corresponding five and nine nozzle tests. However, because the fuel mass flow rate in the jets is smaller for nine nozzles than for five nozzles, the air/fuel ratio in the jet increases more rapidly with ℓ for nine nozzles than for five nozzles. One can imagine that the mixing rate at the jet boundary is nearly the same for the two cases but that the area, per unit mass flow rate of fuel, available for air transport into the jet is greater for nine nozzles than for five nozzles.

(U) The observed increase in air/fuel ratio for Mach 2.0 injection as compared to sonic injection is the result of a greater jet spreading rate for the Mach 2.0 cases. For Mach 2.0 injection, the jet velocity at Station (C) is greater, and the ratio of air velocity to jet velocity (m) is smaller. Equation (10) shows that reducing m increases the jet spreading rate.

(U) As the pressure and mass flow rate increase within a given test, the jet spreading rate does not change significantly. The jet diameter increases, but the fuel mass flow rate within a jet increases roughly as the square of the diameter. Thus, the area per unit mass flow rate for mass transfer into the jet decreases as the mass flow rate in the jet increases, so the air/fuel ratios in the jet decrease as the mass flow rate in the jet increases.

(U) For Test 1-5, where injection is 45 degrees aftward, the air/fuel ratios at corresponding ℓ 's are considerably lower than for Test 1-4, where injection is normal to the projectile axis. The jet spreading rates are not much different for these tests. However, the values of x_c are much larger for Test 1-5 than they are for Test 1-4. Thus, at any given ℓ in Test 1-5, mixing has occurred over a shorter length for Test 1-5 than for Test 1-4, and, accordingly, the air/fuel ratios in the jet are smaller for Test 1-5.

(U) As boattails of increasing angle are added to the test configuration in Tests 1-6 through 1-8, the value for x_c decreases and the jet diameters at Station (C) increase. Thus, the jet area per unit mass flow rate available for mixing increases, and the length over which mixing has occurred at any given ℓ increases. Both of these trends contribute to the overall increase in air/fuel ratios in the jet with increasing boattail angle.

(U) In addition to the calculations described above, jet penetration and mixing calculations were made for 20 hypothetical tests with ARCADENE 168A. The results of these calculations are presented in Tables XV to XXXIV. The trends are the same as observed with ARCADENE 129A.

Table XV. Results of Jet Penetration and Mixing Calculations for Test 1-9.

Propellant: ARCADENE 168A
 Number of nozzles: 5
 Initial jet Mach no.: 1.0
 Normal injection - no boattail

Rocket motor pressure (psia)	Jet mass flow rate (lbm/sec)	Penetration height (in)	Distance (in) to station		Jet diameter (in) at station		Jet Mach no. at station		Jet diameter (in) at $l =$			Air/fuel ratio at $l =$		
			1	C	1	C	2	C	1	2	3	1	2	3
			200	0.00940	0.108	0.124	0.161	0.106	0.163	1.04	2.19	0.839	1.36	1.88
250	0.01175	0.121	0.139	0.180	0.118	0.182	1.06	2.20	0.850	1.37	1.89	78.0	209.0	400.0
300	0.01410	0.133	0.152	0.197	0.128	0.199	1.06	2.20	0.861	1.38	1.90	66.1	176.0	337.0
350	0.01645	0.144	0.165	0.213	0.139	0.215	1.06	2.20	0.872	1.39	1.91	57.6	153.0	292.0
400	0.01880	0.153	0.176	0.227	0.149	0.230	1.06	2.20	0.881	1.40	1.92	51.2	135.0	257.0

UNCLASSIFIED

UNCLASSIFIED

Table XVI. Results of Jet Penetration and Mixing Calculations for Test 1-10.

Propellant: ARCADENE 168A
 Number of nozzles: 9
 Initial jet Mach no.: 2.0
 Normal injection - no boattail

Rocket motor pressure (psia)	Jet mass flow rate (lbm/sec)	Penetration height (in)	Distance (in) to station		Jet diameter (in) at station		Jet Mach no. at station		Jet diameter (in) at $\ell =$			Air/fuel ratio at $\ell =$		
			1	C	1	C	2	C	1	2	3	1	2	3
200	0.00522	0.0962	0.0858	0.124	0.0518	0.0962	2.13	0.0962	0.939	1.58	2.21	222.0	630.0	1244.0
250	0.00652	0.108	0.0959	0.140	0.0569	0.106	2.19	0.106	0.949	1.59	2.23	181.0	513.0	1013.0
300	0.00783	0.118	0.105	0.153	0.0621	0.116	2.20	0.116	0.954	1.60	2.24	152.0	431.0	849.0
350	0.00913	0.127	0.113	0.165	0.0674	0.129	2.19	0.126	0.957	1.60	2.27	131.0	369.0	728.0
400	0.0104	0.136	0.121	0.176	0.0727	0.136	2.16	0.135	0.958	1.60	2.24	115.0	322.0	634.0

Table XVII. Results of Jet Penetration and Mixing Calculations for Test 1-11.

Propellant: ARCADENE 168A
 Number of nozzles: 5
 Initial jet Mach no.: 2.0
 Normal injection - no boattail

Rocket motor pressure (psia)	Jet mass flow rate (lbm/sec)	Penetration height (in)	Distance (in) to station		Jet diameter (in) at station		Jet Mach no. at station		Jet diameter (in) at $\ell =$			Air/fuel ratio at $\ell =$		
			1	C	1	C	2	C	1	2	3	1	2	3
200	0.00940	0.129	0.115	0.167	0.0695	0.129	2.13	3.06	0.953	1.59	2.23	126.0	355.0	699.0
250	0.01175	0.144	0.129	0.187	0.0763	0.143	2.19	3.11	0.965	1.61	2.25	103.0	290.0	570.0
300	0.01410	0.158	0.141	0.206	0.0834	0.156	2.20	3.12	0.971	1.61	2.26	86.5	243.0	478.0
350	0.01645	0.171	0.152	0.222	0.0905	0.169	2.19	3.11	0.975	1.62	2.26	74.5	209.0	410.0
400	0.01880	0.182	0.163	0.237	0.0975	0.182	2.16	3.08	0.979	1.62	2.26	65.3	183.0	358.0

Table XVIII. Results of Jet Penetration and Mixing Calculations for Test 1-12.

Propellant: ARCADENE 168A
 Number of nozzles: 9
 Initial jet Mach no.: 1.0
 Normal injection - no boattail

Rocket motor pressure (psia)	Jet mass flow rate (lbm/sec)	Penetration height (in)	Distance (in) to station		Jet diameter (in) at station		Jet Mach no. at station		Jet diameter (in) at $\ell =$			Air/fuel ratio at $\ell =$		
			1	C	1	C	2	C	1	2	3	1	2	3
			200	0.00523	0.0809	0.0928	0.120	0.0790	0.121	1.04	2.19	0.811	1.33	1.85
250	0.00652	0.0904	0.104	0.134	0.0876	0.135	1.06	2.20	0.820	1.34	1.86	133.0	362.0	701.0
300	0.00783	0.0990	0.114	0.147	0.0958	0.148	1.06	2.20	0.828	1.35	1.87	113.0	305.0	589.0
350	0.00913	0.107	0.123	0.158	0.103	0.160	1.06	2.20	0.836	1.36	1.88	97.9	264.0	508.0
400	0.01044	0.114	0.131	0.169	0.111	0.171	1.06	2.20	0.843	1.36	1.88	86.8	233.0	448.0

UNCLASSIFIED

125

UNCLASSIFIED

Table XIX. Results of Jet Penetration and Mixing Calculations for Test 1-13.

Propellant: ARCADENE 168A
 Number of nozzles: 9
 Initial jet Mach no.: 1.0
 Normal injection - no boattail

126

Rocket motor pressure (psia)	Jet mass flow rate (lbm/sec)	Penetration height (in)	Distance (in) to station		Jet diameter (in) at station		Jet Mach no. at station		Jet diameter (in) at $\ell =$			Air/fuel ratio at $\ell =$		
			1	C	1	C	2	C	1	2	3	1	2	3
			200	0.00522	0.0474	1.36	1.39	790.0	0.121	1.04	2.19	0.153	0.673	1.19
250	0.00652	0.0530	1.37	1.40	876.0	0.135	1.06	2.20	0.161	0.681	1.20	1.55	90.8	290.0
300	0.00783	0.0580	1.40	1.43	958.0	0.148	1.06	2.20	0.165	0.685	1.21	87.5	75.9	243.0
350	0.00913	0.0627	1.42	1.46	0.103	0.160	1.06	2.20	0.165	0.686	1.21	25.8	64.7	208.0
400	0.0104	0.0670	1.46	1.49	0.111	0.171	1.06	2.20	0.165	0.685	1.21	0.00	56.0	181.0

UNCLASSIFIED

UNCLASSIFIED

Table XX. Results of Jet Penetration and Mixing Calculations for Test 1-14.

Propellant: ARCADENE 168A
 Number of nozzles: 9
 Initial jet Mach no.: 1.0
 45-degree injection - 15-degree boattail

Rocket motor pressure (psia)	Jet mass flow rate (lbm/sec)	Penetration height (in)	Distance (in) to station		Jet diameter (in) at station		Jet Mach no. at station		Jet diameter (in) at $l =$			Air/fuel ratio at $l =$		
			1	C	1	C	2	C	1	2	3	1	2	3
200	0.00522	0.0737	0.976	1.02	0.107	0.196	1.06	2.47	0.417	0.975	1.53	34.5	232.0	588.0
250	0.00652	0.0824	1.02	1.06	0.120	0.219	1.05	2.47	0.424	0.981	1.54	26.7	186.0	472.0
300	0.00783	0.0903	1.06	1.11	0.132	0.240	1.05	2.46	0.427	0.984	1.54	21.1	154.0	392.0
350	0.00913	0.0975	1.10	1.16	0.143	0.260	1.04	2.46	0.430	0.985	1.54	17.0	131.0	335.0
400	0.0104	0.104	1.15	1.20	0.154	0.279	1.03	2.45	0.431	0.986	1.54	13.8	114.0	292.0

Table XXI. Results of Jet Penetration and Mixing Calculations for Test 1-15.

Propellant: ARCADENE 168A
 Number of nozzles: 9
 Initial jet Mach no.: 1.0
 45-degree injection - 30-degree boattail

128

Rocket motor pressure (psia)	Jet mass flow rate (lbm/sec)	Penetration height (in)	Distance (in) to station		Jet diameter (in) at station		Jet Mach no. at station		Jet diameter (in) at $\ell =$			Air/fuel ratio at $\ell =$		
			1	C	1	C	2	C	1	2	3	1	2	3
200	0.00522	0.136	0.727	0.794	0.170	0.371	1.02	2.73	0.755	1.35	1.95	110.0	431.0	935.0
250	0.00652	0.152	0.783	0.858	0.190	0.416	1.02	2.73	0.777	1.38	1.97	87.6	350.0	757.0
300	0.00782	0.167	0.835	0.917	0.208	0.455	1.02	2.73	0.796	1.39	1.99	72.2	294.0	638.0
350	0.00913	0.180	0.884	0.972	0.225	0.492	1.02	2.73	0.813	1.41	2.00	60.9	254.0	552.0
400	0.0104	0.193	0.930	1.02	0.240	0.525	1.02	2.73	0.828	1.43	2.03	52.2	224.0	487.0

UNCLASSIFIED

UNCLASSIFIED

Table XXII. Results of Jet Penetration and Mixing Calculations for Test 1-16.

Propellant: ARCADENE 168A
 Number of nozzles: 9
 Initial jet Mach no.: 1.0
 45-degree injection - 45-degree boattail

129

Rocket motor pressure (psia)	Jet mass flow rate (lbm/sec)	Penetration height (in)	Distance (in) to station		Jet diameter (in) at station		Jet Mach no.: at station		Jet diameter (in) at $\ell =$			Air/fuel ratio at $\ell =$		
			1	C	1	C	2	C	1	2	3	1	2	3
200	0.00522	0.318	0.218	0.339	0.306	0.863	1.08	3.09	1.49	2.13	2.77	378.0	969.0	1768.0
250	0.00652	0.356	0.232	0.369	0.335	0.959	1.11	3.12	1.58	2.23	2.87	322.0	821.0	1487.0
300	0.00783	0.390	0.244	0.396	0.360	1.04	1.16	3.14	1.66	2.31	2.95	283.0	717.0	1293.0
350	0.00913	0.421	0.254	0.421	0.381	1.12	1.20	3.17	1.73	2.38	3.03	254.0	641.0	1150.0
400	0.0104	0.450	0.264	0.446	0.399	1.19	1.24	3.20	1.80	2.45	3.10	230.0	581.0	1040.0

UNCLASSIFIED

UNCLASSIFIED

Table XXIII. Results of Jet Penetration and Mixing Calculations for Test 1-17.

Propellant: ARCADENE 168A
 Number of nozzles: 9
 Initial jet Mach no.: 2.0
 45-degree injection - no boattail

130

Rocket motor pressure (psia)	Jet mass flow rate (lbm/sec)	Penetration height (in)	Distance (in) to station		Jet diameter (in) at station		Jet Mach no. at station		Jet diameter (in) at $\ell =$			Air/fuel ratio at $\ell =$		
			1	C	1	C	2	C	1	2	3	1	2	3
200	0.00522	0.0563	1.21	1.25	0.0518	1.25	2.13	3.06	0.193	0.830	1.47	7.12	173.0	545.0
250	0.00652	0.0630	1.22	1.26	0.0569	1.26	2.19	3.11	0.198	0.841	1.48	5.69	142.0	445.0
300	0.00782	0.0690	1.24	1.29	0.0621	1.29	2.20	3.12	0.199	0.842	1.49	4.40	118.0	372.0
350	0.00913	0.0745	1.26	1.31	0.0674	1.31	2.19	3.11	0.197	0.839	1.48	3.32	99.9	316.0
400	0.0104	0.0797	1.29	1.34	0.0727	1.34	2.16	3.08	0.193	0.833	1.47	2.43	85.9	273.0

UNCLASSIFIED

UNCLASSIFIED

Table XXIV. Results of Jet Penetration and Mixing Calculations for Test 1-18.

Propellant: ARCADENE 168A
 Number of nozzles: 9
 Initial jet Mach no.: 2.0
 45-degree injection - 15-degree boattail

131

Rocket motor pressure (psia)	Jet mass flow rate (lbm/sec)	Penetration height (in)	Distance (in) to station		Jet diameter (in) at station		Jet Mach no. at station		Jet diameter (in) at $\ell =$			Air/fuel ratio at $\ell =$		
			1	C	1	C	2	C	1	2	3	1	2	3
200	0.00522	0.0877	0.866	0.925	0.0700	0.158	2.17	3.35	0.459	1.12	1.78	47.4	314.0	803.0
250	0.00652	0.0980	0.900	0.965	0.0797	0.178	2.11	3.30	0.461	1.12	1.78	36.8	248.0	636.0
300	0.00783	0.107	0.936	1.00	0.0891	0.198	2.05	3.24	0.462	1.11	1.77	29.5	204.0	523.0
350	0.00913	0.116	0.972	1.05	0.0982	0.217	1.98	3.18	0.461	1.11	1.76	24.1	172.0	442.0
400	0.0104	0.124	1.00	1.09	0.107	0.235	1.93	3.13	0.461	1.10	1.75	20.0	148.0	382.0

UNCLASSIFIED

UNCLASSIFIED

Table XXV. Results of Jet Penetration and Mixing Calculations for Test 1-19.

Propellant: ARCADENE 168A
 Number of nozzles: 9
 Initial jet Mach no.: 2.0
 45-degree injection - 30-degree boattail

Rocket motor pressure (psia)	Jet mass flow rate (lbm/sec)	Penetration height (in)	Distance (in) to station		Jet diameter (in) at station		Jet Mach no. at station		Jet diameter (in) at $\ell =$			Air/fuel ratio at $\ell =$		
			1	C	1	C	2	C	1	2	3	1	2	3
			200	0.00522	0.162	0.646	0.737	0.121	0.321	1.84	3.34	0.767	1.43	2.09
250	0.00652	0.181	0.695	0.792	0.193	0.365	1.75	3.26	0.786	1.44	2.10	98.5	395.0	867.0
300	0.00783	0.199	0.740	0.844	0.156	0.406	1.68	3.20	0.804	1.45	2.10	81.6	331.0	723.0
350	0.00913	0.215	0.782	0.892	0.172	0.442	1.63	3.16	0.820	1.47	2.11	69.3	284.0	621.0
400	0.0104	0.229	0.822	0.938	0.187	0.477	1.59	3.13	0.835	1.48	2.12	59.8	249.0	544.0

UNCLASSIFIED

132

UNCLASSIFIED

Table XXVI. Results of Jet Penetration and Mixing Calculations for Test 1-20.

Propellant: ARCADENE 168A
 Number of nozzles: 9
 Initial jet Mach no.: 2.0
 45-degree injection - 45-degree boattail

Rocket motor pressure (psia)	Jet mass flow rate (lbm/sec)	Penetration height (in)	Distance (in) to station		Jet diameter (in) at station		Jet Mach no. at station		Jet diameter (in) at $\ell =$			Air/fuel ratio at $\ell =$		
			1	C	1	C	2	C	1	2	3	1	2	3
			200	0.00522	0.378	0.220	0.367	0.255	0.810	1.48	3.37	1.45	2.12	2.78
250	0.00652	0.423	0.233	0.400	0.287	0.908	1.46	3.35	1.54	2.20	2.87	316.0	820.0	1503.0
300	0.00783	0.463	0.245	0.424	0.315	0.995	1.46	3.35	1.62	2.28	2.94	277.0	715.0	1301.0
350	0.00913	0.500	0.256	0.450	0.339	1.07	1.47	3.36	1.69	2.35	3.01	248.0	637.0	1154.0
400	0.0104	0.535	0.266	0.475	0.360	1.14	1.48	3.37	1.75	2.42	3.08	225.0	577.0	1040.0

UNCLASSIFIED

133

UNCLASSIFIED

Table XXVII. Results of Jet Penetration and Mixing Calculations for Test 1-21.

Propellant: ARCADENE 168A
 Number of nozzles: 5
 Initial jet Mach no.: 1.0
 45-degree injection - no boattail

134

Rocket motor pressure (psia)	Jet mass flow rate (lbm/sec)	Penetration height (in)	Distance (in) to station		Jet diameter (in) at station		Jet Mach no. at station		Jet diameter (in) at $\ell =$			Air/fuel ratio at $\ell =$		
			1	C	1	C	2	C	1	2	3	1	2	3
200	0.00940	0.0636	1.37	1.40	0.106	0.163	1.04	2.19	0.188	0.709	1.23	1.26	67.2	210.0
250	0.0117	0.0711	1.38	1.42	0.118	0.182	1.06	2.20	0.200	0.721	1.24	0.817	55.0	170.0
300	0.0140	0.0778	1.41	1.45	0.128	0.199	1.06	2.20	0.208	0.728	1.25	0.350	4.62	143.0
350	0.0164	0.0840	1.43	1.48	0.139	0.215	1.06	2.20	0.212	0.733	1.26	0.00	39.6	123.0
400	0.0188	0.0899	1.47	1.52	0.149	0.230	1.06	2.20	0.215	0.735	1.26	0.00	34.5	108.0

UNCLASSIFIED

UNCLASSIFIED

Table XXVIII. Results of Jet Penetration and Mixing Calculations for Test 1-22.

Propellant: ARCADENE 168A
 Number of nozzles: 5
 Initial jet Mach no.: 1.0
 45-degree injection - 15-degree boattail

135

Rocket motor pressure (psia)	Jet mass flow rate (lbm/sec)	Penetration height (in)	Distance (in) to station		Jet diameter (in) at station		Jet Mach no. at station		Jet diameter (in) at $l =$			Air/fuel ratio at $l =$		
			1	C	1	C	2	C	1	2	3	1	2	3
			200	0.00940	0.0989	0.990	1.05	0.144	0.263	1.06	1.05	0.474	1.03	1.59
250	0.0117	0.110	1.03	2.47	0.161	0.295	1.05	1.09	0.487	1.04	1.60	17.0	113.0	280.0
300	0.0141	0.121	1.08	2.46	0.177	0.323	1.05	2.46	0.498	1.05	1.61	13.5	94.8	234.0
350	0.0164	0.131	1.12	2.46	0.192	0.349	1.04	2.46	0.506	1.06	1.62	10.8	81.1	201.0
400	0.0188	0.140	1.16	2.45	0.206	0.374	1.03	2.45	0.513	1.07	1.62	8.70	70.6	176.0

UNCLASSIFIED

UNCLASSIFIED

Table XXIX. Results of Jet Penetration and Mixing Calculations for Test 1-23.

Propellant: ARCADENE 168A
 Number of nozzles: 5
 Initial jet Mach no.: 1.0
 45-degree injection - 30-degree boattail

Rocket motor pressure (psia)	Jet mass flow rate (lbm/sec)	Penetration height (in)	Distance (in) to station		Jet diameter (in) at station		Jet Mach no. at station		Jet diameter (in) at $l =$			Air/fuel ratio at $l =$		
			1	C	1	C	2	C	1	2	3	1	2	3
200	0.00940	0.183	0.757	0.846	0.227	0.498	1.02	2.73	0.864	1.46	2.06	70.3	267.0	565.0
250	0.0117	0.205	0.814	0.914	0.255	0.558	1.02	2.73	0.899	1.50	2.10	56.2	218.0	461.0
300	0.0141	0.224	0.868	0.977	0.280	0.611	1.02	2.73	0.930	1.53	2.13	46.3	185.0	391.0
350	0.0164	0.242	0.918	1.04	0.302	0.660	1.02	2.73	0.958	1.56	2.16	39.0	160.0	340.0
400	0.0188	0.259	0.965	1.09	0.322	0.705	1.02	2.73	0.984	1.58	2.18	33.3	142.0	301.0

Table XXX. Results of Jet Penetration and Mixing Calculations for Test 1-24.

Propellant: ARCADENE 168A
 Number of nozzles: 5
 Initial jet Mach no.: 1.0
 45-degree injection - 45-degree boattail

137

Rocket motor pressure (psia)	Jet mass flow rate (lbm/sec)	Penetration height (in)	Distance (in) to station		Jet diameter (in) at station		Jet Mach no. at station		Jet diameter (in) at $l =$			Air/fuel ratio at $l =$		
			1	C	1	C	2	C	1	2	3	1	2	3
200	0.00940	0.427	0.292	0.455	0.410	1.16	1.08	3.09	1.75	2.39	3.03	244.0	620.0	1110.0
250	0.0117	0.477	0.311	0.495	0.450	1.29	1.11	3.12	1.87	2.51	3.16	209.0	527.0	939.0
300	0.0141	0.523	0.327	0.531	0.482	1.40	1.16	3.14	1.98	2.62	3.27	183.0	463.0	820.0
350	0.0164	0.565	0.341	0.566	0.511	1.50	1.20	3.17	2.07	2.72	3.37	164.0	414.0	732.0
400	0.0188	0.604	0.354	0.599	0.535	1.60	1.24	3.20	2.16	2.81	3.46	148.0	376.0	663.0

UNCLASSIFIED

UNCLASSIFIED

Table XXXI. Results of Jet Penetration and Mixing Calculations for Test 1-25.

Propellant: ARCADENE 168A
 Number of nozzles: 5
 Initial jet Mach no.: 2.0
 45-degree injection - no boattail

Rocket motor pressure (psia)	Jet mass flow rate (lbm/sec)	Penetration height (in)	Distance (in) to station		Jet diameter (in) at station		Jet Mach no. at station		Jet diameter (in) at $\ell =$			Air/fuel ratio at $\ell =$		
			1	C	1	C	2	C	1	2	3	1	2	3
			200	0.00940	0.0756	1.22	1.27	0.0695	0.129	2.13	3.06	0.216	0.854	1.49
250	0.0117	0.0845	1.23	1.29	0.0763	0.143	2.19	3.11	0.224	0.866	1.51	3.37	82.5	255.0
300	0.0141	0.0926	1.25	3.12	0.0834	0.156	2.20	3.12	0.227	0.870	1.51	2.56	69.0	213.0
350	0.0164	0.100	1.27	3.11	0.0905	0.169	2.19	3.11	0.228	0.870	1.51	1.88	58.7	182.0
400	0.0188	0.107	1.30	3.08	0.0975	0.182	2.16	3.08	0.227	0.867	1.51	1.31	50.7	158.0

UNCLASSIFIED

138

UNCLASSIFIED

Table XXXII. Results of Jet Penetration and Mixing Calculations for Test 1-26.

Propellant: ARCADENE 168A
 Number of nozzles: 5
 Initial jet Mach no.: 2.0
 45-degree injection - 15-degree boattail

139	Rocket motor pressure (psia)	Jet mass flow rate (lbm/sec)	Penetration height (in)	Distance (in) to station		Jet diameter (in) at station		Jet Mach no. at station		Jet diameter (in) at $l =$			Air/fuel ratio at $l =$		
				1	C	1	C	2	C	1	2	3	1	2	3
				200	0.00940	0.118	0.881	0.960	0.0939	0.211	2.17	3.35	0.492	1.16	1.82
250	0.0117	0.132	0.916	1.00	0.107	0.239	2.11	3.30	0.506	1.16	1.82	22.5	147.0	369.0	
300	0.0141	0.144	0.923	1.05	0.120	0.266	2.05	3.24	0.512	1.17	1.82	18.0	121.0	305.0	
350	0.0161	0.156	0.989	1.09	0.132	0.291	1.98	3.18	0.517	1.17	1.81	14.8	103.0	259.0	
400	0.0188	0.166	1.03	1.13	0.144	0.315	1.93	3.13	0.522	1.17	1.81	12.3	89.0	224.0	

UNCLASSIFIED

UNCLASSIFIED

Table XXXIII. Results of Jet Penetration and Mixing Calculations for Test 1-27.

Propellant: ARCADENE 168A
 Number of nozzles: 5
 Initial jet Mach no.: 2.0
 45-degree injection - 30-degree boattail

L40	Rocket motor pressure (psia)	Jet mass flow rate (lbm/sec)	Penetration height (in)	Distance (in) to station		Jet diameter (in) at station		Jet Mach no. at station		Jet diameter (in) at $\ell =$			Air/fuel ratio at $\ell =$		
				1	C	1	C	2	C	1	2	3	1	2	3
200	0.00940	0.218	0.676	0.798	0.162	0.431	1.84	3.34	0.853	1.51	2.17	76.6	298.0	642.0	
250	0.0117	0.243	0.726	0.857	0.187	0.490	1.75	3.26	0.886	1.54	2.20	61.5	241.0	518.0	
300	0.0141	0.267	0.773	0.912	0.210	0.544	1.68	3.20	0.916	1.57	2.22	51.1	203.0	435.0	
350	0.0164	0.288	0.816	0.964	0.231	0.594	1.63	3.16	0.944	1.59	2.24	43.5	176.0	376.0	
400	0.0188	0.308	0.858	1.01	0.250	0.640	1.59	3.13	0.970	1.61	2.56	37.5	155.0	331.0	

UNCLASSIFIED

UNCLASSIFIED

Table XXXIV. Results of Jet Penetration and Mixing Calculations for Test 1-28.

Propellant: ARCADENE 168A
 Number of nozzles: 5
 Initial jet Mach no.: 2.0
 45-degree injection - 45-degree boattail

Rocket motor pressure (psia)	Jet mass flow rate (lbm/sec)	Penetration height (in)	Distance (in) to station		Jet diameter (in) at station		Jet Mach no. at station		Jet diameter (in) at $l =$			Air/fuel ratio at $l =$		
			1	C	1	C	2	C	1	2	3	1	2	3
			200	0.00940	0.508	0.295	0.493	0.342	1.09	1.48	3.37	1.69	2.35	3.02
250	0.0117	0.568	0.313	0.533	0.385	1.22	1.46	3.35	1.81	2.47	3.13	202.0	522.0	941.0
300	0.0141	0.622	0.329	0.569	0.423	1.34	1.46	3.35	1.91	2.58	3.24	117.0	457.0	819.0
350	0.0164	0.672	0.344	0.604	0.455	1.44	1.47	3.36	2.01	2.67	3.33	158.0	408.0	729.0
400	0.0188	0.718	0.357	0.637	0.484	1.54	1.48	3.37	2.09	2.76	3.42	143.0	370.0	660.0

UNCLASSIFIED

141

UNCLASSIFIED

UNCLASSIFIED

(C) APPENDIX II

ANALYTICAL EFFORT CONDUCTED BY ROCKETDYNE DIVISION NORTH AMERICAN ROCKWELL CORPORATION (U)

1. INTRODUCTION

(U) In support of the experimental effort that constituted the major part of this program, Rocketdyne Division of North American Rockwell Corporation conducted an analysis of four of the tests conducted in the Atlantic Research-Navy program.^(3,4) The method of analysis and the results are described below.

2. ANALYTICAL APPROACH

(U) The primary tool was a method of characteristics and base pressure computer program with heat addition described in detail in Reference (20). Figure 66 illustrates how the computer program is used to arrive at a theoretical base pressure.

(U) Shown in Figure 67 are the inputs required for the Method of Characteristics and Base Pressure with Heat Addition Computer Program which for brevity will be referred to as the MOC/BP program. Heat release occurs in Zone I which is bounded by an outer and inner jet boundary. Zone II is comprised of the disturbed or deflected free-stream air between the outer jet boundary and the interaction shock. Undisturbed free-stream air occupies Zone III.

(U) The method of Billig, Orth and Lasky as given in Appendix I is used to provide many of the required inputs. The distance from the injector to the input line is the distance x_c as defined in Appendix I. From Billig's analysis, the jet expands to a pressure equal to ambient at Station (C). (This assumption was modified for the case with burning upstream of Station (C).)

(U) The Mach number and flow area at Station (C) are calculated from Equations (5) and (6), respectively, in Appendix I. The height to the center of the Mach disk, Y_1 , in Figure 67 is calculated from Equation (1) and then multiplied by the square root of the discharge coefficient, defined as the ratio of the mass flow rate reported in Reference (3) to the mass flow rate calculated using the isentropic flow equations. This was done to give close agreement with Cohen's results in Reference (8). In the theoretical mass flow calculations, the chamber pressure is taken to be equal to the static pressure in the primary rocket motor.

(U) The flow area at Station (C) is assumed to be circular in cross section and normal to the body. The height of Point B in Figure 67 is Y_1 plus the radius of the jet at Station (C). The flow angle, θ , from Point A to Point B is assumed to be zero. The Mach number is assumed constant from A to B and equal to M . The input line Zone I stagnation temperature is the propellant equilibrium flame temperature in the rocket chamber. The dimensionless entropy in Zone I is zero. The Zone I gamma, molecular weight, and heat release are given by equilibrium combustion calculations.

(U) The shock shape shown in Figure 67 is calculated using the method given in Reference (21). The equivalence of secondary injection to a blunt body in supersonic flow gives rise to an equivalent body nose radius.

$$r = \left(\frac{4}{\pi C_D} \right)^{1/2} \left(1 + \frac{\Delta h}{V^2} \right)^{1/2} \left(\frac{\dot{m}_j}{\rho V} \right)^{1/2} \quad (12)$$

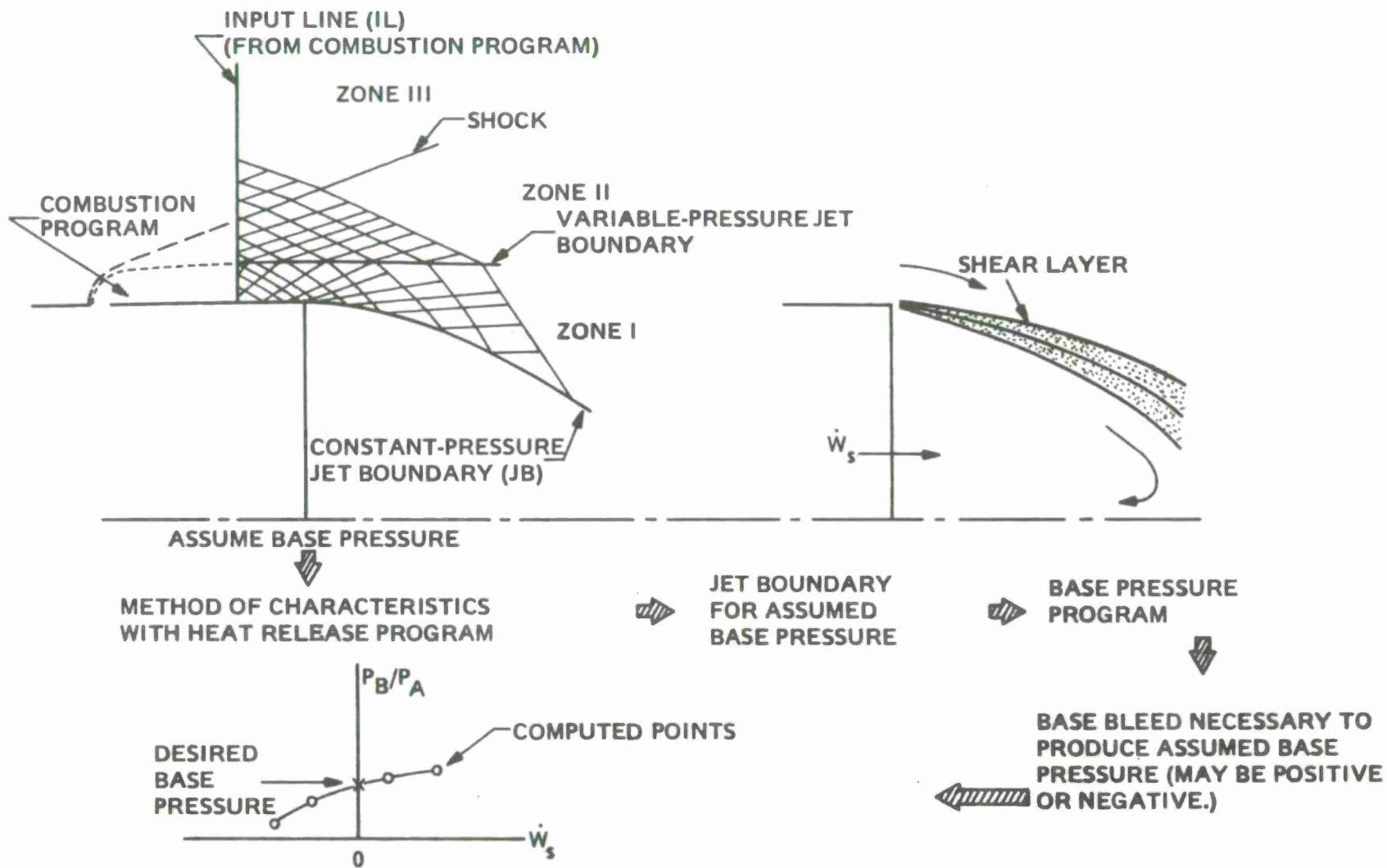


Figure 66. Overall Computer Program Flow Chart.

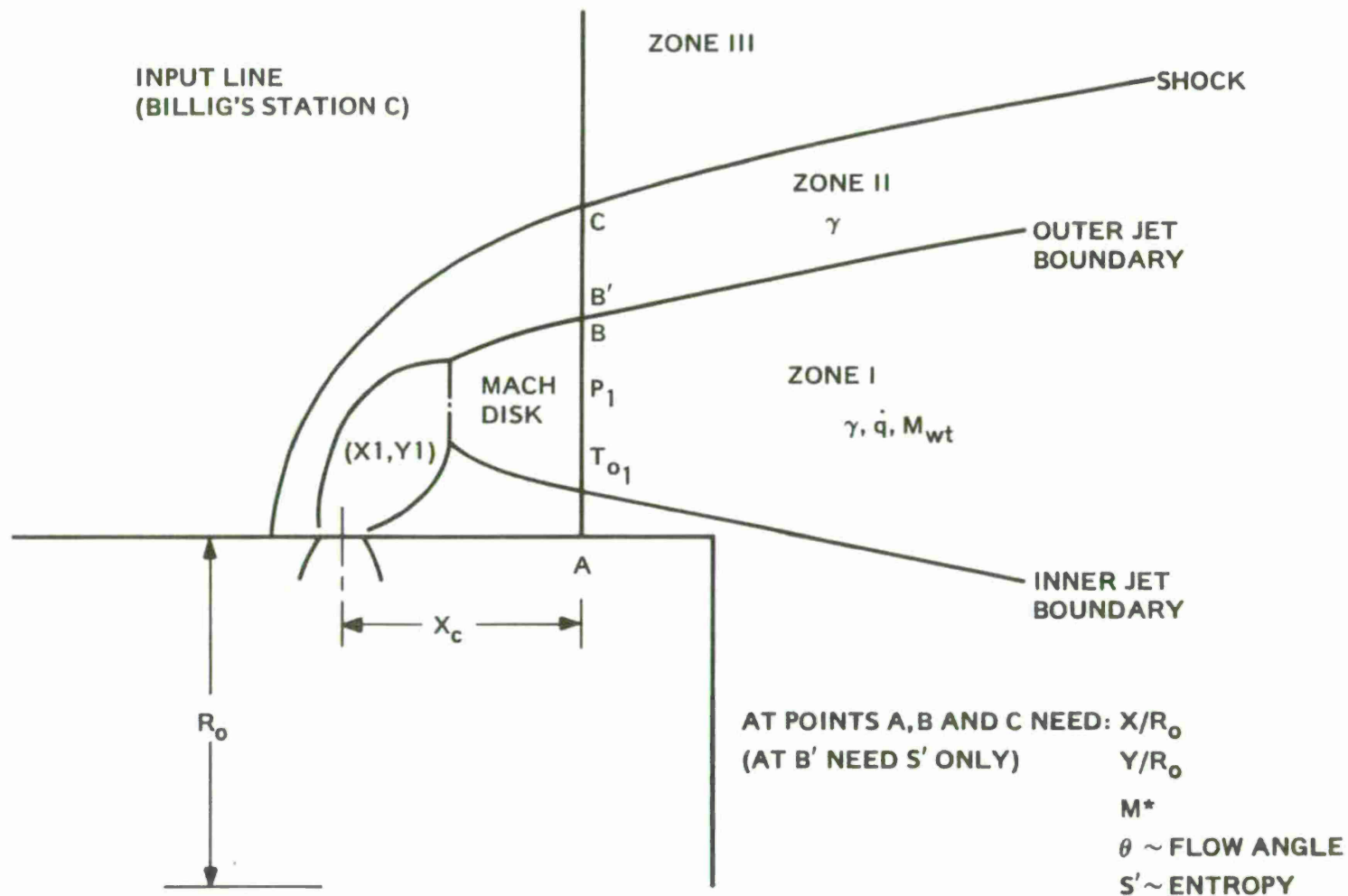


Figure 67. Inputs Needed for Method of Characteristics and Base Pressure with Heat Addition Computer Program.

UNCLASSIFIED

where:

C_D = drag coefficient (nominal = 0.94)

Δh = energy release from injectant to primary flow (assumed zero at the present time)

\dot{m}_i = injectant flow rate

ρ = free-stream density

V = free-stream velocity

The coordinate system used in the shock shape analysis is depicted in Figure 68.

(U) The shock shape itself is calculated using a second-order solution of the cylindrical blast wave:

$$\frac{R_{\pi}}{r} = \left(\frac{\gamma C_D}{J} \right)^{1/4} \left[1 - \lambda \left(\frac{J}{\gamma C_D} \right)^{1/2} \frac{1}{M_o^2} \frac{x}{r} \right]^{1/2} \left(\frac{x}{r} \right)^{1/2} \quad (13)$$

where:

M_o = free stream Mach number

x = distance from shock vertex

r = equivalent body radius defined by Equation (12)

$J = 0.88$ for $\gamma = 1.4$

$\lambda = -1.989$ for $\gamma = 1.4$

} constants from blast wave analysis

The shock stand-off distance Δ is obtained from the following equation found in Reference (22):

$$\frac{\Delta}{r} = 0.143 \exp(3.24/M_o^2) \quad (14)$$

The distance from the shock vertex to the injector center is thus $\Delta + r$.

(U) The shock calculations are done in G.E. timesharing computer program SHOCK2. In addition to obtaining the shock coordinates, the program also calculates the shock angle at each point. The slope at a point is the average of two line segments comprised of the point in question and the previous point and the next succeeding point. Standard oblique shock equations are used to find pressure ratios across the shock, flow deflections, and downstream Mach numbers.

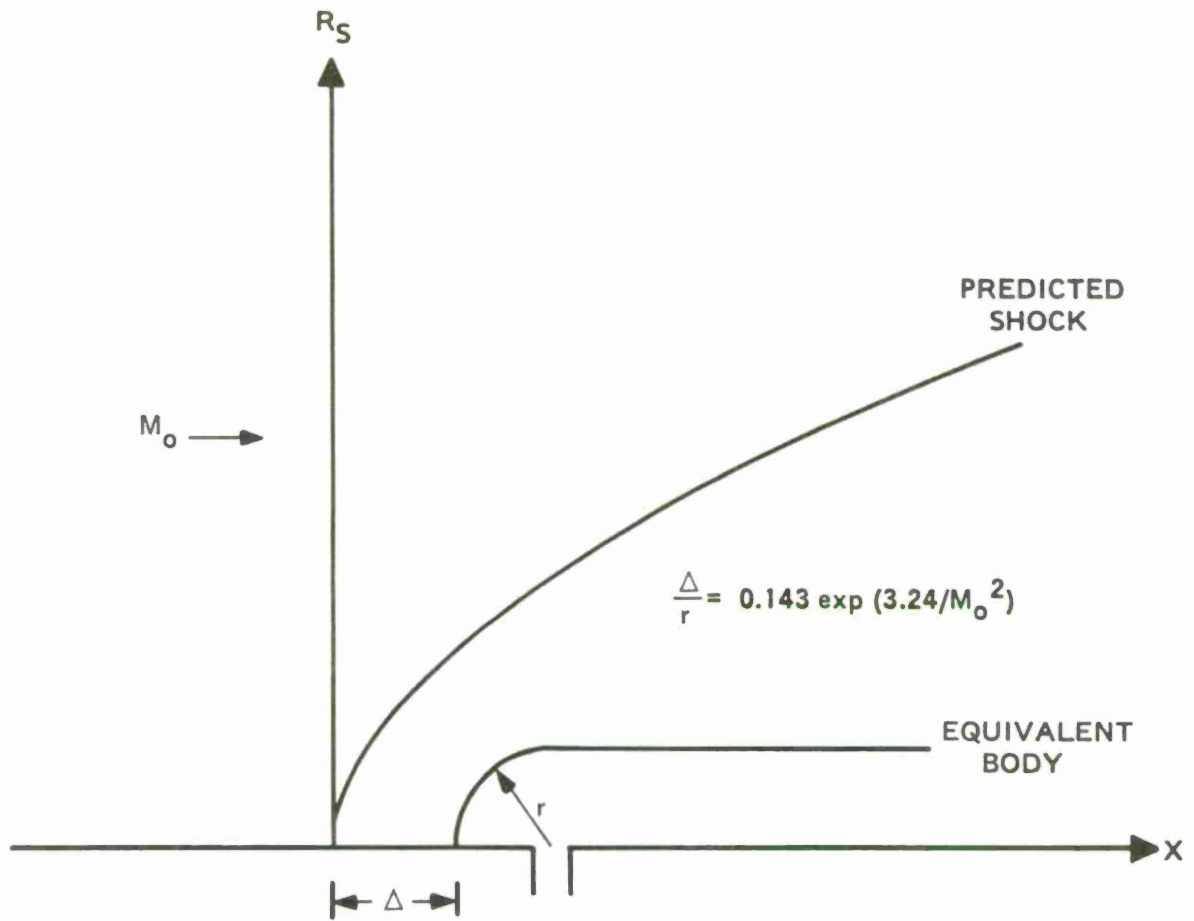


Figure 68. Coordinate System for Shock Shape Analysis.

UNCLASSIFIED

(U) The location of the input line (X_c) is input to SHOCK2 which then interpolates to get the shock location (Point C in Figure 67) and shock angle. Flow angle, downstream M^* , and s' are then calculated. The s' at the Zone II jet boundary point (Point B' in Figure 67) is taken to be that which occurs at a shock point equal to the height of the center of the Mach disk. In other words, the Zone II streamline at B' is assumed to originate at a point on the shock equal to the Mach disk center height.

(U) The Billig model for the flow field near the injector has the critical assumption that the jet expands to ambient pressure at Station (C). The base pressure computer program was run using inputs from the Billig model. The results showed that the heat addition required to increase the wall pressure from ambient at Station (C) to the measured lip pressure yields base pressures substantially higher than those measured by in the Atlantic Research Navy tests (Reference 3). The assumption that there is no heat addition upstream of Station (C) therefore appears to be invalid. Consequently, the Billig approach was modified to account for heat addition upstream of Station (C). A slight pressure rise and a corresponding decrease in Mach number is accomplished by adding a small amount of heat at constant area and with no mass addition.

(U) The conservation equations are:

Mass

$$\dot{m}_1 = \dot{m}_2 \quad (15)$$

Momentum

$$\dot{m}_1 U_1 + P_1 A = \dot{m}_2 U_2 + P_2 A \quad (16)$$

Energy

$$C_p T_1 + \frac{U_1^2}{2} + \Delta H = C_p T_2 + \frac{U_2^2}{2} \quad (17)$$

where

ΔH = heat addition (Btu/lbm)

(U) The subscript 1 corresponds to conditions at Station (C) in Billig's model, before heat addition. Therefore, \dot{m} is the fuel flow rate, P_1 is ambient pressure and T_1 can be calculated knowing M_c , T_o and γ_j . The area, then, is given by

$$A = \frac{\dot{m}_1 R_1 T_1}{P_1 U_1} \quad (18)$$

The subscript 2 refers to conditions at Station (C) after heat has been added. The only unknown is the amount of heat addition.

UNCLASSIFIED

(U) Several iterative-type computer runs were made to determine the amount of heat released upstream of Station (C). For the test condition with ARCADENE 168A, a heat release value of 200 Btu/lbm was selected. For ARCADENE 129A, the value was 100 Btu/lbm.

(U) The heat release upstream of Station (C) has the effect of increasing the pressure and decreasing the Mach number from those values at Station C predicted by Billig's theory. For example, in Test 106 of Reference (3) with ARCADENE 168A, the heat addition resulted in a pressure increase from 8.89 psia (ambient) to 10.71 psia and a Mach number decrease from 1.96 to 1.74 at Station (C).

(U) After the inputs for the MOC/BP program have been determined, a series of computer runs are made to determine the value of a dimensionless heat release parameter, \dot{q}' , which gives a base pressure equal to the wind tunnel result. Ideally, only three computer runs are required and result in a plot such as that shown in Figure 69.

(U) The quantity \dot{W}_s is the nondimensional secondary flow through the base (base bleed). If the guess on \dot{q}' is too high, \dot{W}_s is negative and indicates suction. If it is too low, a positive base bleed is required to yield the desired base pressure. For external burning considerations, zero base bleed yields the desired \dot{q}' .

(U) For the cases considered, the desired \dot{q}' results in a situation whereby recompression cannot be achieved with supersonic calculations. The high heat release rate drives the stream to low supersonic Mach numbers. The angle through which the flow is required to turn is too high for isentropic or oblique shock considerations.

(U) A solution, however, is obtained by extrapolation. Base pressures are obtained for several lower values of \dot{q}' . The \dot{q}' required to yield the desired base pressure is extrapolated as shown in Figure 70. The computer program is run again with the extrapolated \dot{q}' . The jet boundaries are obtained but the recompression details are lost due to the above mentioned problems.

(U) The end result of matching the analytically determined base pressure with the experimental value is determination of the combustion length, L_c . The quantity L_c is buried within the nondimensional \dot{q}' ,

$$\dot{q}' = \left[\frac{\gamma+1}{2(\gamma-1)} \right]^{1/2} \frac{R_0}{(h_{01})} 3/2 \dot{q} K \quad (19)$$

where

γ = ratio of specific heats in the combustion zone

R_0 = base radius, inches

\dot{q} = heat release rate, Btu/(lbm-sec)

h_{01} = stagnation enthalpy on the input line, Btu/lbm

K = dimensional constant = 0.0005268

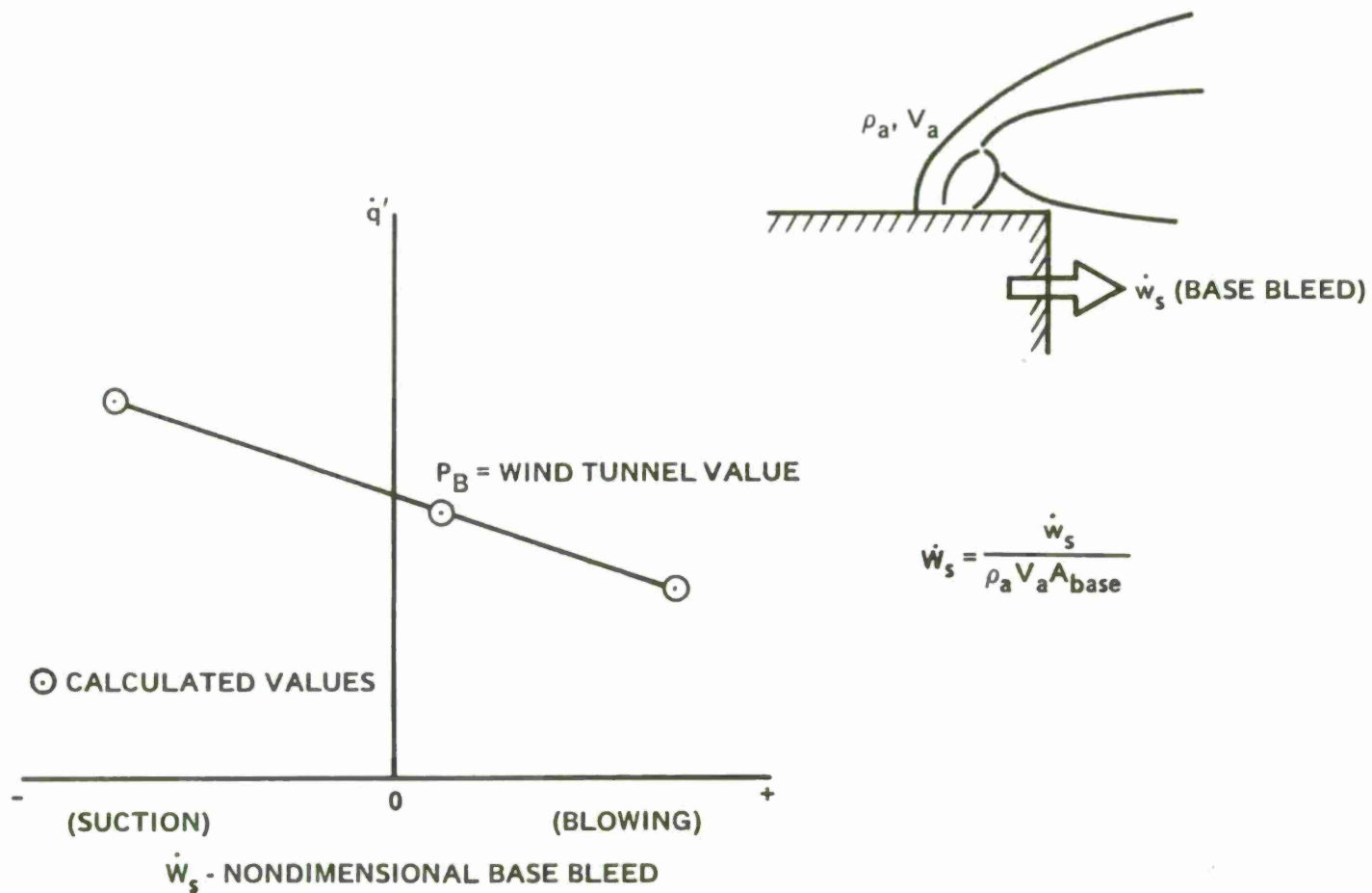


Figure 69. Ideal Method to Determine \dot{q}' for a Given Wind Tunnel Value of P_B .

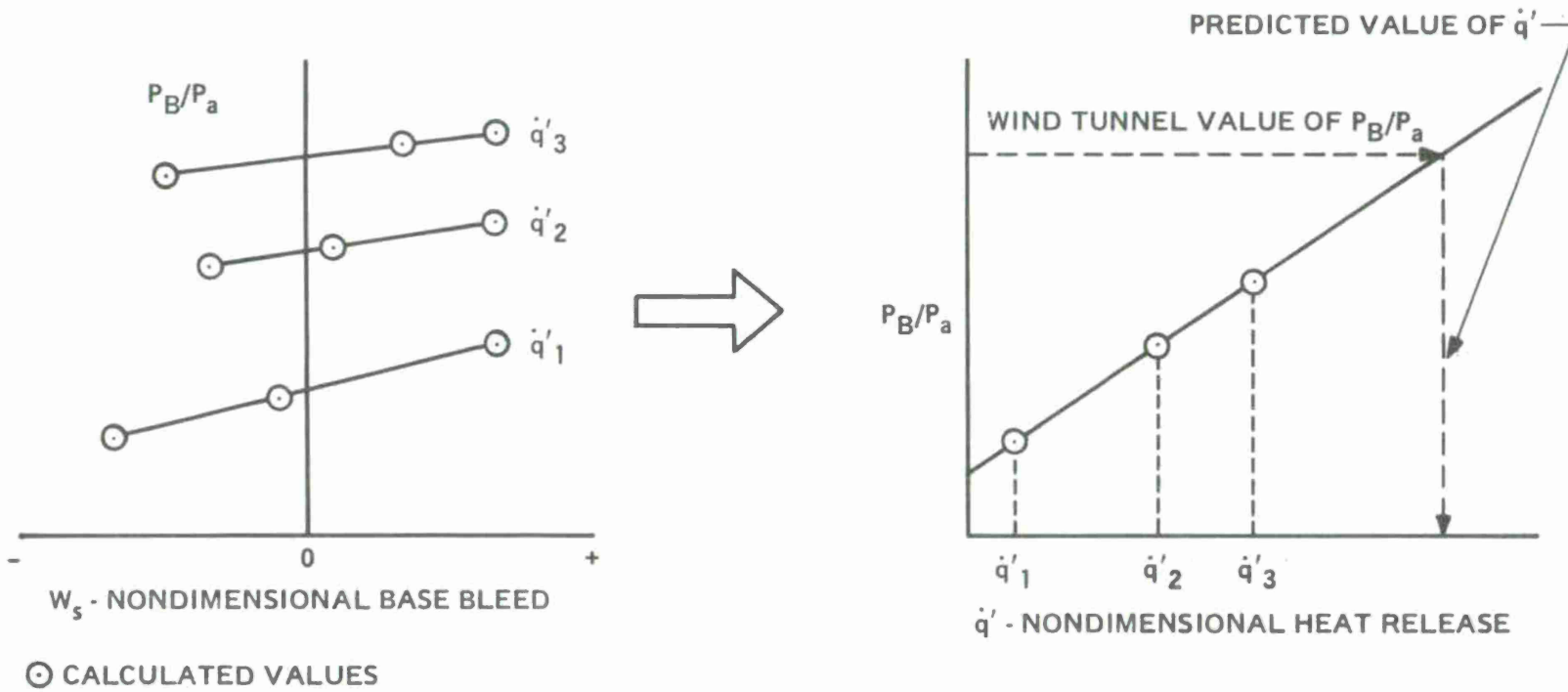


Figure 70. Actual Method used to Obtain \dot{q}' Required to Match Experimental Base Pressure.

(U) The value of q is obtained in the following way,

$$\dot{q} = \frac{\Delta h V}{L_c} \quad \frac{\text{Btu}}{\text{lbm, sec}}$$

where

V = average velocity in the burning region, ft/sec

Δh = total heat release in the burning region, Btu/lbm

(C) The stoichiometric⁵ heat release for ARCADENE 168A was computed to be 386.1 kcal/100 gm. The heat release prior to the mixing with air is 107.7 kcal/100 gm (Reference (3)). The heat release due to mixing with air is the difference or 278.4 kcal/100 gm. With 3.086 pounds of mixture per pound of fuel (M.R. = 2.086), the converted value becomes 1,624 Btu/lb_{mix}. The heat release used in the q' calculation is 1,424 Btu/lb_{mix} (the 200 Btu/lb_{mix} having been released upstream of the input line). The combustion length, L_c , can be calculated from

$$q' = \left[\frac{\gamma + 1}{2(\gamma - 1)} \right]^{1/2} \frac{R_o}{(h_{o1})^{3/2}} \dot{q} K \quad (20)$$

(C) For example, for Test 106

$$\dot{q} = \Delta h V / L_c \quad (21)$$

$$R_o = 2.5 \text{ inches}$$

$$K = 0.0005268$$

$$\gamma = 1.3$$

$$T_{o1} = 6958^\circ R$$

$$C_p = 0.40 \text{ Btu/lb}^\circ R$$

$$h_{o1} = C_p T_{o1} = 2,783 \text{ Btu/lbm}$$

$$\Delta h = 1,424 \text{ Btu/lb}_{\text{mix}}$$

$$V = 5,312 \text{ ft/sec}$$

Equations (20) and (21) then give $L_c = 3.9$ inches.

⁵Stoichiometric to HCl, CO₂, H₂O, and Al₂O₃(ℓ)

~~CONFIDENTIAL~~

(THIS PAGE IS UNCLASSIFIED)

3. RESULTS AND DISCUSSION

(U) The results of Tests 104, 106, 108, and 110 of References (3) and (4) were analyzed. Computer inputs for each of these tests are given in Table XXXV, and Table XXXVI contains theoretical results and comparisons of predicted and actual lip pressures. Figures 71 through 74 show: (1) the predicted jet diameters at the lip, and (2) the shock and inner and outer jet boundaries as calculated by the MOC/BP program.

(U) As shown in Figures 71 through 74, tests with a wide range of injector spacings were investigated. It is assumed in the analysis that the jets are fully merged; i.e., axisymmetric flow is assumed downstream of the MOC/BP input line. The jet spreading calculations indicate that the jets did not merge, especially in Test 108 (Figure 73). This situation results in a "vented" base flow region and requires a three-dimensional solution. Therefore, the poor comparison of theory and experiment for Test 108 (Table XXXVI) is not surprising.

(U) It should also be pointed out that two key inputs to the computer program were \dot{q}' and the amount of heat input between the injectors and Station (C). These quantities were obtained empirically for a given fuel using the test results for the lip pressure and the base pressure. Experimental data such as Schlieren or shadowgraph photos showing jet penetration and jet boundary shapes would be very helpful in determining these quantities. Flow properties in the recompression region would be extremely useful in determining whether the flow remains supersonic in this region. It is quite conceivable that other combinations of \dot{q}' and the heat released upstream of Station (C) can be found to match the lip pressure and base pressure. These other combinations might result in supersonic flow through the recompression region. For example, a high pressure and low Mach number at Station (C) might yield lower \dot{q}' values and result in supersonic recompression. The lip pressure and base pressure only are not enough data to resolve this question.

~~CONFIDENTIAL~~

(THIS PAGE IS UNCLASSIFIED)

Table XXXV. (C) Computer Inputs (U).

Test no.	Fuel ARCADENE	h	P_a	P_c	M_c	P_B	γ	L_{inj}
104	129A	1.04	8.62	9.87	1.80	11.1	1.24	1.50
106	168A	0.67	8.89	10.71	1.74	9.92	1.30	1.50
108	168A	0.69	8.56	10.32	2.07	9.0	1.30	0.59
110	168A	0.52	8.96	10.85	1.72	10.65	1.30	1.00

h = penetration height at Station C, inches

P_a = ambient air pressure

P_c = static pressure at Station C after heat addition, psia

M_c = Mach number at Station C after heat addition

P_B = measured base pressure

L_{inj} = distance from injector to base, inches

Table XXXVI. (C) Computer Results (U).

Test no.	P_B	P_{L_m}	P_{L_p}	\dot{q}	L_c	L_{inj}
104	11.1	12.8	13.0	1.77	3.4	1.50
106	9.92	13.2	12.2	2.33	3.9	1.50
108	9.00	14.8	10.5	2.05	5.0	0.59
110	10.65	14.2	13.8	2.72	3.3	1.00

P_B = measured base pressure, psia

P_{L_m} = measured lip pressure, psia

P_{L_p} = predicted lip pressure, psia

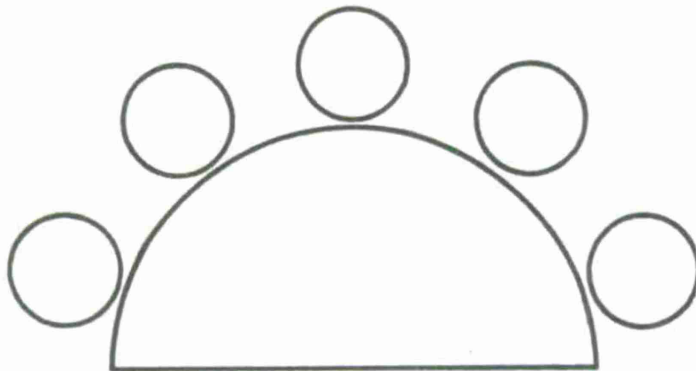
\dot{q} = heat release rate, Btu/lb_{mix} sec, $\times 10^7$

L_c = combustion length, inches

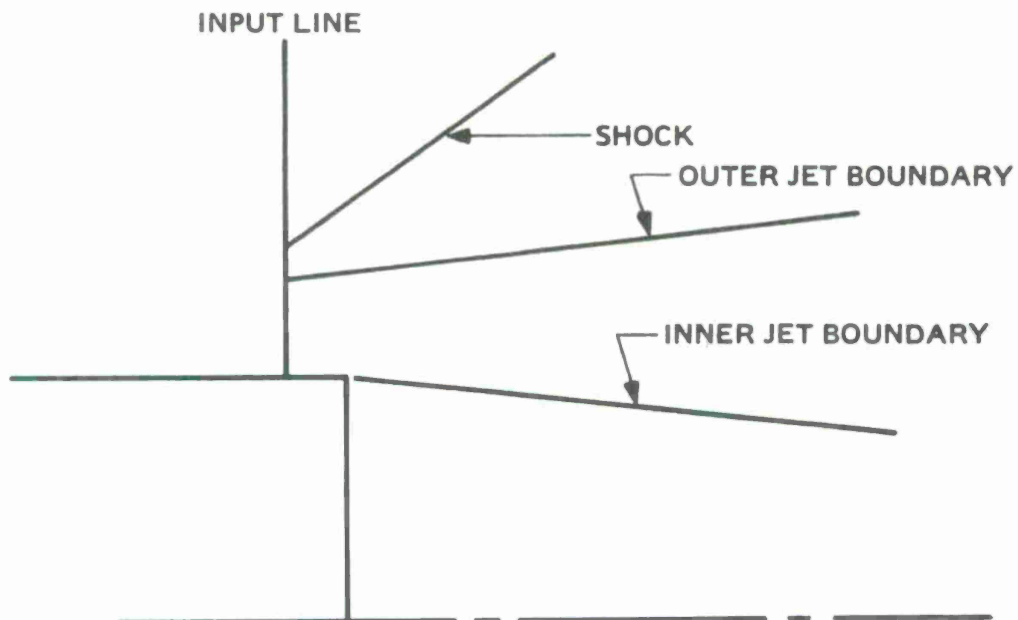
L_{inj} = distance from injector to base, inches

CONFIDENTIAL

(THIS PAGE IS UNCLASSIFIED)



a. Predicted Jet Diameters at Model Lip, Test 104
(Drawn Half Scale).

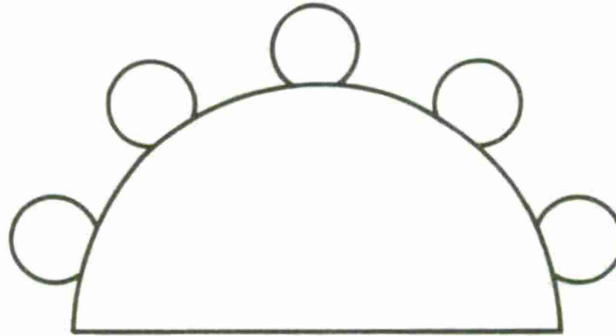


b. Predicted Shock Shape and Jet Boundaries, Test 104.

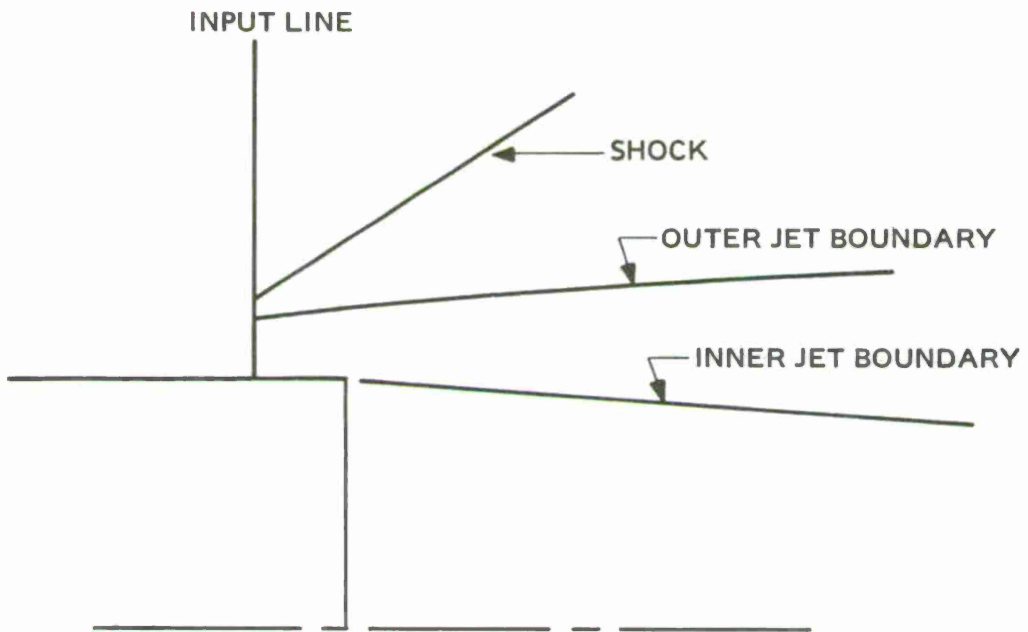
Figure 71. Predictions for Test 104.

CONFIDENTIAL

(THIS PAGE IS UNCLASSIFIED)

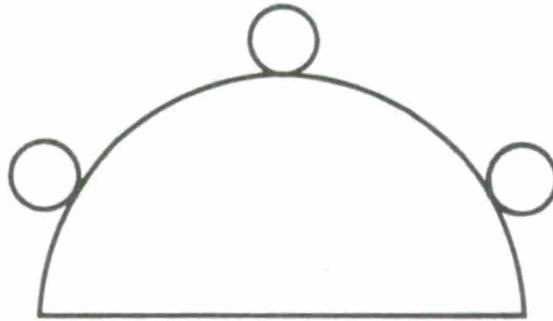


a. Predicted Jet Diameters at Model Lip, Test 106
(Drawn Half Scale).

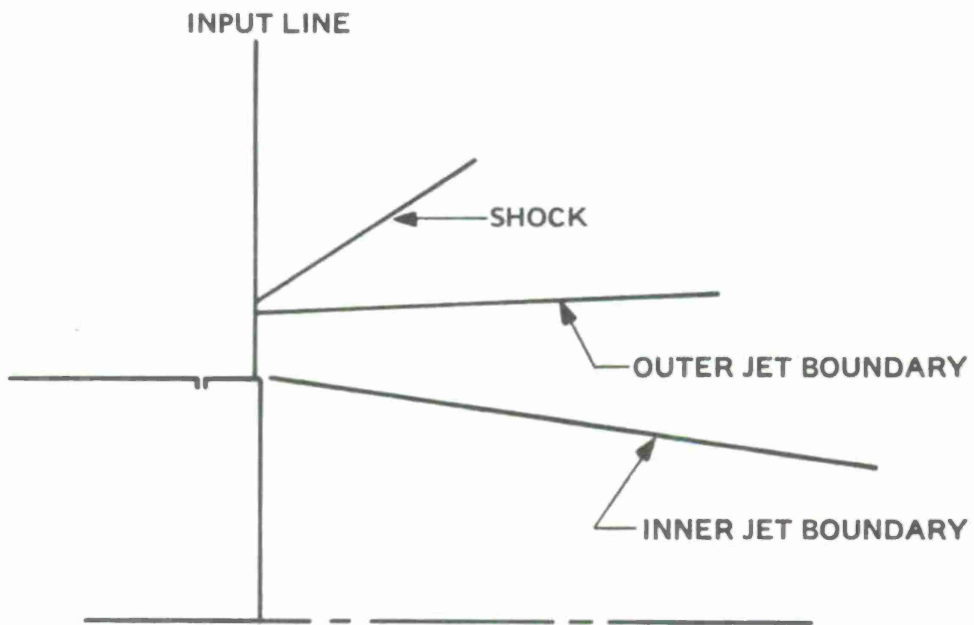


b. Predicted Shock Shape and Jet Boundaries, Test 106.

Figure 72. Predictions for Test 106.

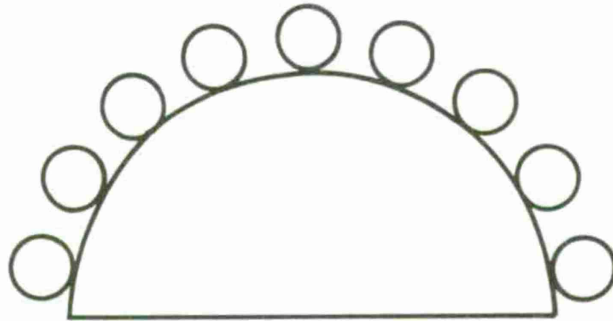


a. Predicted Jet Diameters at Model Lip, Test 108
(Drawn Half Scale).

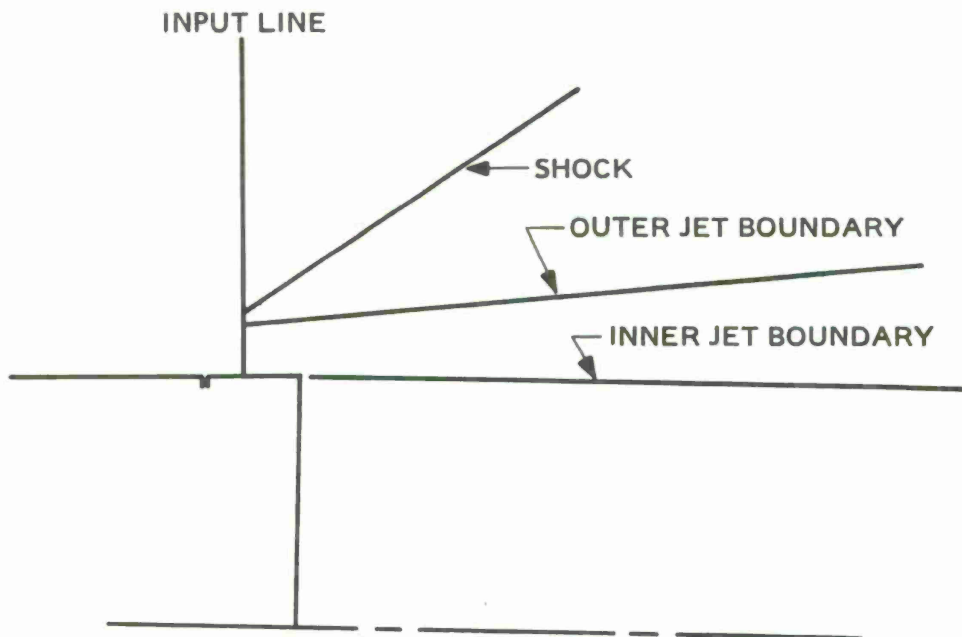


b. Predicted Shock Shape and Jet Boundaries, Test 108.

Figure 73. Predictions for Test 108.



a. Predicted Jet Diameters at Model Lip, Test 110
(Drawn Half Scale).



b. Predicted Shock Shape and Jet Boundaries, Test 110.

Figure 74. Predictions for Test 110.

UNCLASSIFIED

REFERENCES

1. Strahle, W. C., "Theoretical Consideration of Combustion Effects on Base Pressure in Supersonic Flight," *Twelfth Symposium (International) on Combustion*, p. 1163, The Combustion Institute, 1969.
2. Fein, Harvey L., "The Theoretical Performance of a Fuel-Rich Solid Propellant in an External Burning Assisted Projectile (U)," AIAA 7th Propulsion Joint Specialist Conference, June 14-18, 1971, Salt Lake City, Utah, *CPIA Publication 213*. CONFIDENTIAL
3. Fein, H. L., and Shelor, D. E., Contract N00174-71-C-0139, "Establishing the Feasibility of the External Burning Assisted Projectile (U)," Final Report, December 1971. CONFIDENTIAL
4. Fein, H. L., and Shelor, D. E., "Wind Tunnel Tests (U)," Final Report, Contract NOO174-72-C-0105, December 1971. CONFIDENTIAL
5. Harmon, D. B., Or., and Branch, W. H., "ARPA Project PRESTAGE Final Technical Report," Douglas Aircraft Co., DAC58864, October, 1967. CONFIDENTIAL
6. Dugger, G. L., and Monchick, L., "External Burning Ramjet Preliminary Feasibility Study," APL TG-892, March 1967.
7. Baker, W. T., Davis, T., and Mathews, S. E., "Reduction of Drag of a Projectile in a Supersonic Stream by the Combustion of Hydrogen in the Turbulent Wake," The John Hopkins University Applied Physics Laboratory, CM - 673, June 4, 1951.
8. Scanland, T. S., and Hebrank, W. H., "Drag Reduction Through Heat Addition to the Wake of Supersonic Missiles," Ballistic Research Laboratories Memorandum Report No. 596, June 1952.
9. Crocco, L., and Lees, L., *J. Aero Sci.* 19, p. 647, 1952.
10. Smith, R. C., Jr., *J.S.R.* V, p. 1360, 1968.
11. Chang, Paul K., *Separation of Flow*, Pergamon Press, New York (1970), p. 548.
12. Ibid, p. 542.
13. Reid, J., and Hastings, R. C., "Experiments on the Axi-Symmetric Flow over Afterbodies and Bases at $M = 2.0$," Royal Aircraft Establishment Report No. AERO. 2628, October 1959.
14. Alber, I. E., and Lees, L., *AIAA J.*, 6, p. 1343, 1968.
15. Billig, F. S., Orth, R. C., and Lasky, M., "A Unified Approach to the Problem of Gaseous Jet Penetration into a Supersonic Stream," presented at the AIAA 8th Aerospace Sciences Meeting, New York, N. Y., January 19-21, 1970.

UNCLASSIFIED

16. Shapiro, Ascher H., *The Dynamics and Thermodynamics of Compressible Fluid Flow, Volume I*, The Ronald Press Company, New York (1953), p. 466.
17. Abromovich, G. N., *The Theory of Turbulent Jets*, M.I.I. Press, Cambridge, pp. 268-271 (1963).
18. Cohen, L. S., Coulter, L. J., and Egan, W. S., Jr., *AIAA J.*, 9, p. 718, 1971.
19. Ambromovich, G. N., *The Theory of Turbulent Jets*, M.I.I. Press, Cambridge, p. 543 (1963).
20. Hosack, G. A., and O'Leary, R. A., "Base Burning Feasibility Investigation (U)," Rocketdyne, a Division of North American Rockwell, Final Report for Contract DAAH01-70-C-0173, December 1970. CONFIDENTIAL
21. Hsia, Henry Tao-Sye, "Equivalence of Secondary Injection to a Blunt Body in Supersonic Flow," *AIAA J.*, 4, p. 1832, 1966.
22. Ambrosio, A., and Wortman, A., "Stagnation Point Shock Detachment Distance for Flow Around Spheres and Cylinders," *ARS J V*, p. 281, 1962.

UNCLASSIFIED

UNCLASSIFIED

Security Classification

DOCUMENT CONTROL DATA - R & D

(Security classification of title, body of abstract and indexing annotation must be entered when the overall report is classified)

1. ORIGINATING ACTIVITY (Corporate author) Atlantic Research Corporation Shirley Highway at Edsall Road Alexandria, Virginia		2a. REPORT SECURITY CLASSIFICATION CONFIDENTIAL	
		2b. GROUP	
3. REPORT TITLE An Investigation of External Burning Propulsion for the 75mm Projectile (U)			
4. DESCRIPTIVE NOTES (Type of report and inclusive dates) Final Technical Report 1 March 1972 through 30 November 1972			
5. AUTHOR(S) (First name, middle initial, last name) Harvey L. Fein Dwight E. Shelor			
6. REPORT DATE January 1973	7a. TOTAL NO. OF PAGES 160	7b. NO. OF REFS 22	
8a. CONTRACT OR GRANT NO. F04611-72-C-0044	9a. ORIGINATOR'S REPORT NUMBER(S) AFRPL-TR-72-133		
b. PROJECT NO. 3148 Task 10 Program Element 62302F	9b. OTHER REPORT NO(S) (Any other numbers that may be assigned this report)		
c.			
d.			
10. DISTRIBUTION STATEMENT			
11. SUPPLEMENTARY NOTES		12. SPONSORING MILITARY ACTIVITY Air Force Rocket Propulsion Laboratory Edwards, California	
13. ABSTRACT Twenty external burning combustion tests were conducted with a 75mm half-model using the exhausts from fuel-rich solid propellants as the fuels. Test conditions simulated Mach 2.5 and Mach 2.0 flight at both sea level and an altitude of 15,000 feet. Base pressure ratios up to 0.85 were obtained at sea level, while at altitude these ratios were greater than unity. There was strong evidence that a wind tunnel interference effect severely restricted the measured base pressure rises. Since this interference effect would not be present in a real flight environment, flight performance should be significantly better than indicated by the current results.			

UNCLASSIFIED

DD FORM 1 NOV 65 1473

UNCLASSIFIED

Security Classification

UNCLASSIFIED

UNCLASSIFIED

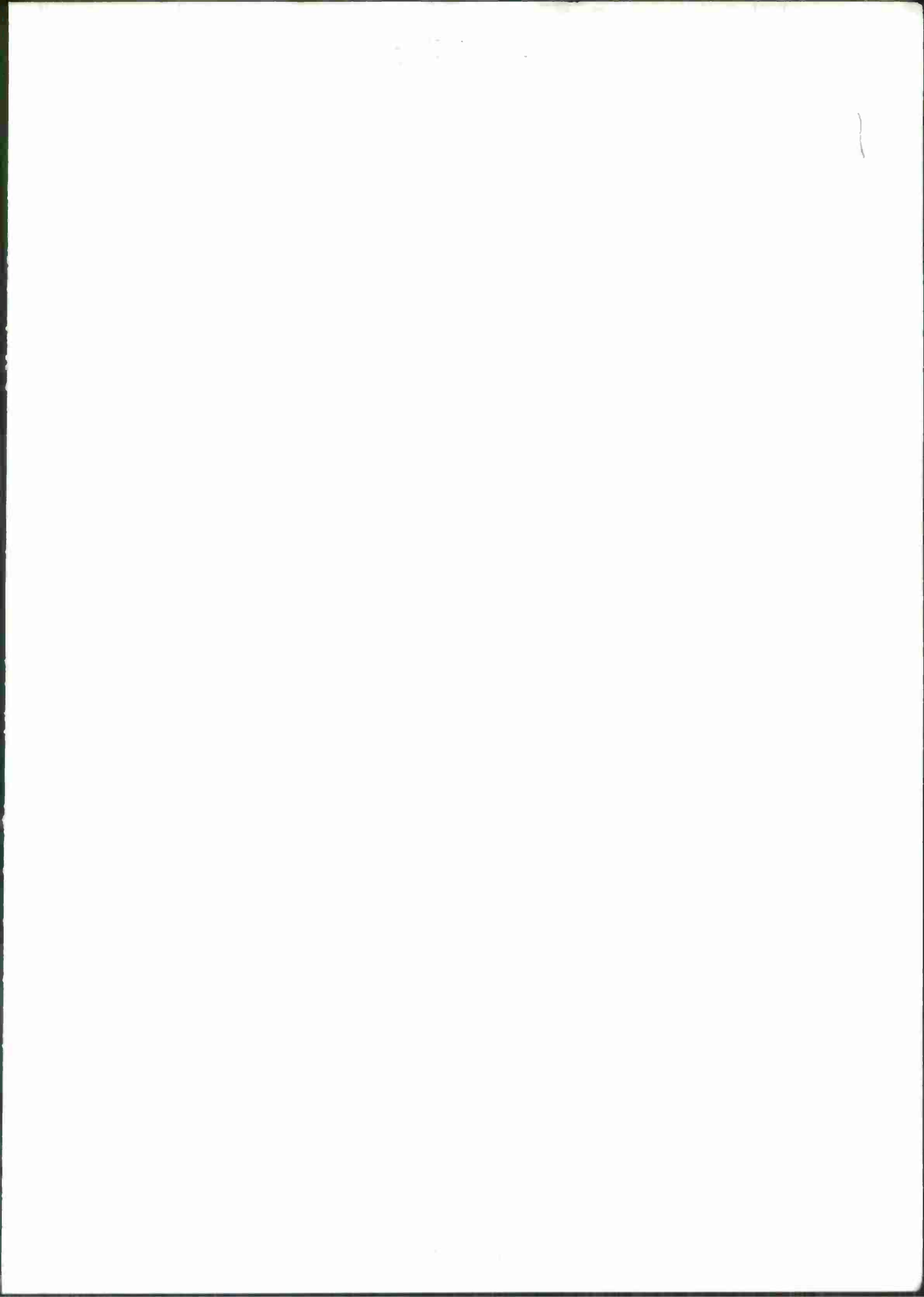
Security Classification

14.	KEY WORDS	LINK A		LINK B		LINK C	
		ROLE	WT	ROLE	WT	ROLE	WT
	External burning Supersonic combustion External burning propulsion Base pressure Base burning						

UNCLASSIFIED

UNCLASSIFIED

Security Classification



~~CONFIDENTIAL~~
UNCLASSIFIED



UNCLASSIFIED

~~CONFIDENTIAL~~